Durham E-Theses

Simulations and observables in relativistic cosmology

BARRERA-HINOJOSA, CRISTIAN,GUZMARO

How to cite:

BARRERA-HINOJOSA, CRISTIAN,GUZMARO (2021) *Simulations and observables in relativistic cosmology* , Durham theses, Durham University. Available at Durham E-Theses Online: http://etheses.dur.ac.uk/14184/

Use policy

The full-text may be used and/or reproduced, and given to third parties in any format or medium, without prior permission or charge, for personal research or study, educational, or not-for-profit purposes provided that:

- a full bibliographic reference is made to the original source
- a link is made to the metadata record in Durham E-Theses
- the full-text is not changed in any way

The full-text must not be sold in any format or medium without the formal permission of the copyright holders.

Please consult the full Durham E-Theses policy for further details.

Academic Support Office, Durham University, University Office, Old Elvet, Durham DH1 3HP
e-mail: e-theses.admin@dur.ac.uk Tel: +44 0191 334 6107
http://etheses.dur.ac.uk

Simulations and observables in relativistic cosmology

Cristian Guzmaro Barrera Hinojosa

Abstract: The huge leap in volume and precision that will be achieved by upcoming large sky surveys will make our observables sensitive to a number of effects previously ignored, such as relativistic effects. These can potentially represent new systematics to take into account, but also new probes for our cosmological models. In this thesis, we explore novel tools to model these type of effects, with a particular emphasis on frame-dragging — the leading order post-Newtonian effect — in cosmological N-body simulations.

In the first part, we discuss the implementation of a new code for general-relativistic simulations in cosmology, GRAMSES. The code is built upon the numerical infrastructure of the RAMSES code, and implements a constrained formulation of general relativity in which scalar and vector modes of the spacetime metric are calculated fully nonlinearly. We perform several tests against both theory and well-established, state-of-the-art relativistic codes, demonstrating that GRAMSES is able to produce robust results. Furthermore, we introduce a new, general method to generate initial conditions for particles, which circumvents the gauge issues affecting the standard prescriptions.

In the second part, we focus on exploring the impact of frame-dragging on different scenarios. Firstly, based on a high-resolution run with GRAMSES, we explore the behaviour of this effect in different types of dark matter haloes. In particular, we show that, although the gravitomagnetic force acting on dark matter is small relative to the Newtonian force, it can be up to one order of magnitude larger than previous literature results. Finally, we explore the possibility of detecting the gravitomagnetic effect that appears in lensing convergence maps via cross-correlations with the kinetic Sunyaev-Zel'dovich effect, which is imprinted in CMB maps. We make forecasts for next-generation weak-lensing surveys such as EUCLID and LSST, and CMB experiments such as Simons Observatory and CMB-S4, and find that the gravitomagnetic effect can be detected on small angular scales, provided that several foreground contaminations can be reliably removed.

Simulations and observables in relativistic cosmology

Cristian Guzmaro Barrera Hinojosa

A thesis presented for the degree of
Doctor of Philosophy

Institute for Computational Cosmology
Department of Physics
Durham University
United Kingdom

November 2021

Dedicated to

Dedicado a toda mi familia.

Contents

List of Figures

List of Tables

Declaration

The work in this thesis is based on research carried out in the Institute for Computational Cosmology, Department of Physics, Durham University, United Kingdom. No part of this thesis has been submitted elsewhere for any other degree or qualification and it is all my own work unless referenced to the contrary in the text.

The content presented in Chapter 2 has been published in:

Cristian Barrera-Hinojosa and Baojiu Li, "GRAMSES: a new route to general relativistic N-body simulations in cosmology. Part I. Methodology and code description", JCAP 01, 007, 2020.

The content presented in Chapter 3 has been published in:

Cristian Barrera-Hinojosa and Baojiu Li, "GRAMSES: a new route to general relativistic N-body simulations in cosmology. Part II. Initial conditions", JCAP 04, 056, 2020.

The content presented in Chapter 4 is based on my own contribution to the work that has been published in:

Julian Adamek, **Cristian Barrera-Hinojosa**, Marco Bruni, Baojiu Li, Hayley J. Macpherson and James B. Mertens, "Numerical solutions to Einstein's equations in a shearing-dust Universe: a code comparison", Class. Quant. Grav. 37, 154001, 2020.

The content presented in Chapter 5 has been published in:

Cristian Barrera-Hinojosa, Baojiu Li, Marco Bruni and Jian-hua He, "Vector modes in ΛCDM: the gravitomagnetic potential in dark matter haloes from relativistic N-body simulations", MNRAS 501, 4, 2021.

The content presented in Chapter 6 has been submitted to MNRAS as:

Cristian Barrera-Hinojosa, Baojiu Li and Yan-Chuan Cai "Looking for a twist: probing the cosmological gravitomagnetic potential via lensing and the kSZ effect", 2021.

The author of the thesis was primarily responsible for all aspects of this publication.

Copyright © November 2021 by Cristian Guzmaro Barrera Hinojosa.

"The copyright of this thesis rests with the author. No quotations from it should be published without the author's prior written consent and information derived from it should be acknowledged."

Acknowledgements

This time at Durham has been quite special, and I would like to start thanking everyone with whom I had the chance to share at some point during these four years.

I'm enormously grateful to Baojiu for being such an amazing supervisor. Thank you for all the support, guidance, and hard work during these four years, as well as for always keeping optimistic about this crazy project that gave me so many headaches, but also many satisfactions.

I want to express my gratitude to Kazuya Koyama and Shaun Cole, for accepting being examiners of my PhD defense, and for their valuable comments and discussions.

I'm very grateful to my collaborators during these years: Hayley, Marco, Julian, Jim, Jianhua and Cai. It has been a pleasure to work with all of you. Thank you for your contributions to the work presented in this thesis. Special thanks to the COSMA support team for making all of my work possible.

Many thanks to all the people from Durham which have made these four years enjoyable at some point in time. Special mention to César, Alma, Omar, Luz, Piotr, Matteo, Christoph, Joaquín, Arnau, Carol, and Claudio, for the good chats and experiences.

My amazing long-term office mates, Josh and Chris, also deserve a special mention. Thank you for making me feel at home at the ICC, as well as for your patience and forgiveness the many times I couldn't make it to coffee time or pub. The pandemic really made me miss all those daily interactions.

I'm grateful to all my friends back in Chile (or elsewhere now). Specially to Sergio, Juana, Amaru, Claudio, Manuel, Nico, Rodrigo and Felipe. I really look forward to sharing some good *chelas* sooner than later!

I also want to thank the people that have inspired me, one way or another, and gave me the confidence and courage to undertake this PhD path: Justo, Domenico and Ernesto.

Last but not least, I want to thank my family, for whom I have far more words of gratitude than I could possibly fit in this page. To my parents and brothers, for their neverending support throughout this strange journey far away from home, and to my wife, Yani, for your comprehension, love, and encouragement, which have kept me sane during the difficult times. You have been essential to make all of this happen!

This thesis was possible thanks to the support of ANID (formerly CONICYT) Chile, through the Becas Chile scholarship programme.

This thesis used the DiRAC@Durham facility managed by the Institute for Computational Cosmology on behalf of the STFC DiRAC HPC Facility (www.dirac.ac.uk). The equipment was funded by BEIS via STFC capital grants ST/K00042X/1, ST/P002293/1, ST/R002371/1 and ST/S002502/1, Durham University and STFC operation grant ST/R000832/1. DiRAC is part of the UK National e-Infrastructure.

Chapter 1

Introduction

1.1 General Relativity

Einstein's General Relativity (GR) is the most successful and accurate description of gravity to date. In this theory, space and time are no longer the static background in which the dynamics of bodies takes place, but they are a single, dynamic entity — spacetime — which can be deformed by the presence of energy and matter. As part of this interplay, particles are forced to move along geodesic trajectories of the spacetime, giving rise to what we experience as gravity. The predictions of GR have been confirmed numerous times, starting by the explanation for the precession of the perihelion of Mercury (Einstein, 1916b) — and anomalous phenomenon at the time — and later by the bending of light by the Sun (Dyson et al., 1920). More recently, the Gravity Probe B satellite (Everitt et al., 2011) measured the frame-dragging effect caused by the rotation of the Earth, which twists its surrounding spacetime, and the LIGO-VIRGO collaboration (Abbott et al., 2016) detected gravitational waves (GW) — propagating ripples in the spacetime — nearly a century after their prediction (Einstein, 1916a).

The fundamental object in this theory is the spacetime metric, $g_{\mu\nu}$, which defines the invariant 4D line element as

$$\mathrm{d}s^2 = g_{\mu\nu}\mathrm{d}x^\mu \mathrm{d}x^\nu \,, \tag{1.1.1}$$

where $x^\mu = (x^0, x^1, x^2, x^3)$ are spacetime coordinates. In this thesis, Greek indices run from 0 to 3, whereas Latin indices from 1 to 3, with repeated indices implying summation. In addition, throughout this Chapter, we adopt units such that the speed of light is set to unity, $c = 1$.

The Einstein field equations govern the dynamics of the spacetime in relation to the matter-energy content. Considering the presence of a Cosmological Constant Λ, these are given by

$$G_{\mu\nu} + \Lambda g_{\mu\nu} = 8\pi G T_{\mu\nu}\,, \tag{1.1.2}$$

where

$$G_{\mu\nu} \equiv R_{\mu\nu} - \frac{1}{2} R g_{\mu\nu}\,, \tag{1.1.3}$$

is the Einstein tensor, $R_{\mu\nu}$ is the Ricci tensor, $R \equiv g^{\mu\nu} R_{\mu\nu}$ the Ricci scalar, G is Newton's constant, and $T_{\mu\nu}$ is the energy-momentum tensor, which describes the matter-energy content. The dynamics of the latter can be derived from the contracted Bianchi identities satisfied by the Einstein tensor,

$$\nabla_\mu G^{\mu\nu} = 0\,, \tag{1.1.4}$$

which implies the local conservation of energy and momentum,

$$\nabla_\mu T^{\mu\nu} = 0\,. \tag{1.1.5}$$

In these, ∇_μ is the covariant derivative associated with $g_{\mu\nu}$, i.e., $\nabla^\mu g_{\mu\nu} = 0$.

A pivotal property of GR is that Eq. (1.1.2) is invariant under general coordinate transformations, i.e., it is a generally covariant theory. This property represents the freedom that we have to choose any particular set of coordinates to carry out calculations without losing physical information. Therefore, from the 10 independent components of $g_{\mu\nu}$, 4 correspond to coordinate reparameterisations and are therefore not physical. At the same time, Eq. (1.1.4) reveals the presence of 4 constraint equations, $G^{0\mu} = 8\pi G T^{0\mu}$, which fix 4 degrees of freedom (DOFs), thus leaving 2 dynamical DOFs in the gravitational field in GR (e.g., the two polarisation states of GWs). In practice, choosing a suitable coordinate system (gauge) can help to simplify the form of the equations for the particular problem at hand, which can be relevant from both analytical and computational standpoints.

1.2 The ΛCDM cosmological model

The study of the Universe as a system in which both its constituents and underlying spacetime evolve in time dates back to Friedmann (1922, 1924); Lemaître (1931); Robertson (1933); Walker (1937). Although the idea was largely dismissed originally, it started to gain terrain

after Hubble established that local galaxies were receding at a speed proportional to their distance (Hubble, 1929), which suggested that the Universe was expanding. Eventually, GR would become the basis of our current concordance cosmological model, ΛCDM.

In order to explain modern observations, the ΛCDM model assumes the existence of two hypothetical components that make up 95% of the total energy budget of our Universe: Cold Dark Matter (CDM), and a Cosmological Constant, Λ, which represents the simplest form of Dark Energy. The former corresponds to a matter component that only acts gravitationally, and was originally motivated by Zwicky (1933) in order to reconcile the large virial velocities observed in the Coma Cluster with its total mass, and later by the apparently flat rotation curves of galaxies (Rubin & Ford, 1970). The need for a Λ-term in Eq. (1.1.2) became clear only about 20 years ago with the discovery of the accelerated cosmic expansion via type Ia supernovae observations (Riess et al., 1998; Perlmutter et al., 1999), an effect that cannot be accounted for in a universe that only contains matter and radiation.

Although ΛCDM is remarkably successful at explaining a plethora of observations, from the distribution of galaxies and gravitational lensing, to the Cosmic Microwave Background (CMB), the physical origins of dark matter and dark energy still remain to be clearly determined, which has motivated a new generation of large-scale galaxy surveys, such as EUCLID, LSST and DESI. For instance, there is an ample spectrum of dark matter candidates, which range from light elementary particles to primordial black holes, and whether this is completely 'cold' is still debated. Likewise, the observed value of Λ is hard to motivate from a fundamental point of view, and alternative dark energy models via modifications of GR, such as Hu-Sawicki $f(R)$-gravity (Hu & Sawicki, 2007) or the DGP braneworld model (Dvali et al., 2000), are still compatible with current observations. More recently, several tensions between the inferred value of cosmological parameters from different observations have emerged. For instance, local measurements of the expansion rate (Riess et al., 2016) seem to differ from that inferred from CMB measurements (Aghanim et al., 2018) by over 3σ. While the origin of such discrepancy could be possibly explained by systematic effects in the observations, it could also be evidence for physics beyond ΛCDM.

The ΛCDM model is based on the Cosmological Principle, according to which the Universe can be treated as homogeneous and isotropic over large enough scales. Observations suggest that such a 'homogeneity scale' is around $\gtrsim$100 Mpc (e.g., Scrimgeour et al., 2012). The most general spacetime metric satisfying these properties is the Friedmann-Lemaître-Robertson-

Walker (FLRW) metric which, adopting the $(-,+,+,+)$ signature, is given by

$$\mathrm{d}s^2 = -\mathrm{d}t^2 + a^2(t)\gamma_{ij}\mathrm{d}x^i\mathrm{d}x^j\,, \tag{1.2.1}$$

where t is the cosmic (physical) time, x^i are comoving Cartesian coordinates, $a(t)$ is the scale factor, and γ_{ij} is the metric describing a 3-dimensional space with constant curvature K which classifies the spatial geometry of the FLRW universe as Euclidean ($K = 0$), spherical ($K > 0$) or hyperbolic ($K < 0$). The spatial metric in the general case is given by

$$\gamma_{ij}\mathrm{d}x^i\mathrm{d}x^j = \mathrm{d}r^2 + \chi^2(r)(\mathrm{d}\theta^2 + \sin^2\theta\mathrm{d}\varphi^2)\,, \tag{1.2.2}$$

where

$$\chi(r) = \begin{cases} r & \text{Euclidean case,} \quad K = 0\,, \\ \frac{1}{\sqrt{K}}\sin(\sqrt{K}r) & \text{spherical case,} \quad K > 0\,, \\ \frac{1}{\sqrt{|K|}}\sinh(\sqrt{|K|}r) & \text{hyperbolic case,} \quad K < 0\,. \end{cases} \tag{1.2.3}$$

The scale factor $a(t)$ describes the relative size of the spatial hypersurfaces at different times, and the expansion rate of is quantified by the Hubble parameter

$$H(t) \equiv \frac{1}{a}\frac{\mathrm{d}a}{\mathrm{d}t} \equiv \frac{\dot{a}}{a}\,, \tag{1.2.4}$$

which is positive (negative) for an expanding (contracting) universe. Observations show that our Universe is currently expanding at a rate of $H_0 = 67.36 \pm 0.54$ km/s/Mpc (Aghanim et al., 2018),[1] H_0 being the Hubble constant.

The matter-energy content of the Universe is typically described as a perfect fluid, whose energy-momentum tensor can be written as

$$T_{\mu\nu} = (\rho + p)u_\mu u_\nu + p g_{\mu\nu}\,, \tag{1.2.5}$$

where $u^\mu = \mathrm{d}x^\mu/\mathrm{d}\tau$ is the four-velocity of the fluid, τ being the proper time, ρ its density and p its pressure. In the FLRW Universe, the cosmic fluid properties can also be described as homogeneous and isotropic, i.e., as strictly time-dependent. Since after the end of the inflationary period, the Universe was first dominated by radiation, then by matter, and eventually by dark energy, it is essential to understand how the energy-density of the different

[1] This is the value obtained using CMB data from PLANCK assuming a ΛCDM model. Local measurements based on type Ia supernovae find a value close to $H_0 = 73.24 \pm 1.74$ km/s/Mpc (Riess et al., 2016), which remains in tension with the previous result.

components evolves. From the $\nu = 0$ component of Eq. (1.1.5), we get the continuity equation for each component,

$$\frac{\mathrm{d}\rho}{\mathrm{d}t} + 3H(\rho + p) = 0\,. \tag{1.2.6}$$

Hence, assuming a constant equation-of-state parameter $w = p(t)/\rho(t)$, we find

$$\rho(t) = \rho_0 a^{-3(1+w)}\,. \tag{1.2.7}$$

In Eq. (1.2.7), and in the remainder of this thesis, the subscript 0 is used to denote the present-day values. This shows that the density of radiation ($w = 1/3$) and of matter ($w = 0$) respectively dilute as $\propto a^3$ and $\propto a^4$. Likewise, this shows that the density of Λ ($w = -1$) remains constant, as expected.

The evolution of the scale factor is dictated by Eq. (1.1.2). From the 00-component and trace-part of the ij-component, we find the first and second Friedmann equations,

$$H^2 + \frac{K}{a^2} = \frac{8\pi G}{3}\rho + \frac{\Lambda}{3}\,, \tag{1.2.8}$$

$$\frac{\mathrm{d}H}{\mathrm{d}t} + H^2 = -\frac{4\pi G}{3}(\rho + 3p) + \frac{\Lambda}{3}\,. \tag{1.2.9}$$

It is customary to write Eq. (1.2.8) using the solutions to Eq. (1.2.7) as

$$H = H_0\sqrt{\Omega_m a^{-3} + \Omega_r a^{-4} + \Omega_K a^{-2} + \Omega_\Lambda}\,, \tag{1.2.10}$$

where we have introduced a set of dimensionless density parameters (present-day values) for matter, radiation, Λ, and spatial curvature, respectively defined as

$$\Omega_m \equiv \frac{\rho_{m,0}}{\rho_{\mathrm{c},0}}\,, \quad \Omega_r \equiv \frac{\rho_{r,0}}{\rho_{\mathrm{c},0}}\,, \quad \Omega_\Lambda \equiv \frac{\Lambda}{3H_0^2}\,, \quad \Omega_K \equiv \frac{-K}{H_0^2}\,. \tag{1.2.11}$$

In these, $\rho_{\mathrm{c},0} \equiv 3H_0^2/8\pi G$ is the critical density of the Universe today. The joint analysis of CMB measurements, including information about temperature, polarisation, and lensing, together with Baryon Acoustic Oscillations (BAO) data from galaxy surveys, finds that $\{\Omega_m, \Omega_\Lambda, \Omega_K\} = \{0.3111 \pm 0.0056, 0.6889 \pm 0.0056, 0.0007 \pm 0.0019\}$ (Aghanim et al., 2018), which shows that the Universe is spatially flat to a good approximation. Therefore, we set $\Omega_K = 0$ for the remainder of this thesis.

Finally, solving Eq. (1.2.10) for a universe dominated by each individual species, we find that

$$a(t) \propto \begin{cases} t^{\frac{2}{3(1+w)}} & w \neq -1\,, \\ e^{Ht} & w = -1\,. \end{cases} \tag{1.2.12}$$

In particular, the second line of (1.2.12) describes the exponential cosmic expansion driven

by the cosmological constant Λ, which is expected to take place in the far future when the Universe is completely dominated by this component.

Naturally, the above description is valid above the homogeneity scale in an statistical sense, but it is not enough to explain the distribution of cosmic structures and their physical properties. The most common way to study these is to consider the FLRW as a 'background' and introduce perturbations to represent the inhomogeneities. However, due to the coordinate-invariance of GR discussed in Section 1.1, there is no unique way to describe such a perturbed universe, but one is free to fix 4 residual 'gauge' DOFs that correspond to the freedom of choosing a coordinate system.

In the description of the FLRW Universe above, we have implicitly selected a coordinate system such that particles expanding with the Universe remain at fixed values of the comoving coordinates, but this does not need to be the case once perturbations are included. In the latter case, the two options that immediately appear are to attach our coordinate system to either the points in the unperturbed spacetime, or to the perturbed cosmic fluid. The former corresponds to the *Newtonian gauge*, and observers in this gauge will detect peculiar velocities and gravitational forces. Moreover, the Newtonian limit is straightforward in this gauge, and hence it is widely used to study structure formation. On the other hand, the second option corresponds to the *synchronous comoving gauge*, in which observers will not measure peculiar velocities nor a gravitational field since they are free-falling with the particles. The drawbacks of this gauge is that it can become ill-defined if the particles intersect each other, and the Newtonian limit is not direct. Nonetheless, this gauge plays an important role in the study of perturbations during inflation.

While the Newtonian gauge only describes two scalar DOFs in the metric, it can be generalized into the *Poisson gauge* (or longitudinal gauge). In this gauge, the linearly perturbed metric takes the form

$$\mathrm{d}s^2 = -(1+2\Phi)\mathrm{d}t^2 + a^2(t)\left[(1-2\Psi)\delta_{ij} + h_{ij}\right]\mathrm{d}x^i\mathrm{d}x^j + 2\delta_{ij}B^i\mathrm{d}x^j\mathrm{d}t\,, \tag{1.2.13}$$

where Φ and Ψ are scalar DOFs, which correspond to the Bardeen potentials (Bardeen, 1980), B^i correspond to vector DOFs, which satisfy the transverse (divergence-free) condition $\partial_i B^i = 0$, $\partial_i \equiv \partial/\partial x^i$ being the partial derivative with respect to the comoving Cartesian coordinates, and h_{ij} are tensor DOFs, which are transverse and traceless, i.e., $\partial_i h^{ij} = 0 = h^i_i$. Structure formation in ΛCDM is mainly driven by the presence of scalars and hence the latter types of DOFs are typically neglected for such purpose. Likewise, the anisotropic stress is

usually very small and sets the approximation $\Phi = \Psi$, so that a single, scalar DOFs is to be determined. Under these assumptions, a combination of the 00 and $0i$ components of the Einstein's equations Eq. (1.1.2) yields the following form of the Poisson equation in Fourier space

$$-k^2\Phi = 4\pi G a^2 \left[\bar{\rho}\delta - 3\frac{H}{k^2}(\bar{\rho}+\bar{p})\theta\right] , \tag{1.2.14}$$

where

$$\delta(\mathbf{x},t) \equiv \frac{\rho(\mathbf{x},t)}{\bar{\rho}(t)} - 1 \tag{1.2.15}$$

$$\theta(\mathbf{x},t) \equiv \partial_i v^i , \tag{1.2.16}$$

are the overdensity and velocity divergence fields, respectively, and quantities with overbar represent background values. In addition, the conservation equations $\nabla_\mu T^{\mu i} = 0$ and $\nabla_\mu T^{\mu 0} = 0$, correspond to the relativistic Euler and continuity equations, which respectively take the form (Ma & Bertschinger, 1995)

$$\dot{\theta} + H\theta = -\nabla^2\Phi , \tag{1.2.17}$$

$$\dot{\delta} + \theta - 3\dot{\Phi} = 0 . \tag{1.2.18}$$

The last term in the left-hand side of Eq. (1.2.18) can be interpreted as a GR effect due to the expansion of the volume elements, which can be shown to be small on scales inside the horizon, i.e., when $k \gg \mathcal{H}$, $\mathcal{H} = aH$ being the conformal Hubble factor. Similarly, the last term in the right hand side of Eq. (1.2.14) is suppressed by $\mathcal{H}/k$ with respect to $\bar{\rho}\delta$, which is the source of the gravitational potential in Newtonian gravity. On the other hand, these terms become important on horizon ($k \simeq \mathcal{H}$) and super-horizon ($k \ll \mathcal{H}$) scales and thus are essential for a consistent description of the Universe on large scales.

Although the standard perturbation theory approach is exceptionally useful to predict the large-scale properties of the observed Universe, at late times the results start to break down on scales of tens of Mpc, where the overdensity field starts to become nonlinear and complex cosmic structures start to develop. Moreover, the perfect-fluid (dust) approximation of CDM also breaks down at late times as this enters the multi-streaming regime and shell (orbit) crossing events become frequent. One important consequence of this phenomenon is that the velocity field of CDM, which in perturbation theory only accounts for a curl-free component via Eq. (1.2.16), can develop vorticity, which corresponds to a rotational (divergence-free) component. In fact, vorticity vanishes exactly in a perfect fluid (Lu et al., 2009), hence

perturbation theory cannot capture this effect at any order adopting such a model. These limitations serve as motivations for the use of N-body simulations for the accurate study of our Universe, which we introduce next.

1.3 Newtonian simulations of structure formation

As an alternative to avoid the shortcomings of perturbation theory, we can simplify the problem of solving GR by adopting the Newtonian limit, which is valid for high densities and velocities as long as gravity remains weak, and as long as matter is moving slowly compared to the speed of light, i.e., $|\mathbf{v}| \ll c$, $\mathbf{v}$ being the peculiar velocity. These are reasonably good approximations for the cosmological dynamics of non-relativistic matter such as CDM, as confirmed by the remarkable success of Newtonian simulations at explaining the observable Universe during the last decades (e.g., Springel et al., 2005; Vogelsberger et al., 2014; Schaye et al., 2015).

In the Newtonian approximation, the relevant set of equations to solve correspond to a self-gravitating collisionless fluid, given by

$$\nabla^2\Phi_{\rm N} = 4\pi G\bar{\rho}a^2\delta_{\rm sim}\,, \qquad \text{Poisson} \tag{1.3.1}$$

$$\dot{\mathbf{v}} + H\mathbf{v} + \frac{1}{a}(\mathbf{v}\cdot\nabla)\mathbf{v} = -\frac{1}{a}\nabla\Phi_{\rm N}\,, \qquad \text{Euler} \tag{1.3.2}$$

$$\frac{\partial\delta_{\rm sim}}{\partial t} + \frac{1}{a}\nabla\cdot(1+\delta_{\rm sim})\mathbf{v} = 0\,, \qquad \text{continuity} \tag{1.3.3}$$

where ∇ is the flat-space gradient operator, and we have used $\delta_{\rm sim}$ to denote the overdensity field used in the simulations.

However, cosmological N-body simulations do not solve the above fluid equations directly but rather discretise the fluid in terms of particles, which are regarded as samples of its phase-space distribution. Since the position and velocity of each individual particle is tracked, the velocity field of CDM is allowed to have different values at a given position, and in this way the shell-crossing issue affecting the fluid model approach is avoided. At the same time, alternatively to solving Eq. (1.3.1), we can directly calculate the force acting on the i-th simulation particle, located at the position $\mathbf{r}_i$, as

$$\mathbf{F}_i = -Gm_i\sum_{j\neq i}^{N}\frac{m_j}{r_{ij}^3}\mathbf{r}_{ij}\,, \tag{1.3.4}$$

where N is the number of particles in the simulations, m_j is the mass of the j-th particle, $\mathbf{r}_{ij} = \mathbf{r}_i - \mathbf{r}_j$, and $r_{ij} = |\mathbf{r}_{ij}|$. Hence, there are two major approaches to calculate the

gravitational interaction between the particles in a simulation. On the one hand, particle-mesh (PM) codes solve the Poisson equation (1.3.1) on a grid that covers the whole simulation volume via a finite difference approximation, and the force acting on a given particle can be evaluated by interpolating gradients of the gravitational potential to its position. Given that at late times the density of matter can vary many orders of magnitude from voids — extremely underdense regions that contain very few or no galaxies — to the core of dark matter haloes, adaptive-mesh refinement (AMR) codes such as RAMSES (Teyssier, 2002) can achieve high spatial (or force) resolution on high-density regions very efficiently.

On the other hand, particle-tree codes, such as GADGET-2 (Springel, 2005), use Eq. (1.3.4) to calculate the short-range force acting on a given particle due to neighbouring particles by direct summation,[2] while the long-range contribution from distant particles — which is smaller in magnitude — is treated separately to minimise the number of computations; either by grouping particles together (multipole expansion method), e.g. GADGET-2 (Springel, 2005) and AREPO (Weinberger et al., 2020), or by solving Eq. (1.3.1) using mesh-based Fourier methods (Tree-PM method), e.g. GADGET-2 and GIZMO (Hopkins, 2015).

Let us now briefly discuss Newtonian simulations from a GR perspective.[3] Firstly, we note that Eqs. (1.3.1)-(1.3.3) do not coincide with their counterparts from the Poisson gauge, Eqs. (1.2.14)-(1.2.18). This is expected since, by construction, the Newtonian equations are valid on scales $k \gg \mathcal{H}$ — where relativistic effects are not present, but at the same time it makes their interpretation on large-scales non-trivial; the latter is critical for modern sky surveys as these will sample large-scale modes. The modern, relativistic interpretation of Newtonian simulations is done in terms of the so-called 'N-body' gauge (Fidler et al., 2015), which is fixed such that, the equations of motion for matter, as well as the Poisson equation, take the exact same form as in the Newtonian theory. This interpretation, however, is done in the linear regime of GR, and only taking into account scalar perturbations. More in-depth discussion on this aspect is presented in Chapter 3, as this is crucial for setting up correct initial conditions from perturbation theory.

Although Newtonian simulations can be given a relativistic interpretation, some relativistic effects still lie beyond this picture. In particular, the Newtonian approximation does not solve the equations that govern the vector and tensor DOFs present in Eq. (1.2.13), as well as that for the second scalar potential, Ψ. Furthermore, some drawbacks become apparent

[2] In practice, a short-scale cut-off (softening length) is required in order to avoid divergences in Eq. (1.3.4) when particles are too close to each other.

[3] This is discussed in detail in Chapter 3.

when relativistic species are considered and hence the Newtonian approximation is violated. For instance, the inclusion of neutrino particles in the simulations often requires modifying the equations of motion to have an approximately relativistic form in order to avoid reaching super-luminal speeds (Elbers et al., 2020). In addition, it has been argued that the quasi-static approximation does not hold well in some dark energy models (Sawicki & Bellini, 2015).

1.4 Relativistic effects in cosmology

In the coming decade, a number of large sky surveys, such as DESI (Aghamousa et al., 2016), EUCLID (Laureijs et al., 2011), LSST (Weinberg et al., 2013) and SKA (Dewdney et al., 2013), will map the large-scale structure (LSS) of the Universe with exquisite detail, and the resulting data will allow cosmological parameters to be measured with unprecedented precision. As the precision and volume of observations keep improving, it is more important than ever to be able to make correct physical interpretations of these data, and this means that we must have accurate theoretical predictions of the observables, taking into account various systematic effects that were neglected in the past, as is the case of GR effects.

A family of relativistic effects come into play when we take into account the fact that our telescopes do not observe the intrinsic distribution of matter, but its projection into the past light-cone. This introduces a number of corrections to the galaxy number counts (Bonvin & Durrer, 2011) which encode physical effects undergone by the photons in their propagation across the inhomogeneous Universe, such as the Doppler effect, gravitational redshift, and the integrated Sachs-Wolfe (ISW) effect. They can also affect other observables such as the brightness-temperature fluctuations from 21 cm intensity mapping experiments, e.g., SKA (Hall et al., 2013), as well as the luminosity distance from type-Ia supernovae observations (Bonvin et al., 2006), and similarly the gravitational wave luminosity distance that will be measured by future detectors such as LISA (Garoffolo et al., 2020).

As mentioned before, the metric DOFs that are missed by Newtonian simulations can also introduce GR effects in our observables. In particular, the leading-order post-Newtonian correction to Newtonian gravity corresponds to the gravitomagnetic (frame-dragging) potential — a vector-type (spin-1) perturbation of the gravitational field that describes the twisting of the spacetime due to rotational matter flows. The effects of frame-dragging around the Earth have been detected in the last two decades by the Gravity Probe B satellite (Everitt et al.,

2011). For this, the satellite was equipped with a set of gyroscopes, and followed a polar orbit around the Earth for nearly 16 months. According to GR, Earth's rotation exerts a frame-dragging effect on the gyroscopes, which causes a precession of about 40 milliarcseconds per year that is perpendicular to the orbital plane. Taking into account the various systematics involved, the detection of such a small effect, in agreement with GR, was achieved with a $\sim 20\%$ error.

At the cosmological level, the frame-dragging effect is encoded by B^i in Eq. (1.2.13), but so far its faint observable signatures are swamped by the Newtonian signal (e.g., Cuesta-Lazaro et al., 2018). The post-Friedmann expansion developed by Bruni et al. (2014); Milillo et al. (2015) has enabled to study some of its properties based on Newtonian N-body simulations (Thomas et al., 2015a) in an approximate yet nonlinear way. This has been possible because, at leading order in such an expansion, the gravitomagnetic field is sourced by the rotational component of the *Newtonian* momentum field through an elliptic-type (Poisson-like) equation.

A unified, nonlinear GR treatment of structure formation and spacetime may also shed light on the long-standing issue of the back-reaction effect (Buchert & Räsänen, 2012), i.e., the impact of matter inhomogeneities on the cosmic expansion rate. The assumption of a FLRW background in Newtonian simulations effectively turns the Hubble parameter into an external input that is dissociated from the structure formation history. Furthermore, attempts to include this back-reaction in Newtonian simulations result in null contributions by construction (Buchert & Ehlers, 1997; Kaiser, 2017; Buchert, 2018). Even if the size of the back-reaction effects remains controversial, and hence it may not fulfill its original purpose of explaining the observed accelerated cosmic expansion on its own, it has been argued (Heinesen & Buchert, 2020) that this could still contribute to our understanding of this phenomenon, and to possibly alleviating the current 3σ tension between the Hubble constant determination from the local (Riess et al., 2016) and distant (Aghanim et al., 2018) Universe. Recent studies of back-reaction effects in a GR framework show that local deviations from the average expansion rate of the Universe can be substantial in underdense regions (Bentivegna & Bruni, 2016) and might impact our estimation of cosmological parameters in a ΛCDM model even at the percent level (Macpherson et al., 2018a). In any case, a fully nonlinear, general relativistic framework is needed in order to reach conclusive answers to this problem in the late-time Universe (Buchert et al., 2015; Roukema, 2018; Roukema et al., 2019; Vigneron & Buchert, 2019).

1.5 Relativistic simulations in cosmology

The development of cosmological simulations of structure formation based on GR has received increasing attention in the last few years, not only as a more accurate counterpart to Newtonian simulations in the era of precision cosmology, but also as a natural framework to study phenomena beyond the Newtonian approximation. The rise of modern N-body cosmological simulations taking a leap beyond the Newtonian approximation was first achieved by the *gevolution* code (Adamek et al., 2013, 2014, 2015, 2016a). This code is based on a weak-field expansion around a FLRW background, in which certain terms in the equations for the gravitational sector are truncated, while the energy-momentum tensor components can remain large in amplitude, and become 'dressed' by the weakly perturbed metric. Following the standards set by state-of-the-art Newtonian simulations, in *gevolution* the dark matter content of the Universe is described as a particle ensemble, which allows one to track them even after trajectory-crossing occurs. The latter is crucial for getting a realistic structure formation history as this phenomenon appears in the formation of virialised dark matter haloes.

Another interesting path for implementing general relativistic cosmological simulations is to resort to Numerical Relativity, which condenses the theoretical and numerical tools needed for modelling relativistic systems. This approach is based on the 3+1 spacetime foliation, in which the Einstein's field equations are projected onto 3D hypersurfaces that can be evolved forward in time. Incidentally, such a formalism was originally developed by Arnowitt et al. (1959) to construct a Hamiltonian formulation of GR, which plays a central role in theories of quantum gravity.

Even if the first applications of numerical relativity to study cosmological spacetimes were explored during the 80's (Goldwirth & Piran, 1989), modern developments in this direction arguably started with the COSMOGRAPH code (Mertens et al., 2016; Giblin et al., 2016) and the investigations of Bentivegna & Bruni (2016), followed by that of Macpherson et al. (2017). Some of these GR codes based on numerical relativity share a common feature of being developed upon the Einstein Toolkit (Löffler et al., 2012), an open-source community infrastructure for relativistic astrophysics. These works implement the Baumgarte-Shapiro-Shibata-Nakamura (BSSN) formulation for a numerically stable spacetime evolution (Nakamura et al., 1987; Shibata & Nakamura, 1995; Baumgarte & Shapiro, 1999) — one of the cornerstones in modern numerical relativity — and general relativistic hydrodynamics for the matter sector. This latter aspect, however, is different from standard cosmological sim-

ulations and the approximation of treating CDM as a fluid means that particle trajectories after shell crossing in bound structures are not exactly followed during the simulation. As an example, a comparison of fully non-linear GR simulations with pressureless dark matter fluid and Newtonian N-body simulations shows partial discrepancies inside the (Newtonian) dark matter haloes where the weak field condition is violated (East et al., 2018), but the different treatments for matter make the results difficult to assess and hence demands a fully GR cosmological N-body simulation (East et al., 2019).

The first implementations of three-dimensional *N-body* simulations based on numerical relativity were carried out in the late 90's for the study of black hole formation (Shibata, 1999), and various groups have implemented these in general relativistic cosmological codes in recent years. In Giblin et al. (2018) the full Einstein equations are solved using the BSSN formalism with different gauge conditions, and featuring a tri-cubic spline (TCS) scheme for increasing the smoothness of the density field described by the particle ensemble. The code introduced in Daverio et al. (2019) adopts the damped CCZ4 formalism (Bona et al., 2003; Gundlach et al., 2005; Alic et al., 2012) for solving the Einstein equations coupled to a leapfrog (Kick-Drift-Kick) scheme for particles, and can achieve a stable evolution of cosmological simulations up to redshift $z \sim 10$. The numerical relativity code from Pretorius & East (2018); East et al. (2019) is well-established and solves the Einstein equations using a generalised harmonic formalism (Pretorius, 2005) and AMR. This has been extensively applied for running simulations of both compact objects and, more recently, to cosmological scenarios. While numerical relativity codes allow one to run full GR simulations, their numerical implementation and long-term stability are very challenging due to the presence of dynamical DOFs in the metric. It is well known that the evolution equations for the gravitational sector in the $3+1$ formalism are only weakly hyperbolic and hence numerically unstable (Kidder et al., 2001), a problem that in the BSSN formalism is fixed by the introduction of additional dynamical variables. In addition, solving the evolution equations accurately requires fine time-steps, which in the case of cosmological simulations can become several orders of magnitude smaller than the time scale over which the particles are typically evolved. However, assuming that GW (which are the only dynamical DOF in GR) do not play a significant role in the cosmological dynamics and its back-reaction on the spacetime, it is possible to follow a formulation in which we can neglect these so that time evolution is only due to the matter sector. This is very much in the similar spirit as the 'waveless theories of gravity' developed originally by Isenberg in the late 70's but unpublished at the time (Isenberg, 2008), and latter by Wilson & Mathews (1989), who sought the natural generalisation of Newtonian gravity within GR.

The GRAMSES code, introduced in Chapter 2, follows this approach, and thus represents a new approach for general-relativistic N-body simulations in cosmology.

1.6 Outline of this Thesis

In this thesis, we aim to develop cosmological N-body simulations based on GR, as a novel numerical tool for an accurate and efficient modelling of some of the most prominent relativistic effects. At the same time, we aim to explore in detail the imprints of these effects — particularly of frame-dragging — in cosmological observables, as well as their role in future sky surveys.

The remainder of this thesis is organised as follows. In Chapter 2 we introduce GRAMSES, a newly-developed general-relativistic code for N-body simulations in cosmology based on RAMSES. In Chapter 3 we discuss the method used to generate the correct initial conditions (i.e., particles' position and velocity) for the GR simulations. In Chapter 4 we study the effect of frame-dragging in light propagation in a toy Universe, which is used as a test to compare a coordinate-independent prediction (i.e. an observable in a GR sense) obtained from different state-of-the-art GR codes for their validation. In Chapter 5 we study the vector modes of ΛCDM, namely the vorticity of the dark matter velocity field, as well as the gravitomagnetic potential. In Chapter 6 we investigate the detectability of the cosmological frame-dragging effect via cross-correlations of weak-lensing and the kinetic Sunyaev-Zel'dovich (kSZ) effect imprinted in the CMB. Finally, in Chapter 7 we discuss the main conclusions and outlooks of potential research directions that could go beyond the results presented in this thesis.

Chapter 2

The GRAMSES code

2.1 Introduction

In this Chapter we introduce GRAMSES, a new code which combines a set of features of state-of-the-art general relativistic codes aimed at fully non-linear and background-independent cosmological structure formation simulations. In order to deal with the nonlinear general relativistic equations for the gravitational sector in an optimal way for cosmology, GRAMSES adopts a so-called fully constrained formulation of GR (Bonazzola et al., 2004; Cordero-Carrión et al., 2008), in which only elliptic-type partial differential equations (PDEs) are solved to reconstruct the spacetime metric in the absence of GWs (Cordero-Carrión et al., 2009; Cordero-Carrion et al., 2012). GRAMSES solves these PDEs using multigrid Gauss-Seidel relaxation, and offers an N-body description for non-relativistic dark matter particles that supports AMR to increase force resolution in high-density regions, so that the cosmic web formed in the simulations can be resolved to a high degree of details even after shell crossing. Our code is based on the publicly-available, free-licensed N-body and hydrodynamical simulation code RAMSES (Teyssier, 2002), which is efficiently parallelised using Message Passing Interface (MPI). Particles are evolved along geodesics using a leapfrog method, and the particle-to-mesh projection and force interpolation is performed in a Cloud-In-Cell (CIC) scheme (Hockney & Eastwood, Inc., Bristol, PA, USA, 1988).

The Chapter is organised as follows. In Section 2.2 we introduce the equations for the gravitational sector in the fully constrained ADM $(3+1)$ formulation of GR, while in Section 2.3 we describe the matter sector. In Section 2.4 we discuss the code structure and the numerical implementations of the GR equations in GRAMSES, and in Section 2.5 we present some test results for the calculation of the relativistic source terms as well as for the multigrid

and geodesic solvers. Finally, in Section 2.6 we present some first results for cosmological simulations in a ΛCDM universe, although the generation of initial conditions and physical implications will be addressed in Chapter 3.

Throughout this Chapter we adopt the $(-,+,+,+)$ signature for the spacetime metric. Geometric units, where $G = c = 1$, are used in the theory part of the Chapter for brevity, but this are restored in Section 2.4 in order to introduce code units (which are used in the actual equations solved in GRAMSES). Greek indices run from 0 to 3, whereas Latin ones from 1 to 3 only, with repeated indices implying summation.

2.2 Field equations for the gravitational sector

In this section we review some fundamental aspects of numerical relativity that are at the core of this work. For a comprehensive discussion on these topics we refer the reader to Alcubierre (2008); Baumgarte & Shapiro (2010); Masaru (2015).

2.2.1 The Arnowitt-Deser-Misner formalism

In the ADM (3+1) formalism (Arnowitt et al., 1959), the 4-dimensional spacetime is foliated into 3-dimensional hypersurfaces of constant times characterised by some unit vector n^μ, with which we can write a set of evolution and constraint equations for the variables (γ_{ij}, K_{ij}), representing the (induced) spatial metric of the 3-dimensional embedded manifold and its extrinsic curvature, respectively. The spacetime metric in the ADM formalism is given by

$$\mathrm{d}s^2 = g_{\mu\nu}\mathrm{d}x^\mu \mathrm{d}x^\nu = -\alpha^2 \mathrm{d}t^2 + \gamma_{ij}(\beta^i \mathrm{d}t + \mathrm{d}x^i)(\beta^j \mathrm{d}t + \mathrm{d}x^j), \tag{2.2.1}$$

in which the lapse function α and shift vector β^i represent gauge (or coordinate) DOF. The projection of the Einstein equations into the 3-dimensional hypersurfaces yields the Hamiltonian constraint and the momentum constraint, respectively given by

$$R + K^2 - K_{ij}K^{ij} = 16\pi\rho\,, \tag{2.2.2}$$

$$D_j(K^{ij} - \gamma^{ij}K) = 8\pi S^i\,, \tag{2.2.3}$$

where $K = \gamma^{ij}K_{ij}$ is the trace of the extrinsic curvature, D_i the covariant derivative associated with the spatial metric γ_{ij} and R the Ricci scalar. Here, we have introduced the energy density ρ and the momentum density S_i measured by a normal observer n^μ, which are calculated by

projecting the energy-momentum tensor as

$$\rho \equiv n_\mu n_\nu T^{\mu\nu} \,, \tag{2.2.4}$$

$$S_i \equiv -\gamma_{i\mu} n_\nu T^{\mu\nu} \,, \tag{2.2.5}$$

where $n_\mu = (-\alpha, 0)$. In addition to the constraint equations (2.2.2) and (2.2.3), which offer no dynamics, the evolution equations for (γ_{ij}, K_{ij}) are

$$(\partial_t - \mathcal{L}_\beta)\gamma_{ij} = -2\alpha K_{ij} \,, \tag{2.2.6}$$

$$(\partial_t - \mathcal{L}_\beta)K_{ij} = -D_i D_j \alpha + \alpha(R_{ij} - 2K_{ik}K^k_j + KK_{ij}) - 8\pi\alpha\left[S_{ij} - \frac{1}{2}\gamma_{ij}(S-\rho)\right] \,, \tag{2.2.7}$$

where

$$\mathcal{L}_\beta \gamma_{ij} = D_i\beta_j + D_j\beta_i \,, \tag{2.2.8}$$

and

$$\mathcal{L}_\beta K_{ij} = \beta^k \partial_k K_{ij} + K_{ik}\partial_j\beta^k + K_{kj}\partial_i\beta^k \,, \tag{2.2.9}$$

correspond to Lie derivatives along β^i. In addition to the matter source terms (2.2.4) and (2.2.5), in Eq. (2.2.7) we have defined the spatial stress $S_{ij} \equiv \gamma_{i\mu}\gamma_{j\nu}T^{\mu\nu}$, with $S = \gamma^{ij}S_{ij}$ its trace.

In order to disentangle the physical and gauge DOF at the nonlinear level we can resort to decompose (γ_{ij}, K_{ij}). As a method to single out a particular degree of freedom in the spatial metric γ_{ij}, we use the conformal transformation (Lichnérowicz, 1952)

$$\gamma_{ij} = \psi^4 \bar{\gamma}_{ij}, \tag{2.2.10}$$

where $\psi = \gamma^{1/3}$ is the conformal factor, $\bar{\gamma}_{ij}$ the conformal metric, and $\gamma \equiv \det(\gamma_{ij})$ the determinant of the metric γ_{ij}. We also introduce a conformal transformation for the traceless part of the extrinsic curvature $A_{ij} \equiv K_{ij} - \gamma_{ij}K/3$ as

$$A^{ij} = \psi^{-10}\bar{A}^{ij} \,.$$

Notice that for raising and lowering indices of the conformal (overbarred) quantities we use $\bar{\gamma}^{ij}$ and $\bar{\gamma}_{ij}$, respectively. Then, the Hamiltonian (2.2.2) and momentum (2.2.3) constraints can be rewritten as

$$8\bar{D}^2\psi - \psi\bar{R} - \frac{2}{3}\psi^5 K^2 + \psi^{-7}\bar{A}_{ij}\bar{A}^{ij} = -16\pi\psi^5\rho \,, \tag{2.2.11}$$

$$\bar{D}_j\bar{A}^{ij} - \frac{2}{3}\psi^6\bar{\gamma}^{ij}\bar{D}_j K = 8\pi\psi^{10}S^i \,. \tag{2.2.12}$$

2.2.2 The conformal transverse traceless decomposition

By applying the Conformal Transverse Traceless (CTT) decomposition (York, 1979) (also known as York-Lichnerowicz formulation), we can further isolate DOF in the extrinsic curvature by decomposing the traceless, symmetric tensor $\bar{A}^{ij}$ into a transverse-traceless (TT) part which is divergenceless, and a longitudinal part that is written in terms as the vector gradient of a vector potential, namely

$$\bar{A}^{ij} = \bar{A}^{ij}_{TT} + \bar{A}^{ij}_{L} \,, \tag{2.2.13}$$

with $\bar{D}_j \bar{A}^{ij}_{TT} = 0$ and

$$\bar{A}^{ij}_{L} = \bar{D}^i W^j + \bar{D}^j W^i - \frac{2}{3}\bar{\gamma}^{ij}\bar{D}_k W^k \equiv (\bar{L}W)^{ij} \,, \tag{2.2.14}$$

where W^j can be regarded as a vector potential and $\bar{L}$ is the longitudinal operator (also known as vector gradient or conformal Killing operator). Then, the momentum constraint (2.2.12) can be written in terms of the vector potential as

$$(\bar{\Delta}_L W)_i - \frac{2}{3}\psi^6 \bar{D}_i K = 8\pi\psi^6 S_i \,, \tag{2.2.15}$$

where $(\bar{\Delta}_L W)^i \equiv \bar{D}_j \bar{A}^{ij}$ is the vector Laplacian, and we have used that $\bar{\gamma}_{ij}\bar{\gamma}^{jk} = \delta^k_i$. A convenient feature about the previous equation is that we can decouple it from the rest in some particular cases, e.g., if we take $K = 0$ (a maximal slicing) and identify the conformal source term as

$$s_i \equiv \psi^6 S_i. \tag{2.2.16}$$

Notice that the TT part of $\bar{A}^{ij}$ is not constrained by (2.2.15); in fact $\bar{A}^{ij}_{TT}$ are dynamical DOF connected with gravitational waves. Then, if we want to find a solution in the absence of GW for a given 3-dimensional hypersurface at $t = t_0$ we might take $\bar{A}^{ij}_{TT} = 0$, but since this is a dynamical quantity, we do not have the freedom to fix this again at a $t > t_0$ time slice but we would need to solve the evolution equations to propagate them. We will come back to this point in the next section when we introduce the 'waveless approximation'.

2.2.3 Gauge fixing

As discussed in the previous subsection, the conformal decomposition and the CTT approach recast the constraint equations in a convenient form without any assumption about the way that the system evolves, and then the lapse function α and shift vector β^i remain completely

unspecified. Even if we have complete freedom to choose them as they correspond to picking a coordinate system, in practice not all options are physically or numerically convenient. For instance, the simplest option $\alpha = 1$ and $\beta^i = 0$, known as geodesic slicing (or synchronous gauge) is not always suitable since coordinates can become ill-defined at some point during the evolution of the system, e.g., when shell crossing (or orbit crossing) occurs, as it is expected for collisionless particles.

In order to study cosmological (i.e., expanding/contracting) spacetimes, a convenient prescription to choose α is by applying the so-called Constant Mean Curvature (CMC) slicing condition (Smarr & York, 1978a), in which we can set

$$K = -3H(t)\,, \tag{2.2.17}$$

where a fiducial Hubble parameter $H \equiv \dot{a}/a$ has been introduced (being a a fiducial scale factor). Then, the lapse function can be found by solving the following constraint arising from (2.2.2) and the trace of (2.2.7) in terms of conformal variables,

$$\bar{D}^2(\alpha\psi) = \alpha\psi\left[\frac{7}{8}\psi^{-8}\bar{A}_{ij}\bar{A}^{ij} + \frac{5}{12}\psi^4 K^2 + \frac{1}{8}\bar{R} + 2\pi\psi^4(\rho + 2S)\right] - \psi^5\dot{K}\,. \tag{2.2.18}$$

Notice that in this scheme H (or a) is just a prescribed function for fixing the gauge, and in principle does not represent average (or background) properties of the universe. Nonetheless, we can still fix it by demanding that this satisfy the 'reference' (or 'background') Friedmann equations

$$H^2 = \frac{8\pi}{3}(\hat{\rho}_m + \rho_\Lambda)\,, \tag{2.2.19}$$

$$H^2 + \dot{H} = -4\pi(\hat{\rho}_m + \rho_\Lambda + 3\hat{P})\,, \tag{2.2.20}$$

where $\hat{\rho}_m$ and ρ_Λ are the homogeneous[1] matter and dark energy densities in the reference spacetime, respectively, and $\hat{P} = \hat{S}/3$. The advantage of introducing the fiducial Friedmann equations (2.2.19) and (2.2.20) is that we can subtract 'background' quantities from the full GR equations, which is more numerically convenient than to solve them directly. A similar idea is also exploited in Giblin et al. (2017), where a reference FLRW spacetime is conveniently subtracted (but under geodesic slicing), and the application of a fiducial Hubble parameter as part of the CMC slicing condition is later considered in Giblin et al. (2018). We

[1]Note that we use an overhat to denote the homogeneous matter quantities in order to avoid confusion with the overbars used above to denote geometric quantities constructed from the conformal metric $\bar{\gamma}_{ij}$. For ρ_Λ, on the other hand, we omit the overhat for brevity because it does not have an inhomogeneous part.

remark that, on itself, this 'background' subtraction does not constitute an approximation nor a perturbative approach, but rather it is simply a reformulation of the equations using a cosmologically motivated slicing condition.

On the other hand, to fix the remaining gauge freedom let us consider the Minimal Distortion (MD) condition, in which β^i is chosen such that it minimises the time rate of change of $\bar{\gamma}_{ij}$ during the propagation of spatial coordinates from one hypersurface to the next one. From the traceless part of (2.2.6) in terms of conformal quantities, we find

$$\bar{A}^{ij} = \frac{\psi^6}{2\alpha}\left[(\bar{L}\beta)^{ij} + \partial_t \bar{\gamma}^{ij}\right], \tag{2.2.21}$$

and the MD gauge condition corresponds to demand (Smarr & York, 1978a,b)

$$D^i(\gamma^{1/3}\partial_t \bar{\gamma}_{ij}) = 0\,. \tag{2.2.22}$$

Let us remark here that, contrary to the decomposition (2.2.14) discussed in the CTT approach, in (2.2.21) $\bar{A}^{ij}$ has both longitudinal and transverse components even when the MD condition (2.2.22) is satisfied. Then, using the MD condition (2.2.22) the momentum constraint (2.2.12) translates into the following elliptic equation for the shift vector

$$(\bar{\Delta}_L\beta)^i + (\bar{L}\beta)^{ij}\bar{D}_j \ln\psi^6 = 2\psi^{-6}\bar{A}^{ij}\bar{D}_j\alpha + 16\pi\psi^4\alpha S^i, \tag{2.2.23}$$

where we have also used the CMC condition to simplify the momentum constraint. In the rest of this Chapter, we assume that the CMC slicing condition (2.2.17) is satisfied, and we use the reference FLRW equations (2.2.19) and (2.2.20) to determine K and $\dot{K}$. Therefore, the lapse function is fixed by the constraint (2.2.18). On the other hand, while (2.2.23) fixes the shift vector compatible with the MD gauge condition (2.2.22), as we will discuss below, solving this equation is not the most convenient option for cosmological simulations, hence an approximate version will be instead adopted for GRAMSES.

2.2.4 The fully constrained formulation of GR

One of the fingerprints of GR is that gravity is no longer a static field as in Newton's theory, where the gravitational potential Φ_N is completely 'slaved' by the matter distribution, but it hosts two dynamical DOF representing ripples in the spacetime. Due to their faint nature, the existence of these GW has been only recently confirmed by LIGO (Abbott et al., 2016, 2017) – about a century after its theoretical prediction (Einstein, 1916a) – and has opened up a plethora of new possibilities for exploring our Universe. However, in the context of cos-

mological structure formation and its back-reaction these play a subdominant role, and then one might try to reconstruct the spacetime in absence of GW while retaining all other virtues of GR. Therefore, as a natural extension of Newtonian N-body simulations, we propose to use a formulation of GR featuring only elliptic equations as a first step.

In order to achieve this within the CTT approach, the first step would be to construct the initial data by choosing a conformally flat metric $\bar{\gamma}_{ij} = \delta_{ij}$ as well as $\bar{A}^{ij}_{TT} = 0$. However, after we fix the gauge assuming the MD condition (2.2.22), there is no remaining freedom to enforce these conditions for $t > 0$ since $h_{ij} \equiv \bar{\gamma}_{ij} - \delta_{ij}$ and $\bar{A}^{ij}_{TT}$ actually satisfy evolution equations. Then, as a possible way to have a fully constrained system of GR equations where the effect of GW in the cosmological dynamics is neglected, following Bonazzola et al. (2004); Cordero-Carrión et al. (2008) we make the approximations

$$\bar{\gamma}_{ij} = \delta_{ij}, \quad \bar{A}^{ij}_{TT} = 0 \qquad \forall t\,. \tag{2.2.24}$$

This approach follows the similar spirit as in the 'waveless theories of gravity' developed originally by Isenberg (2008) and later by Wilson & Mathews (1989), and its application is supported by previous works from both theoretical and numerical standpoints. In Cordero-Carrión et al. (2009) it has been explicitly shown, by using post-Newtonian expansions, that the conformal flatness approximation and the neglect of the TT term (2.2.24) are accurate even in highly relativistic regimes (further details on this point are discussed the in Appendix of Cordero-Carrión et al. (2009)). Furthermore, in Cordero-Carrion et al. (2012) the authors discuss a 'passive' method to compute the GW emission within this formulation by solving the hyperbolic evolution equations, but without including its back-reaction onto the dynamics of the system, as well as the so-called fully constrained formulation (FCF, Bonazzola et al., 2004; Cordero-Carrión et al., 2008; Cordero-Carrión et al., 2014) in which the latter is properly included. These approaches to go beyond the simple approximation (2.2.24) can be potentially implemented in GRAMSES, but this will be left for a future version.

Therefore, adopting the conformal flatness approximation we can set $\partial_t \bar{\gamma}^{ij} = 0$ in (2.2.21), with which the equation governing the shift vector, (2.2.23), is simplified to (Cordero-Carrión et al., 2008)

$$(\bar{\Delta}_L \beta)^i = 2\partial_j \left(\alpha \psi^{-6} \bar{A}^{ij}_L\right). \tag{2.2.25}$$

It is worthwhile to remark that the conformal flatness approximation provides two useful aspects for this approach. On the one hand, it simplifies the dynamical and constraint equations, in particular because in Cartesian coordinates $\bar{D}_i \to \partial_i$, which drastically reduces

the computational complexity of the problem. On the other hand, the metric automatically satisfies the condition (2.2.22). If the conformal flatness approximation is not used, such as in the extended versions of the constrained formulation of GR discussed in Cordero-Carrión et al. (2014), the second point is no longer true, but instead (2.2.22) becomes a condition on h_{ij}, i.e.,

$$D^i(\gamma^{1/3}\partial_t h_{ij}) = 0\,. \tag{2.2.26}$$

Hence, we can regard the interplay between the MD gauge condition and the conformal flatness approximation as qualitatively similar to the one in the commonly-used Poisson (or longitudinal) gauge; in this, the analogue of (2.2.26) is the gauge condition $\partial_i h^{ij} = 0 = \delta^{ij} h_{ij}$ (TT condition) and it is customary (in the context of structure formation) to approximate $h_{ij} = 0$ to neglect the GW content, which automatically satisfies the latter gauge condition.

It can be useful to count DOFs after having fixed the gauge as well as having adopted the conformal flatness approximation. We know that (in 4 dimensions) $g_{\mu\nu}$ has 4 gauge (redundant) DOFs which are fixed by the gauge choices, as well as $6 = 2+2+2$ independent physical DOFs which correspond to the scalar, vector and tensor modes, respectively. The CMC and MD gauge conditions, Eq. (2.2.17) and Eq. (2.2.22), place conditions on the metric variables α and $\bar{\gamma}_{ij}$ and fix the 4 gauge DOFs. It would then appear that the approximations Eq. (2.2.24) place further conditions on the metric variables and thus over-constrain the system. This is because $\bar{\gamma}_{ij}$ effectively contains 5 DOFs (notice that one scalar DOF, ψ, has already been factored out of γ_{ij} when defining $\bar{\gamma}_{ij}$), all of which are set to zero by using the conformal flatness approximation, $\bar{\gamma}_{ij} = \delta_{ij}$. However, the gauge condition (2.2.22) — which fixes 3 DOFs — is a subset of $\bar{\gamma}_{ij} = \delta_{ij}$, while the latter additionally sets the 2 tensor modes (associated to GWs) to zero. Hence, the condition (2.2.24) effectively removes all GW content and its back-reaction on spacetime from the system, and in so far as these back-reactions have a negligible effect on the structure formation in cosmology, the approximation (2.2.24) is good. The conformal flatness approximation has been shown to be accurate for astrophysical systems such as the rotational collapse of cores of (super)massive stars and merger of binary neutron stars (Cordero-Carrión et al., 2009), where gravity is not exceedingly strong. Hence, under this approximation, there are four physical non-dynamical DOFs in the system, the scalar variable ψ which is determined by the Hamiltonian constraint (2.2.11), plus one scalar and two vector modes contained in the shift vector β^i which are obtained from (2.2.25) under the conformal flatness approximation (this is different from the commonly-used Poisson gauge, e.g., in *gevolution*, where the shift only contains vector DOFs). Below in this Chapter we shall

demonstrate that GR simulations using this formula are able to predict the scalar and vector modes accurately. A detailed discussion on how the MD gauge singles out the dynamical wave modes of $\bar{\gamma}_{ij}$ can be found in Appendix A of Smarr & York (1978b).

Under this fully constrained formulation of GR, the gravitational sector equations can be conveniently solved with the following sequence of steps:

1. Using the CTT decomposition, we solve the momentum constraint (2.2.15) as an elliptic equation for the longitudinal part of $\bar{A}^{ij}$,

$$(\bar{\Delta}_L W)_i = 8\pi s_i, \tag{2.2.27}$$

where $s_i \equiv \psi^6 S_i = \gamma^{1/2} S_i$ is the conformal momentum density. After this, we construct the traceless part of the extrinsic curvature as

$$\bar{A}^{ij}_L = (\bar{L}W)^{ij} \equiv \bar{A}^{ij}\,, \tag{2.2.28}$$

where in the last step we have neglected $\bar{A}^{ij}_{TT}$ due to the approximation (2.2.24).

2. We solve the Hamiltonian constraint (2.2.11), with (2.2.19) subtracted, as an elliptic equation for the conformal factor ψ

$$\bar{\nabla}^2\psi = -2\pi\psi^{-1}s_0 - \frac{1}{8}\psi^{-7}\bar{A}_{ij}\bar{A}^{ij} + 2\pi\psi^5\hat{\rho}_m\,, \tag{2.2.29}$$

where $s_0 \equiv \psi^6\rho_m = \gamma^{1/2}\rho_m$ is the conformal matter density. Here $\bar{\nabla}$ is $\bar{D}$ with $\bar{\gamma}_{ij} = \delta_{ij}$ due to the conformal flatness approximation.

3. We determine the lapse function from the CMC slicing condition (2.2.17)

$$\bar{\nabla}^2(\alpha\psi) = \alpha\left[2\pi\psi^{-1}(s_0+2s) + \frac{7}{8}\psi^{-7}\bar{A}_{ij}\bar{A}^{ij} + \psi^5\left(\frac{5K^2}{12} + 2\pi\rho_\Lambda\right)\right] - \psi^5\dot{K}, \tag{2.2.30}$$

where we have used (2.2.19)-(2.2.20) as well as defined $s \equiv \psi^6 S = \sqrt{\gamma}S^i_i$.

4. Finally, we determine the shift vector from the momentum constraint (2.2.25).

5. Then, the current state of the gravitational field is characterised by the spacetime metric

$$\mathrm{d}s^2 = -\alpha^2\mathrm{d}t^2 + \psi^4\delta_{ij}(\beta^i\mathrm{d}t + \mathrm{d}x^i)(\beta^j\mathrm{d}t + \mathrm{d}x^j)\,. \tag{2.2.31}$$

6. The metric (2.2.31) is used to solve the equations of motion (EOM) for particles, and evolve the system.

Notice that in this scheme (2.2.30) plays the role analogous to the Poisson equation in Newtonian gravity as it determines the g_{00} metric component $\alpha \sim 1+\Phi$. However, (2.2.30) includes a term that is linearly proportional to α and therefore it formally resembles a finite-range (Yukawa-like) potential, which means that the gravitational force appears 'screened' in the CMC gauge. This seems to indicate that it would translate in a suppression of the matter power spectrum at large scales. However, as we will discuss later in Section 2.6, this 'screening' simply represents the effect by the choice of gauge on the simulated matter or velocity power spectrum.

2.3 The matter sector

In GRAMSES we implement a fully general relativistic N-body system for dark matter following the ADM formalism, with which we can describe the matter content in the 3-dimensional hypersurface and its time evolution, rather than dealing directly with 4-dimensional quantities. In GR the equation of motion for collisionless particles is the geodesic equation

$$u^\mu \nabla_\mu u_\nu = 0, \tag{2.3.1}$$

which for the spatial components reads

$$\frac{\mathrm{d}u_i}{\mathrm{d}t} = -\alpha u^0 \partial_i \alpha + u_j \partial_i \beta^j - \frac{u_j u_k}{2u^0} \partial_i \gamma^{jk}\,, \tag{2.3.2}$$

where the time-component u^0 is determined from the normalisation condition $u^\mu u_\mu = -1$ as

$$u^0 = \alpha^{-1} \sqrt{1 + \gamma^{ij} u_i u_j}\,. \tag{2.3.3}$$

The relation between u_j and the 3-velocity (coordinate velocity) $v^i \equiv \mathrm{d}x^i/\mathrm{d}t = u^i/u^0$ is

$$\frac{\mathrm{d}x^i}{\mathrm{d}t} = \frac{\gamma^{ij} u_j}{u^0} - \beta^i. \tag{2.3.4}$$

Naturally, the Newtonian limit is recovered with $u_i \ll 1$, $\gamma^{ij} \to \delta^{ij}$, $\alpha \to (1 + \Phi_N)$ and $\beta^i \to 0$, where Φ_N is the Newtonian gravitational potential, in which case (2.3.2) reduces to Newton's second law (in a comoving coordinate system) and $\mathrm{d}x^i/\mathrm{d}t = u^i$. Eq. (2.3.4) shows the nontrivial relationship between the velocities u_i and u^i. To be clear, in the code implementation below we shall only use u_i with a lower index, and similarly we always use β^i with an upper index.

After we evolve particles with (2.3.2) and (2.3.4) we can calculate the matter source terms appearing in the equations for the gravitational sector (2.2.27)-(2.2.30). For this purpose, it

is convenient to introduce a set of conformal source terms defined as

$$s_0 = \sqrt{\gamma}\rho\,, \tag{2.3.5}$$

$$s_i = \sqrt{\gamma}S_i\,, \tag{2.3.6}$$

$$s_{ij} = \sqrt{\gamma}S_{ij}\,. \tag{2.3.7}$$

We will show below that these quantities are analogous to the usual 'comoving' ones and correspond to those actually determined numerically in the CIC scheme. For example, the 'density' contrast for s_0, defined as $\delta s_0/s_0$, corresponds to the local fluctuation of the particle number count rather than the relativistic energy density. This is more convenient in practice because we naturally would like to follow 'particles' rather than the 'density field' in simulations: the same particle can contribute different energy densities at different places, and the relativistic correction effect can be calculated according to the local metric γ_{ij}. We will discuss the implication of this on the generation of initial conditions in Chapter 3.

2.4 Numerical implementation

Let us now describe the actual implementation of the fully constrained formulation of GR and the matter evolution equations in GRAMSES. For this purpose, we recast the GR equations using the code units detailed next. Notice that these are derived from the GR equations in physical units rather in geometric units, i.e., accounting for all G and c factors.

2.4.1 Code units

The gravitational sector

In order to implement the GR equations in GRAMSES we introduce a set of dimensionless quantities that are based on H_0^{-1} for measuring time, the box size L for spatial coordinates, the critical density $\rho_c = 3H_0^2/8\pi G$ and the fractional matter density $\Omega_m \equiv \hat{\rho}_{m,0}/\rho_c$ (today's values satisfying the fiducial FLRW equations (2.2.19) and (2.2.20)):

$$\tilde{x} = \frac{x}{L}, \qquad d\tilde{t} = H_0\frac{\mathrm{d}t}{a^2}, \qquad \tilde{s}_0 = \frac{s_0}{\Omega_m\rho_c}, \qquad \tilde{s}_i = \frac{s_i}{\Omega_m\rho_c c} \qquad \tilde{s} = \frac{s}{\Omega_m\rho_c c}, \tag{2.4.1}$$

$$\tilde{c} = \frac{c}{LH_0}, \quad \tilde{K} = a^2\tilde{c}LK, \quad \tilde{\bar{A}}_{ij} = a^{-1}\tilde{c}L\bar{A}_{ij}, \quad \tilde{U} = a\tilde{c}^2L^{-1}U, \quad \tilde{V}_i = a\tilde{c}^2V_i\,, \tag{2.4.2}$$

$$\tilde{\beta}^i = a^2\tilde{c}\beta^i, \qquad \tilde{b} = a^2\tilde{c}L^{-1}b, \quad \tilde{B}^i = a^2\tilde{c}B^i\,. \tag{2.4.3}$$

Notice that, in order to simplify the equations in code units, we have introduced the super-comoving coordinate time $\tilde{t}$ (Martel & Shapiro, 1998), and for $\tilde{s}_i$ and $\tilde{s}$ we have introduced a c^{-1} factor that's not present in $\tilde{s}_0$. In addition, rather than solving the nonlinear equations for the conformal factor and the lapse function, it is more convenient to reparametrise them by definining new variables $\tilde{\Phi}$ and $\tilde{\Psi}$ as

$$\alpha \equiv 1 + \frac{\tilde{\Phi}}{a^2\tilde{c}^2}\,, \tag{2.4.4}$$

$$\psi \equiv a^{1/2}\left(1 - \frac{\tilde{\Psi}}{2a^2\tilde{c}^2}\right)\,, \tag{2.4.5}$$

where $\tilde{c}$ is the speed of light in code units. This way, both $\tilde{\Phi}$ and $\tilde{\Psi}$ are quantities measuring deviations from their reference FLRW values (but no linearisation on $\tilde{\Phi}$ or $\tilde{\Psi}$ is carried out). Using this scheme, we can write the momentum constraint (2.2.27) as

$$(\tilde{\bar{\Delta}}_L \tilde{W})_i = 3\Omega_m a \tilde{s}_i. \tag{2.4.6}$$

The Hamiltonian constraint (2.2.29) can be written as

$$\left(1 - \frac{\tilde{\Psi}}{2a^2\tilde{c}^2}\right)\tilde{\bar{\nabla}}^2\tilde{\Psi} = \frac{3}{2}a\Omega_m\left[\tilde{s}_0 - \left(1 - \frac{\tilde{\Psi}}{2a^2\tilde{c}^2}\right)^6\right] + \frac{\tilde{\bar{A}}_{ij}\tilde{\bar{A}}^{ij}}{4}\left(1 - \frac{\tilde{\Psi}}{2a^2\tilde{c}^2}\right)^{-6}. \tag{2.4.7}$$

Next, using the the 2$^{\text{nd}}$ Friedmann equation (2.4.12) and the Hamiltonian constraint (2.4.7), the CMC condition (2.2.30) in code units becomes

$$\begin{aligned}\tilde{\bar{\nabla}}^2\left[\tilde{\Phi}\left(1 - \frac{\tilde{\Psi}}{2a^2c^2}\right)\right] =& \frac{Q}{a^2c^2}\tilde{\Phi} + \frac{3a\Omega_m}{2}\left(1 - \frac{\tilde{\Psi}}{2a^2c^2}\right)^{-1}\left[\tilde{s}_0 - \left(1 - \frac{\tilde{\Psi}}{2a^2c^2}\right)^6 + \tilde{s}_m\right] \\ &+ \tilde{\bar{A}}_{ij}\tilde{\bar{A}}^{ij}\left(1 - \frac{\tilde{\Psi}}{2a^2c^2}\right)^{-7},\end{aligned} \tag{2.4.8}$$

where

$$Q = \frac{3}{4}a\Omega_m\left(1 - \frac{\tilde{\Psi}}{2a^2c^2}\right)^{-1}\left[\tilde{s}_0 + 5\left(1 - \frac{\tilde{\Psi}}{2a^2c^2}\right)^6 + 2\tilde{s}_m\right] + \frac{7\tilde{\bar{A}}_{ij}\tilde{\bar{A}}^{ij}}{8}\left(1 - \frac{\tilde{\Psi}}{2a^2c^2}\right)^{-7}. \tag{2.4.9}$$

Finally, the MD condition (2.2.25) in code units is

$$(\tilde{\bar{\Delta}}_L\tilde{\beta})^i = 2a^3\tilde{\partial}_j\left(\alpha\psi^{-6}\tilde{\bar{A}}^{ij}\right). \tag{2.4.10}$$

In addition, the Friedmann equations (2.2.19) and (2.2.20) in code units are

$$\frac{1}{a^4}\frac{\tilde{K}^2}{12} = \frac{3}{4}\Omega_m\left(a^{-3}\hat{\tilde{\rho}}_{m,0} + \frac{\Omega_\Lambda}{\Omega_m}\right), \tag{2.4.11}$$

$$\frac{1}{a^4}\frac{\tilde{K}^2}{3} - \frac{1}{a^2}\frac{\mathrm{d}(a^{-2}\tilde{K})}{\mathrm{d}\tilde{t}} = -\frac{3\Omega_m}{2}\left(a^{-3}\hat{\tilde{\rho}}_{m,0} + \frac{\Omega_\Lambda}{\Omega_m} + \hat{\tilde{S}}\right), \tag{2.4.12}$$

where $\hat{\tilde{\rho}}_{m,0} \equiv \hat{\tilde{S}}_0 = 1$ is the homogeneous (comoving) density field in code units, $\Omega_\Lambda \equiv 8\pi G\rho_\Lambda/3H_0^2$, and $\hat{\tilde{S}} = 3\hat{\tilde{P}}$ (with $\tilde{s} = \psi^6\tilde{S}$).

The matter sector

For writing the EOM for particles in code units, we introduce the following dimensionless quantities for the particle's 4-velocity and mass:

$$\tilde{u}^\alpha = \frac{u^\alpha}{LH_0}, \quad \tilde{m} = \frac{m}{\Omega_m\rho_c L^3}. \tag{2.4.13}$$

Then, the system consisting of Eqs. (2.3.2)-(2.3.4) becomes

$$\frac{\mathrm{d}\tilde{u}_i}{\mathrm{d}\tilde{t}} = -\tilde{W}\tilde{c}a^2\tilde{\partial}_i\alpha + \tilde{u}_j\tilde{\partial}_i\tilde{\beta}^j - \alpha\frac{\tilde{u}_j\tilde{u}_k}{2\tilde{W}}\tilde{c}a^2\tilde{\partial}_i\gamma^{jk}, \tag{2.4.14}$$

$$\tilde{v}^i \equiv \frac{\mathrm{d}\tilde{x}^i}{\mathrm{d}\tilde{t}} = \frac{\tilde{c}}{\tilde{W}}\alpha a^2\gamma^{ij}\tilde{u}_j - \tilde{\beta}^i, \tag{2.4.15}$$

where

$$\tilde{W}^2 \equiv (\alpha\tilde{u}^0)^2 = \tilde{c}^2 + \gamma^{ij}\tilde{u}_i\tilde{u}_j, \tag{2.4.16}$$

is the Lorentz factor in code units.

Finally, for the numerical implementation of the matter source terms in Eqs. (2.3.5)-(2.3.7) we need to specify a prescription to calculate them. For this we consider an ensemble of N identical particles of rest mass m treated in a Cloud-in-cell (CIC) scheme. Then, the contributions to each matter source term in Eqs. (2.3.5)-(2.3.7) due to a particle at position $(\tilde{x}_p, \tilde{y}_p, \tilde{z}_p)$ can be calculated (Shibata, 1999) as

$$(\tilde{s}_0)_{i+1/2\mp1/2,j+1/2\mp1/2,k+1/2\mp1/2} = \frac{\tilde{f}_x^\pm\tilde{f}_y^\pm\tilde{f}_z^\pm}{\Delta\tilde{V}_{ijk}}\frac{\tilde{m}\tilde{W}}{\tilde{c}}, \tag{2.4.17}$$

$$(\tilde{s}_l)_{i+1/2\mp1/2,j+1/2\mp1/2,k+1/2\mp1/2} = \frac{\tilde{f}_x^\pm\tilde{f}_y^\pm\tilde{f}_z^\pm}{\Delta\tilde{V}_{ijk}}\frac{\tilde{m}\tilde{u}_l}{\tilde{c}}, \tag{2.4.18}$$

$$(\tilde{s}_{lm})_{i+1/2\mp1/2,j+1/2\mp1/2,k+1/2\mp1/2} = \frac{\tilde{f}_x^\pm\tilde{f}_y^\pm\tilde{f}_z^\pm}{\Delta\tilde{V}_{ijk}}\frac{\tilde{m}\tilde{u}_l\tilde{u}_m}{\tilde{W}\tilde{c}}, \tag{2.4.19}$$

where

$$\begin{aligned}\tilde{f}_x^+ &\equiv (\tilde{x}_{i+1} - \tilde{x}_p)/\Delta\tilde{x}_i,\\ \tilde{f}_y^+ &\equiv (\tilde{y}_{i+1} - \tilde{y}_p)/\Delta\tilde{y}_i,\\ \tilde{f}_z^+ &\equiv (\tilde{z}_{i+1} - \tilde{z}_p)/\Delta\tilde{z}_i,\end{aligned} \tag{2.4.20}$$

represent the relative position of the particle inside the i-th cell in the x, y and z direction, respectively, with $\tilde{f}_y^- = 1 - \tilde{f}_y^+$, $\tilde{f}_y^- = 1 - \tilde{f}_y^+$, $\tilde{f}_z^- = 1 - \tilde{f}_z^+$, and $\Delta\tilde{V}_{ijk} = \Delta\tilde{x}\Delta\tilde{y}\Delta\tilde{z}$ is the cell volume.

In the remainder of this Chapter we will only deal with quantities in code units and the tilde will be dropped to avoid cluttered notation.

2.4.2 Code structure

Let us now describe the logic flow of the global solution scheme implemented in GRAMSES. We recall that in this code time evolution is only due to particles, and these are evolved in a leapfrog scheme detailed in Appendix A. At a given timestep n, using the positions and velocities $\{x^n, u^{n-1/2}\}$ for particles and the GR fields values $\{\Psi^n, \Phi^n, \beta^{i^n}\}$ the code takes the following main steps:

1. Optional (`gr_newtonian`): Solve Newtonian gravity to get Φ_N^{n+1}.
2. Optional (`gr_newtonian`): Temporarily synchronise velocities with Φ_N^{n+1}: $u^{n-1/2} \longmapsto u_N^n$.
3. Calculate the source terms of the GR equations using the currently-available velocity and GR potential fields.
4. Optional (`gr_newtonian`): Revert the temporary synchronisation done in step 5: $u_N^n \longmapsto u^{n-1/2}$.
5. Solve the ten GR field equations: $\{\Psi^n, \Phi^n, \beta^{i^n}\} \longmapsto \{\Psi^{n+1}, \Phi^{n+1}, \beta^{i^{n+1}}\}$.
6. Synchronise velocities (last 'Kick' from previous timestep: $u^{n-1/2} \longmapsto u^n$).
7. Update velocities (first 'Kick' of the current timestep: $u^n \longmapsto u^{n+1/2}$).
8. Update positions using $u^{n+1/2}$ ('Drift': $x^n \longmapsto x^{n+1}$).
9. Go to step 1 with the replacement $n + 1 \longmapsto n$ and repeat the process for the next timestep.

We address these points in detail in the next subsections.

2.4.3 Multigrid solver for the gravitational sector

Let us now discuss the main points of the multigrid (Press et al., 2007) implementation of the GR equations for the gravitational sector. For this purpose, it is convenient to first split the equations into the Poisson-like ones and the non-Poisson-like ones.

Poisson-like equations

In the solution scheme for the gravitational sector we have eight linear Poisson-type equations arising from the vector Laplacians (2.4.6) and (2.4.10) respectively, i.e.,

$$\nabla^2 V_i = 3\Omega_m a s_i, \tag{2.4.21}$$

$$\nabla^2 U = -\frac{1}{4}\partial_j V^j, \tag{2.4.22}$$

$$\nabla^2 B^i = 2\partial_j \left[\left(1 + \frac{\Phi}{a^2c^2}\right) \left(1 - \frac{\Psi}{2a^2c^2}\right)^{-6} \bar{A}^{ij} \right], \tag{2.4.23}$$

$$\nabla^2 b = -\frac{1}{4}\partial_j B^j, \tag{2.4.24}$$

where $W_i \equiv V_i + \partial_i U$ and $\beta^i \equiv B^i + \partial^i b$ have been used to cast these equations in the form of a standard Poisson equation.

In order to solve the above equations numerically, we need to represent them in a discrete form. If we consider a uniform grid with cubic cell size h, these equations are formally equivalent to

$$\mathcal{L}^h(\varphi^h) = f^h\,, \tag{2.4.25}$$

where $\mathcal{L}^h$ is the Laplacian operator and f^h a source term. The former is discretised using the standard second order formula

$$\nabla^2\varphi = \frac{1}{h^2}(\varphi_{i+1,j,k} + \varphi_{i-1,j,k} + \varphi_{i,j+1,k} + \varphi_{i,j-1,k} + \varphi_{i,j,k+1} + \varphi_{i,j,k-1} - 6\varphi_{i,j,k})\,, \tag{2.4.26}$$

where $\varphi_{l,m,n}$ is the value of the field φ in the grid cell with index (l, m, n).

The actual discretisation method for f^h depends on the particular source term under consideration. In our implementation, the source f^h for Eq. (2.4.21) is calculated using the CIC scheme, while the sources for the rest of these equations correspond to divergences which are calculated using finite differences with a 3-point stencil, e.g.,

$$\partial_l V^l = \frac{1}{2h}(V^x_{i+1,j,k} + V^y_{i,j+1,k} + V^z_{i,j,k+1} - V^x_{i-1,j,k} - V^y_{i,j-1,k} - V^z_{i,j,k-1})\,, \tag{2.4.27}$$

$$\partial_l \bar{A}'^{lm} = \frac{1}{2h}(\bar{A}'^{xm}_{i+1,j,k} + \bar{A}'^{ym}_{i,j+1,k} + \bar{A}'^{zm}_{i,j,k+1} - \bar{A}'^{xm}_{i-1,j,k} - \bar{A}'^{ym}_{i,j-1,k} - \bar{A}'^{zm}_{i,j,k-1})\,, \tag{2.4.28}$$

where $\bar{A}'^{lm} \equiv \left(1+\frac{\Phi}{a^2c^2}\right)\left(1-\frac{\Psi}{2a^2c^2}\right)^{-6}\bar{A}^{lm}$. The extrinsic curvature term itself is calculated as

$$\bar{A}_{ij} = \partial_i V_j + \partial_j V_i - \frac{1}{2}\delta_{ij}\partial_k V^k + 2\partial_i\partial_j U\,. \tag{2.4.29}$$

Notice that for the non-diagonal components of $\bar{A}_{ij}$ we need to calculate cross-derivatives of U that depend on the diagonal neighbours of the central cell, for which we use a second-order-accuracy formula. Then, for a cross-derivative in the xy plane (contributing to $\bar{A}_{xy}$) we use the discrete expression

$$\partial_x\partial_y U = \frac{1}{4h^2}(U_{i+1,j+1,k} + U_{i-1,j-1,k} - U_{i-1,j+1,k} - U_{i+1,j-1,k})\,, \tag{2.4.30}$$

and equivalent ones for cross-derivatives in the xz and yz planes.

As a side point, we note that the left-hand sides of Eqs. (2.4.21)-(2.4.24) have the 'cyclic' property, e.g., if one sums up the values of $\nabla^2 U$ from all cells with the same y, z (but different x) coordinates, the result is zero, which is guaranteed by the nature of finite difference. The same periodic property is also held by the right-hand sides of Eqs. (2.4.22)-(2.4.24) by default, which means that these equations are numerically 'self-consistent'. For Eq. (2.4.21), however, its right-hand side does not automatically satisfy the 'cyclic' property, which could potentially lead to the situation where the two sides of the equation cannot be numerically identical. To prevent this issue, for Eq. (2.4.21) we have redefined its source term f^h as $f^h - \langle f^h\rangle$, where $\langle f^h\rangle$ is the mean value of f^h on the whole domain grid (the finest grid with uniform resolution that covers the whole simulation box).

The discrete version of Eq. (2.4.25) is then solved using a Gauss-Seidel (pseudo-time) relaxation method, which after a given number of iterations converges to a solution $\hat{\varphi}^h$. Then, the residual at the fine level is defined as

$$\epsilon^h \equiv \mathcal{L}^h(\hat{\varphi}^h) - f^h\,. \tag{2.4.31}$$

In order to improve the accuracy of the solution found using relaxation on the fine grid h (and hence reduce ϵ^h), instead of keeping iterating on the same grid we can accelerate the process by moving to a coarser grid with cell size $H = 2h$, which is then associated with the multigrid level $\ell - 1$ (with ℓ representing the finest grid). Since in Eq. (2.4.25) the operator $\mathcal{L}^h(\varphi^h)$ is linear, the coarsified equation is

$$\mathcal{L}^H(\varphi^H) - \mathcal{L}^H(\mathcal{R}\hat{\varphi}^h) \equiv \mathcal{L}^H(\delta\varphi^H) = -\mathcal{R}\epsilon^h\,, \tag{2.4.32}$$

where $\mathcal{R}$ is the restriction operator and $\delta\varphi^H \equiv \varphi^H - \mathcal{R}\hat{\varphi}^h$. The coarse-level equation (2.4.32)

is then solved using Gauss-Seidel relaxation and the solution $\delta\hat{\varphi}^H$ found after a given number of iterations is used to correct the fine solution $\hat{\varphi}^h$ by means of a prolongation step

$$\hat{\varphi}^h \leftarrow \hat{\varphi}^h + \mathcal{P}(\delta\hat{\varphi}^H)\,, \tag{2.4.33}$$

where $\mathcal{P}$ is the prolongation operator that maps the information from coarse to fine grids. In practice, we use all coarse levels from $(\ell-1)$ down to 1 (the level at which the whole simulation box is divided into 8 cells) for our multigrid implementation, and arrange them in a 'V-cycle': instead of correcting the level-ℓ solution immediately after solving the equation on level-$(\ell-1)$, the process of solving coarser-level equations goes all the way down to level 1, and the correction process then goes all the way up to level ℓ. This has greatly improved the speed at which a solution with acceptable accuracy is achieved.

Non-Poisson-like equations

Let us now discuss the implementation of the Hamiltonian constraint and the CMC condition, which correspond to the nonlinear PDEs solved in the code.

4.3.2.1 Hamiltonian constraint

In the multigrid language, the Hamiltonian constraint (2.4.7) at the fine level can be formally written as

$$\mathcal{L}^h(\Psi^h) = f^h\,, \tag{2.4.34}$$

where

$$\begin{aligned}\mathcal{L}^h(\Psi^h) &\equiv \left(1-\frac{\Psi^h}{2a^2c^2}\right)\nabla^2\Psi^h + \frac{3}{2}a\Omega_m\left[\left(1-\frac{\Psi^h}{2a^2c^2}\right)^6 - 1\right] - \frac{\bar{A}_{ij}\bar{A}^{ij}}{4}\left(1-\frac{\Psi^h}{2a^2c^2}\right)^{-6}\,,\\ f^h &\equiv \frac{3}{2}a\Omega_m(s_0-1)\,.\end{aligned} \tag{2.4.35}$$

Notice that by keeping the density term s_0 in the source f^h (rather than absorbing it in the definition of $\mathcal{L}^h$) we avoid using a separate array for restricting s_0 from fine to coarse level but, and thus we only need to restrict the differential operator coefficient $\bar{A}_{ij}\bar{A}^{ij} \subset \mathcal{L}^h(\Psi^h)$. However, as we discussed above for the case of Poisson-like equations, since our solution needs to satisfy periodic boundary condition, we need to regularise this equation to ensure that the numerical self-consistency condition $\langle\mathcal{L}^h\left(\Psi^h\right)\rangle = 0$ is satisfied[2]. Then, dividing both sides of

[2]Note that in this case $\langle f^h\rangle$ is guaranteed to be zero by the periodic boundary condition of s_0 and the subtraction of 1 in Eq. (2.4.35).

Eq. (2.4.34) by $\left(1-\frac{\Psi^h}{2a^2c^2}\right)$ and taking the mean on both sides, we identify the regularisation term

$$F^h = \frac{3}{2}a\Omega_m\left(1-\frac{\Psi^h}{2a^2c^2}\right)^{-1}\left[s_0-\left(1-\frac{\Psi^h}{2a^2c^2}\right)^6\right]+\frac{\bar{A}_{ij}\bar{A}^{ij}}{4}\left(1-\frac{\Psi^h}{2a^2c^2}\right)^{-7}, \tag{2.4.36}$$

and the regularised version of (2.4.7) solved in the code reads

$$\tilde{\mathcal{L}}^h(\Psi^h) \equiv \mathcal{L}^h(\Psi^h)+\langle F^h\rangle\left(1-\frac{\Psi^h}{2a^2c^2}\right) = f^h\,, \tag{2.4.37}$$

which corresponds to a redefinition of our differential operator at the fine level. Then, the residual at the fine level is defined as

$$\epsilon^h_\Psi \equiv \tilde{\mathcal{L}}^h(\hat{\Psi}^h)-f^h\,. \tag{2.4.38}$$

Next, at level $\ell-1$ the coarsified version of this nonlinear equation has the generic form

$$\tilde{\mathcal{L}}^H(\Psi^H) = \tilde{\mathcal{L}}^H(\mathcal{R}\hat{\Psi}^h)-\mathcal{R}\epsilon^h_\Psi\,, \tag{2.4.39}$$

where $\hat{\Psi}^h$ is the solution obtained at the fine level, $\mathcal{R}$ is the restriction operator. In principle we could also regularise the equation at the coarse level, but in practice this is not needed if the fine level is already regularised.

4.3.2.2 The CMC condition

In order to optimally solve the CMC condition (2.4.8) in the multigrid scheme we introduce the combination

$$\xi \equiv \Phi\left(1-\frac{\Psi}{2a^2c^2}\right)\,, \tag{2.4.40}$$

which avoids the use of additional arrays for storing the restricted field Ψ while solving for Φ on coarse levels. Then, in terms of ξ the CMC equation (2.4.8) at the fine level can be written formally as

$$\mathcal{L}^h(\xi^h) = f^h\,, \tag{2.4.41}$$

where

$$\begin{aligned}\mathcal{L}^h(\xi^h) &\equiv \nabla^2\xi^h-\left(1-\frac{\Psi}{2a^2c^2}\right)^{-1}\frac{Q}{a^2c^2}\xi^h\,, &(2.4.42)\\ f^h &\equiv \frac{3a\Omega_m}{2}\left(1-\frac{\Psi}{2a^2c^2}\right)^{-1}\left[s_0-\left(1-\frac{\Psi}{2a^2c^2}\right)^6+s_m\right]+\bar{A}_{ij}\bar{A}^{ij}\left(1-\frac{\Psi}{2a^2c^2}\right)^{-7}\,,\end{aligned}$$

and Q is given by (2.4.9). After subtracting the mean from *both* sides, the regularised equation becomes

$$\mathcal{L}^h(\xi^h) = f^h - \left\langle f^h \right\rangle - \left\langle \left(1 - \frac{\Psi}{2a^2c^2}\right)^{-1} \frac{Q^h}{a^2c^2}\xi^h \right\rangle \equiv \tilde{f}^h. \tag{2.4.43}$$

This means that for solving this equation at the coarse level it is sufficient to restrict the operator coefficient $\left(1 - \frac{\Psi}{2a^2c^2}\right)^{-1} \frac{Q}{a^2c^2} \subset \mathcal{L}^h(\xi^h)$. Further, similar to the Poisson-like equations, the regularisation term in (2.4.43) is absorbed in the source term, so there is no redefinition of the differential operator but of f^h. Then, the residual at the fine level in this case is

$$\epsilon_\xi^h \equiv \mathcal{L}^h(\hat{\xi}^h) - \tilde{f}^h\,. \tag{2.4.44}$$

On the other hand, at $\ell - 1$ the coarsified equation is

$$\mathcal{L}^H(\xi^H) = \mathcal{L}^H(\mathcal{R}\hat{\xi}^h) - \mathcal{R}\epsilon_\xi^h\,, \tag{2.4.45}$$

where $\hat{\xi}^h$ is the solution obtained at the fine level. As in the case of the Hamiltonian constraint, there is no need to regularise this equation at the coarse level.

2.4.4 Particles evolution

After having reconstructed the spacetime by computing the metric components $(\gamma_{ij}, \alpha, \beta^i)$ in a fully nonlinear fashion, we can then solve the EOM for particles. Drawing the analogy with the Newtonian case, the geodesic equation can be rewritten effectively as

$$\frac{\mathrm{d}u_i}{\mathrm{d}t} = F_i\,, \tag{2.4.46}$$

$$\frac{\mathrm{d}x^i}{\mathrm{d}t} = \left(1 + \frac{\Phi}{a^2c^2}\right)\left(1 - \frac{\Psi}{2a^2c^2}\right)^{-4} \frac{c}{W}\delta^{ij}u_j - \beta^i\,, \tag{2.4.47}$$

$$F_i = -\frac{W}{c}\partial_i\Phi + u_j\partial_i\beta^j - \frac{W^2 - c^2}{Wc}\frac{1 + \frac{\Phi}{a^2c^2}}{1 - \frac{\Psi}{2a^2c^2}}\partial_i\Psi\,, \tag{2.4.48}$$

where

$$W^2 \equiv (\alpha u^0)^2 = c^2 + a^{-2}\left(1 - \frac{\Psi}{2a^2c^2}\right)^{-4}\delta^{ij}u_iu_j\,. \tag{2.4.49}$$

In the Newtonian limit the 'force term' given by (2.4.48) reduces to $F_i \to -\partial_i\Phi$, but in the GR case this depends not only on gradients of the various gravitational fields (and on the fields themselves), but also on u_i. In practice, this means that we cannot compute all the contributions to (2.4.48) in the same way as the default RAMSES code (or any standard Newtonian code) does. Therefore, in GRAMSES we divide the Kick step (2.4.46) into a sequence of 5 substeps, each one updating the particle velocity using one force contribution on the right

hand side of (2.4.48), which is decomposed as $F_i = \sum_j c_j (f_j)_i$ with

$$c_j = -u_j \qquad (f_j)_i = -\partial_i \beta^j \,, \qquad j = 1,2,3 \tag{2.4.50}$$

$$c_4 = \frac{W^2 - c^2}{Wc} \frac{1 + \frac{\Phi}{a^2c^2}}{1 - \frac{\Psi}{2a^2c^2}} \qquad (f_4)_i = -\partial_i \Psi \,, \tag{2.4.51}$$

$$c_5 = \frac{W}{c} \qquad (f_5)_i = -\partial_i \Phi \,. \tag{2.4.52}$$

Notice that in doing this we are using the (partially) updated velocity during each substep. Of these five substeps, (2.4.52) is the dominant one in most realistic situations as it corresponds to the standard Newtonian force in the Newtonian limit.

As an attempt to preserve the Stormer-Verlet scheme as best as we can, the last Kick in the KDK scheme is done following (2.4.50) to (2.4.52), i.e., with the largest contribution to F_i included last (see Appendix A). In contrast, for the first Kick step (before updating the particles' positions) we use the reverse order, i.e., with the largest contribution included first. Again, this is because that, according to the Stormer-Verlet scheme, during the first Kick the 'force' should be evaluated using $u^{n+1/2}$, which implies an implicit equation for the latter (since this is the very velocity that we want to update to). Hence, as an approximation we use the synchronised velocity u^n and the largest contribution during the first substep of the Kick, which then yields a velocity $u_*^{n+1/2}$ that will be the close to $u^{n+1/2}$, and this is then used in the next substeps to calculate the corrections. Finally, the positions are updated in the Drift step (2.4.47) in a single calculation once the velocities have been fully updated by the previous prescription.

2.4.5 Calculation of matter sources

A key difference in the calculation of the general relativistic matter source terms in Eqs. (2.3.5)-(2.3.7) with respect to the Newtonian case is that the former depend not only on u_i but also on Ψ through the Lorentz factor Eq. (2.4.49). For calculating these we use the already-known values Ψ^n, with which the GR equations are solved to get the updated metric components $\{\Psi^{n+1}, \Phi^{n+1}, \beta^{i\,n+1}\}$. This is equivalent to the numerical implementation in the *gevolution* code, where the geometric corrections in the energy-momentum tensor at a given timestep are calculated using the values from the previous timestep (Adamek et al., 2016b). More explicitly, the CIC quantities depend on these as

$$s_0 \propto W(\Psi^n, u^{n+1/2}) \,, \tag{2.4.53}$$

$$s_i \propto u_i^{n+1/2} \,, \tag{2.4.54}$$

$$s_{ij} \propto \frac{u_i^{n+1/2} u_j^{n+1/2}}{W(\Psi^n, u^{n+1/2})} \,. \tag{2.4.55}$$

Note that as the second 'Kick' step – which takes particle velocities from $u^{n+1/2}$ to u^{n+1} and therefore 'synchronises' particle velocities – is done *after* we solve the GR equations, at the time when the code calculates the matter source terms for the GR equations what are available are the fully updated positions at timestep $(n+1)$, x^{n+1}, and the partially-updated velocities $u^{n+1/2}$ (which are still delayed by half a timestep). This issue is not present in the Newtonian case since the gravitational potential (and hence the force) is *independent* of the particle velocities, and we expect that the use of $u^{n+1/2}$ instead of u^{n+1} in the matter source calculation should be a good approximation given the generally small timesteps for simulations.

Nevertheless, GRAMSES has an option to remedy the fact that we only have $u^{n+1/2}$ to calculate the GR source terms, by using a temporary 'Newtonian' synchronisation from solving the standard Newtonian gravity. With this option switched on, the code uses the Newtonian gravitational potential Φ_N to temporarily update the velocities $u^{n+1/2} \longmapsto u_N^{n+1}$, which are then used to calculate the source terms as a better approximation than using $u^{n+1/2}$ directly in Eqs. (2.4.53)-(2.4.55). Then, after the GR equations are solved, we can *exactly revert* the velocities back to $u^{n+1/2}$, before carrying the Kick step normally (see appendix A).

2.5 Code tests

We have performed several code tests for GRAMSES, particularly aimed to test the implementations of the linear and nonlinear solvers of the ten GR potentials, the subroutines that calculate new GR quantities, as well as the geodesic solver.

2.5.1 Static tests

Let us first discuss the tests that require no cosmological evolution, for which we set the fiducial scale factor to $a = 1$. The results shown in this section correspond to simulations with a box size $L = 256$ Mpc$/h$ and $N_p = 256^3$ particles, and they are used to check the subroutines in GRAMSES to calculate the matter and geometric source terms, and to solve the relevant PDEs for the gravitational sector.

Matter and geometric source terms

While in Newtonian N-body simulations the matter density field is the only source term feeding the gravitational potential, in GRAMSES the picture is more intricate: the Poisson-like equations (2.4.21)-(2.4.24) feature the momentum density s_i, the divergence of GR potentials and also that of the traceless part of the extrinsic curvature, i.e., $\partial_j \bar{A}^{ij}$. Furthermore, for the non-Poisson-like equations, (2.4.7) and (2.4.8), we also need to calculate terms such as the contraction $\bar{A}_{ij}\bar{A}^{ij}$, the density s_0 and the trace $s = \gamma^{ij}s_{ij}$. Clearly, the calculation of the last two quantities is more complicated than that of s_i since they depend nonlinearly on u_i through the Lorentz factor W as can be seen from (2.4.17)-(2.4.19). Since in the CIC scheme particles may contribute to different cells depending on their positions, in order to assess the calculation of these quantities, in the tests we fix the particle positions and velocity values by hand, as well as Ψ, so we can compare against analytical expressions for the matter source terms.

Figure 2.1 shows the results for the CIC calculation of s_0 and two s_i components when using a uniform particle distribution, a velocity field $u_i = 0.3c \sin 2\pi x_i$ and $\Psi = c^2 \sin 2\pi x \sin 2\pi y \sin 2\pi z$, where c is the speed of light in code units. We find good agreement since the difference with respect to their analytical counterparts remains below 10^{-5}, and the structures observed for this in the bottom panels of Figure 2.1 stem from the shape of the functions on the top panels.

Regarding the geometric source terms, in Figure 2.2 we show the calculation of $\partial_i \bar{A}^{yi}$ and $\bar{A}_{ij}\bar{A}^{ij}$ which involve the discrete formulae, (2.4.28), (2.4.29) and (2.4.30). In order to compare with analytical expressions for this quantities we use $V_i = U = \sin 2\pi x \sin 2\pi y \sin 2\pi z$ as an input for the relevant code subroutines. The agreement found from Fig 2.2 is roughly one order of magnitude worse than for the matter source terms in Fig 2.1 but is still nonetheless stays around 10^{-4} for both $\partial_i \bar{A}^{yi}$ and $\bar{A}_{ij}\bar{A}^{ij}$. Naturally, the accuracy in the calculation of these quantities is expected to be different as they depend on how fine is the mesh used to perform the finite differences involved in their calculations, and the agreement shown in Fig. 2.2 is consistent with the grid used for these tests. Similar to Fig. 2.1, the structure of the difference observed in the bottom panels of Fig. 2.2 follows from the shape of the testing functions.

We have done similar tests as in Figures 2.1 and 2.2, using different choices of particle velocities, and different functional forms for Ψ, U and V_i. For all these tests we found similar agreement between the code results and the analytical predictions. For simplicity, the extra

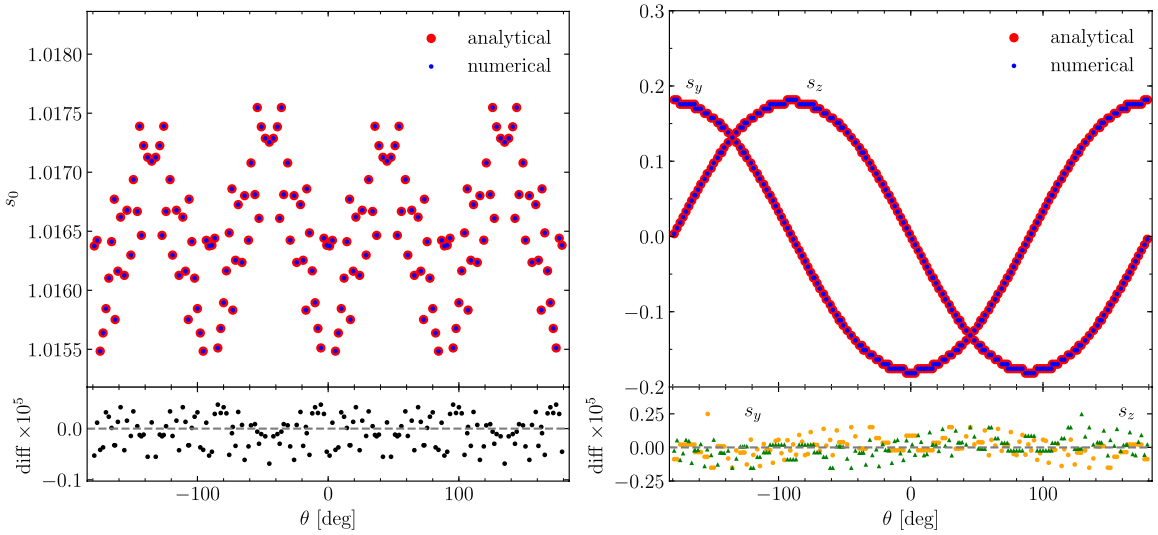

Figure 2.1: GRAMSES calculation of the relativistic matter density s_0 (left panel) and momentum density components $s_{y,z}$ (right panel). The values are plotted along a circle with radius $r = \sqrt{x^2 + y^2} = 0.1$ (in code units) measured from the box centre in the y-z plane, for $\theta \in [-\pi, \pi]$. In the upper panels the blue and red symbols respectively show the code result and the analytical prediction (see the main text for details), while the lower panels show their difference.

tests are not shown here.

Homogeneous density field

We next show some test cases for the linear and nonlinear equation solvers implemented in GRAMSES. The simplest possibility of such tests for the gravitational sector is to reconstruct the spacetime due to a homogeneous density configuration which corresponds to an FRLW (Einstein-de Sitter) solution. In our test, we set $s_0 = 1$ and $s_i = s = 0$.

Recall that the CMC gauge condition is fixed with the aid of the fiducial Friedmann equations (2.4.11) and (2.4.12) and hence the Hamiltonian constraint (2.4.7) and CMC condition (2.4.8) have the 'background' solutions $\Psi = \Phi = 0$. Likewise, it is also straightforward to find that the linear GR equations (2.4.21)-(2.4.24) are trivially solved, i.e., $V_i = U = B^i = b = 0$, in this case. In Figure 2.3 we show the numerical solutions for Ψ and Φ that are obtained by the nonlinear Gauss-Seidel relaxation solver[3] implemented in GRAMSES after performing the relaxation starting from two sets of random initial guesses (green triangles and red circles). As the figure shows, there is a very good agreement in the numerical solutions to both GR potentials regardless of the initial guess from where the relaxation is started.

[3]While technically speaking the CMC gauge condition (2.4.41) is a linear equation, in GRAMSES it is solved using the same nonlinear relaxation solver as in the Halmiltonian constraint (2.4.34).

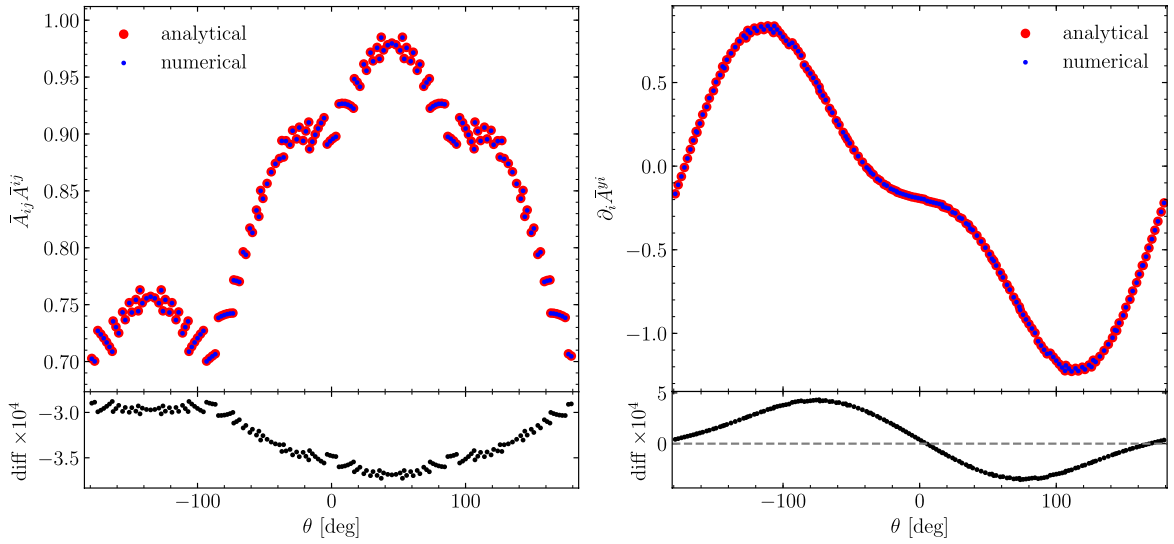

Figure 2.2: The same as Figure 2.1 but shows the code calculation of the geometric source terms $\bar{A}_{ij}\bar{A}^{ij}$ (left panel) and $\partial_i \bar{A}^{yi}$ (right panel).

We have tested the solutions to the other GR potentials finding similarly good agreements. To save space, here we only show the results for the two most complicated equations.

Point-like, sinusoidal and spherically symmetric sources

In order to add some nontrivial features to the test (as opposed to the case with a homogeneous matter field), we have also tested GRAMSES's relaxation solvers for the Poisson-type and non-Poisson-type equations individually by using various configurations for the source terms. For instance, for the Poisson-type equations (2.4.22)-(2.4.24) we know that the solution for a point-like source located at x_p is simply given by Green's function

$$\varphi = -\frac{1}{4\pi}\frac{1}{|x - x_p|}\,. \tag{2.5.1}$$

We test this point-like source scenario by initialising the value of the source in a single cell of the simulation box (at position x_p) to a constant: in the case of (2.4.21) this is equivalent to having a single particle in the centre of a cell so that it contributes only to that same cell in the CIC scheme, while for the other linear equations this corresponds to having a non-zero value for their geometric source terms in a single cell of the domain grid. The left panel of Figure 2.4 shows the numerical solution to (2.4.22) in such case and its comparison with the exact analytical solution, (2.5.1). We note that the numerical solution deviates from the exact one towards the centre of the simulation box as well as towards the box boundary. Both discrepancies can be understood in terms of the discrete nature of the numerical simulation:

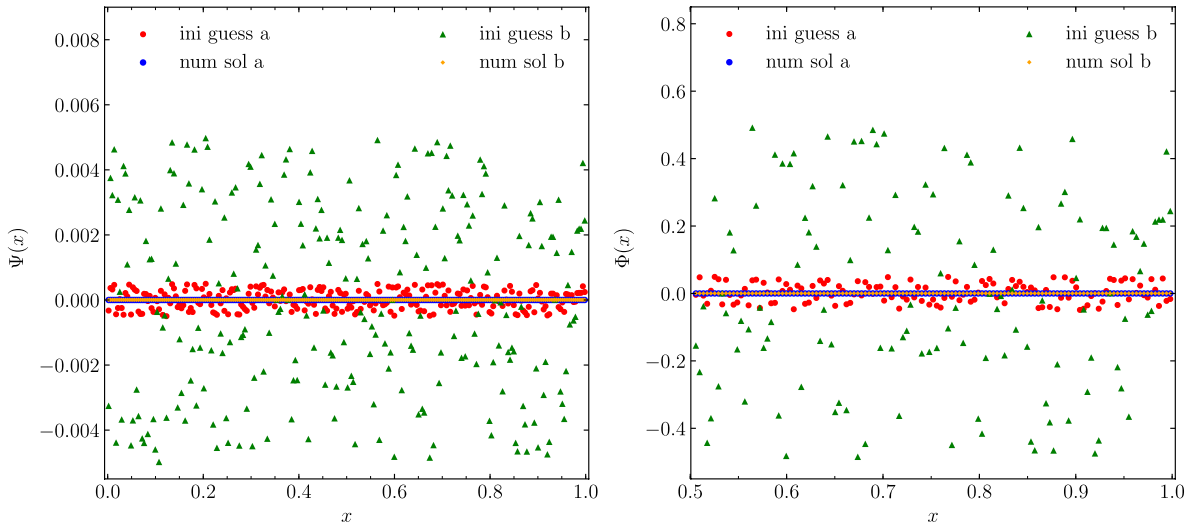

Figure 2.3: Numerical solutions for the GR potentials $\Psi(x)$ (left panel) and $\Phi(x)$ (right panel) obtained through the Gauss-Seidel relaxation method starting from two different sets of initial random guesses (red circles and green triangles) in a FRW (Einstein-de Sitter) universe. The x coordinate spans the whole simulation box in the range $[0, 1]$ in code units. The GRAMSES solutions for both initial guesses (blue circles and orange squares) after relaxation agree well with the analytical solution, which is identically zero (black solid line).

on the one hand, when approaching the source position resolution effects become important and the isotropy respected by the exact solution is broken. On the other hand, towards the box boundary the effect of the finite box size and the periodic boundary conditions imposed on the numerical solution causes deviations from the exact solution (2.5.1) which decays at infinity. Analogue results for the case of a Schwarzschild spacetime in isotropic coordinates are found in Adamek et al. (2016b) and for point-like mass tests of modified gravity codes, e.g., Li et al. (2012).

The non-Poisson-type equations (2.4.7) and (2.4.8) do not have exact analytical solutions for configurations such as point mass to compare against. As an alternative, we have used an inverse approach in which we choose some functional form for Ψ or Φ by hand and solve (2.4.7) and (2.4.8) for some of the source terms under certain simplifications, which can be then used as input to GRAMSES, to check the agreement of its resulting numerical solutions to Ψ, Φ with the above choices.

In Figure 2.4 we show the results of such procedure using Ψ with two different functional forms: $\Psi(x) = 10^{-2} \sin 2\pi x$ and $\Psi(r) = \exp\left[-(r-0.5)^2/10^2\right]$ which are then used in Eq. (2.4.7) to analytically solve for $s_0 = s_0(x)$ and $\bar{A}_{ij}\bar{A}^{ij} = \bar{A}_{ij}\bar{A}^{ij}(r)$, respectively, assuming all other source terms to be zero (here r is measured from the centre of the box). These are used as inputs for the GRAMSES nonlinear solver. For the sinusoidal test (middle panel of Figure

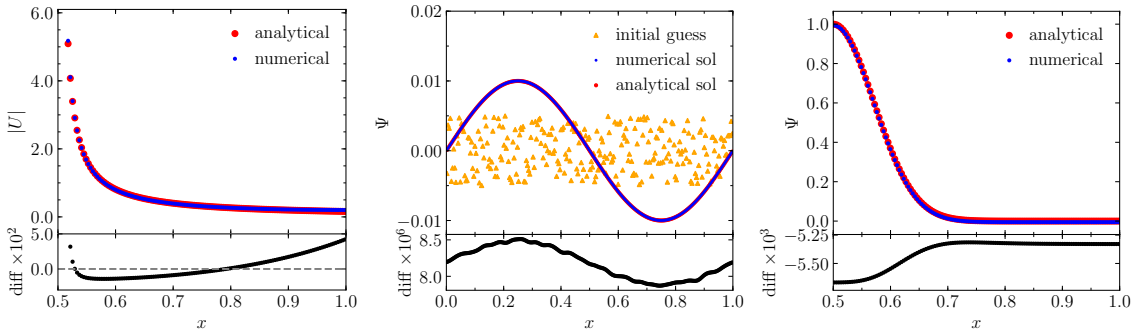

Figure 2.4: Tests of GRAMSES's numerical solutions for the GR potentials obtained through the multigrid Gauss-Seidel relaxation method. *Left panel*: point-like source test for a Poisson-type equation. Here x represents the distance to the point-like source, which is placed in the central cell of the simulation box, in code unit. *Middle panel*: test of the Ψ equation with analytical solution $\Psi = 10^{-2}\sin 2\pi x$ (see the main text for a description of how the test configuration $s_0 = s_0(x)$ is set up). *Right panel*: similar to the middle panel, but for a test configuration for which the Ψ field has a spherically symmetric solution $\Psi(r) = \exp\left[-(r-0.5)^2/10^2\right]$ (using a source $\bar{A}_{ij}\bar{A}^{ij} = \bar{A}_{ij}\bar{A}^{ij}(r)$ as described in the main text); the horizontal coordinate spans half of the simulation box along the x direction, in the range $[0.5, 1]$ in code units. In all cases, the blue and red symbols in the upper subpanel are respectively the numerical and exact analytical solutions, while the lower subpanel shows their difference. The orange symbols in the middle panel are the random initial guess for the relaxation.

2.4) we find that the numerical solution deviates less than 10^{-5} from the exact solution (we also include the initial random guess for the relaxation in that plot), while deviations for the spherically symmetric test (right panel of Figure 2.4) are larger but still better than those for the point-like test. Similar to the latter case, the numerical solution in the spherically symmetric test also suffers from the effects of periodic boundary conditions which depends on the rate at which the tail of the exponential function decays. Like before, we have tried more test settings and carried out similar tests for other equations as well. As all the tests result in similar agreement between numerical and exact solutions, we shall not show those tests here to save space.

Note that, in GRAMSES, the numerical errors of these solutions are controlled by using a measure of the magnitude of the residual ϵ defined in Eq. (2.4.31) for the Poisson-like equations and defined in Eq. (2.4.38) for the non-Poisson-like equations, which is fundamentally different from standard numerical relativity codes in which the full evolution equations for the gravitational sector are solved. In the latter, the accuracy of the numerical solutions is monitored by substituting them into the momentum and Hamiltonian constraint equations, thereby quantifying the measure of 'constraint violation'. However, since in the GR formulation implemented in GRAMSES the constraint equations are actually used as part of the the

solution scheme, the numerical errors are entirely controlled by the residual ϵ. Some threshold value for ϵ is specified in order to achieve the desired accuracy through the multigrid Gauss-Seidel relaxation solvers, which can be made smaller to increase the solution accuracy at the cost of using more iterations. For example, for our chosen threshold value for ϵ, the $\mathcal{O}(10^{-5})$ error in the numerical solution for Ψ shown in Fig. 2.4 (middle panel) is comparable to the level of Hamiltonian constraint violations typically found in other numerical relativity codes (Mertens et al., 2016; Daverio et al., 2019).

It is worthwhile to remark that the $\mathcal{O}(10^{-5})$ accuracy used in the above tests might be insufficient to calculate some GR effects reliably, such as the difference $\Psi - \Phi$, which in ΛCDM is typically around $\mathcal{O}(10^{-9})$ (Adamek et al., 2016a). This would require to set the target ϵ_Ψ and ϵ_ξ (which control the error in Ψ and Φ, respectively) to be well below the latter value, to ensure that the solutions are accurate enough across the simulation volume. This is doable, but we have not tested the performance of the code in such a case. Alternatively, one could modify the code to solve an equation for $\Psi - \Phi$ directly, and hence set a target accuracy for this difference. This will not be pursued here.

2.5.2 Dynamical tests

To test the time integration part of the code, which is determined by the evolution of particles along geodesics as discussed in Section 2.4.4, we consider two typical scenarios, including an FLRW robustness test and the evolution of a linear density perturbation. For these tests we use a box size $L = 256$ Mpc$/h$ with $N_p = 128^3$ particles. The discussion on the cosmological runs using higher-resolution specifications is presented in Section 2.6.

FLRW robustness test

We now present the test for the robustness of the evolution of a FLRW universe. For this, we initially set a completely homogeneous and static particle distribution at $z = 99$ as determined from the reference Friedmann equations (2.2.19) and (2.2.20). This scenario represents the simplest test of the geodesic solver as ideally particles should remain at fixed positions. In order to test the robustness of the numerical FLRW evolution we introduce tiny initial inhomogeneities by using a space-dependent initial random guess of order $\mathcal{O}(10^{-8})$ for the solutions of $\{V_i, U, B^i, b, \Psi, \Phi\}$, with which the multigrid relaxation solvers of the respective PDEs converge to solutions that are not exactly zero. After this, the geodesic equations (2.4.46) and (2.4.47) are solved using these solutions and, because the solutions to

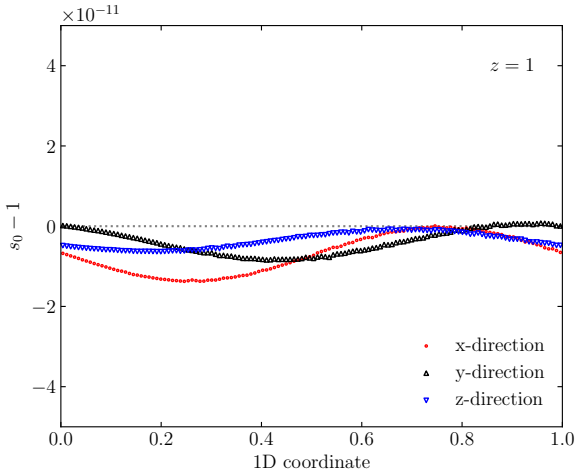

Figure 2.5: The FLRW robustness test for time integration in GRAMSES. An initial numerical error is introduced in the first time step of the simulation, through a random initial guess for the relaxation solvers of the gravitational potentials, which drives the particles away from initial exact homogeneity. We plot the resulting density field s_0 at $z = 1$ along three random lines, each chosen along one axis of the simulation box, while the dashed horizontal gray line represents the exact FLRW value, $s_0 = 1$.

the potentials are not exactly homogeneous due to the numerical errors, non-zero gradients of them and therefore forces result and the particles are driven away from their original positions, which effectively introduces an initial deviation from homogeneity in the density field of $\mathcal{O}(10^{-14})$. Then, in the new timestep the CIC source terms use the updated particle information and the non-exact solutions from the previous timestep are used as initial guesses for the gravitational solver. In this way, the cycle is repeated in such a way that the numerical error becomes accumulated over time. In Fig. 2.5 we show the resulting matter density field obtained at $z = 1$ along three different directions across the simulation box. The error found in Fig. 2.5 is of around the same order of magnitude as the typical values obtained for the FLRW robustness test in other cosmological GR codes (Mertens et al., 2016).

As a sanity check, we have also carried out the same test but by using zeros as the initial guesses for the relaxation solvers for the different gravitational potentials. In this case, the initial guess (zero) is the exact solution for all the potentials, and no force is exerted on the particles, which in turn stay at their initial positions during the whole simulation (exact FLRW solution). We have also checked that the long wavelength feature of s_0 along each direction shown in Fig. 2.5 is an artefact of the Gauss-Seidel relaxation solver. This type of solver efficiently eliminates the short wavelength modes of the error in the initial guess, while long wavelength modes require more iterations and can survive the convergence criteria. Then, these long wavelength modes in the gravitational potentials get imprinted in the matter

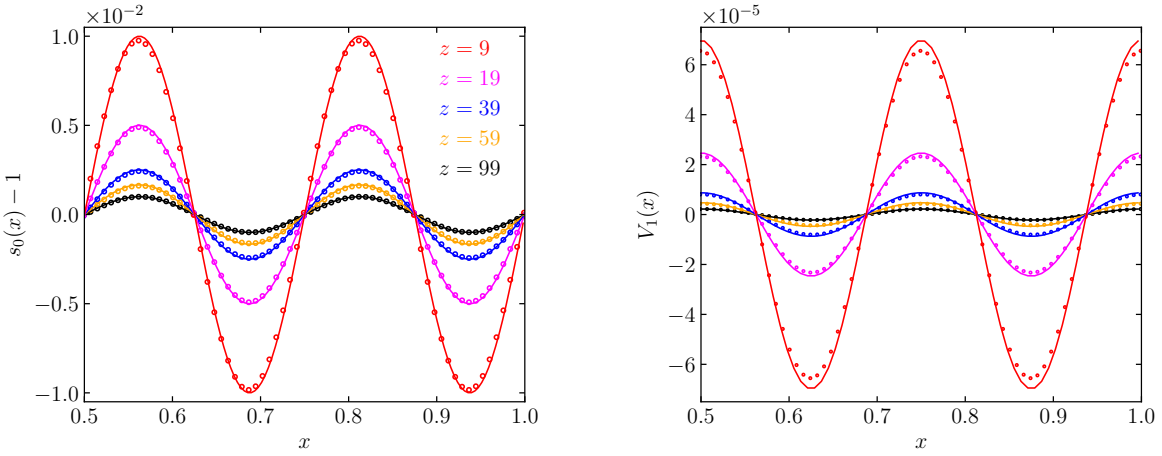

Figure 2.6: Evolution, between $z_{\rm ini} = 99$ and $z = 9$, of a single-mode density perturbation for testing the time integration subroutines of GRAMSES. *Left panel*: The density field profile at different output redshifts (circles) and the corresponding linear theory predictions (solid line). *Right panel*: Evolution of the V_1 potential from both simulation (dots) and linear theory (solid line), which is linked to the momentum density field through (2.4.21). The output redshifts (encoded by colour) match those from the density field in the left panel. At $z = 9$, the relative deviations at the maxima with respect to the linear theory solutions are 4.0% and 9.6% for s_0 and V_1, respectively.

sector throughout the evolution of the system, although they do not affect the good agreement with the exact solution as shown in Fig. 2.5.

Linear density perturbation

As a second test for the geodesic solver, here we present the evolution of a perturbed density field that is initialised at $z_{\rm ini} = 99$ to $\delta s_0 = A \sin 2\pi n x$, with $A = 10^{-2}$ and $n = 4$. This can be considered as a single mode of a density field. The linear velocity field is inferred from the Zel'dovich approximation (Zeldovich, 1970),

$$v^x = \frac{AH}{2\pi n} \cos 2\pi n x \,. \tag{2.5.2}$$

This density perturbation is then evolved by the code on a ΛCDM FLRW background (the details of this ΛCDM model are the same as for the cosmological tests below and, as they are not important for the test here, we postpone the mentioning of them to the next section).

In this test, the density perturbation is expected to scale at linear order as $\propto a$, and the momentum (or velocity) field as $\propto a^{-3/2}$. The density field profile at different output redshifts (circles) and the corresponding analytical predictions (solid line) is shown in the left panel of Fig. 2.6. We find good agreement at all considered redshifts, though it becomes worse towards low z as expected. At $z = 9$, the relative deviation with respect to the linear theory

solution is 4.0% at the maxima.

For the momentum density (or equivalently velocity) field, we show the results for the V_1 potential, which is related to it through the momentum constraint (2.4.21), in the right panel of panel of Fig. 2.6. We find that in this case the solution deviates slightly more rapidly from the analytical prediction toward late times compared to the density case, but still follows expectation very well. A somewhat similar situation is also encountered in other numerical relativity codes, where the momentum constraint violations are usually more severe than those found for the Hamiltonian constraint (Mertens et al., 2016; Macpherson et al., 2018a; Daverio et al., 2019). In this case, at $z = 9$ we find a 9.6% of relative deviation with respect to the linear theory solution at the maxima.

2.6 Cosmological simulations

In this section we present some of the first results of GRAMSES cosmological simulations in a ΛCDM universe using three different setups. We use a simulation with comoving box size $L = 512h^{-1}$Mpc and $N_p = 512^3$ dark matter particles, with the AMR option switched off, to generate the different maps shown in Fig. 2.7 for visualisation. For the analyses of the matter and velocity divergence power spectra we use big box size simulation with $L = 4h^{-1}$Gpc and $N_p = 1024^3$, with AMR switched on, and we compare against a Newtonian simulation run using the default RAMSES code with identical specifications. Finally, we use a high-resolution simulation with $L = 256h^{-1}$Mpc and $N_p = 512^3$ for the power spectra of the scalar and vector modes of the shift vector (again with AMR switched off). The initial conditions (IC) for both the GR and the Newtonian simulations are generated at $z_{\rm ini} = 49$ using the same random number sequence as seed in order to suppress the effect of realisation scatter in our results. For all the simulations, the cosmological parameters used for the ΛCDM model are $\{\Omega_\Lambda = 0.6928, \Omega_m = 0.3072, \Omega_K = 0, h = 0.68\}$. Since GRAMSES works in a different gauge than standard N-body simulations, the generation of IC is nontrivial; here we simply mention that the ICs were generated using a new technique specifically developed for GRAMSES, and will defer a detailed description of it to Chapter 3. Throughout the analysis, the redshift values quoted for the relativistic simulation correspond to those determined from the reference cosmology Eq. (2.2.19) and Eq. (2.2.20) (fixed by the CMC slicing), which coincides with the background of the Newtonian counterpart.

Fig. 2.7 is a visual illustration of the maps of three GR matter source terms, s_0 (top row), $\theta = \nabla \cdot u$ (middle row) and $s = \gamma^{ij} s_{ij}$ (bottom row), in a slice of constant z coordinate

randomly selected from the smaller GRAMSES simulation. The three columns correspond to three different redshifts, $z = 9$, 4, 1 (in the reference cosmology) from left to right. One can see that as time advances and structure formation progresses, finer features start to appear in all three quantities, and their amplitudes also increase; these results are as expected. In addition, the main features in all three quantities have good correspondences, with high-density regions having larger values of s_0, θ and s, and vice versa. Note the amplitude of s, which has a maximum of order 10^{-4} at $z = 1$ that is much smaller than the perturbation in s_0; according to Eq. (2.4.19), this indicates that $(u/c)^2 = (\tilde{u}/\tilde{c})^2 \lesssim \mathcal{O}(10^{-4})$ because in code units $\tilde{m} = 1$.

Figure 2.8 presents maps from the same slice as Fig. 2.7, but for various GR quantities or their scalar combinations. From top to bottom the rows show respectively α, ψ, $|\beta|$ (the amplitude of β_i) and $\bar{A}_{ij}\bar{A}^{ij}$. A logarithmic colour scale is used for α, ψ and $\bar{A}_{ij}\bar{A}^{ij}$, while a linear colour scale is used for $|\beta|$, in order to make the features in the maps clearer. To avoid the plot getting too cluttered, we have not shown the colour bars. In all cases, the same colour scheme in Python (the 'jet' scheme) is used, but is 'regulated' such that the reddest (bluest) colour represents the maximum (minimum) of the field values in all pixels of a given map. This is done deliberately: had we used a fixed maximum and minimum value for a quantity at all redshifts, the $z = 9$ maps would appear uniform and almost completely erased of details. In contrast, the 'regulation' not only makes the features at high redshifts clearer, but also demonstrates that, apart from amplitudes, the qualitative patterns of these features barely evolve in time: indeed, there is hardly any visual difference between the left and the middle columns. This is because the GR potentials usually satisfy a Poisson-like equation[4], which in Fourier space takes the form $k^2 \times$ field $=$ source, so that the field value scales as k^{-2} and so is dominated by the large-scale modes (the reason why the maps in Figure 2.8 generally lack the much finer details present in the maps of Figure 2.7). These modes remain linear over time, so that their amplitudes grow quickly while the qualitative patterns change much more slowly. The maps for α and ψ are almost identical, with their colours flipped, which is what is expected from Eqs. (2.2.29) and (2.2.30).

[4]The deviations from Poisson, such as the inclusion of nonlinear source terms or, like the case of $\bar{\alpha}$, the addition of an extra Yukawa term (i.e., the term linear in ξ in Eq. (2.4.42)), do not affect the qualitative discussion here.

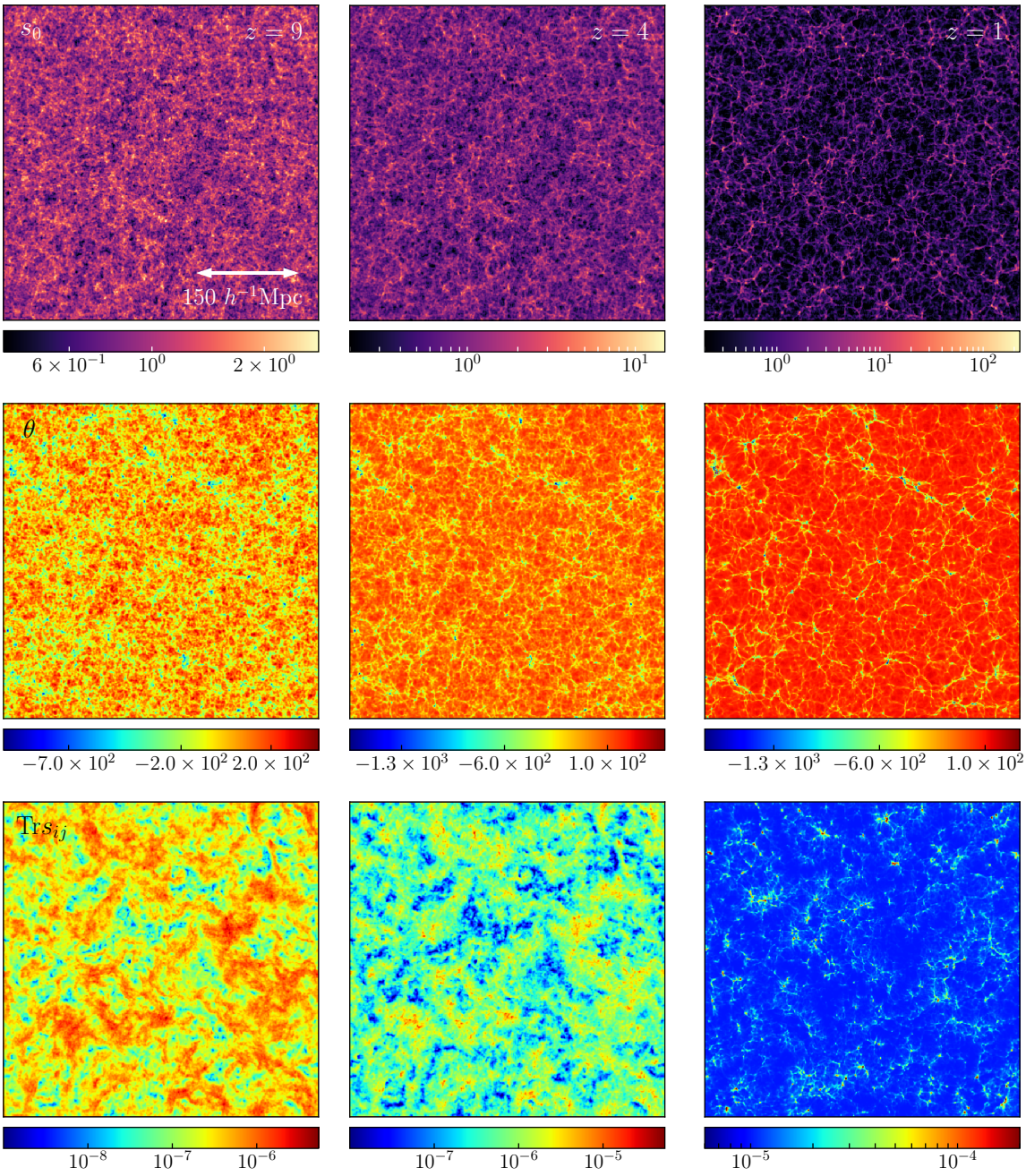

Figure 2.7: The evolution of the three matter sources in GR – the density field s_0 (top row), velocity divergence $\theta = \nabla \cdot u$ (middle row) and the trace of the anisotropic stress $s \equiv \mathrm{Tr} s_{ij} = \gamma^{ij} s_{ij}$ (bottom row) – for three redshifts, $z = 49$ (left column), 4 (middle column) and 1 (right column). Each panel shows a 2D slice map with constant z coordinate selected from the 512 Mpc/h GRAMSES simulation box.

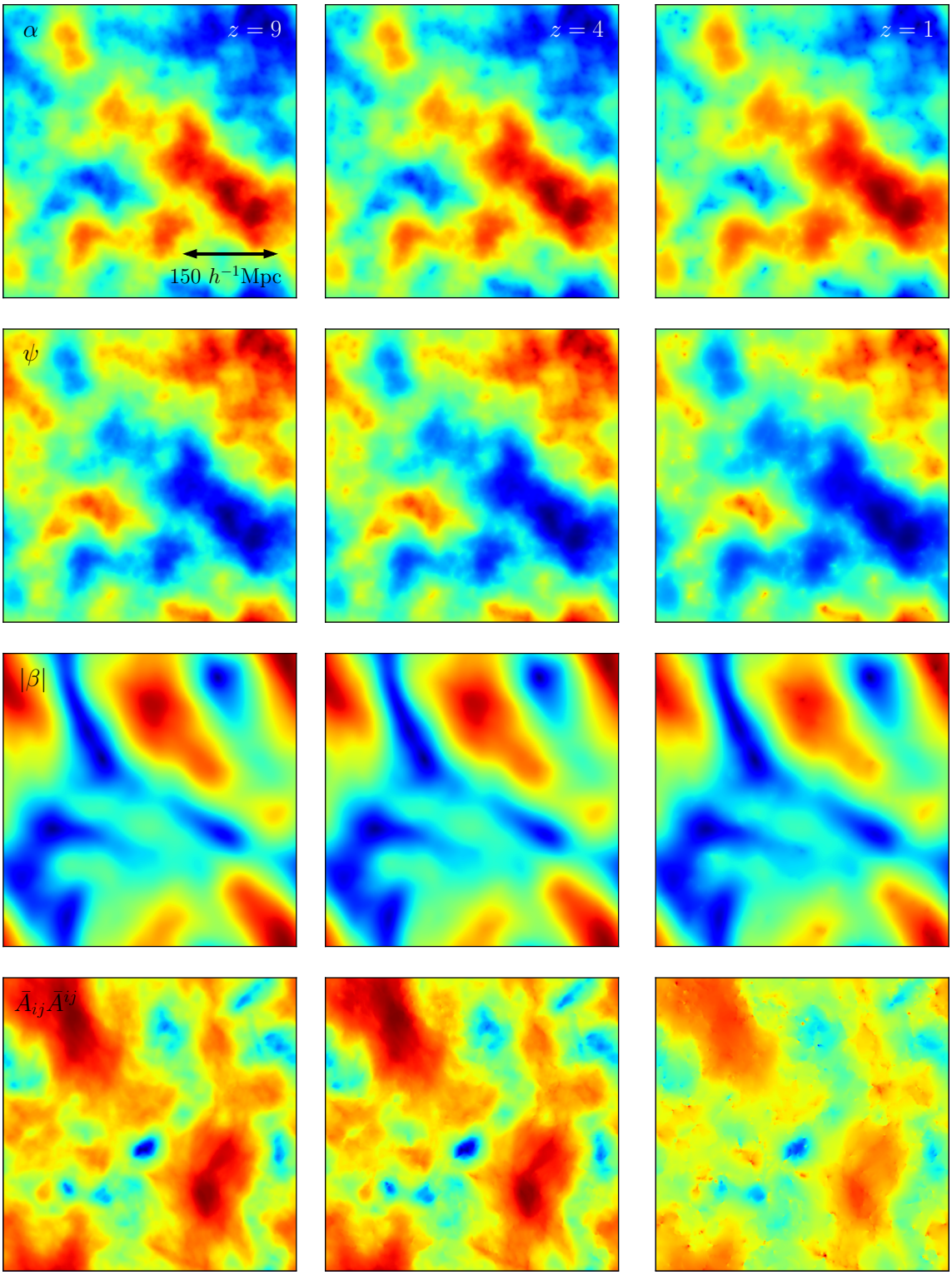

Figure 2.8: As Fig. 2.7, but for the GR potentials or their scalar combination, α (top row), ψ (second row), $|\beta| \equiv \sqrt{\beta_1^2 + \beta_2^2 + \beta_3^2}$ (third row) and $\bar{A}_{ij}\bar{A}^{ij}$ (bottom row). See the main text for more details.

2.6.1 Matter and velocity power spectra

Having displayed some visualisation of the simulation outputs from GRAMSES in the previous subsection, we next show a few more quantitative results to illustrate that the code works properly. Figure 2.9 shows the matter power spectra from the $4h^{-1}$Gpc simulations mentioned above, for six output redshifts from $z = 49$ (initial redshift, top left panel) to $z = 1$ (bottom right panel). Within each panel, the top subpanel shows the absolute power spectra and the bottom subpanel shows the relative difference between GRAMSES (CMC-MD-gauge spectrum for the particle number count perturbations, $\delta s_0/s_0$) and RAMSES (synchronous-gauge spectrum for the energy density perturbations, $\delta\rho/\rho$). For comparison, we also show the linear theory predictions for these two spectra using a modified version of the CAMB code (Lewis et al., 2000): these are respectively the blue and black solid lines in the top subpanels, while the solid lines in the bottom subpanels denote their relative differences. The magenta symbols in the top subpanels show the GRAMSES results as measured using the power spectrum code POWMES (Colombi et al., 2009): while they agree with linear theory rather well on intermediate and small scales, for the largest scale probed at $z = 49$ POWMES fails to recover the upturn predicted by linear theory (the blue solid line). The orange and red symbols, on the other hand, are the power spectra for the GRAMSES and RAMSES simulations measured using the DTFE code[5] (Cautun & van de Weygaert, 2011), which does capture the upturn. Therefore, in the bottom panels we show the ratio between the spectra measured using DTFE (red symbols). This comparison poses an interesting question regarding the applicabilities of the different methodologies to calculate the power spectrum when it deviates significantly from the usual behaviour observed in the synchronous gauge[6] (e.g., on large scales due to the gauge difference). Furthermore, the prediction of actual observable quantities in GR is not straightforward and requires the application of ray tracing algorithms acting either in real time (on-the-fly) or in a post-processing step. The former has been implemented for RAMSES in Barreira et al. (2016) and could serve as a starting point to implement a general relativistic version in GRAMSES in the future.

[5]The DTFE code tessellates the simulation volume following the Delaunay triangulation scheme, where the 3D space is decomposed into tetrahedrons whose vertices are simulation particles. The (density or velocity divergence) field value in each tetrahedron is determined by the corresponding particle quantities (mass and velocity) on its four vertices. The values in the tetrahedrons are then interpolated to a regular grid to give the field values on the latter, from which the corresponding power spectra can be measured using normal fast Fourier transform. This is particularly useful for the velocity field, since it can help to avoid the numerical problem of directly interpolating to a regular grid, which often leads to certain grid cells having zero velocity. See Cautun & van de Weygaert (2011) for more details.

[6]Note that at the largest scale probed by POWMES the CMC-MD-gauge power spectrum is nearly two orders of magnitude larger than that in the synchronous gauge.

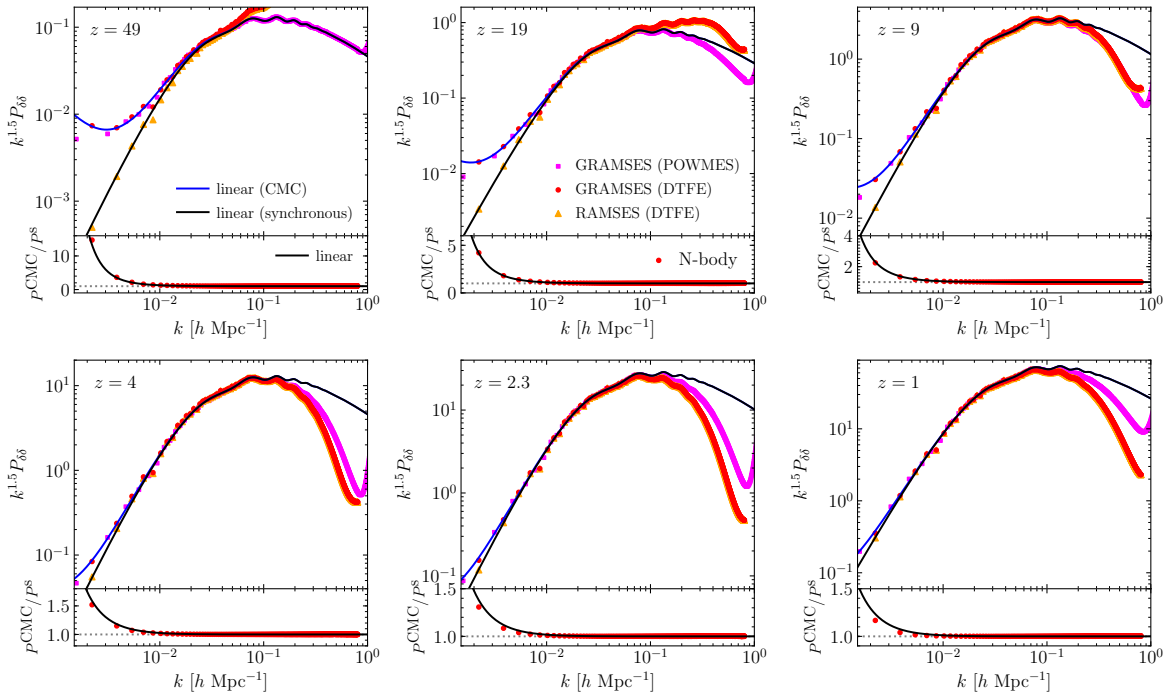

Figure 2.9: The comparison of the matter power spectra from our GRAMSES (GR) and RAMSES (Newtonian) simulations in the 4 Gpc/h box, at 6 redshifts, from $z = 49$ (upper left) to $z = 1$ (lower right). In each panel, the upper subpanel shows the absolute power spectrum measured using POWMES and DTFE, while the lower subpanel shows the ratio between GRAMSES and RAMSES. Note that the GRAMSES result is the power spectrum of the particle number count field in the CMC gauge ($P^{\rm CMC}$), while the RAMSES result is that of the energy density field in the synchronous gauge $P^{\rm S}$. The solid lines are the corresponding linear theory predictions for these power spectra obtained using a modified version of CAMB.

From Figure 2.9 we see that on large scales the simulation result agrees with linear-theory prediction very well for all redshifts shown. Note that the relative difference between the two power spectra at the largest scale probed by DTFE starts from $\sim 1500\%$ at $z = 49$ and decreases to $\lesssim 20\%$ at $z = 1$, which is a very large range of change that is properly reproduced by GRAMSES. Towards low redshift a small discrepancy from linear theory appears: this is partly because of the smaller differences between the power spectra in the CMC-MD and synchronous gauges, and partly because of the coarse time resolution in our simulation (which has fewer than 50 time steps between $z = 49$ and $z = 1$). Due to the low resolution of the simulation we shall not focus on the results at small scales.

Figure 2.10 is similar to Fig. 2.9, but shows the power spectrum of the velocity divergence (θ defined above). The blue and black solid lines in the upper subpanels are respectively the velocity convergence power spectra in the CMC and Newtonian gauge calculated by a modified version of the CAMB code, and the solid lines in the lower subpanels are their relative differences. Here all the simulation spectra have been measured by the DTFE code.

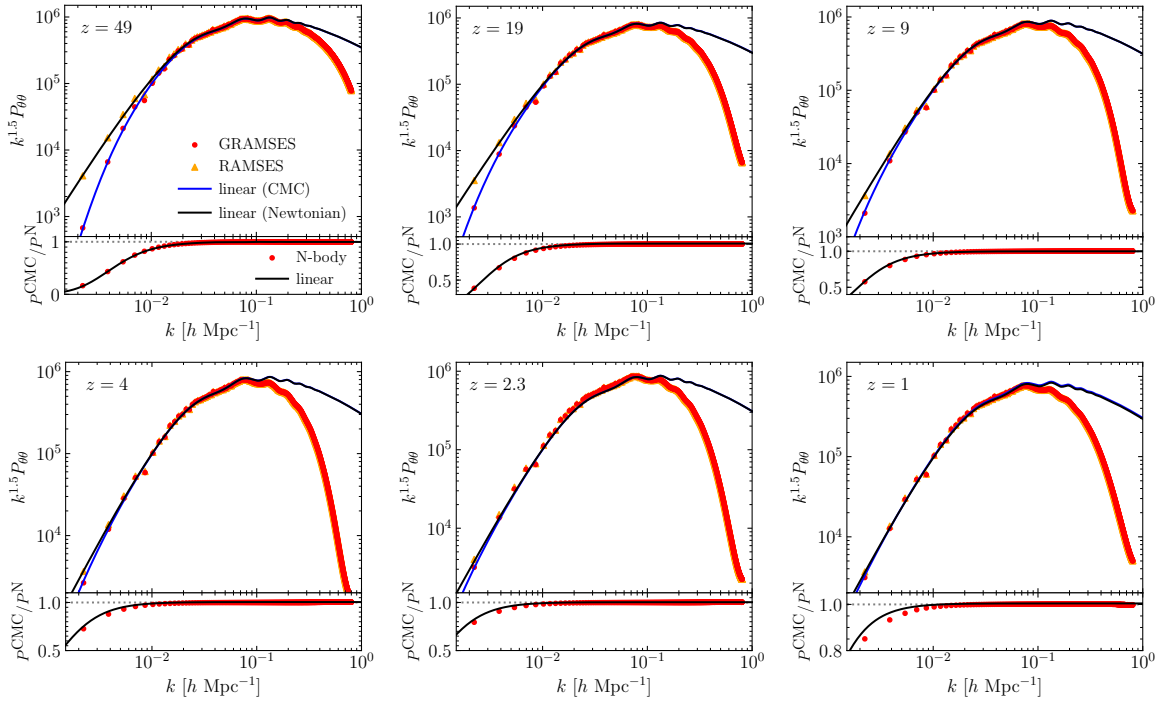

Figure 2.10: The same as Figure 2.9, but shows the velocity divergence power spectra predicted by the 4 Gpc/h GRAMSES (GR) and RAMSES (Newtonian) simulations. The former makes use of the CMC-MD gauge, while the latter follows the velocity field in the Newtonian gauge. All simulation results are measured using DTFE, and the solid lines are the linear-theory predictions obtained using a modified version of CAMB.

A similar level of agreement between the linear theory predictions and simulations to what is shown in Figure 2.9 can be found here, where at the largest scale probed by DTFE the relative difference between the GRAMSES and RAMSES results changes strongly from $\sim 1000\%$ at $z = 49$ to $\sim 20\%$ at $z = 1$. While the matter power spectra from the GRAMSES GR simulations are consistently higher than those from the RAMSES Newtonian simulations, the velocity power spectra show the opposite trend (this is in agreement with the findings of Flender & Schwarz (2012), whose uniform-expansion gauge corresponds to our CMC gauge) – this is partially why the difference between the matter power spectra in the two simulations decreases over time.

Let us remark here that neither the matter power spectrum $P_{\delta\delta}(k)$ nor the velocity divergence power spectrum $P_{\theta\theta}$ are gauge invariant quantities and the differences on large scales seen in Figures 2.9 and 2.10 are therefore not physical effects. However, being able to reproduce the expected gauge effects in our simulations is a useful test of the numerical implementation itself. We have stated briefly above that the $P_{\delta\delta}$ measured from the GRAMSES simulations are the power spectra for the particle number count perturbations in the CMC-MD gauge, while the $P_{\delta\delta}$ measured from the RAMSES simulations are for the energy density field in the

synchronous gauge. We have also compared $P_{\theta\theta}$ from RAMSES with the Newtonian gauge results from linear theory. These issues are indeed intricately related to the fact that the initial conditions in our GR simulations have to be generated in a way compatible with our gauge choice (see, e.g., Fidler et al., 2017b, 2015; Valkenburg & Hu, 2015), and as mentioned above these topics will be discussed in depth in Chapter 3.

2.6.2 The shift vector power spectrum

Let us now discuss some results on the shift vector power spectrum from GRAMSES. This is a particularly interesting quantity since it is related to 'frame-dragging', a GR effect which has been measured in the Solar System (Everitt et al., 2011). Contrary to the longitudinal gauge commonly adopted for late-time cosmology, in the MD gauge the shift vector has both scalar and vector components, i.e. $\beta^i = \beta^i_s + \beta^i_V$. In perturbation theory, β^i_V appears as a gauge-invariant, second order quantity (at lowest order) that is only sourced by the product of the first order scalar perturbations δ and v (Matarrese et al., 1998b; Lu et al., 2009) in the perfect fluid case. However, in N-body simulations the shell-crossing of dark matter particles induces velocity dispersion and sources the rotational velocity. Expanding Eq. (2.4.21) and (2.4.23) up to second order in perturbation theory, it can be shown that the dimensionless power spectrum $\Delta(k) \equiv k^3 P(k)/(2\pi^2)$ for β^i_V is given by (Lu et al., 2009)

$$\Delta_{\beta^V}(k) = \frac{9\Omega_m^2 H_0^4}{2a^2c^2k^2} \int_0^\infty \mathrm{d}v \int_{|1-v|}^{1+v} \mathrm{d}u \Pi \left[\Delta_{\delta\delta}(ku)\Delta_{vv}(kv) - \frac{v}{u}\Delta_{\delta v}(ku)\Delta_{\delta v}(kv) \right] , \tag{2.6.1}$$

where

$$\Pi(u,v) = u^{-2}v^{-4}\left[4v^2 - (1+v^2-u^2)^2\right] , \tag{2.6.2}$$

and $v = k'/k$, $u = \sqrt{1+v^2-2v\cos\theta}$, with $\cos\theta = k'^i k_i / \sqrt{k'^i k'_i k^j k_j}$. Due to the convolution in (2.6.1) a given k-mode of Δ_{β^V} can receive contributions from arbitrarily short and long-wavelength k'-modes of $\Delta_{\delta\delta}$, Δ_{vv} and $\Delta_{\delta v}$. This makes its comparison against simulation results intricate as the latter has intrinsic cut-off scales due to its discrete nature; on the one hand, the simulation cannot access long-wavelength modes beyond the fundamental mode $k = 2\pi/L$, while on the other hand the contributions coming from short-wavelength modes can be contaminated by modes beyond the Nyquist frequency $k = \pi N_p^{1/3}/L$. In principle, there is no clear correspondence between the aforementioned modes and the cutoff scales needed in (2.6.1) in order to compare faithfully against the simulation results. For our current comparison we adopt such modes as hard cut-offs and show results only up to 25% of the Nyquist frequency (Adamek et al., 2014).

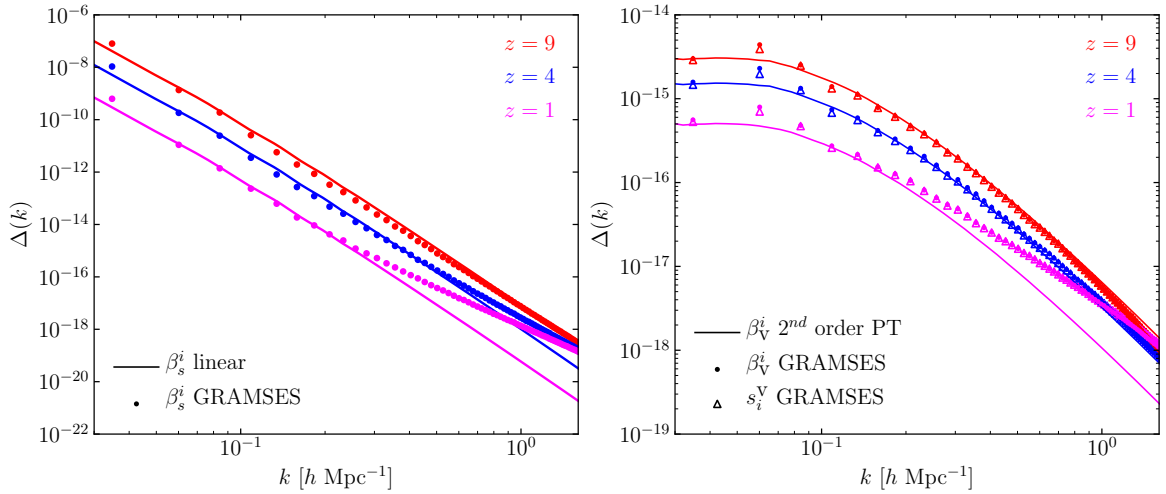

Figure 2.11: Power spectra of the scalar mode (left panel) and vector modes (right panel) of the shift vector from the GRAMSES simulation with box size $L = 256\text{Mpc}/h$ and $N_p = 512^3$ particles. The $\Delta_{s_i^V}$ power spectrum shown in the right panel is normalised to match the units of β_V^i. In each case we show modes up to 25% of the Nyquist frequency of the simulation, i.e. $\pi N_p^{1/3}/(4L)$.

We note that, as a consequence of the method for solving the vector Laplacian equations (2.4.6) and (2.4.10), there is no complete separation of scalar and vector modes of β^i and W_i in (2.4.21)-(2.4.23). While (2.4.22) and (2.4.24) guarantee that U and b are scalars, B^i and V_i contain both scalar and vector modes. Hence, in order to safely extract $\beta_V^i = B_V^i$ from B^i as a post-processing we apply a discrete curl operator ($\nabla\times$) to remove any scalar component in the latter, after which we can use the relation $k^2 P_{\beta^v}(k) = P_{\nabla\times\beta}(k)$ to get Δ_{β^V}. As a consistency check we have also calculated the curl of the full momentum density s_i which sources β^i through the momentum constraint Eq. (2.4.22), a procedure that has been previously applied to extract the shift vector from Newtonian simulations under a post-Friedmann approach in Bruni et al. (2014); Thomas et al. (2015c).

Figure 2.11 shows the power spectra for β_s^i (left panel) and β_V^i (right panel) extracted from the high-resolution GRAMSES simulation at three redshifts: $z = 9$ (red), 4 (blue) and 1 (magenta). The solid curves denote the predictions of linear perturbation theory (for β_s^i) and second order perturbation theory (for β_V^i), while the symbols are simulation results; for β_V^i the open triangles and filled circles represent respectively the power spectra for s_i^V and β_V^i. In both cases, the solid curves and symbols agree well, especially at higher redshifts.

We find that on large scales the scalar mode of the shift vector (left panel) can be many orders of magnitude larger than the vector mode (right panel), and thus the curl method described above is necessary to isolate the latter. As we discussed below Eq. (2.2.25), the

existence of this scalar mode within the shift vector is a result of the MD gauge condition (2.2.22), and shows that the fully constrained formulation adopted in GRAMSES successfully accounts for all the scalar and vector modes of the metric. The specification of cutoffs for the second order perturbation theory prediction (2.6.1) leads to a power loss in $\Delta_{\beta V}$ and can affect the matching to simulation results especially on large scales. However, the good agreement between perturbative and numerical results shown in the right panel of Fig. 2.11 for $z = 9$ and $z = 4$ is consistent with previous studies showing that the vorticity component of the velocity field (which is absent in the perfect fluid approximation) is subdominant with respect to the product of the first order scalar perturbations δ and v (Bruni et al., 2014; Jelic-Cizmek et al., 2018).

2.7 Summary

In this Chapter we have presented the GRAMSES code, a new implementation of general relativistic N-body AMR simulations in cosmology. This code brings together several advantages of current GR codes under a fully constrained formulation in which dynamical DOF of the metric can be isolated in a consistent and convenient way for cosmological simulations of structure formation. The current version of GRAMSES does not include the evolution equations for tensor modes, the omission of which is expected to have negligible impact on this kind of simulations and whose implementation is therefore left as a future project. Combined with the N-body particle methods for standard cosmological simulations, it can accurately solve the nonlinear Einstein equations all the way down to deeply nonlinear scales on which particle orbit crossing is frequent. We have discussed the relevant theoretical background upon which this is based as well as its numerical implementation in detail.

Multigrid relaxation, adaptive mesh refinement and efficient MPI parallelisation are three of the key features of GRAMSES, which are inherited from its parent code – the publicly-available N-body and hydrodynamical simulation solver RAMSES (Teyssier, 2002). These are what will enable GRAMSES to run large simulations for cosmological volumes while at the same time resolving scales well within virialised structures. In this Chapter we have opted to not devote much space to the description of these features, as they are well-established techniques nowadays and a lot of details can be found from the RAMSES code paper, references therein and its derived literature. However, let us briefly mention that the computation of geometric source terms for the Einstein equations in the ADM formalism – such as $\bar{A}_{ij}\bar{A}^{ij}$ and $\partial_i \bar{A}^{ij}$ – are actually nontrivial at the boundaries of refined meshes, which is largely due to the fact

that $\bar{A}_{ij}$ itself already involves up to second-order derivatives of the GR potentials V_i and U. Furthermore, the use of AMR increases the memory requirement of the code: without AMR, the different GR potentials, for a given time step, can be calculated sequentially so that the same array can be recycled for storing them; with AMR and the associated adaptive timestepping, the GR potentials must be kept for longer because they are needed to set up the boundary conditions for the refinement in all subtimesteps, and so we opt to create a separate array for each GR potential.

We have conducted various code tests to verify that all the source terms are computed correctly and that the implemented multigrid relaxation and geodesic solvers are reproducing the correct solutions for test cases where these can be calculated analytically or can be derived in alternative ways. We also successfully ran a cosmological simulation for a ΛCDM universe in a general relativistic setting. The maps produced in this GR simulation show expected features, and a more detailed quantitative analysis shows that the matter and velocity power spectra from the GR simulation display the expected behaviour for the CMC-MD gauge on large scales. The $L = 4h^{-1}$Gpc test simulations used to compare the relativistic and Newtonian codes also show that GRAMSES is roughly ten times more computationally expensive than its parent code – RAMSES. This number can be estimated from the ratio between the numbers of PDEs that are needed to solve the gravitational sector in each code, taking into account the fact that the non-Poisson-like equations solved in GRAMSES are only mildly nonlinear so that they are not significantly more expensive to solve than the standard Poisson equation. Nonetheless, compared to standard numerical relativity codes, an advantage of GRAMSES is that no evolution equations for gravity need to be solved in the formalism implemented so that relatively large time steps can be used. When GW are also implemented, their finite propagation speed impose additional requirements for the time stepping of the simulations, which could substantially increase the computational costs, although we do not expect this to be the case for cosmological simulations.

A few words to compare GRAMSES and *gevolution* are in order here, considering that they appear to share some common features. While the current implementation of GRAMSES solves all the relevant metric DOF from nonlinear elliptic equations, *gevolution* employs a mixture of linearised elliptic, parabolic and hyperbolic equations. As *gevolution* adopts the Poisson gauge, the vector modes are cleanly isolated within the shift vector β^i. This is not the case in GRAMSES, in which the elliptic equations mix one scalar mode in β^i, and a post-processing step is required if their separation is needed, as discussed in Section 2.6.2. For tensor modes, in *gevolution* they are solved from a linearised hyperbolic equation, while these

are not taken into account in the current GRAMSES version, although the framework allows one to include them by solving additional nonlinear time evolution equations. In any case, the facts that *gevolution* is based on the weak field expansion and utilises Fourier transforms in the gravitational solver may boost its overall performance, while the AMR nature of GRAMSES may make it more suitable in situations where one wishes to focus on high-density regions.

The generation of initial condition for GRAMSES simulations will be addressed in Chapter 3. Nonetheless, we can mention here that in order to generate initial conditions in the CMC-MD gauge we have modified the CAMB and 2LPTic (Crocce et al., 2006) codes. The former is used to generate the matter power spectrum implementing the gauge transformations at the initial redshift $z_{\rm ini}$ of the simulation, but also on two neighbouring ones (one at a slightly higher while the other a slightly lower redshift). Then, our modified 2LPTic code realizes this power spectrum to calculate the particle positions in the standard way, but the velocity is calculated by finite-differentiating the particle displacements of the two neighbouring snapshots. This has the advantage of being independent of an explicit parameterisation of the growth factor (and growth rate) which can become scale-dependent in certain gauges and dark energy/modified gravity models and thus violate a basic assumption (scale-independent linear growth rate) of the default 2LPTic code.

The code can be particularly useful for capturing relativistic effects in large-scale simulations as well as for studying problems beyond the Newtonian approximation such as the effect of large density contrasts on the surrounding spacetime and its impact on the estimation of cosmological parameters. Due to perturbed photon geodesics, distant objects can have observed redshifts, angular positions and fluxes which deviate from the true values. This can lead to various effects in observations such as in the galaxy density field (Yoo et al., 2009; Challinor & Lewis, 2011; Bonvin & Durrer, 2011). While subtle, these effects are detectable using suitable estimators, and their detectability varies with redshift, scale and estimator (e.g., Bonvin et al., 2016; Gaztanaga et al., 2017; Bonvin et al., 2017; Borzyszkowski et al., 2017; Giusarma et al., 2017; Alam et al., 2017b,a). To fully accurately study such effects in future galaxy surveys and how they could impact on the estimation of cosmological parameters and constraints on models, realistic mock galaxy catalogues based on cosmological simulations are needed (Borzyszkowski et al., 2017); such simulations should ideally have large volumes to capture the very large scale effects, but also resolve nonlinear scales and even virialised objects to more accurately predict the nonlinear effects (e.g., Zhu et al., 2017; Breton et al., 2019). Another interesting topic is the back-reaction effect of space-time averaging on the expansion rate (Buchert & Räsänen, 2012), an effect the exact size of which is still being

debated and which can have important implications on the understanding of the cosmic acceleration or cosmological parameter estimations, which is a nonlinear effect that cannot be fully captured by linear perturbation theory (Bentivegna & Bruni, 2016) and is therefore better to be quantified using N-body simulations that solve the nonlinear Einstein equations inside the most nonlinear virialised objects. In addition, the implementation of scalar field dark energy or modified gravity models in GRAMSES is potentially interesting as it would allow one to study the evolution of the new DOF inside virialised dark matter haloes and their impact on the GR effects (Thomas et al., 2015a; Reverberi & Daverio, 2019).

Chapter 3

Initial conditions for relativistic N-body simulations

3.1 Introduction

In Chapter 2 we have introduced a new code for general relativistic N-body simulations, GRAMSES (Barrera-Hinojosa & Li, 2020). We will now address the issue of generating particle initial conditions (ICs) – namely, positions and velocities – for simulations using this and other general relativistic codes. The proper generation of ICs is an essential part of the pipeline since the gauge choice in GRAMSES – a combination of constant mean curvature (CMC) slicing and minimal distortions (MD) – means that standard ICs generated for Newtonian N-body simulations are not in the gauge used by GRAMSES. This is because, in the linear regime, where the synchronous gauge is well defined, the density perturbation and velocity field used in Newtonian simulations are equal to the corresponding quantities in the synchronous and Newtonian gauges, respectively (Chisari & Zaldarriaga, 2011; Flender & Schwarz, 2012; chan Hwang et al., 2012). Standard initial condition codes, such as 2LPTic (Scoccimarro, 1998; Crocce et al., 2006), GRAFIC (Bertschinger, 2001) or MPGRAFIC (Prunet et al., 2008), are tailored for this type of simulations and use parameterisations for the growth factor and growth rate that could break down in other gauges. It is therefore necessary to modify the methods for generating initial particle data to make them compatible with GRAMSES simulations.

Contrary to numerical relativity codes based on the hyperbolic formulations of General Relativity (GR), such as Mertens et al. (2016); Macpherson et al. (2017); Daverio et al. (2019),

GRAMSES implements the fully constrained formulation, where the gravitational sector does not require the specification of ICs as the time evolution is fully encoded in the matter sources, and therefore the initial particle data is the only type of ICs needed for such simulations, in an analogous way to standard Newtonian simulations.

For cosmological simulations of this type, the usual approach to generate particle positions from a given density field is to use the displacement vector field, where one relies on the fact that the initial density field is nearly homogeneous, and that tiny perturbations arise from slightly displacing the particles from a regular configuration such as a grid or glass (Baugh et al., 1995). At first order in perturbation theory, the solution of the displacement is simply given by the Zel'dovich approximation (Zeldovich, 1970). On the other hand, the velocity can be calculated by using the first-order continuity equation, although this requires additional information about the density field, in particular its time evolution, which at the linear level is encoded in the linear growth rate f_1. However, the latter quantity depends on both the gauge used for the overdensity, as well as the underlying theory of gravity, and one has to be careful about the parameterisation of f_1 adopted even in a non-relativistic scenario. For instance, it is well-known that the growth rate (and growth factor) becomes scale-dependent in many modified gravity or dark energy models (Linder & Cahn, 2007; Narikawa & Yamamoto, 2010). Another potential limitation of this method is that, as we shall note later, it is possible that the overdensity and velocity fields from a given gauge do not satisfy the 'standard' (or 'Newtonian') form of the continuity equation even if the conservation of the energy momentum tensor holds, since in general the continuity equation also contains curvature perturbation terms, which for Newtonian N-body simulations can be properly taken into account (Fidler et al., 2015). A general approach to tackle this problem has been implemented in FALCONIC code (Valkenburg & Hu, 2015), which is capable of generating ICs for a wide range of theories of gravity, including those having perturbations in non-standard matter components at high redshift, as well as for models with imperfect fluids such as neutrinos.

In order to circumvent the gauge issues when calculating the velocity field for GRAMSES simulations, we propose a finite difference method in which, roughly speaking, two particle snapshots close to the initial redshift — and generated using the same random number seeds — are compared to obtain the velocity field connecting them. This is a very straightforward but versatile approach due to the advantage of being independent of an explicit parameterisation of the growth factor, as the information about the evolution of the density field is drawn from the comparison of the snapshots. We have implemented this finite difference method

by modifying the 2LPTic code. As the input for solving the displacement vector problem at a given redshift, the default 2LPTic code uses a matter power spectrum rather than the density field itself. In order to calculate the spectrum in the CMC gauge, we use a modified version of the CAMB (Lewis et al., 2000) which implements suitable gauge transformations from the default synchronous gauge used in such code. Since for the finite difference calculation of the velocity we need the displacement vectors from two subsequent snapshots, in the modified 2LPTic code we additionally input two neighbouring matter power spectra (one at a slightly higher redshift while the other at a slightly lower redshift than the true initial time). Then, the code realises these power spectra to calculate the particle positions in the standard way, but the velocity is calculated by finite differencing the particle displacements from the two neighbouring snapshots. In this way, the velocity can be calculated even in cases where basic assumptions of the default 2LPTic code, such as scale-independent growth rate, are violated.

The rest of this Chapter is organised as follows. Given that the gauge choice for GRAMSES and its role in the fully constrained formulation of GR have been described in details in Chapter 2, in Section 3.2 we only briefly recall some aspects that are relevant for the current project. In Section 3.3 we discuss the gauge transformations that connect the CMC-MD gauge to the synchronous and Newtonian gauges, and that allow us to deal with the gauge issues behind the generation of ICs. In Section 3.4.1 we briefly discuss the standard displacement vector method for the generation of the particle ICs from an initial matter density field, and we point out its potential limitations when dealing with general relativistic N-body simulations, while in Section 3.4.2 we explain how it is compatible with Newtonian simulations. In Section 3.4.3 we show that this method is also compatible with the generation of particle positions for GRAMSES by identifying carefully the overdensity variable used in the simulation (Valkenburg & Hu, 2015), but that velocities remain affected by the gauge dependence. As a way to overcome this gauge issue, in Section 3.4.4 we discuss how to calculate the initial particle velocities via a finite difference method. Then, in Section 3.5 we present results regarding the ICs for GRAMSES simulations, as well as a comparison to the standard method. Finally, we wrap up in Section 3.6 with a summary and some outlook.

As in Chapter 2, in the following we adopt the $(-,+,+,+)$ signature for the spacetime metric as well as the unit $c = 1$. Greek indices run from 0 to 3, whereas Latin ones from 1 to 3 only, with repeated indices implying summation.

3.2 The gauge choice in GRAMSES

The gauge choice for GRAMSES simulations and its implications in the constrained formulation of GR has been discussed in detail in Chapter 2. However, for the sake of completeness and notation we briefly discuss some relevant aspects next. In the $3+1$ formalism the spacetime metric takes the form

$$\mathrm{d}s^2 = g_{\mu\nu}\mathrm{d}x^\mu \mathrm{d}x^\nu = -\alpha^2 \mathrm{d}t^2 + \gamma_{ij}\left(\beta^i \mathrm{d}t + \mathrm{d}x^i\right)\left(\beta^j \mathrm{d}t + \mathrm{d}x^j\right), \tag{3.2.1}$$

where γ_{ij} is the induced metric on the spatial hypersurfaces, while the lapse function α and shift vector β^i represent the diffeomorphism invariance of GR. Even though in principle we have the complete freedom to choose the gauge, in practice not all options are physically or numerically convenient. As an example, the geodesic slicing (or synchronous gauge) is characterised by $\alpha = 1$ and $\beta^i = 0$, but it can become ill-defined when shell crossing (or trajectory crossing) occurs, as is expected for collisionless particles in cosmological simulations. For this type of simulation, a convenient prescription for α is applying the so-called Constant Mean Curvature (CMC) slicing condition (Smarr & York, 1978a), in which the trace of the extrinsic curvature of the spatial hypersurfaces is fixed as a function of time only,

$$K = -3H(t), \tag{3.2.2}$$

where $H \equiv \dot{a}/a$ represents a fiducial Hubble parameter (with a being a fiducial scale factor). Here, H (and a) is just a prescribed function for fixing the spacetime foliation and in principle does not have to represent average (or background) properties of the actual universe. Nevertheless, we can still fix H such that it satisfies some 'reference' Friedmann equations (Giblin et al., 2017, 2018). Under the CMC slicing, the lapse can be found by solving

$$\bar{\nabla}^2(\alpha\psi) = \alpha\left[2\pi\psi^{-1}(s_0 + 2s) + \frac{7}{8}\psi^{-7}\bar{A}_{ij}\bar{A}^{ij} + \psi^5\left(\frac{5K^2}{12} + 2\pi\rho_\Lambda\right)\right] - \psi^5\dot{K}\,. \tag{3.2.3}$$

Here, ψ represents the conformal factor which connects γ_{ij} to the conformal metric $\bar{\gamma}_{ij}$ through $\gamma_{ij} = \psi^4\bar{\gamma}_{ij}$, with $\bar{\gamma} \equiv \det(\bar{\gamma}_{ij}) = 1$, $\bar{\nabla}^2 \equiv \bar{\gamma}^{ij}\bar{D}_i\bar{D}_j$ is the covariant Laplace operator associated with $\bar{\gamma}_{ij}$ (and $\bar{D}_i$ the associated covariant derivative), and $\bar{A}_{ij}$ is the traceless part of the extrinsic curvature tensor $\bar{K}_{ij}$. Furthermore, ρ_Λ is the dark energy density appearing in the reference Friedmann equations, and the conformal matter source terms are defined as

$$s_0 = \sqrt{\gamma}\rho\,, \tag{3.2.4}$$

$$s_i = \sqrt{\gamma}S_i\,, \tag{3.2.5}$$

$$s_{ij} = \sqrt{\gamma} S_{ij} \,. \tag{3.2.6}$$

and $s = \gamma^{ij} s_{ij}$, where ρ, S_i and S_{ij} are the projections of the energy momentum tensor, $T^{\mu\nu}$, onto the spatial hypersurfaces. It can be shown that Eqs. (3.2.4)-(3.2.6) are analogous to the usual 'comoving' matter source terms and correspond to those actually determined numerically such as in a Cloud-in-Cell (CIC) scheme (Masaru, 2015). In particular, in Section 3.4.3 we will show that at the linear level the 'density' contrast for s_0, defined as $\delta s_0/s_0$, corresponds to local fluctuations in the particle number density rather than the relativistic energy density ρ. In practice, this is more convenient for N-body simulations as in these we are interested in following 'particles' rather than the full 'energy density field' itself: a given particle can contribute different energy densities at different positions, and the relativistic correction effect can be calculated once we have the local values of the spatial metric γ_{ij}. This has important implications on the generation of ICs as we will see in Section 3.4.1.

After adopting the CMC slicing condition Eq. (3.2.2), we still have gauge freedom to choose spatial coordinates on each spatial hypersurface as represented by the three degrees of freedom in β^i. Instead of fixing β^i 'statically', such as in synchronous gauge (where it vanishes at all times), we can use this freedom to propagate the spatial coordinates from a hypersurface at t to the next one at $t + \delta t$ in such a way that the 'distortion' of local volume elements due to coordinate effects is minimised. For this purpose, we apply the Minimal Distortion (MD) gauge condition (Smarr & York, 1978a,b), in which we demand

$$D^i(\gamma^{1/3} \partial_t \bar{\gamma}_{ij}) = 0 \,, \tag{3.2.7}$$

with D_i the covariant derivative associated with γ_{ij}. Using the MD condition Eq. (3.2.7), the momentum constraint and evolution equation for γ_{ij} combine into the following elliptic equation for the shift vector

$$(\bar{\Delta}_L \beta)^i + (\bar{L}\beta)^{ij} \bar{D}_j \ln \psi^6 = 2\psi^{-6} \bar{A}^{ij} \bar{D}_j \alpha + 16\pi \psi^4 \alpha S^i, \tag{3.2.8}$$

where

$$(\bar{L}\beta)^{ij} \equiv \bar{D}^i \beta^j + \bar{D}^j \beta^i - 2/3 \bar{\gamma}^{ij} \bar{D}_k \beta^k$$

is a conformal Killing operator and $(\bar{\Delta}_L \beta)^i \equiv \bar{D}_j (\bar{L}\beta)^{ij}$ a conformal vector Laplacian. However, the MD gauge condition Eq. (3.2.8) is actually simplified in the constrained formulation of GR adopted in GRAMSES, in which tensor modes of the metric are consistently neglected and hence no evolution equations for gravity are required to be solved. Following Bonazzola

et al. (2004); Cordero-Carrion et al. (2008), in this scheme we make the approximations

$$\bar{\gamma}_{ij} = \delta_{ij}, \quad \bar{A}^{ij}_{\rm TT} = 0 \qquad \forall t\,, \tag{3.2.9}$$

where $\bar{A}^{ij}_{\rm TT}$ is the transverse-traceless (TT) part of $\bar{A}^{ij}$. This approach follows the same spirit as the 'waveless theories of gravity' developed originally by Isenberg Isenberg (2008) and later by Wilson and Mathews in Wilson & Mathews (1989). We refer the reader to Chapter 2 for more discussion on this formalism as well as to Bonazzola et al. (2004); Cordero-Carrion et al. (2008); Cordero-Carrión et al. (2009) for its foundations and numerical applications to relativistic simulations of compact objects. With the conformal flatness approximation from Eq. (3.2.9), Eq. (3.2.8) is simplified to

$$(\bar{\Delta}_L \beta)^i = 2\partial_j \left(\alpha\psi^{-6}\bar{A}^{ij}_{\rm L}\right)\,, \tag{3.2.10}$$

where $\bar{A}^{ij}_{\rm L}$ is the longitudinal part of $\bar{A}^{ij}$. We remark that with this gauge condition, the shift vector β^i has both scalar (longitudinal) and vector (transverse) modes, which makes it different from the shift vector appearing in the commonly-used Poisson gauge where it contains purely vector perturbations. Throughout this Chapter, we refer to the combinations of both CMC slicing and MD conditions as the 'CMC-MD' gauge, though 'CMC' will often be used for the same meaning in order to avoid cluttered notation.

3.3 Gauge transformations

Since the gauge issue plays an important role in the generation of ICs, in this section we shall briefly discuss gauge transformations to understand how the main quantities from the CMC-MD gauge are connected to those in the synchronous and Newtonian gauges at first order in perturbation theory. A comparison of the latter two gauges to the CMC gauge is given in Flender & Schwarz (2012) where this is referred to as the 'Uniform Expansion' gauge, but here we will also give details on the MD gauge for the choice of spatial coordinates as well as on the equations in the 3+1 formalism. For the synchronous gauge and Newtonian gauge quantities we will stick to the convention of notation of Ma & Bertschinger (1995).

3.3.1 The geometric sector

Under an infinitesimal reparameterisation of coordinates, $x^\mu \to x'^\mu = x^\mu + \xi^\mu$, the metric components transform as

$$g_{\alpha\beta}(x) = g'_{\alpha\beta}(x) + g_{\mu\alpha}\partial_\beta\xi^\mu + g_{\mu\beta}\partial_\alpha\xi^\mu + \xi^\mu\partial_\mu g_{\alpha\beta}\,, \tag{3.3.1}$$

where $g'_{\alpha\beta}$ is the spacetime metric in the new coordinate system, and we have expanded this around the original spacetime point x^μ as

$$g'_{\alpha\beta}(x') \approx g'_{\alpha\beta}(x) + \xi^\mu\partial_\mu g_{\alpha\beta}(x).$$

To connect with standard perturbation theory and the different gauges used in cosmology, we linearise the $3+1$ metric in Eq. (3.2.1) around a Friedmann-Lemaître-Robertson-Walker (FLRW) background with metric $\mathrm{diag}(-1, a^2\delta_{ij})$, which coincides with the 'fiducial' background introduced through the CMC slicing condition. Then, we apply Eq. (3.3.1) to obtain the transformation laws for the perturbed $3+1$ metric in terms of cosmic time t and comoving spatial coordinates x^i. The conformal factor defined through the relation $\gamma_{ij} = \psi^4\bar{\gamma}_{ij}$ is perturbed at first order as $\psi = a^{1/2}(1 - \Psi/2)$, while the perturbed conformal metric is $\bar{\gamma}_{ij} = \delta_{ij} + h_{ij}$. Therefore, the metric components of the linearised Eq. (3.2.1) are

$$g_{00} = -(1+2\Phi)\,, \tag{3.3.2}$$

$$g_{0i} = \beta_i\,, \tag{3.3.3}$$

$$\gamma_{ij} = a^2[(1-2\Psi)\delta_{ij} + h_{ij}]\,, \tag{3.3.4}$$

where we have introduced the lapse perturbation $\Phi \equiv \alpha - 1$ and h_{ij} is a traceless tensor, i.e. $\gamma^{ij}h_{ij} = 0$. Then, applying the transformation law Eq. (3.3.1) we find that the metric perturbations transform as

$$\Phi' = \Phi + \dot{\xi}_0, \tag{3.3.5}$$

$$\beta'_i = \beta_i - \dot{\xi}_i - \partial_i\xi_0 + 2H\xi_i, \tag{3.3.6}$$

$$\gamma'_{ij} = \gamma_{ij} - \partial_i\xi_j - \partial_j\xi_i + 2a\dot{a}\delta_{ij}\xi_0, \tag{3.3.7}$$

where $H \equiv \dot{a}/a = -K/3$ is the Hubble parameter fixed by the CMC foliation, Eq. (3.2.2). From the trace and traceless parts of (3.3.7) we find, respectively,

$$\Psi' = \Psi - H\xi_0 + \frac{1}{3}a^{-2}\delta^{ij}\partial_j\xi_i\,, \tag{3.3.8}$$

$$h'_{ij} = h_{ij} - a^{-2}(\partial_j\xi_i + \partial_i\xi_j) + \frac{2}{3}a^{-2}\delta^{kl}\partial_k\xi_l\delta_{ij}\,. \tag{3.3.9}$$

At the linear level, the MD condition Eq. (3.2.7) reduces to

$$\partial^i h'_{ij} = 0\,, \tag{3.3.10}$$

so that Eq. (3.3.9) can be used to connect the spatial components of the gauge transformation variable ξ^μ with $\partial^i h_{ij}$, which can in turn be used to link the spatial coordinates in the two gauges. It is useful to note that if $h_{ij} = 0$ in a given gauge, such as in the case of Newtonian gauge (or Poisson gauge in the absence of tensor perturbations), then $\xi_i = 0$ and the spatial coordinates in such a gauge are equivalent to those in the MD gauge (at first order).

3.3.2 The matter sector

For the matter sector, let us consider the energy-momentum tensor of the form

$$T^\mu_\nu = (\rho + P)u^\mu u_\nu + P\delta^\mu_\nu + \Sigma^\mu_\nu\,, \tag{3.3.11}$$

in which $u^\mu = \mathrm{d}x^\mu/\mathrm{d}\tau$ is the 4-velocity of the fluid, ρ is the energy density, P the pressure and Σ^μ_ν the anisotropic stress tensor. Under the infinitesimal coordinate reparameterisation, the transformation law for Eq. (3.3.11) is

$$T^\alpha_\beta(x) = T'^\alpha_{\ \beta}(x) + T'^\alpha_{\ \nu}\partial_\beta\xi^\nu - T'^\mu_{\ \beta}\partial_\mu\xi^\alpha + \xi^\lambda\partial_\lambda T'^\alpha_{\ \beta}. \tag{3.3.12}$$

Using that $-T^0_0 = \rho = \bar{\rho}(1+\delta)$, where the overbar means that $\bar{\rho}$ is the background density (throughout this, overbar always has this meaning when applied to matter quantities and δ is the density contrast, we find that the latter transforms as

$$\delta = \delta' + 3H(1+w)\xi_0\,, \tag{3.3.13}$$

where we have used the background continuity equation $\dot{\bar{\rho}} + 3H\bar{\rho}(1+w) = 0$, and $w \equiv \bar{P}/\bar{\rho}$ is the equation-of-state parameter for a given species, and again an overbar is used in $\bar{P}$ to highlight that this is the mean pressure. Similarly, since $T^0_i = (\bar{\rho} + \bar{P})u^0 u_i$, where $u^0 = 1$ to first order, and $T^i_j = (\bar{P} + \delta P)\delta^i_j + \Sigma^i_j$, with $\Sigma^i_i = 0$, we find that the lower-index velocity transforms as

$$u'_i = u_i - \partial_i\xi_0\,, \tag{3.3.14}$$

while the upper-index velocity transforms as

$$u'^i = u^i + a^{-2}\delta^{ij}\dot{\xi}_j - 2a^{-2}H\delta^{ij}\xi_j\,. \tag{3.3.15}$$

Equations (3.3.13), (3.3.14) and (3.3.15) can be used to transform the density and velocity from the CMC-MD gauge to other gauges. In particular, by using the aforementioned fact that $\xi_i = 0$ when connecting the MD gauge with Newtonian gauge in Eq. (3.3.15) we find that the 4-velocity u^i is actually the same in both gauges. However, this is only true for the upper-index velocity u^i, while u_i transforms with $\partial_i \xi_0$ as shown by Eq. (3.3.14). We will come back to this point later.

For the sake of completeness, in Appendix B we include additional details about the mapping between the linearised fields and evolution equations in the CMC-MD gauge and their counterparts in the synchronous and Newtonian gauges.

3.4 The generation of initial conditions

Before discussing the method for the generation of ICs for particles, we remark that in the constrained formulation implemented in GRAMSES (Bonazzola et al., 2004; Cordero-Carrion et al., 2008), the initial data for the metric is entirely determined by the initial particle data, as there are no dynamical degrees of freedom in the metric (tensor modes) due to the approximations in Eq. (3.2.9).

At early times, when fluctuations around the FLRW background universe are small, it is usually assumed that standard perturbation theory is accurate and allows one to set ICs for N-body simulations, which then take care of the nonlinear evolution throughout the late-time universe. This is usually done by solving the linear perturbation equations for the coupled cosmic fluid numerically in a Boltzmann code such as CAMB (Lewis et al., 2000) or CLASS (Lesgourgues, 2011; Blas et al., 2011), or even at second order such as in SONG (Pettinari et al., 2013). From this, the density and velocity fields of the cosmic fluid are obtained at some high redshift, typically in the range $49 \lesssim z_{\rm ini} \lesssim 99$. In the case of Gaussian initial perturbations, these are fully characterised by the two-point correlation function (or the power spectrum in Fourier space). However, in order to actually use this cosmic fluid data as the ICs for an N-body code, it requires a method for mapping this to the particles' phase space. For the following discussion we assume that no vorticity is present at the initial redshift, although this is naturally developed at late times due to the nonlinear evolution.

3.4.1 The displacement vector method

The problem of realising an initial matter power spectrum $P_\Delta(k; z_{\rm ini})$ related to some Gaussian random field $\Delta(\mathbf{x}; z_{\rm ini})$ using a particle distribution can be approached in terms of a density-displacement duality. Then the generation of particles' initial positions reduces to the calculation of a displacement vector χ^i which maps the positions from a regular grid or glass configuration (Baugh et al., 1995), q^i, to the perturbed positions, $x^i(\mathbf{q})$, via

$$x^i(\mathbf{q}) = q^i + \chi^i(\mathbf{q})\,. \tag{3.4.1}$$

Equation (3.4.1) can be regarded as a coordinate transformation from some virtual coordinate system q^i with constant mass (or charge) density per coordinate volume $\bar{Q}$ to a physical coordinate system x^i where the density field $Q(\mathbf{x}) = \bar{Q}\,[1 + \Delta(\mathbf{x})]$ is inhomogeneous[1]. By virtue of mass conservation, this mapping must satisfy

$$\bar{\rho}\mathrm{d}^3\mathbf{q} = \bar{\rho}\,[1 + \Delta(\mathbf{x})]\,\mathrm{d}^3\mathbf{x}\,. \tag{3.4.2}$$

Since $\mathrm{d}^3\mathbf{x}/\mathrm{d}^3\mathbf{q} = \det(J)$, where $J^i_j = \delta^i_j + \partial\chi^i/\partial q^j$ is the Jacobian of the transformation (3.4.1), we can expand Eq. (3.4.2) perturbatively if $|\partial\chi^i/\partial q^j| \ll 1$. Then, at the linear level we find

$$\Delta(\mathbf{x}) = -\partial_i\chi^i\,, \tag{3.4.3}$$

which corresponds to the Zel'dovich approximation (Zeldovich, 1970) and defines the displacement vector at the initial redshift $z_{\rm ini}$. Consequently, the particles' coordinate velocity can be calculated as

$$v^i \equiv \frac{\mathrm{d}x^i}{\mathrm{d}t} = \dot{\chi}^i\,, \tag{3.4.4}$$

where we note that, at first order, the spatial components of the 4-velocity and coordinate velocities coincide, i.e., $u^i = v^i/u^0 \approx v^i$. Using Eqs. (3.4.3) and (3.4.4), it is straightforward to show that Δ and v^i satisfy the linear continuity equation,

$$\partial_i v^i + \dot{\Delta} = 0\,. \tag{3.4.5}$$

Namely, in this method, the overdensity variable Δ to which χ^i is related, and the velocity variable v^i, which is calculated from the latter, are generically linked through the 'standard' ('or Newtonian') continuity equation, Eq. (3.4.5). For this reason, we can consider $\{\Delta, v^i\}$ as

[1] Note that here we use Q (Δ) rather than ρ (δ) to denote the density (overdensity) variable since this does not necessarily correspond to the physical ρ appearing in the energy-momentum tensor Eq. (3.3.11), as we will see later.

'conjugate' variables. Let us point out that this is the first limitation that this method has when trying to deal with the generation of ICs for general relativistic simulations, since in a completely arbitrary gauge there is no guarantee that the continuity equation Eq. (3.4.5) would actually hold for the 'density' and 'velocity' that appear in $T^{\mu\nu}$, and hence the overdensity in such a gauge and the inferred velocity through the displacement vector method are not necessarily conjugate variables. As we will discuss in Section 3.4.2, this issue is actually not present in Newtonian N-body simulations.

Naturally, Eq. (3.4.5) shows that, in order to calculate the particles' velocity we require not exactly information about the initial density fluctuations $\Delta(z_{\rm ini})$ (encoded in $P_\Delta(k; z_{\rm ini})$), but indeed about its time evolution. At linear order, the overdensity can be written in terms of a linear growth factor as $\Delta(k; z) = D_1 \Delta(k; z = 0)$, with $D_1 = 1$ at $z = 0$, so that the velocity is given by

$$\partial_i v^i = -H f_1 \Delta \,, \tag{3.4.6}$$

where $f_1 \equiv \mathrm{d} \ln D_1 / \mathrm{d} \ln a$ is the linear growth rate. As a result, we can determine the velocities from Eq. (3.4.6) by using the input density field $\Delta(z_{\rm ini})$ alongside with some numerical values or fit for f_1, which depends on the actual model and theory of gravity. In fact, it is well-known that D_1 and f_1 are in general scale-dependent in modified gravity and dark energy models (Linder & Cahn, 2007; Narikawa & Yamamoto, 2010), in which case the simulation particles are displaced along curved trajectories, rather than straight lines, over time (Valkenburg & Hu, 2015), even in the linear regime.

3.4.2 The gauge correspondence in Newtonian N-body simulations

In this section, we discuss how the ICs generated by the displacement vector method above are consistent with standard Newtonian N-body simulations. The reason behind this is that, in a correspondence between Newtonian theory and GR at the linear level, these simulations use mixed gauges (Chisari & Zaldarriaga, 2011; Flender & Schwarz, 2012; chan Hwang et al., 2012) – the density field tracked can be identified as in the synchronous gauge, while the velocity field corresponds to the Newtonian gauge (but note that one loses track of the synchronous gauge when structure formation progresses to the nonlinear regime where particle trajectories cross each other). In order to understand this, let us start with the Newtonian gauge metric

$$\mathrm{d}s^2 = -(1 + 2\psi)\mathrm{d}t^2 + a^2(1 - 2\phi)\delta_{ij}\mathrm{d}x^i\mathrm{d}x^j, \tag{3.4.7}$$

where ψ and ϕ are the gauge-invariant Bardeen potentials (Bardeen, 1980). In this gauge, the (00), the $(0i)$ and the traceless part of the (ij) components of the Einstein equation in Fourier space are correspondingly given by

$$k^2\phi + 3\frac{\dot{a}}{a}\left(\dot{\phi} + \frac{\dot{a}}{a}\psi\right) = -4\pi G a^2 \bar{\rho}\delta^{\mathrm{N}}{}_{\mathrm{tot}}, \tag{3.4.8}$$

$$k^2\left(\dot{\phi} + \frac{\dot{a}}{a}\psi\right) = 4\pi G a^2\left(\bar{\rho} + \bar{P}\right)\theta^{\mathrm{N}}{}_{\mathrm{tot}}, \tag{3.4.9}$$

$$k^2\left(\phi - \psi\right) = 12\pi G a^2\left(\bar{\rho} + \bar{P}\right)\Theta^{\mathrm{N}}{}_{\mathrm{tot}}, \tag{3.4.10}$$

where θ is the velocity divergence, $\left(\bar{\rho} + \bar{P}\right)\Theta \equiv -(\hat{k}_i\hat{k}_j - 1/3\delta_{ij})\Sigma^i_j$, and we have used a superscript N to denote Newtonian-gauge quantities from the energy-momentum tensor and the subscript 'tot' means this is the total contribution from all matter species (the symbols without this subscript denote the corresponding quantities for individual species). The Einstein equations (3.4.8)-(3.4.10) can be combined into

$$k^2\phi = -4\pi G a^2\bar{\rho}\left[\delta^{\mathrm{N}}{}_{\mathrm{tot}} + \frac{3H}{k^2}(1+w)\theta^{\mathrm{N}}{}_{\mathrm{tot}}\right]. \tag{3.4.11}$$

In addition, the continuity equation $\nabla_\mu T^{\mu 0} = 0$ and the Euler equation $\nabla_\mu T^{\mu i} = 0$ are, respectively, given as (Ma & Bertschinger, 1995)

$$\dot{\delta}^{\mathrm{N}} + (1+w)\left(\theta^{\mathrm{N}} - 3\dot{\phi}\right) + 3\frac{\dot{a}}{a}\left(\frac{\delta P}{\delta\rho} - w\right)\delta^{\mathrm{N}} = 0, \tag{3.4.12}$$

$$\dot{\theta}^{\mathrm{N}} + \frac{\dot{a}}{a}(1-3w)\,\theta^{\mathrm{N}} + \frac{\dot{w}}{1+w}\theta^{\mathrm{N}} - \frac{\delta P/\delta\rho}{1+w}k^2\delta^{\mathrm{N}} + k^2\Theta^{\mathrm{N}} - k^2\psi = 0\,. \tag{3.4.13}$$

In the linear regime, these equations govern the evolution of δ^{N} and θ^{N} of each non-interacting component of the cosmic fluid independently, although the metric perturbations are sourced by all of them through the Einstein equations (3.4.8)-(3.4.10). In the case of dark matter (as is the case of N-body simulations), we have $\Theta^{\mathrm{N}} = w = \dot{w} = \delta P/\delta\rho = 0$, and (3.4.12) and (3.4.13) reduce respectively to

$$\dot{\delta}^{\mathrm{N}} + \theta^{\mathrm{N}} - 3\dot{\phi} = 0, \tag{3.4.14}$$

$$\dot{\theta}^{\mathrm{N}} + \frac{\dot{a}}{a}\theta^{\mathrm{N}} - k^2\psi = 0, \tag{3.4.15}$$

where $\dot{\phi} \neq 0$ and $\psi \neq \phi$ in general when the Universe is not matter dominated. Note that Eq. (3.4.14) actually does not have the standard form of the continuity equation, Eq. (3.4.5), and thus $\{\delta^{\mathrm{N}}, v^i_{\mathrm{N}}\}$ are not 'conjugate' variables, i.e., they seem to be incompatible with the displacement vector method Naturally, in the special case of pure dark matter domination, where $\dot{\phi} = 0$, Eq. (3.4.14) does take the standard form, and although this renders $\{\delta^{\mathrm{N}}, v^i_{\mathrm{N}}\}$

compatible with the displacement vector method, we note that Eqs. (3.4.11, 3.4.14, 3.4.15) still take different forms from the particle drift and kick equations and the Poisson equation used in traditional Newtonian N-body simulations (note that even if $\dot{\phi} = 0$ is a good approximation when radiation and the cosmological constant can both be neglected, at late times we generally have $\dot{\phi} \neq 0$). Indeed, it is well-known that $\delta^{\rm N}$ on large scales is different from the density field measured directly from a snapshot of traditional Newtonian N-body simulations. One can, nevertheless, still develop a consistent relativistic N-body simulation in the Newtonian gauge, by solving these equations, together with any evolution equation for the total anisotropic stress (which is needed to connect $\phi \neq \psi$) within the simulation. This is in principle the same approach as taken by GR simulation codes such as *gevolution* (Adamek et al., 2016b) or GRAMSES.

Next, consider the same set of Einstein equations and matter conservation laws written in terms of synchronous gauge variables. In this gauge, the metric with scalar perturbations is given by

$$\mathrm{d}s^2 = -\mathrm{d}t^2 + a^2(\delta_{ij} + h\delta_{ij}/3 + h^{||}_{ij})\mathrm{d}x^i\mathrm{d}x^j, \tag{3.4.16}$$

where $h^{||}_{ij} = (\partial_i\partial_j - \delta_{ij}/3)(h + 6\eta)$, in which η, h are the two metric potentials (Ma & Bertschinger, 1995). In this gauge, the relevant equation is the $(0i)$ component of the Einstein equation,

$$k^2\dot{\eta} = 4\pi G a^2 \left(\bar{\rho} + \bar{P}\right)\theta^{\rm S}_{\rm tot}, \tag{3.4.17}$$

where we have used a superscript S to denote synchronous-gauge quantities from the matter sector. The continuity equation in this gauge takes the form

$$\dot{\delta}^{\rm S} + (1+w)\left(\theta^{\rm S} + \frac{1}{2}\dot{h}\right) + 3\frac{\dot{a}}{a}\left(\frac{\delta P}{\delta\rho} - w\right)\delta^{\rm S} \;=\; 0\,. \tag{3.4.18}$$

Using the gauge transformations Eq. (3.3.13) and Eq. (3.3.15), it can be shown that δ and θ in synchronous and Newtonian gauges are related by (Ma & Bertschinger, 1995)

$$\delta^{\rm N} \;=\; \delta^{\rm S} - \frac{3H}{2k^2}(1+w)\left(\dot{h} + 6\dot{\eta}\right), \tag{3.4.19}$$

$$\theta^{\rm N} \;=\; \theta^{\rm S} + \frac{1}{2}\left(\dot{h} + 6\dot{\eta}\right). \tag{3.4.20}$$

From Eq. (3.4.19) and (3.4.20), it is clear that the combination $\delta + \frac{3H}{k^2}(1+w)\theta$ is gauge invariant, i.e.,

$$\delta^{\rm N} + \frac{3H}{k^2}(1+w)\theta^{\rm N} = \delta^{\rm S} + \frac{3H}{k^2}(1+w)\theta^{\rm S}. \tag{3.4.21}$$

Therefore Eq. (3.4.11) can be written as

$$k^2\phi = -4\pi G a^2 \bar{\rho}\left[\delta^{\rm S}_{\rm tot} + \frac{3H}{k^2}(1+w)\theta^{\rm S}_{\rm tot}\right]. \tag{3.4.22}$$

In a universe with collisionless dark matter and a cosmological constant (i.e., with negligible contributions from radiation and baryons) we have $\theta^{\rm S}_{\rm tot} = 0$, so that Eq. (3.4.22) becomes

$$k^2\phi = -4\pi G a^2 \bar{\rho}\delta^{\rm S}\,, \tag{3.4.23}$$

where $\delta^{\rm S}$ is the density contrast of dark matter only. We recognise Eq. (3.4.23) as taking the same form as the standard Poisson equation that is being solved in Newtonian N-body simulations to determine the gravitational potential at each time step, and the overdensity variable used as the source is equal to that in the synchronous gauge rather than to $\delta^{\rm N}$. Similarly, under the gauge transformation Eq. (3.4.20), for dark matter, Eq. (3.4.18) becomes

$$\dot{\delta}^{\rm S} + \theta^{\rm N} = 0\,, \tag{3.4.24}$$

where we have used $\dot{\eta} = 0$ which is a consequence of $\theta^{\rm S}_{\rm tot} = 0$ by assuming there is no radiation or baryons in Eq. (3.4.17). As a result, Eq. (3.4.24) suggests that, under the presence of dark matter and Λ, synchronous-gauge density contrast and the Newtonian-gauge velocity[2] satisfy the formal continuity equation, Eq. (3.4.5), while $\delta^{\rm N}$ and $v^i_{\rm N}$ actually satisfy Eq. (3.4.14). This fact, together with Eq. (3.4.15) (with $\psi = \phi$) and the Poisson equation Eq. (3.4.23) suggest that it can then be considered that it is the pair $\{\delta^{\rm S}, v^i_{\rm N}\}$ that is actually solved in Newtonian N-body simulations (Flender & Schwarz, 2012; Chisari & Zaldarriaga, 2011), and $\{\delta^{\rm S}, v^i_{\rm N}\}$ are in fact conjugate variables so that the displacement vector method can be consistently applied to generate the ICs for this kind of simulations. Following (3.4.6), for Newtonian N-body simulations the velocity can be calculated consistently by solving

$$\partial_i v^i_{\rm N} = -H f_1 \delta^{\rm S}\,. \tag{3.4.25}$$

[2]Note that this is a slight abuse of terminology as these two gauges have different spatial hypersurfaces and one cannot naturally define a 'Newtonian-gauge' velocity in the synchronous gauge (Flender & Schwarz, 2012). This, however, does not affect the numerical evaluation, and the '$\theta^{\rm N}$' here should be considered as a combination of synchronous-gauge quantities (cf. Eq. (3.4.20)) that takes the same value as the Newtonian-gauge velocity $\theta^{\rm N}$ (with the comparison understood to be done for positions in these two gauges that correspond to the same point in the unperturbed background spacetime). In addition, note that the velocity is $v^i_{\rm S} = 0$ in the synchronous gauge, and the time variation of the energy density contrast $\delta^{\rm S}$ is only due to deformations in the spatial part of the metric, so that a particle's coordinate in the synchronous gauge, $x^i_{\rm S}$, remains constant over time; in contrast, in N-body simulations particle coordinates do evolve over time – this suggests that this 'mixed-gauge' view of Newtonian N-body simulations is a practical rather than a fundamental one (see also Fidler et al. (2015) for a more recent approach to this issue).

In standard ICs codes such as 2LPTic (Scoccimarro, 1998; Crocce et al., 2006) the growth rate is parameterised as $f_1 = \Omega_m(a)^{0.6}$ (Lahav et al., 1991), with $\Omega_m(a) = \Omega_{m,0}a^{-3}/(H/H_0)^2$, which is valid only for the growth rate of $\delta^{\rm S}$ in a ΛCDM universe and is fully compatible with a standard Newtonian simulation. Moreover, this allows one to calculate second order corrections for the displacement vector based on approximations specific for this scenario, which serve to generate accurate ICs at even lower redshifts, so that the N-body system can be evolved for a shorter period of time. In contrast, in GR simulations only the Zel'dovich approximation has been used so far.

Before moving to the gauge used in gramses, we briefly mention that an alternative approach to interpret Newtonian N-body simulations from a relativistic point of view are the recently-proposed N-body (Fidler et al., 2015) and Newtonian motion (Fidler et al., 2016, 2017a) gauges, in which the coordinate system is defined such that the linearised dynamical equations of GR match the Newtonian counterparts when considering non-relativistic species, and first-order corrections arising from the latter can be consistently included (Fidler et al., 2017b; Adamek et al., 2017a). Interested readers can find more details in these references. Let us also note that strictly speaking the identification of the synchronous gauge variable $\delta^{\rm S}$ only makes sense in the linear regime before particle stream crossing, and it becomes ill-defined in the nonlinear regime. On the other hand, on the nonlinear, subhorizon, scales, the difference from the Newtonian gauge density perturbation is suppressed as the gauge difference formally scales with $(aH/k)^2$, see Eq. (3.4.19). This is a subtle point to bear in mind in the approach taken here, while a more sophisticated gauge definition can eliminate it: N-body gauge, for example, offers a unified treatment of these two different regimes by stitching together different subhorizon patches of space using a global coordinate system.

3.4.3 Initial conditions for gramses simulations

Let us now move on to some relevant aspects for the generation of ICs in the CMC-MD gauge. As in the case of the previous subsection, we start by presenting the continuity equation in this gauge, so that we can identify the actual variables being used in gramses simulations and assess its compatibility with the displacement vector method. It can be shown that the continuity equation $\nabla_\mu T^{\mu 0} = 0$ in the CMC gauge, at linear order, takes the form

$$\dot{\delta}^{\rm C} + (1+w)\left(\partial_i u^i_{\rm C} - 3\dot{\Psi}\right) + 3\frac{\dot{a}}{a}\left(\frac{\delta P}{\delta\rho} - w\right)\delta^{\rm C} = 0, \tag{3.4.26}$$

where the subscript/superscript C is used to denote CMC-MD gauge quantities from the matter sector. If we consider collisionless non-relativistic dark matter, this reduces to

$$\dot{\delta}^{\mathrm{C}} + \partial_i u^i_{\mathrm{C}} - 3\dot{\Psi} = 0\,. \tag{3.4.27}$$

Clearly, Eq. (3.4.27) resembles the Newtonian-gauge continuity equation Eq. (3.4.14), and the term $3\dot{\Psi}$ is not present in either the standard form of the continuity equation Eq. (3.4.5), or in the mixed-gauge version used in Newtonian simulations, Eq. (3.4.24). This additional term represents a volume change due to relativistic deformations of space, which can create an under-dense or over-dense region even in the absence of any peculiar motion of matter (Fidler et al., 2015). In fact, given that an infinitesimal 3-dimensional volume element is distorted, at linear order, by the factor $\sqrt{\gamma} = a^3(1 - 3\Psi)$, from Eq. (3.2.4) we can show that the fluctuations in the conformal density field s_0 are given by

$$\delta s_0 \equiv \frac{s_0 - \bar{s}_0}{\bar{s}_0} = \delta^{\mathrm{C}} - 3\Psi\,. \tag{3.4.28}$$

where as before an overbar denotes background value. This corresponds to a particle number density contrast in the CMC gauge:

$$\delta^p \equiv \delta^{\mathrm{C}} - 3\Psi\,, \tag{3.4.29}$$

with which Eq. (3.4.27) is cast into the standard form of the continuity equation

$$\dot{\delta}^p + \partial_i u^i_{\mathrm{C}} = 0. \tag{3.4.30}$$

This indicates that $\{\delta^p, u^i_{\mathrm{C}}\}$ are conjugate variables, so that u^i_{C} can be generated by using Eq. (3.4.30) with δ^p as an input. In this situation, δ^p can be regarded as fluctuations in the 'bare' density field (Valkenburg & Hu, 2015) as the spacetime curvature is not included, and at the linear level this corresponds to the perturbations in the conformally-scaled density s_0 which is used in GRAMSES. For an N-body simulation, using s_0 rather than ρ is more convenient in practice since we are interested in following 'particles' rather than the total 'energy density field' itself, and the (non-conformal) energy density field at a given instant can be separately calculated by inverting Eq. (3.2.4) once the spatial metric γ_{ij} is solved.

Notice, however, that the identification of $\delta^p = \delta s_0$ is only made at linear order in perturbation theory, which is sufficient for the purpose of setting up ICs. At the nonlinear level, the density field in Eq. (3.2.4) contains additional contributions because $\rho = (\alpha u^0)^2 \rho_0$, where ρ_0 is the actual rest-mass of the system. The extra factor αu^0 actually corresponds to a Lorentz factor

which contributes a quadratic term in the velocity that does not affect the generation of ICs at the linear level. In GRAMSES, s_0 is constructed in a completely nonlinear way using the particles' positions and velocities in a Cloud-in-Cell (CIC) scheme, as well as the updated values of the metric components.

Interestingly, it can be shown that using the gauge transformations Eqs. (3.3.8), (3.3.9) and (3.3.13), as well as the linearised MD condition Eq. (3.3.10), we can rewrite the right-hand side of Eq. (3.4.29) in terms of synchronous gauge variables as (bear in mind that δ^p is the particle number density contrast in the CMC gauge)

$$\delta^p = \delta^{\mathrm{S}} - 3\eta\,. \tag{3.4.31}$$

We note that, while $\dot{\eta} = 0$ in the dark-matter and Λ dominated eras, η is in general not zero, which means that δ^p and δ^{S} differ by a scale-dependent function whose shape has been fixed by its evolution at higher redshifts, when the contribution of radiation cannot be neglected. Since it can be shown that $u^i_{\mathrm{C}} = u^i_{\mathrm{N}}$ (with contravariant index), as discussed in Section 3.3.2, the fact that Eq. (3.4.24) and Eq. (3.4.30) have the same form is consistent with δ^p differing from δ^{S} only by a time-independent quantity.

Notice, however, that Eq. (3.4.30) can be used to calculate the 4-velocity u^i (with upper index) rather than u_i, and it is the latter that is the actual variable which appears in the $3+1$ form of the geodesic equation written as a first-order system which is implemented in GRAMSES (Baumgarte & Shapiro, 2010). For non-relativistic particles, this is given at linear order by

$$\frac{\mathrm{d}x^i}{\mathrm{d}t} = a^{-2}\delta^{ij}u_j - a^{-2}\delta^{ij}\beta_i, \tag{3.4.32}$$

$$\frac{\mathrm{d}u_i}{\mathrm{d}t} = -\partial_i\Phi\,, \tag{3.4.33}$$

where the shift vector β^i appears explicitly due to to the relation

$$u_i = a^2\delta_{ij}\left(u^j + \beta^j\right)\,. \tag{3.4.34}$$

The correction due to the shift vector in Eq. (3.4.34), which in the MD gauge is given by Eq. (3.2.10), is taken into account in GRAMSES itself when starting the simulation by solving the linearised version of the momentum constraint for β^i at z_{ini} (just for once), i.e.,

$$(\bar{\Delta}_L\beta_{\mathrm{ini}})^i - 6\Omega_m\beta^i_{\mathrm{ini}} = 6\frac{\Omega_m}{a}u^i_{\mathrm{ini}}\,, \tag{3.4.35}$$

such that the initial lower-index 4-velocity u_i^{ini} can be constructed using Eq (3.4.34), only

after which does the actual simulation start. Note that this means that the particle velocity fed into GRAMSES is u^i rather than u_i.

Even though we have shown that $\{\delta^p, u^i_{\rm C}\}$ are conjugate variables, and that we can calculate $u^{\rm C}_i$ using Eq. (3.4.34) and Eq. (3.4.35), there is still one remaining caveat which is the fact that the growth rate of the number density perturbation δ^p is not known, so that if we insist on using the analog of (3.4.6) to calculate $u^i_{\rm C}$, then f_1 needs to be found numerically by solving the evolution equation for δ^p that can be derived from the corresponding Euler equation and Eq. (3.4.30). This is doable, but it is not the approach that we shall follow here.

Another alternative approach to generate simulation ICs for the CMC gauge is by exploiting the relation $u^i_{\rm C} = u^i_{\rm N}$, and splitting the generation of ICs into two steps: in the first we generate particle displacements using the power spectrum of δ^p as input, while in the second we generate the velocity $u^i_{\rm N}$ by applying the standard method based on Eq. (3.4.6), using the power spectrum of $\delta^{\rm S}$ (which has scale-independent linear growth) rather than δ^p. This actually is a neat and simpler way than the more general method presented in Section 3.4.4, and there is a potential of applying similar tricks to generate ICs in other gauges (though we shall not explore this here). We have checked that the relative difference between the velocity divergence power spectra of the ICs generated by using these two methods is well below 0.1%.

3.4.4 A finite difference method for the calculation of initial velocities

To avoid using an explicit parameterisation of f_1 for the calculation of velocities, we introduce a finite difference approach. Here, instead of using a single power spectrum $P_\Delta(k; z_{\rm ini})$ at $z_{\rm ini}$ as in the standard displacement vector method based on the Zel'dovich approximation, we use two additional power spectra $P_\Delta(k; z_\pm)$ from the neighbouring redshifts $z_\pm = z_{\rm ini} \pm \Delta z$, with $\Delta z \ll z_{\rm ini}$ which will provide the information needed about the growth rate of density perturbations around $z_{\rm ini}$. Then, rather than using Eq. (3.4.5) or Eq. (3.4.6) to calculate the initial velocity, we take the finite difference $\Delta x^i \equiv x^i(z_-) - x^i(z_+)$ directly from the definition of coordinate velocity in Eq. (3.4.4), i.e.

$$v^i \approx \frac{\Delta x^i}{\Delta t} = \frac{H}{a}\frac{\chi^i(z_-) - \chi^i(z_+)}{2\Delta z}\,, \tag{3.4.36}$$

where $\chi^i(z_\pm)$ are the displacement vectors calculated from $P_\Delta(k; z_\pm)$ via the Zel'dovich approximation Eq. (3.4.3) at the neighbouring redshifts $z_\pm$. The advantage of using Eq. (3.4.36) over Eq. (3.4.6) is that this approach is independent of the underlying theory of gravity or

gauge used since this information is entirely drawn from the input power spectra (obtained from a suitable linear Boltzmann code for the model), and can be applied as long as the density perturbations and velocity needed are conjugate variables. Importantly, to create the random realisations of $\chi(z_{\rm ini})$ and $\chi(z_\pm)$ from $P_\Delta(k;z_{\rm ini})$ and $P_\Delta(k;z_\pm)$, the same random number sequence, and hence random number seeds, should be used to ensure that we have generated three consecutive snapshots for the 'same' particles.

The fact that the velocity calculation in Eq. (3.4.36) relies entirely on the input power spectra to generate the ICs can potentially become problematic due to the generic presence of radiation at $z_{\rm ini}$ in the linear code, which contributes to the growth rate of matter and drives $\dot{\eta}$ away from zero. In order to suppress this effect, the two neighbouring power spectra $P_\Delta(k;z_\pm)$ can be calculated by evolving $P_\Delta(k;z_{\rm ini})$ under the linear theory assuming matter domination. We will show how this can be done in particular for the case of GRAMSES ICs in Section 3.5.

Figure 3.1 illustrates the gauge effects (for synchronous and CMC gauges) on the matter power spectrum (left panel), as well as the scale dependence of f_1 due to radiation in these two gauges (right panel). Here, the growth rates of δ^p and $\delta^{\rm S}$ are obtained by taking finite difference between snapshots in each gauge. Since in Fourier space $P_{\delta\delta}(k;z)=|\delta(k;z)|^2$, this is given by

$$f_1^{\rm FD}(z)=\frac{1}{2a\Delta z}\frac{\sqrt{P_{\delta\delta}(z_-)}-\sqrt{P_{\delta\delta}(z_+)}}{\sqrt{P_{\delta\delta}(z)}}\,, \tag{3.4.37}$$

where the FD superscript means that the left-hand side quantity has been obtained using a finite difference. In this we use the power spectra obtained from a modified version of CAMB, which works for different gauges. From the right panel of Fig. 3.1 we can see that, even for synchronous gauge, the presence of radiation has a noticeable effect at large scales and boosts the growth rate by $\sim 2\%$ with respect to the linear-theory prediction for a matter dominated universe ($f_1=1$), and there is an approximately 1% suppression on sub-horizon scales, where gauge effects are not present. For the CMC-MD case, the gauge effects on the overdensities and the scale dependence of the growth rate are also evident from Fig. 3.1, as we can see that the power spectra and growth rates agree in both gauges at scales inside the horizon, but there is a dramatic suppression of the growth rates toward large scales in the CMC-MD gauge. This effect arises due to the η in Eq. (3.4.31), which dominates the shape of the power spectrum below $k\lesssim 10^{-3}h{\rm Mpc}^{-1}$, as can be seen from the left panel of Fig. 3.1. Since η does not evolve considerably on the redshift range shown, at very large scales the matter power spectrum of δ^p remains roughly constant in time, resulting in the strongly suppressed growth

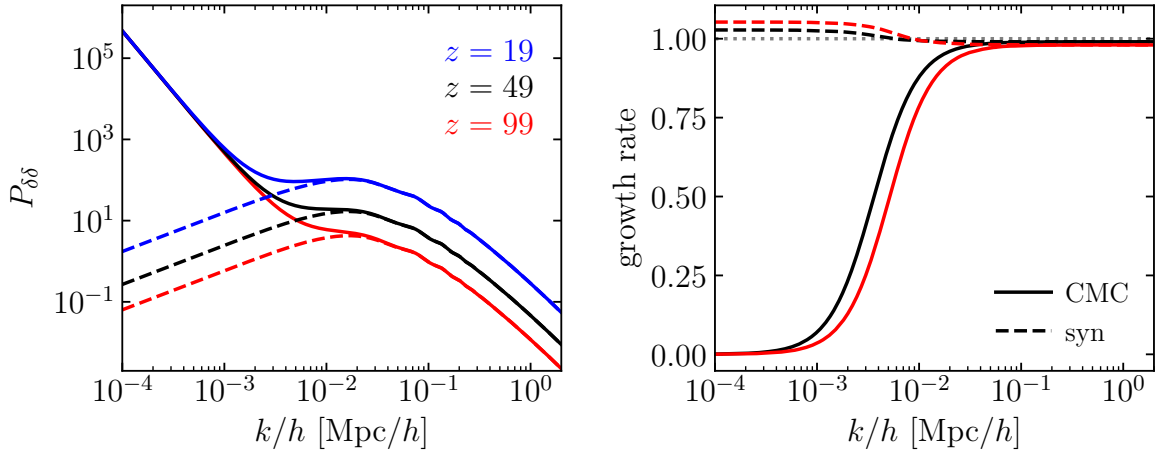

Figure 3.1: *Left panel*: a comparison of matter power spectra in the CMC-MD gauge (solid line) and synchronous gauge (dashed line) for three different redshifts – $z = 99$ (red), 49 (black) and 19 (blue) – as obtained from a modified version of CAMB. *Right panel*: the growth rates in these two gauges calculated by finite difference of two neighbouring power spectra around the three aforementioned redshifts with $\Delta z = 0.5$, see Eq. (3.4.37). As a reference, the gray dotted line shows the linear-theory prediction $f_1 = 1$ for synchronous gauge in a matter dominated universe.

rate depicted in the right panel of Fig. 3.1.

For Newtonian simulations, a common approach to take into account the presence of radiation, at least at the linear level, is through the so-called 'back-scaling' method. In this approach, the input power spectrum used to generate the ICs is given by the linear code at $z = 0$ rather than at the actual starting redshift of the simulation. Then, this power spectrum is evolved backwards, up to $z_{\rm ini}$, using a growth factor derived from Newtonian theory (where no radiation is present), resulting in a matter power spectrum $\tilde{P}_\Delta(k; z_{\rm ini})$ that does not agree with the Boltzmann code at $z_{\rm ini}$ but that allows one to generate 'artificial' ICs that guarantees that the simulation will reproduce the correct matter overdensities on linear scales at $z = 0$ due to this particular calibration. An alternative, relativistic back-scaling approach has been discussed in Fidler et al. (2017b); Adamek et al. (2017a), in which the resulting output of the simulation is interpreted in terms of a different gauge with the aid of a modified version of CLASS.

The finite-difference method described above can in principle be used in combination with the 'back-scaling' method, with the latter providing the linear power spectra at not just $z_{\rm ini}$ but also $z_\pm$. However, our ultimate goal is to start from a more accurate IC, while also including radiation effects in the simulation itself, e.g., by treating radiation as linear perturbations and interfacing with a Boltzmann code such as CAMB or CLASS during the N-body simulation to calculate relevant quantities. The latter is what we plan to do in the future simulations,

which is another reason why in this Chapter we do not follow the back-scaling approach.

3.5 Results

In this section, we present results on the generation of ICs for GRAMSES using the finite difference method described in Section 3.4.4. We have implemented this method in 2LPTic code, so that the initial particle positions are calculated with the Zel'dovich approximation (3.4.3) at $z_{\rm ini}$, as in the default 2LPTic code[3], but their velocities are calculated using the finite difference expression (3.4.36). For all realisations of the density field we use the same random seed in order to suppress realisation scatter in our results. As previously mentioned, the default 2LPTic code uses second-order corrections for the calculation of the displacement vector, while our method implements only linear perturbations as this is enough for the purpose of fixing the gauge issues and generating ICs for GRAMSES consistently, so these are turned off for comparison. Initial conditions generated by this method have been used to run the first GRAMSES cosmological simulations discussed in Chapter 2, based on Barrera-Hinojosa & Li (2020). The input matter power spectra for the ICs generation are obtained from a modified version of CAMB implementing Eq. (3.4.31) to relate δ^p to the synchronous-gauge overdensity $\delta^{\rm S}$ which is the default variable used in such code.

Let us add some details on how we address the problem of radiation in the generation of ICs for GRAMSES. The latter appears because the three power spectra outputted by the Boltzmann code do contain the effects from radiation, but the N-body simulation is only for dark matter. For this particular case, we can use Eq. (3.4.31) to enforce the $\dot{\eta} = 0$ condition via

$$\delta^p(k; z_\pm) = \frac{D_1(z_\pm)}{D_1(z_{\rm ini})}\delta^{\rm S}(k; z_{\rm ini}) - 3\eta(k; z_{\rm ini})\,, \tag{3.5.1}$$

where on the right-hand side η is a scale-dependent function constant in time, evaluated at $z_{\rm ini}$. Then, it is sufficient to calculate the linear growth factor in the synchronous gauge, $D_1(z)$, with which $\delta^{\rm S}$ can be evolved from $z_{\rm ini}$ to $z_\pm$ in the absence of radiation while keeping η fixed by outputting $\eta(z_{\rm ini})$ from CAMB. As a result, $P_{\delta\delta}(k; z_\pm) = |\delta^p(k; z_\pm)|^2$ can be constructed from (3.5.1) in such a way that it is completely free from radiation effects and can be used to generate the velocities for the GRAMSES N-body simulation using Eq. (3.4.36).

[3]Contrary to the default 2LPTic code, however, we do not use the 'back-scaling' of a $z = 0$ input power spectrum with a growth factor parameterisation but directly use the one generated by the Boltzmann code at $z_{\rm ini}$.

There is an additional subtlety to take into account in order to compare the ICs from this method against the ones generated from default 2LPTic, which is that the normalisation[4] of the matter power spectra $P_\Delta(k; z_\pm)$ is required as an input (while the default 2LPTic code only requires this at $z_{\rm ini}$). These have associated values of σ_8 at the neighbouring redshifts $z_\pm$ and directly affect the calculation of the displacement vectors and hence the velocity via Eq. (3.4.36). Therefore, even the Newtonian velocity calculated by the finite difference method will not necessarily coincide with what is calculated by using the growth rate f_1 parameterisation implicit in the default 2LPTic code. In order to make these comparable, we can get a linear-theory prediction for the σ_8 values at the neighbouring redshifts by applying the linear growth rate as

$$\sigma_8^{\rm S}(z_\pm) = \frac{D_1(z_\pm)}{D_1(z_{\rm ini})}\sigma_8^{\rm S}(z_{\rm ini})\,, \tag{3.5.2}$$

so we can use these rather than the CAMB output values at $z_\pm$.

Similarly, in the CMC gauge, we can use Eq. (3.5.1) to estimate σ_8^p from linear theory: its values at the neighbouring redshifts with fixed η can be calculated as

$$\sigma_8^p(z_\pm) = \sqrt{\left[\frac{D_1(z_\pm)}{D_1(z_{\rm ini})}\sigma_8^{\rm S}(z_{\rm ini})\right]^2 + 9[\sigma_8^\eta(z_{\rm ini})]^2 - 6\frac{D_1(z_\pm)}{D_1(z_{\rm ini})}\left[\sigma_8^{{\rm S}\eta}(z_{\rm ini})\right]^2}\,, \tag{3.5.3}$$

where σ_8^η represents the normalisation of the power spectrum $P_{\eta\eta}$, and $\sigma_8^{{\rm S}\eta}$ that of the cross spectra between $\delta_{\rm S}$ and η. We calculate this cross-term by evaluating Eq. (3.5.3) at the initial redshift $z_{\rm ini}$, i.e.,

$$[\sigma_8^{{\rm S}\eta}(z_{\rm ini})]^2 = \frac{[\sigma_8^{\rm S}(z_{\rm ini})]^2 - [\sigma_8^p(z_{\rm ini})]^2 + 9[\sigma_8^\eta(z_{\rm ini})]^2}{6}\,. \tag{3.5.4}$$

This way, we can ensure that the power spectra normalisation at the neighbouring redshifts is consistent with those constructed from Eq. (3.5.1).

In order to illustrate how well this method works, we generate the ICs for two different setups; a low-resolution one with a comoving box size of $L = 4h^{-1}$Gpc and $N_p = 1024^3$ dark matter particles, and a high-resolution one with $L = 256h^{-1}$Mpc and the same number of particles. We also use two different initial redshifts, and the power spectra measured from these ICs are compared against linear-theory predictions obtained from the modified CAMB version.

Figure 3.2 shows the matter power spectrum of the ICs generated by both the standard

[4] By 'normalisation' here we mean the linear-theory root-mean-squared fluctuation of matter smoothed on $8h^{-1}$Mpc scales, σ_8. In 2LPTic code, the value of σ_8 is required as an input to get the correct amplitude of the initial matter density field.

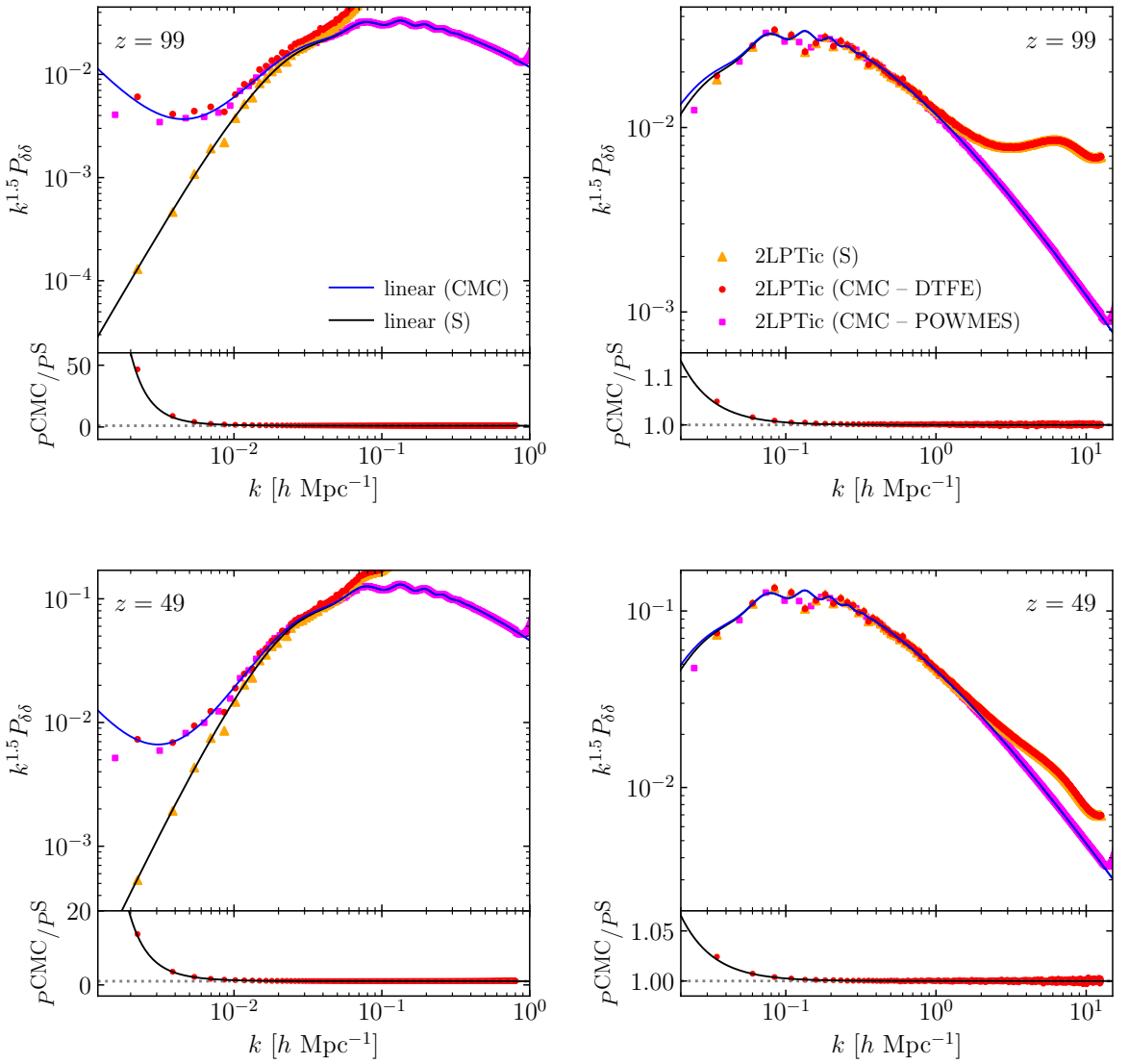

Figure 3.2: Matter power spectra of ICs generated by both standard and modified 2LPTic codes. *Left panels*: results for the low-resolution setup ($L = 4h^{-1}$Gpc and $N_p = 1024^3$) for $z_{\rm ini} = 99$ (top) and $z_{\rm ini} = 49$ (bottom). *Right panels*: results for the high-resolution setup ($L = 256h^{-1}$Mpc and $N_p = 1024^3$) for $z_{\rm ini} = 99$ (top) and $z_{\rm ini} = 49$ (bottom). In all panels, the linear-theory predictions for synchronous and CMC gauges are represented by the solid black and blue lines, respectively. The red circles in the bottom sub-plots represent the ratio between $P_{\delta\delta}$ in the CMC-MD and synchronous gauges as measured by DTFE code, while the solid black line represents the ratio between the linear-theory curves.

and modified version of 2LPTic. In the case of the CMC-MD gauge, this is measured from the ICs data in two different ways; one is using the DTFE code (Cautun & van de Weygaert, 2011) along with NBODYKIT (Hand et al., 2018) (red circles), and the second one is applying POWMES (Colombi et al., 2009) (magenta squares). The reason for this is that the former captures more accurately the turnover on large scales due to gauge effects but might lose accuracy towards shorter wavelength modes, while POWMES has a better performance

when approaching the Nyquist frequency but eventually fails at capturing the largest-scale components appearing in this particular gauge. For the synchronous gauge case (orange triangles) only DTFE and NBODYKIT are applied. Figure 3.2 shows good agreement between the linear-theory predictions and the 2LPTIC results for both the high and low resolution setups and both initial redshifts, although the latter decreases towards larger scales where gauge effects dominate. On these scales we can also see that the ICs data seem to mismatch the linear theory prediction curve, but this is normally the case due to realisation scatter and cosmic variance. However, since the ICs have been generated using the same initial random seeds in all cases, this effect is removed in the ratio between the power spectra in the two gauges, as can be seen from the lower subpanels of each panel.

Figure 3.3 is similar to Fig. 3.2, but shows the results for the velocity divergence $\theta \equiv \nabla \cdot u$ power spectra of the ICs generated using the original 2LPTIC code (stars) as well as the modified version implementing the finite difference calculation for the velocity field Eq. (3.4.36) for both the Newtonian gauge (circles) and CMC-MD gauge (triangles). In all cases, θ is calculated using the DTFE code. As Eq. (3.4.36) depends on Δz, we have tried four different values of Δz – $1, 0.5, 0.25, 0.05$ – to assess the correct magnitude to be used and how this affects the calculation of the velocity field. In the lower subpanels of each panel, we show the relative difference between the Newtonian velocity divergences $\partial_i u^i_{\rm N}$ obtained from the modified and default 2LPTIC code, where sub-percent differences are found for all probed scales and all Δz values used, and the amplitude seems robust against spatial resolution. This result suggests that, at least for the case of Newtonian gauge, the finite difference method can be used to generate the ICs for cosmological simulations regardless of specifications and matching the default 2LPTIC code accuracy (at least up to first order). Nonetheless, we notice that using a value of Δz that is too small might introduce some scatter, while increasing Δz will monotonically increase the amplitude of the relative difference so that this might eventually become unacceptable (e.g., larger than $\mathcal{O}(1\%)$). From Fig. 3.3 we note that $\Delta z/z_{\rm ini} \sim 1\%$ is enough to suppress noise while keeping the relative difference with respect to the default code under 0.03% in all cases.

As we have remarked before, the ICs method generates u^i while u_i (lower index) is the actual variable used to solve the geodesic equation in the standard $3+1$ (ADM) form implemented in the simulations. Thus, in Fig. 3.3 the results for the $\theta_{\rm C} = \partial^i u^{\rm C}_i$ spectra (triangles) have been obtained from the initial GRAMSES snapshot, which is outputted after the code solves Eq. (3.4.35) to get the shift vector β^i and calculates $u^{\rm C}_i$ from Eq. (3.4.34) to start the actual simulation with. This is how GRAMSES operates, so that only u^i is needed as an input in

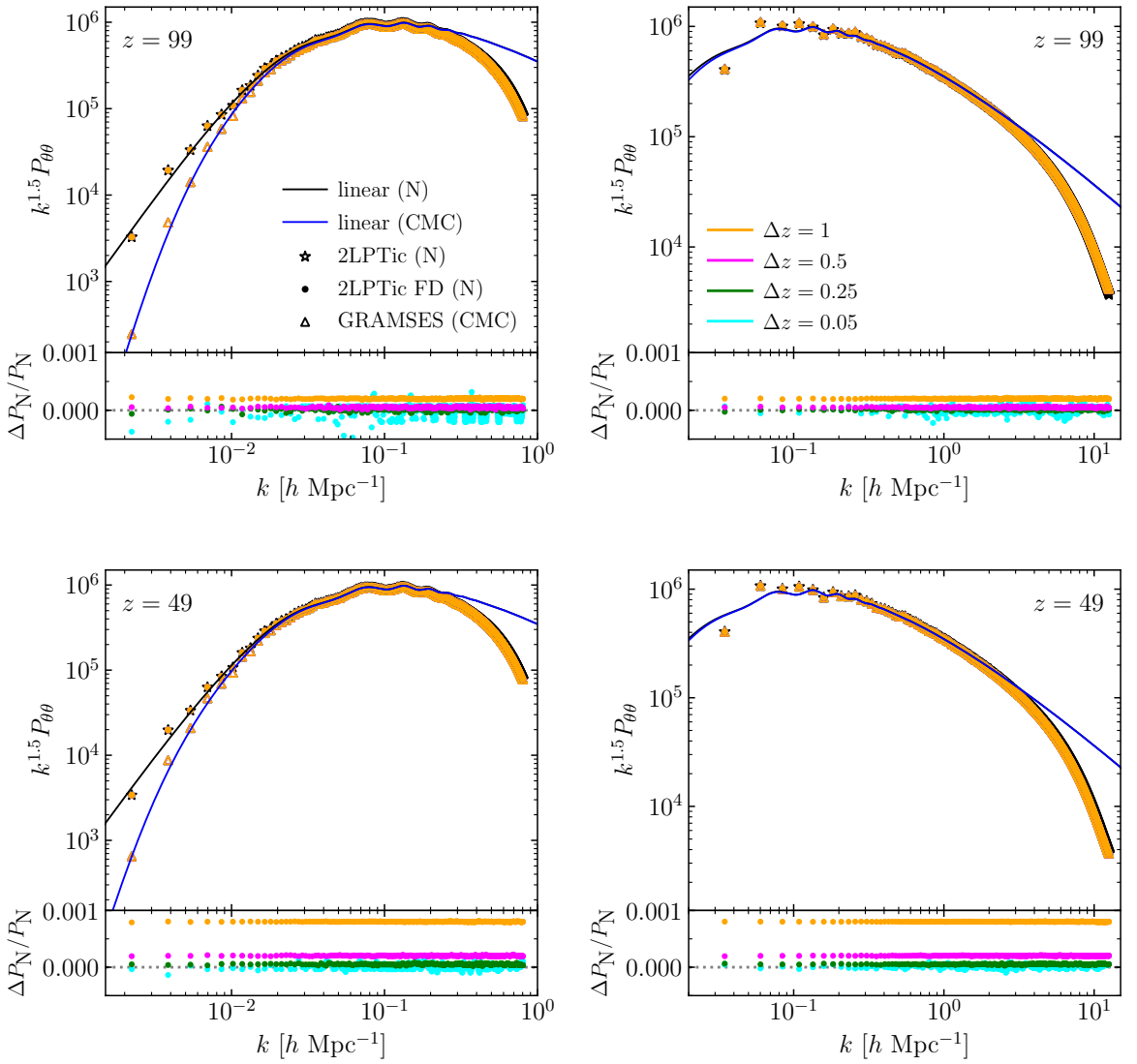

Figure 3.3: Velocity divergence ($\theta \equiv \nabla \cdot u$) power spectra for the Newtonian gauge measured from the ICs generated by the standard 2LPTic code (stars) and its modified version (circles), as well as the CMC-MD result obtained from the GRAMSES correction (triangles) discussed in the main text. *Left panels*: results for the low-resolution setup ($L = 4h^{-1}$Gpc and $N_p = 1024^3$) for $z_{\rm ini} = 99$ (top) and $z_{\rm ini} = 49$ (bottom). *Right panels*: results for the high-resolution setup ($L = 256h^{-1}$Mpc and $N_p = 1024^3$) for $z_{\rm ini} = 99$ (top) and $z_{\rm ini} = 49$ (bottom). In all panels, the linear-theory predictions for Newtonian and CMC-MD gauges are represented by the solid black and blue lines, respectively. The bottom sub-panels of each plot show the relative difference between the Newtonian gauge results for the different values of Δz.

the ICs. In this case, we also find good agreement with the linear-theory expectations for both simulation setups (left and right panels) and redshifts (top and bottom panels), and the deviation from linear theory at small scales (which is also present in the Newtonian gauge cases) is due to spatial resolution effects.

Finally, to briefly illustrate the impact of radiation effects and the σ_8 normalisation on the generation of ICs, in Fig. 3.4 we show the results when linear-theory corrections are not

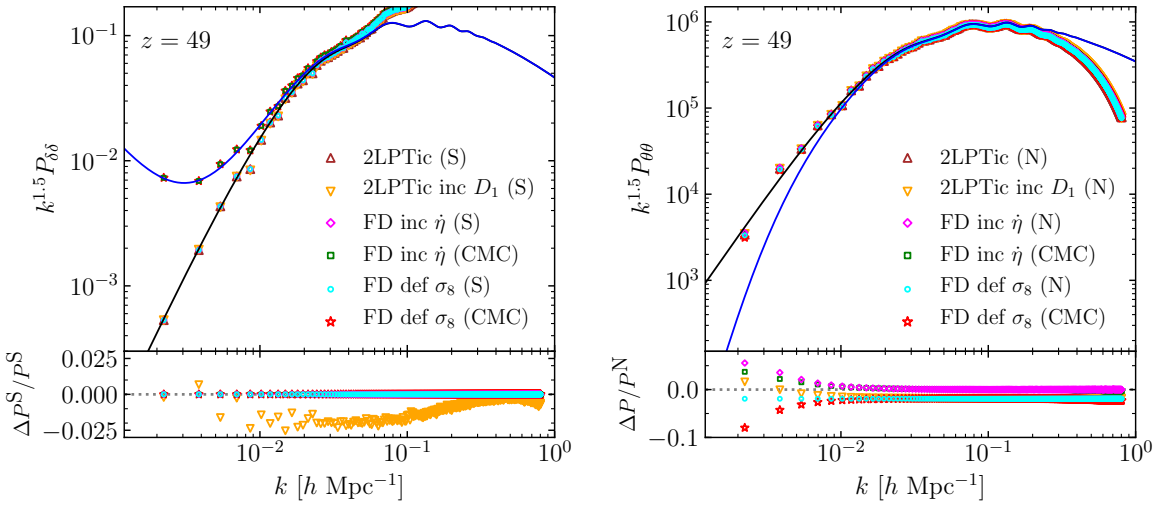

Figure 3.4: The impact of radiation and σ_8 normalisation on the generation of ICs. The results from the default 2LPTic code, where the linear growth factor D_1 is used to 'back-scale' the $z = 0$ matter power spectrum to $z_{\rm ini}$, is also included (orange triangles). The default case (brown triangles), which is used as the denominator to calculate the relative differences in the lower subpanels, also uses the standard 2LPTic code but feeds it with the matter power spectrum at $z_{\rm ini}$ and sets $D_1 = 1$. *Left panel*: matter power spectra for the overdensity in the synchronous (S) gauge, $\delta^{\rm S}$, as well as for the particle number overdensity δ^p in the CMC gauge. *Right panel*: velocity divergence ($\theta = \partial_i u^i$) power spectra, where u^i represents the conjugate variable to either $\delta^{\rm S}$ (N) or δ^p (CMC); note that in the case of the CMC gauge the velocity divergence is not $\partial^i u_i^{\rm C}$. The solid curves denote the linear-theory predictions using the same colours as the previous figures. See the main text for more details of the symbols.

applied, i.e., when skipping Eqs. (3.5.1)-(3.5.4), as well as the case where the 'back-scaling' method of the standard 2LPTic is used (orange triangles). In the latter case, a $z = 0$ power spectrum from CAMB is provided as an input and the code uses the theoretical value of D_1 to scale it back to $z_{\rm ini}$. Both panels in Fig. 3.4 show the results from the standard 2LPTic code with no 'back-scaling' (i.e., feeding the 2LPTic code with the linear power spectrum at $z_{\rm ini}$ and setting $D_1 = 1$; brown triangles) and from the finite difference method for the cases where either: 1) η is not kept constant for the default gauge used in 2LPTic (magenta diamonds) and the CMC gauge (green squares), and 2) when σ_8 is not corrected for the default gauge (cyan circles) and the CMC gauge (red stars). In this case we use the setup with $L = 4h^{-1}$Gpc and $N_p = 1024^3$, and $\Delta z = 0.5$ for the finite difference calculations.

In the left panel of Fig. 3.4, we show $P_{\delta\delta}$ for all cases in the top panel, and the relative differences with respect to the default case (represented by the brown triangles) are shown in the bottom panel. From the latter, we can see that the back-scaled case (orange triangles) shows a suppression of up to $\sim 2.5\%$, which is because radiation and baryons are present in the forward linear-theory calculation (by CAMB) all the way down to $z = 0$, while D_1 is

calculated by assuming a universe with only dark matter and cosmological constant (so that there is an inconsistency). As expected, the synchronous-gauge results for the cases where $\dot{\eta} \neq 0$ (magenta diamonds) and where σ_8 is not corrected for (cyan circles) agree perfectly with the default case, since these corrections apply only to the neighbouring snapshots used for the velocity calculation (via finite difference), while the particle displacements in the ICs are obtained by using solely the matter power spectrum at $z_{\rm ini}$, which are not affected by these corrections.

In the right panel of Fig. 3.4, we present the power spectra for the velocity divergences associated to the overdensity variables for all cases shown in the left panel in the top, and the relative differences of $P_{\theta\theta}$ with respect to the default case (Newtonian-gauge velocity obtained by using the 2LPTic code without doing the D_1 'back-scaling'; brown triangles) are plotted in the bottom. By comparing the various Newtonian-gauge results it can be seen that, when the σ_8 correction is not used in the finite difference calculation (cyan circles) a constant $\sim 2\%$ suppression is found, while the effect of $\dot{\eta} \neq 0$ (magenta diamonds) only appears at large scales. The 'back-scaled' case (orange triangles) shows a combination of these behaviours.

The CMC-MD gauge results in the right panel of Figure 3.4 showing the effect of $\dot{\eta} \neq 0$ (green squares) and that of no σ_8 correction (red stars) are for the u^i velocity obtained via the finite-difference method using the δ^p power spectrum. Here, we compare the power spectra of $\partial_i u^i_{\rm C}$ (symbols labelled with '(CMC)' in the legend) with those of $\partial_i u^i_{\rm N}$ (symbols labelled with '(N)'), as we expect the two to be equal to each other since $u^i_{\rm C} = u^i_{\rm N}$ (see Appendix B). The default case, the relative differences of all the other cases with respect to which are shown in the lower subpanel, is '2LPTic (N)', which represents the velocity field generated using the 2LPTic code without back-scaling. The deviations from the default case can be understood as the effects of $\dot{\eta} \neq 0$ or not applying the σ_8 correction. For example, for $\partial_i u^i_{\rm N}$ (cyan circles), not correcting for σ_8 causes a constant shift; the same constant shift appears for $\partial_i u^i_{\rm C}$ (red stars) at $k \gtrsim 0.01h{\rm Mpc}^{-1}$, but on even larger scales the deviation gets larger. On the other hand, not enforcing $\dot{\eta} = 0$ while applying the σ_8 correction (purple diamonds and green squares) leads to good agreement with the default case on small scales, whilst deviations still remain on large scales $k \lesssim 0.02h{\rm Mpc}^{-1}$.

3.6 Summary

In this Chapter, we have addressed the generation of ICs data for relativistic N-body simulations, and in particular for GRAMSES. We have revised the standard method where the

calculations of particles' positions and velocities are both done using the displacement vector, highlighting its limitations when it comes to models beyond ΛCDM or gauges other than synchronous gauge overdensity and Newtonian gauge velocity, $\{\delta^{\rm S}, u^i_{\rm N}\}$. In order to overcome these issues, we have proposed a finite difference calculation for the particles' velocities such that no explicit parameterisation of the growth factor (and growth rate) is required.

In this approach, not only do we need the matter power spectrum $P_{\delta\delta}$ at the initial redshift $z_{\rm ini}$, but it is also required at two neighbouring redshifts (one slightly higher and the other slightly lower). Then, an ICs code is applied to realise these three power spectra (using the same random number seed) to calculate the particle positions at the three redshifts, the central one of which is used as the real particle positions at $z_{\rm ini}$, while the velocities of the particles are calculated by finite-differencing their displacements in the two neighbouring snapshots (this is the simplest way to do finite difference, and more accurate ways are also possible although they generally require more snapshots to be generated). In this way, the basic assumption of a scale-independent linear growth rate of the usual ICs codes (for Newtonian simulations) is avoided, and the method can be applied to generate the initial conditions for any model – as long as the pair $\{\delta, u^i\}$ used obey the formal continuity equation Eq. (3.4.5) – since all the information needed is drawn from the three input matter power spectra. For illustration, we have implemented this finite difference method of the velocity in a modified 2LPTIC code, and the matter power spectrum for the relevant gauge is calculated using a modified version of the Boltzmann code CAMB. The implementation is straightforward, involving minimal modifications to the default 2LPTic code, and we expect this to be true for other standard N-body ICs codes.

We have discussed additional steps to remove the radiation effects that might propagate from the power spectra from the Boltzmann code to the N-body initial condition generated by this approach, as N-body simulations concern only dark matter. These are related to the dynamics of the synchronous-gauge variable η and can become non-negligible at large scales. In order to compare with the default 2LPTic code, we have also discussed how to correct the σ_8 value at the two neighbouring redshifts $z_\pm$. Then, by measuring the matter and velocity divergence power spectra we have shown that the finite difference method can recover the ICs as generated by the default 2LPTIC code with sub-percent accuracy at all probed scales and Δz-values, independently of the spatial resolution. For the case of ICs for the CMC-MD gauge, we have compared against the linear-theory predictions for $P_{\delta\delta}$ and $P_{\theta\theta}$, finding also good agreement. Since this method calculates the upper-index velocity, u^i, we have also described an additional step carried out in GRAMSES itself before the simulation starts which

allows one to calculate u_i, since this is the variable that is actually used in the $3+1$ form of the geodesic equation for particles. The ICs generated this way have been used to run the ΛCDM GR cosmological simulations with GRAMSES presented in Barrera-Hinojosa & Li (2020), which are discussed in Chapter 2.

Chapter 4

The frame-dragging effect in a shearing-dust universe

4.1 Introduction

Frame dragging, also known as the Lense–Thirring effect, is a key prediction of GR that can be pictured as the result of a rotating body twisting its surrounding spacetime, which prevents nearby observers from remaining at rest with respect to a distant one — an effect measured in the Solar System by Gravity Probe B (Everitt et al., 2011). This effect is described by the vector modes of the spacetime metric, which are typically carried by the non-diagonal components $\beta_i \equiv g_{0i}$. This is conventionally referred to as the shift vector or gravitomagnetic vector potential[1]. Qualitatively, frame dragging plays the gravitational analogue of electromagnetic induction — so the responsible vector field is often referred to as gravitomagnetic potential. An important property of the frame-dragging potential is that, in a post-Friedmann (post-Newtonian) expansion of GR, this represents the lowest order correction to Newtonian gravity (Bruni et al., 2014), which makes it an ideal target for testing GR codes.

The aim of this Chapter is to further test GRAMSES and validate that, in a more complicated and physically nontrivial case, the code is able to accurately calculate an intrinsically relativistic effect, such as frame-dragging, that does not suffer from contamination due to Newtonian effects. While in principle the code's prediction can be validated against perturbation theory in a suitable regime, we would also like to validate the solution in the nonlinear

[1] Naturally, this is in gauges where the shift vector does not vanish, e.g., the Poisson gauge. If it does, then the vector modes are present in the spatial part of the metric, g_{ij}.

regime. The latter can be done by comparing the results obtained by different GR codes. For this purpose, we will next introduce the 'shearing-dust' universe toy model. Devised a test, this is not meant to represent a cosmological model of *our* Universe, but it is a scenario built in such a way that the frame-dragging effect is particularly large. We will run a simulation for this shearing-dust universe model using GRAMSES, and the result will be compared against a set of state-of-the-art GR codes, each one using different numerical implementations and/or approximations to solve the Einstein equation; the FLRW solver (Macpherson et al., 2017) which is part of the Einstein Toolkit[2] (ET), CosmoGRaPH (Mertens et al., 2016) and *gevolution* (Adamek et al., 2016b). While in this Chapter we will focus on the implementations and results from GRAMSES, the full comparison can be found in Adamek et al. (2020).

In contrast to Newtonian codes, the comparison of the outputs from different GR codes presents an extra complication since these can depend on the particular gauge adopted. Therefore, it is necessary to construct an actual *observable* quantity that can be used to 'measure' the frame-dragging effect under any coordinate system.

Let us set up a scenario where the spacetime metric initially carries only one vector perturbation encoded by the shift vector $\beta^i = (\beta^x(y), 0, 0)$, while for convenience the scalar and tensor modes are not excited. In addition, let us pick an observer O located at the origin of the coordinate system at all times, $\mathbf{x}_O = \mathbf{0}$, where the metric satisfies the symmetry $\mathbf{x} \to -\mathbf{x}$. Let us also consider two events equidistant from O on the initial spatial hypersurface, A and B. These are located at $\mathbf{x}_A = (-L, 0, 0)$ and $\mathbf{x}_B = (0, -L, 0)$, respectively, and emit a flash of light in all directions. Hence, the null geodesics followed by the photons, and which connect each of these two events with the worldline of the observer, are affected in different ways since the ray coming from A travels close to a plane of symmetry, while the ray coming from B travels almost orthogonal to it, as sketched in Fig. 4.1. In such a scenario, we then expect that the photons get 'lensed' by the presence of the frame-dragging field, hence an observable effect is that the angle ϑ between the two incoming rays that is measured by the observer O is not exactly 90 degrees as it would be in flat spacetime.

Then, considering the observer O at rest, i.e., $u^\mu \propto (1, \mathbf{0})$, the dot-product of the spatial components of the two null vectors k_i^A and k_j^B of the respective incoming photons is given by

$$\cos\vartheta = \left.\frac{\mathbf{k}^A \cdot \mathbf{k}^B}{||\mathbf{k}^A||\ ||\mathbf{k}^B||}\right|_O , \tag{4.1.1}$$

[2] einsteintoolkit.org

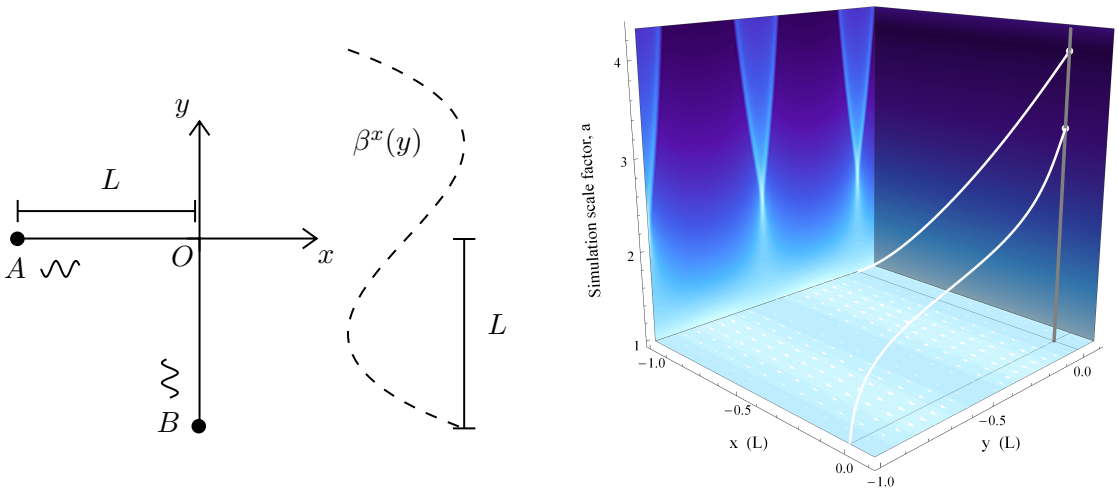

Figure 4.1: Left: Sketch of the shearing-dust universe model. In this, two photons are shot from A and B toward an observer O located at $(x, y) = (0, 0)$, and their spacetime trajectories are bent by the frame-dragging field β^x that is sourced by the dynamics of a pressureless fluid (dust). Then, the observer measures a deflection angle between the two photons, as well as a time delay. Right: 3D $(a(t), x, y)$ rendering of the sketch shown in the left panel, taken from Adamek et al. (2020). This plot shows how photon trajectories (white lines) are bent by frame-dragging and eventually intersect with the observer's wordline (gray), in general at different times. Lighter (darker) regions in the background correspond to higher (lower) densities, and the arrows in the bottom depict the matter velocity field on the initial hypersurface.

where $\mathbf{k}^A \cdot \mathbf{k}^B = \gamma^{ij} k_i^A k_j^B$ is the dot-product with respect to the spatial metric γ_{ij}, and $||\mathbf{k}|| = \sqrt{\mathbf{k} \cdot \mathbf{k}}$, and $|_O$ is used to denote quantities evaluated at the observer's location. We remark that this simple expression is valid since, by construction, $\beta^i = g^{0i}$ vanishes at O due to symmetry. On the other hand, besides deflecting the photons, the frame-dragging field can also cause a time-delay effect which can result in non-simultaneous arrivals of the flashes at the observer, as depicted in Fig. 4.1 (right panel). In such a case, the k^μ vector arriving first at O will need to be parallel-transported along the observer's wordline until the arrival of the second pulse before Eq. (4.1.1) can be evaluated. This effect will be discussed in detail in Section 4.5.1. Hence, Eq. (4.1.1) is the observable quantity that we want to measure from the GR simulations.

Throughout this Chapter, we will geometric units, in which $G = c = 1$.

4.2 Initial data

We will now construct initial conditions (ICs) for the problem proposed above. We will do it in such a way that: i) no scalar or tensor modes are excited at the initial hypersurface,

and ii) the connection to perturbation theory can be done straightforwardly, which makes it easier to validate the results from simulations in the linear regime.

We start by considering the standard ADM (3+1) metric

$$\mathrm{d}s^2 = g_{\mu\nu}\mathrm{d}x^\mu \mathrm{d}x^\nu = -\alpha^2 \mathrm{d}t^2 + \gamma_{ij}\left(\beta^i \mathrm{d}t + \mathrm{d}x^i\right)\left(\beta^j \mathrm{d}t + \mathrm{d}x^j\right), \tag{4.2.1}$$

and in order to excite a single vector mode we specify the following initial data for the metric and extrinsic curvature:

$$\begin{aligned}
\alpha_* &= 1\,, && (4.2.2)\\
\beta^i_* &= \frac{3b}{4\pi a_*}\sin\frac{2\pi y}{L}\delta^{ix}\,, && (4.2.3)\\
\gamma^*_{ij} &= a_*^2\delta_{ij}\,, && (4.2.4)\\
K_* &= -3H(t_*)\,, && (4.2.5)\\
\bar{A}^{ij*}_L &= \frac{a_*^3}{2}(\partial^i\beta^j + \partial^j\beta^i) = a_*^2\frac{3b}{4L}\cos\frac{2\pi y}{L}(\delta^{ix}\delta^{yj} + \delta^{iy}\delta^{xj})\,, && (4.2.6)\\
\bar{A}^{ij*}_{TT} &= 0\,, && (4.2.7)
\end{aligned}$$

where L is the characteristic length scale of the vector perturbation which also determines the size of the comoving simulation volume, b is a dimensionless amplitude parameter, a is the scale factor, H the Hubble parameter, K is the trace of the extrinsic curvature, and the asterisk indicates that a quantity is evaluated on the initial hypersurface. We note that b will play the role of perturbation parameter in a perturbative expansion, but we will keep the expressions at the exact level for the moment. Notice that the conformal-flatness approximation is exact for the spatial metric Eq. (4.2.4), which also satisfies the Dirac gauge condition, $\partial^i\gamma_{ij} = 0$, and K is compatible with the constant-mean-curvature (CMC) slicing condition, $K = -3H$, that is adopted in GRAMSES.

Having fixed the ICs for the metric sector above, we can now solve the Hamiltonian and momentum constraints to obtain compatible initial data for the matter sector in an exact way. We assume that initially matter can be described as a pressureless perfect fluid (i.e., dust), so that the stress-energy tensor is given by

$$T^{\mu\nu} = \rho_0 u^\mu u^\nu\,, \tag{4.2.8}$$

where ρ_0 is the rest mass-energy density and u^μ is the four-velocity of the fluid. The Hamiltonian and momentum constraint equations under the conformal-flatness approximation and

CMC gauge condition are (e.g., Barrera-Hinojosa & Li, 2020)

$$8\bar{D}^2\psi - \frac{2}{3}\psi^5 K^2 + \psi^{-7}\bar{A}_{ij}\bar{A}^{ij} = -16\pi\psi^5\rho_0\Gamma^2\,, \tag{4.2.9}$$

$$\bar{D}_j\bar{A}^{ij} = 8\pi\psi^{10}\rho_0\Gamma u^i\,, \tag{4.2.10}$$

respectively, where $\Gamma \equiv \alpha u^0 = \sqrt{1+\gamma^{ij}u_i u_j}$ is the relativistic Lorentz factor. Given the metric data Eqs. (4.2.2)-(4.2.7) we have a closed system of equations from which we can determine ρ_0^* and u_x^*. Then, solving Eqs. (4.2.9) and (4.2.10), we find

$$\rho_0^* = 3\frac{\left(16\mathcal{H}_*^2L^2 - 3b^2\cos^2\frac{2\pi y}{L}\right)^2 - 64\pi^2b^2\sin^2\frac{2\pi y}{L}}{128\pi a_*^2L^2\left(16\mathcal{H}_*^2L^2 - 3b^2\cos^2\frac{2\pi y}{L}\right)}\,, \tag{4.2.11}$$

$$u_x^* = -a_*\frac{8\pi b\sin\frac{2\pi y}{L}}{\sqrt{(16\mathcal{H}_*^2L^2 - 3b^2\cos^2\frac{2\pi y}{L})^2 - 64\pi^2b^2\sin^2\frac{2\pi y}{L}}}\,, \tag{4.2.12}$$

$$u_*^0 = a_*^{-1}\frac{16\mathcal{H}_*^2L^2 - 3b^2\cos^2\frac{2\pi y}{L}}{\sqrt{\left(16\mathcal{H}_*^2L^2 - 3b^2\cos^2\frac{2\pi y}{L}\right)^2 - 64\pi^2b^2\sin^2\frac{2\pi y}{L}}}\,, \tag{4.2.13}$$

along with $u_*^y = u_*^z = 0$. The velocity profile $u_x^* = u_x^*(y)$ is shown in the right panel of Fig. 4.1 (bottom part), and describes a counter-stream fluid which is able to excite rotational modes as desired. This velocity field has a qualitatively similar profile as the frame-dragging field shown in the left panel of the same figure.

4.3 Linear theory solution for the vector potential

Although the above ICs are fully nonlinear, the evolution of the shift vector is non-trivial to solve for at the nonlinear level, where also the scalar and tensor degrees of freedom can be excited. Therefore, it is useful to work out the linear theory solution of the equations solved in the constrained formulation of GR used by GRAMSES. At first order in the parameter b, the ICs, Eqs. (4.2.11)-(4.2.12), are given by

$$\rho_0^* = \frac{3H_*^2}{8\pi} + \mathcal{O}(b^2)\,, \tag{4.3.1}$$

$$u_*^0 = a_*^{-1} + \mathcal{O}(b^2)\,, \tag{4.3.2}$$

$$u_x^* = -a_*\frac{\pi b}{2(\mathcal{H}_*L)^2}\sin\frac{2\pi y}{L} + \mathcal{O}(b^3)\,, \tag{4.3.3}$$

and we have the following matter source terms at the initial hypersurface:

$$\rho^* \equiv \rho_0^*\Gamma_*^2 \quad = \rho_0^* + \mathcal{O}(b^2)\,, \tag{4.3.4}$$

$$S_i^* \equiv \rho_0^* \Gamma_* u_i^* = \rho_0^* u_i^* + \mathcal{O}(b^3)\,, \tag{4.3.5}$$

where we have used that $\Gamma_* \equiv \alpha^* u_*^0 = 1 + \mathcal{O}(b^2)$. Using these we can solve the momentum constraint at the initial hypersurface,

$$(\bar{\Delta}_L W^*)_i = \partial^2 W_i^* + \frac{1}{3}\partial_i \delta^{kl} \partial_k W_l^* = 8\pi s_i^*\,, \tag{4.3.6}$$

where $s_i = a^3 S_i$ at the linear level. Since $u_i^* = (u_x^*(y), 0, 0)$, only the x-component of Eq. (4.3.6) is actually non-trivial,

$$\left(\bar{\Delta}_L W^*\right)_x = -\frac{3a_*^2 \pi b}{2L^2} \sin\frac{2\pi y}{L}\,. \tag{4.3.7}$$

In order to solve the vector Laplacian we decouple this equation in terms of auxiliary variables as $W_i = V_i + \partial_i U$. Then, we have

$$\nabla^2 V_x^* = -\frac{3a_*^2 \pi b}{2L^2} \sin\frac{2\pi y}{L}\,, \tag{4.3.8}$$

$$\nabla^2 U^* = -\frac{1}{4}\partial_i V^{i*} = 0 \qquad \Longrightarrow\ U^* = 0, \tag{4.3.9}$$

where the latter equation shows that there is no scalar mode excited in W_i^*, i.e. $\partial_i W_*^i = 0$. Then, integrating Eq. (4.3.8) twice w.r.t. y, we find that

$$V_x^* = \frac{3a_*^2 b}{8\pi} \sin\frac{2\pi y}{L}\,. \tag{4.3.10}$$

Using these solutions, $W_i^* = (V_x^*(y), 0, 0)$, and that $W^i = \bar{\gamma}^{ij} W_j$, we can calculate $\bar{A}_*^{ij}$ from $\bar{A}^{ij} = \bar{D}^i W^j + \bar{D}^j W^i - \frac{2}{3}\bar{\gamma}^{ij}\bar{D}_k W^k \equiv (\bar{L}W)^{ij}$, where the only non-zero component is $\bar{A}_*^{xy} = \partial^y W_*^x$, which is given by

$$\bar{A}_*^{xy} = \frac{3a_*^2 b}{4L} \sin\frac{2\pi y}{L}\,. \tag{4.3.11}$$

We can now solve the equation for the shift-vector, which at first order is reduced to $(\bar{\Delta}_L \beta)^i = 2a^{-3}\partial_j \bar{A}^{ij}$. As before, we note that in our case the only non-vanishing component is

$$(\bar{\Delta}_L \beta_*)^x = 2a_*^{-3}\partial_y \bar{A}_*^{xy}\,, \tag{4.3.12}$$

and using the decomposition $\beta^i = B^i + \partial^i b$ this is decoupled into

$$\nabla^2 B_*^x = 2a_*^{-3}\partial_y \bar{A}_*^{xy}\,, \tag{4.3.13}$$

$$\nabla^2 b_* = -\frac{1}{4}\partial_j B_*^j = 0 \qquad \Longrightarrow\ b_* = 0\,, \tag{4.3.14}$$

where the latter equation shows that there is no scalar mode excited in the shift, as we wanted. Then, using Eq. (4.3.11) in Eq. (4.3.13) we conclude that the only non-vanishing component of the shift vector $\beta^i_* = (B^x_*, 0, 0)$ is

$$\beta^x_* = \frac{3b}{4\pi a_*} \sin \frac{2\pi y}{L} \,, \tag{4.3.15}$$

which is identical to the *exact* expression of the initial data, Eq. (4.2.3). Indeed, this linear theory solution is the starting point behind the construction of this problem, which we then assume to be an exact solution and the matter data has been constructed non-perturbatively to guarantee that this is the case. Naturally, the solution Eq. (4.3.15) is only valid at the initial hypersurface. By a similar procedure as above, it can be shown that the vector mode evolves as

$$\beta^x(a) = \frac{3b}{4\pi} \frac{a^2_*}{a^3} \sin \frac{2\pi y}{L} \,, \tag{4.3.16}$$

i.e., it decays over time as $\propto a^{-3}$.

4.4 Realising the initial density field with particles

So far, we have fixed the initial data for the metric and curvature, as well as for the density and velocity field of the fluid. However, in GRAMSES we simulate matter as an N-body system: let us now discuss how the ICs for the N-body simulations are set up. As usual, in order to get the initial particles' positions, we need to sample the initial density field of the fluid in a discrete way. In this Section we summarise the method to 'realise' the density field in terms of particles, and we highlight some important differences with respect to a standard cosmological simulation. In order to calculate the initial particles' positions correctly, we shall use the initial 'number' density field. This is given by

$$n(y) \equiv \rho^*_0 \Gamma_* \,, \tag{4.4.1}$$

where $\Gamma_* = \alpha_* u^0_* = \sqrt{1 + \gamma^{ij}_* u^*_i u^*_j}$ is the relativistic Lorentz factor at the initial time. The relation between Eq. (4.4.1) and the conformal energy density used by GRAMSES to solve the GR equations (Barrera-Hinojosa & Li, 2020), s_0, is

$$s_0 = n\Gamma \,. \tag{4.4.2}$$

If the velocities are non-relativistic then $s_0 \approx n$, but the contribution from Γ can be noticeable in this problem[3] when $b \sim (\mathcal{H}_* L)^2$. In any case, it is the number density n which is needed to generate the particles' positions for the simulations. Then, using Eq. (4.2.13), the number density Eq. (4.4.1) takes the form

$$n(y) = \frac{3}{128\pi L^2}\sqrt{\left(16\mathcal{H}_*^2 L^2 - 3b^2\cos^2\frac{2\pi y}{L}\right)^2 - 64\pi^2 b^2 \sin^2\frac{2\pi y}{L}}\,. \tag{4.4.3}$$

To calculate the particles' positions from Eq. (4.4.3) we follow the density-displacement duality approach in one spatial dimension, which is a particular case of the ICs generation discussed in Chapter 3. Thus, we start by considering the coordinate transformation between two coordinate systems; the physical one (y) and a virtual one (q), given by

$$y = q(y) + \chi(y)\,, \tag{4.4.4}$$

where y correspond to the final (displaced) particles' positions, q are their coordinates in the regular (grid/glass-like) configuration used as starting point, and χ represents the displacement field that maps them in such a way that it generates the desired density configuration. Invoking mass (or more precisely, particle-number) conservation, we have the relation

$$n\mathrm{d}y = \langle n\rangle \mathrm{d}q\,, \tag{4.4.5}$$

where

$$\langle n\rangle = \frac{1}{L}\int_0^L n(y)\mathrm{d}y\,, \tag{4.4.6}$$

is the *mean* particle number density as described by the regular q-coordinates. Now, rather than inverting the coordinate transformation Eq. (4.4.4) perturbatively for χ (as it is customary for cosmological simulations), given that the density field is essentially 1D we can use Eq. (4.4.5) directly to find the final particles' perturbed positions y defined through the implicit equation

$$\frac{1}{\langle n\rangle}\int^y n(y')\mathrm{d}y' = q(y)\,. \tag{4.4.7}$$

We have implemented this approach in MATHEMATICA,[4] where the integration of the number density field in Eq. (4.4.7) is carried out numerically, and a built-in root-finding algorithm is used to calculate the displaced positions y using the unperturbed values $q(y)$ as the initial

[3] The magnitude of the parameter b is constrained by the weak energy condition $\rho_0^* > 0$ at t_*: values $b > 2H_*^2 L^2/\pi$ are unphysical. For $H_* L > \pi\sqrt{2/3}$, i.e. for exact perturbations outside the Hubble horizon, the physical range of b is even more restricted, becoming bounded from above by $b < 4\sqrt{3H_*^2 L^2 - \pi^2}/3$.

[4] wolfram.com/mathematica

guess. The latter are defined in terms of a regular grid with the same size as the one that will be used by the N-body simulation. The y-positions (ICs) are then read when the initial particle data is loaded by GRAMSES [5].

There is a subtle and yet important point regarding the applicability of this method to reconstruct the initial density field Eq. (4.4.3) in comparison to a standard cosmological simulation of our Universe. In standard cosmological codes, including GRAMSES, the internal density field is calculated by normalising the number density field by its *background* value $\bar{n}$ (defined as the case where $b = 0$), i.e. $n/\bar{n}$, while for the calculation of the particles' positions in Eq. (4.4.7) the actual density variable used is $n/\langle n\rangle$, where the brackets denote the mean (or *spatial averaging*) that is calculated from Eq. (4.4.6). This is because, in order to calculate the displacements from the mass-conservation law Eq. (4.4.5), it is the mean value of the density that corresponds to the regular configuration described by the q-coordinates, and in general $\langle n\rangle \neq \bar{n}$. In principle, the mass-conservation law Eq. (4.4.5) can still be satisfied if we absorb the difference between these two quantities using the coordinate redefinition $\tilde{q} = \bar{n}/\langle n\rangle q$, which amounts to changing the size of the volume occupied by the particles in the regular configuration. However, for the particular problem under consideration this will affect the correct periodicity ($2\pi/L$) of the density field, which defines the correct periodic boundary conditions for the problem (and makes it suitable to run using cosmological codes).

The difference between background and mean values appears in the first place due to the nonlinear initial density field. Indeed, the ratio $\langle n\rangle/\bar{n}$ is $\simeq 130\%$ for $b \simeq (\mathcal{H}_* L)^2$, and thus it might introduce sizeable errors in the ICs if not taken into account properly, which then propagate to the final frame-dragging observable. In order to correct this miss-match between $\bar{n}$ and $\langle n\rangle$, while still calculating the displacements in the (correct) way described above, we have boosted the internal particles' mass used in the simulation by the factor $\langle n\rangle/\bar{n}$, so that the resulting internal number density field used by simulation is correct even if the displacements where generated using the mean value instead of the background one, as the density-displacement duality requires. Again, this problem is not present in the ICs of standard cosmological simulations, as they start at a redshift where the density field is close to linear.

There is a second potential source of error in the reconstruction of the initial density field

[5] This is done by `init_part` in pm/init_part.f90. The code only needs to read standard ICs files (e.g. GADGET-type files generated by the 2LPTIC code (Crocce et al., 2006)) that have the correct box size and number of particles for a given case, but the particle data will be overwritten with the ICs calculated for this problem.

which is related to the alignment between the regular distribution (grid) from which the displacements χ are calculated, and the grid cell centres of the simulation itself, which can affect the CIC calculations of density and momentum performed in GRAMSES. In principle, it is natural to make a correspondence between the positions of the particles in the regular template that are used to generate the ICs, and the simulation's cell centres.[6] In other words, the particles are regarded as displaced away from fiducial *cell centres*, which would later correspond to cell centres in the simulation's grid where the CIC operates. However, a sampling problem can occur when the maxima/minima of the number density field actually lie on the *cell boundaries* of the q-space, and thus the above correspondence introduces some error in the CIC calculation of such extreme values, as we will show. In summary, in these cases we find that calculating χ by displacing particles away from the *cell boundaries* allows one to sample such maxima/minima directly and thus does not suffer from this problem.

Let us illustrate this issue by using a simpler expression for the density field, given by (in this we use ρ rather than n, which does not affect the reasoning)

$$\rho = 1 + A \sin 2\pi y \,, \tag{4.4.8}$$

where $A = \text{const.}$, and $y \in (0, 1)$. Using the density-displacement method, the displacements are given by $\chi = A/(2\pi) \cos 2\pi y$. Now, let us consider the cell centres as the regular template for the particles. Given a 1-dimensional grid of size N, these correspond to

$$q_i = (2i - 1)/(2N) \,, \tag{4.4.9}$$

where $i = 1, 2, ..., N$ labels the cells, and the cell size is $\Delta y = 1/N$. Let us now see how the CIC scheme samples the minimum of the density field Eq. (4.4.8) that is located at $y = 3/4$. In general, this point lies between the cell centres q_- (slightly to its left) and q_+ (slightly to its right), and their respective cell indices are given by $i_- = 3/4N$ and $i_+ = 3/4N + 1$.[7] Then, these cell centres have q-coordinate values and associated displacements given by

$$q_\pm = \frac{3}{4} \pm \frac{1}{2N} \,, \tag{4.4.10}$$

$$\chi_\pm = \pm \frac{A}{2\pi} \sin \frac{\pi}{N} \,. \tag{4.4.11}$$

These are schematically represented in Fig. 4.2. In 1D, the CIC assignment to get the density

[6] Regardless of how exactly the ICs have been generated, when the simulation is initialised the particles are assigned to the simulation's cells that initially contain them, and their initial positions slightly deviate from the cell centres.

[7] Notice that the point $y = 3/4$ can be directly sampled by i_- if N has a value such that $3/4N$ is an integer.

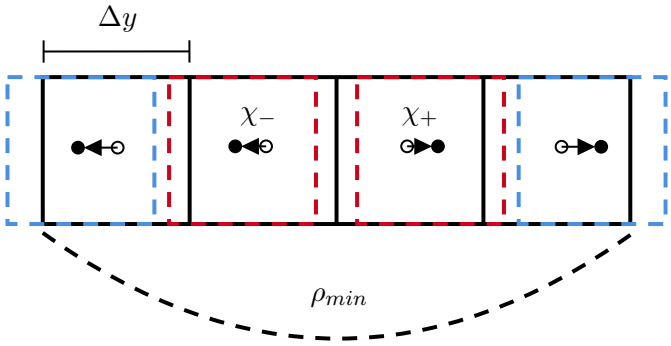

Figure 4.2: Schematic representation of the grid cells, and the displaced particles that sample the density field ρ. Coloured dashed lines represent the particles' clouds (of same size as grid cells, Δy), which do not overlap with their host cells completely due to the displacement field χ. The unperturbed (perturbed) particles' positions are represented by empty (filled) circles. The black dashed line on the bottom represents the local shape of the density field, whose local minimum $\rho_{\rm min}$ lies exactly at the boundary between the two central cells, whose corresponding particles are displaced away to left (χ_-) and right (χ_+).

at a given cell centre takes the form

$$\rho^{\rm CIC}(q_\pm) = \frac{f^\pm}{\Delta y}\,, \tag{4.4.12}$$

where $f^\pm$ are the weights of each particle, which can be calculated easily as these correspond to the overlapping of the particle's clouds in that cell. As shown by Fig. 4.2, the particles have been displaced away from the minimum, so that the CIC density at the $i_\pm$ cells only receives contributions from its own particles, with weights $f^\pm = \Delta y - |\chi_\pm|$. Hence, using Eq. (4.4.11) the CIC density field at the cells $i_\pm$ turns out to be

$$\rho^{\rm CIC}(q_\pm) = 1 - \frac{AN}{2\pi}\sin\frac{\pi}{N}\,. \tag{4.4.13}$$

We can get insight from this result considering the limit where the number of cells is large, $N \gg 1$, where we find that

$$\rho^{\rm CIC}(q_\pm)\Big|_{N\gg1} \to 1 - \frac{A}{2}\,. \tag{4.4.14}$$

Equation (4.4.14) shows that, even in an infinitely fine grid, the CIC value of the overdensity $\delta = \rho - 1$ at the cells that are closest to the peak has a 50% error w.r.t. the density field being sampled. This shows that no matter how close to the 'true' minimum at $y = 3/4$ the neighbouring sampling points $q_\pm$ are, the problem will persist as long as these points do not sample the peaks directly.

Conversely, as shown below, we have found that this problem does not appear when the regular grid template for particles corresponds to the cell *boundaries* rather than cell centres,

so we have adopted this prescription in our calculations. Repeating the above exercise in such a case, the $q_i^{\rm wall}$ coordinates of the particles in the regular template are

$$q_i^{\rm wall} = i/N \qquad\qquad i = 1, 2, ..., N\,, \tag{4.4.15}$$

where we have now used the 'wall' subscript to distinguish from the previous discussion. Then, evaluating the displacement field at the positions of the particles associated with the cells at the left and right of $\rho_{\rm min}$, $q_\pm^{\rm wall} = q_i^{\rm wall}(i_\pm)$, we have

$$\chi_+^{\rm wall} = \frac{A}{2\pi}\sin\frac{2\pi}{N}\,, \tag{4.4.16}$$

$$\chi_-^{\rm wall} = 0\,, \tag{4.4.17}$$

i.e., the particle located exactly at the wall at $q_- = 3/4$ is not displaced, while the 'next' particle at $q_+ = 3/4 + 1/N$ is displaced to the right. Then, the value of the CIC density on the right cell is given by

$$\rho^{\rm CIC}(q_+^{\rm cent}) = 1 - \frac{AN}{2\pi}\sin\frac{2\pi}{N}\,, \tag{4.4.18}$$

where $q_+^{\rm cent}$ is a reminder that $\rho^{\rm CIC}$ is always evaluated at the cell centres, regardless of the prescription used to deposit the particles. This expression only differs from (4.4.13) by a factor of 2 in the argument of the sin function. Nonetheless, this is critical, as we can check that in the limit $N \gg 1$, the value of the density field on this cell now approaches $1 - A$, which is exactly the value of $\rho_{\rm min}$.

We remark that the above issue is not present in ICs of standard N-body simulations constructed from a glass-like configurations, as such a particle template is not homogeneous.

4.5 Ray tracing and calculation of the relativistic observable

The above ICs can be used to run a simulation of the shearing-dust universe model with GRAMSES, which can solve the dynamics of matter and geometry. Nonetheless, to calculate the final observable in this problem we need to consider the impact of frame-dragging on photons, as depicted in Fig. 4.1, which requires to perform relativistic ray tracing. This represents a post-processing step. We will now discuss how this aspect is implemented, and how this is connected to the observable $\cos\vartheta$ given by Eq. (4.1.1). By definition, the geodesic equations parallel-transport velocity vectors $k^\mu = {\rm d}x^\mu/{\rm d}\lambda$ along the integral curves of the same field,

$$k^\mu \nabla_\mu k^\nu = 0\,, \tag{4.5.1}$$

for a photon 4-vector k^μ, or for non-relativistic matter with the replacement $k^\mu \to u^\mu$. In order to integrate this numerically using the simulation data, we use the 3+1 form of these equations,

$$\frac{\mathrm{d}k_i}{\mathrm{d}t} = -\alpha k^0 \partial_i \alpha + k_j \partial_i \beta^j - \frac{1}{2k^0} k_j k_k \partial_i \gamma^{jk} \,, \tag{4.5.2}$$

$$\frac{\mathrm{d}x^i}{\mathrm{d}t} = \gamma^{ij} \frac{k_j}{k^0} - \beta^i \,. \tag{4.5.3}$$

Since we are interested in describing how the light rays shoot from events A and B propagate towards the observer at the origin, this system needs to be solved for (x^i_A, k^A_i) and (x^i_B, k^B_i). Naturally, since these are test rays they do not interact with each other nor affect the properties of the spacetime. While the arrival of the rays at O imposes clear boundary conditions for x^i_A and x^i_B, the initial conditions for k^A_i and k^B_i (i.e. the initial propagation directions) are not trivial to define in a 'forward' ray-tracing sense: in the absence of any perturbation, the flashes should be shoot from A and B pointing straight towards the observer, but since the perturbation 'bends' the geodesics, these actually need to be shoot at some unknown angle, otherwise they will simply not arrive at the observer O.

Equations (4.5.2) and (4.5.3) are solved non-perturbatively using a ray-tracing code written in MATHEMATICA which takes as input the spacetime metric data from the simulation[8]. In order to get the correct initial shooting directions, this code requires the specification of an initial guess as well as a search region and applies a root-finding algorithm to find the actual geodesics connecting the events A and B to the observer at O. With the solutions for k^A_i and k^B_i determined numerically, we can finally evaluate the *observable*, which for an observer at rest is given by Eq. (4.1.1) provided the vectors are observed simultaneously. For non-simultaneous arrivals, one vector needs to be parallel transported along the observer's wordline until the second photon arrives. This appears as a higher-order effect in perturbation theory, and in most cases introduces only minor corrections, although it can be regarded as another GR observable on its own.

4.5.1 Parallel transport

Let us now discuss the parallel-transport equations, which can be used to evaluate the observable for the case of the non-simultaneous arrival of the incoming photons from events A

[8] The original ray-tracing code was written by James Mertens for synchronous gauge applications, and we have only done some minor modifications to include the non-vanishing shift in our gauge, which contributes to both the geodesic and parallel-transport equations.

and B. The parallel transport equation $u^\mu \nabla_\mu k_\nu = 0$ can be written as

$$\frac{\mathrm{d}k_i}{\mathrm{d}t} = -\alpha k^0 \partial_i \alpha + k_j \partial_i \beta^j - \frac{1}{2u^0} u_l k_j \partial_i \gamma^{lj} + \alpha \left(\frac{u_k}{u^0} k^0 - k_k \right) K_i^k \,. \tag{4.5.4}$$

where u^μ is the four-velocity of the observer. Given that the parallel transport will be carried out along the observer's worldline, Eq. (4.5.4) is meant to be evaluated along this spacetime curve. In the coordinate system used for the problem, the observer is located at rest at the origin, thus $u^\mu \propto (1, \mathbf{0})$. In addition, we have $\partial_i \alpha|_O = 0$ due to the symmetry of the problem. Therefore, evaluating Eq. (4.5.4) at O, it takes the form

$$\frac{\mathrm{d}k_i}{\mathrm{d}t}\Big|_O = k_j \partial_i \beta^j|_O - \alpha k_j K_i^j|_O \,, \tag{4.5.5}$$

where we have included the notation $|_O$ to highlight that this is integrated purely in time at $y = 0$, where the observer remains located at all times. Furthermore, the observable Eq. (4.1.1) is evaluated using the metric at the time the second ray arrives. It is useful to express the curvature term using the evolution equation for the spatial metric (which is the definition of K_{ij}), i.e.

$$K_{ij} = -\frac{1}{2\alpha}(\partial_t \gamma_{ij} - D_i \beta_j - D_j \beta_i) \,, \tag{4.5.6}$$

where D_i represents the covariant derivative associated to γ_{ij}. Using that $D_i \beta^j = \partial_i \beta^j + \Gamma^j_{il} \beta^l$, where Γ^j_{il} are the Christoffel symbols related to the spatial metric γ_{ij}, we have

$$\frac{\mathrm{d}k_i}{\mathrm{d}t}\Big|_O = k_j \partial_i \beta^j|_O + \frac{k_j}{2} \gamma^{jk} \partial_t \gamma_{ik}|_O - \frac{k_j}{2}(\partial_i \beta^j - \Gamma^j_{il} \beta^l + \gamma^{jk} \gamma_{il} \partial_k \beta^l + \gamma^{jk} \gamma_{il} \Gamma^l_{km} \beta^m)|_O \,. \tag{4.5.7}$$

Since under the conformal transformation the Christoffel symbols change as

$$\Gamma^i_{jk} = \bar{\Gamma}^i_{jk} + 2(\delta^i_j \bar{D}_k \ln \psi + \delta^i_k \bar{D}_j \ln \psi - \bar{\gamma}_{jk} \bar{\gamma}^{il} \bar{D}_l \ln \psi) \,, \tag{4.5.8}$$

by using the conformal-flatness condition this is simplified to

$$\Gamma^i_{jk} = 2(\delta^i_j \partial_k \ln \psi + \delta^i_k \partial_j \ln \psi - \delta_{jk} \partial^i \ln \psi) \,, \tag{4.5.9}$$

where $\partial^i = \delta^{il} \partial_l$. Since due to symmetry we also have $\partial_i \psi|_O = 0$, then $\Gamma^i_{jk}|_O = 0$ and the parallel-transport equations reduce to

$$\frac{\mathrm{d}k_i}{\mathrm{d}t}\Big|_O = k_j \partial_i \beta^j|_O + \frac{k_j}{2} \gamma^{jk} \partial_t \gamma_{ik}|_O - \frac{k_j}{2}(\partial_i \beta^j + \gamma^{jk} \gamma_{il} \partial_k \beta^l)|_O \,. \tag{4.5.10}$$

Then, the non-vanishing components of these equations are explicitly written as

$$\frac{\mathrm{d}k_x}{\mathrm{d}t}\Big|_O = \frac{1}{2}\left(k_x \gamma^{xx} \partial_t \gamma_{xx} - \gamma^{yy} \gamma_{xx} k_y \partial_y \beta^x\right)|_O \,, \tag{4.5.11}$$

$$\frac{\mathrm{d}k_y}{\mathrm{d}t}\Big|_O = \frac{1}{2}\left(k_y\gamma^{yy}\partial_t\gamma_{yy} - \gamma^{yy}\gamma_{yy}k_y\partial_y\beta^y + k_x\partial_y\beta^x + k_y\partial_y\beta^y\right)|_O\,. \tag{4.5.12}$$

This coupled system of first-order in time, ordinary differential equations, needs to be solved for the k_x and k_y components of the first light ray arriving at the observer until the second ray arrives. This is done numerically in a module of the aforementioned ray-tracing code.

4.5.2 Time stepping for the simulation snapshots

In order to carry out the numerical time integration of the geodesic equations (4.5.2) and (4.5.3) as well as parallel-transport equations (4.5.11) and (4.5.12) in the ray-tracing code, we use the simulation data as inputs, and hence interpolations in both time and space are required. For simplicity, we output data (snapshots) from the simulation on a constant-timestep basis, and we fix this using the criterion

$$\Delta t = n_t \Delta x\,, \tag{4.5.13}$$

where $\Delta x = L/N$ is the spatial resolution of the simulation, and the parameter n_t controls their frequency. Eq. (4.5.13) should not be confused with the *timestep of the simulation*, which is internally fixed by the code. n_t needs to be tuned in order to suppress time-resolution effects in the final observable, and we have found that $n_t = 4$ is sufficient for all explored cases.

Since the bending (or lensing) of the null geodesics due to frame dragging results in a time delay of the light rays compared to their propagation in the background, the simulation should allow the system to evolve for enough time for these to actually reach the observer. This time-delay effect is small for most probed values of b and $\mathcal{H}_* L$ but can become non-negligible in the nonlinear regime. If we allow the light rays to travel a number of box-crossings, $n_L \geq 1$, the corresponding cosmic time to evolve the simulation is $t_{\rm end} = n_L L$ (recall that $c = 1$) and the minimum number of snapshots $n_{\rm snap}^{\rm min}$ required for a timestep fixed by Eq. (4.5.13) is given by

$$n_{\rm snap}^{\rm min} = \left[\frac{n_L N}{n_t}\right]\,, \tag{4.5.14}$$

where the brackets denote the nearest-integer part of the number. Since GRAMSES (as well as RAMSES) outputs the snapshots based on a list of scale factor values given in the input parameters file, we need to calculate the set of a–values corresponding to Δt fixed by Eq. (4.5.13). To find this, we can use the 1st Friedmann equation considering $\Omega_m = 1$, i.e., $H = H_0 a^{-3/2}$,

hence the cosmic time at a given a can be calculated as

$$t = \frac{2}{3H_0} a^{3/2} \,, \tag{4.5.15}$$

or inverting this expression we can get $a(t)$

$$a = \left(\frac{3H_0}{2} t\right)^{2/3} \,. \tag{4.5.16}$$

By construction, the ICs are specified at a_* with which we can calculate the initial time t_* from Eq. (4.5.15), while the subsequent output times are given by $t_n = t_* + n_{\rm snap}\Delta t$, where $n_{\rm snap} = 1, 2, ..., n_{\rm snap}^{\rm min}$ labels the $n_{\rm snap}$-th snapshot of the simulation. Then, using Eq. (4.5.16) the output scale factors for the simulation are given by

$$a_n = \left(a_*^{3/2} + \frac{3H_0}{2} n_{\rm snap}\Delta t\right)^{2/3} \,. \tag{4.5.17}$$

As it will become clear from the perturbation theory calculation, it is actually more convenient to integrate the geodesic equations in term of conformal time, τ, rather than coordinate time (although for numerical integration it does not make a difference). Repeating the argument in the case of conformal time, using that $a(\tau) = \left(\frac{H_0}{2}\tau\right)^2$ we find

$$a_n = \left(a_*^{1/2} + \frac{H_0}{2} n_{\rm snap}\Delta\tau\right)^2 \,, \tag{4.5.18}$$

where $\tau_n = \tau_* + n_{\rm snap}\Delta\tau$, and $\Delta\tau$ replaces Δt in the time-stepping criterion Eq. (4.5.13).

At this point, let us give a word of caution about the GRAMSES (and RAMSES) snapshots and their corresponding scale factors. The `dump_all` subroutine[9] – which triggers once the current scale factor of the simulation is one from the input a-list – is called at the *beginning* of each code's timestep, before any gravity or matter array has been updated, which means that the data written in a given snapshot is actually *delayed by one code timestep*. In other words, the scale factor at which the code outputs the data does not exactly matches that of the data itself. Naturally, the finer the code timestep is, the smaller the difference between two consecutive scale factor of the simulation are. This mismatch can introduce percentage-level errors in the results for the current toy model. However, this is not a real issue for actual cosmological simulations, which use comparatively much finer timesteps.

[9] See `amr/output_amr.f90` and `amr/amr_step.f90`.

4.5.3 Linear solution to the null geodesic equations

Let us now calculate the linear theory prediction for the observable Eq. (4.1.1). In order to evaluate this we need to solve the geodesic equation at first order in $b \ll 1$. In this case, the system reduces to

$$\frac{\mathrm{d}k_i}{\mathrm{d}t} = k_x \partial_i \beta^x \,, \tag{4.5.19}$$

$$\frac{\mathrm{d}x^i}{\mathrm{d}t} = \gamma^{ij}\frac{k_j}{k^0} - \beta^i \,, \tag{4.5.20}$$

where k^0 is fixed by the null geodesic condition as $k^0 = \alpha^{-1}\sqrt{\gamma^{ij}k_i k_j}$. Notice that at the background level $\mathrm{d}\bar{k}_i/\mathrm{d}t = 0$ and then the trajectories are straight rays, $\bar{x}^i \propto \tau$, where $\mathrm{d}\tau = \mathrm{d}t/a$.

Given the form of the shift vector $\beta^x = \beta^x(y)$ in Eq. (4.3.16), from the first line of Eq. (4.5.19) we have that $\mathrm{d}k_x/\mathrm{d}t = \mathrm{d}k_z/\mathrm{d}t = 0$, while the remaining equations are

$$\frac{\mathrm{d}k_y}{\mathrm{d}t} = k_x \partial_y \beta^x \,, \tag{4.5.21}$$

$$\frac{\mathrm{d}x}{\mathrm{d}t} = \gamma^{xx}\frac{k_x}{k^0} - \beta^x \,, \tag{4.5.22}$$

$$\frac{\mathrm{d}y}{\mathrm{d}t} = \gamma^{yy}\frac{k_y}{k^0} \,, \tag{4.5.23}$$

$$\frac{\mathrm{d}z}{\mathrm{d}t} = \gamma^{zz}\frac{k_z}{k^0} = 0 \,. \tag{4.5.24}$$

To solve this system we consider the rays A and B which end up at the observer O. At first order, the perturbed rays can be written as

$$k_x^A = k^A(1 + bc_x^A), \qquad k_y^A = k^A(0 + bc_y^A), \qquad k_z^A = 0 \,, \tag{4.5.25}$$

$$k_x^B = k^B(0 + bc_x^B), \qquad k_y^B = k^B(1 + bc_y^B), \qquad k_z^B = 0 \,, \tag{4.5.26}$$

and the conditions for their initial and final positions are

$$\{x_A(t_*), y_A(t_*)\} = \{-L, 0\} \,, \qquad \{x_A(t_O), y_A(t_O)\} = \{0, 0\} \,, \tag{4.5.27}$$

$$\{x_B(t_*), y_B(t_*)\} = \{0, -L\} \,, \qquad \{x_B(t_O), y_B(t_O)\} = \{0, 0\} \,. \tag{4.5.28}$$

Taking into account the perturbed rays Eqs. (4.5.25) and (4.5.26), it is straightforward to show that the observable Eq. (4.1.1) at leading order in the expansion w.r.t. b is given by

$$\cos\vartheta_{\mathrm{lin}} = b(c_y^A + c_x^B)|_O \,, \tag{4.5.29}$$

where we have used the lin subscript to denote this is the linear solution. Hence, we notice that

this does not depend upon the perturbations c_x^A and c_y^B. We next calculate the perturbations needed to evaluate Eq. (4.5.29).

Ray A

For the trajectory of ray A, from Eq. (4.5.22) we find

$$\frac{\mathrm{d}x_A}{\mathrm{d}t} = \sqrt{\gamma^{xx}} - \beta^x \tag{4.5.30}$$

$$\implies x_A(t) = x_A(t_*) + \int_{t_*}^{t} dt' a^{-1} - \int_{t_*}^{t} dt' \beta^x(t', y_A(t'))\,. \tag{4.5.31}$$

Let us note that up to first order in b, it is sufficient to evaluate the perturbation β^x in the last term of the r.h.s. along the *unperturbed* trajectory – just like in the usual Born approximation – since any correction to this is higher order in the parameter b. Furthermore, applying Eq. (4.5.23) for ray A we note that is $y_A \sim \mathcal{O}(b)$, as in the absence of perturbations it would travel strictly along the x direction, see Fig. 4.1. Then, expanding the shift vector argument as $\sin(2\pi y_A/L) \approx b - b^3/3! + ...$, we note that the last term in Eq. (4.5.31) does not contribute (since $\beta^x \propto b$ on its own) and we are simply left with

$$x_A(t) = -L + (\tau - \tau_*)\,, \tag{4.5.32}$$

where we have used that $d\tau = dt/a$. This shows that the x–component of the trajectory for ray A is not deflected at the linear level. From this we also find the time of arrival set by the conditions Eq. (4.5.27) is $\tau_O = L + \tau_*$.

For the y-direction of ray A, let us first solve the equation for k_y^A to determine the perturbation c_y^A. Since $k_y^A = \bar{k}^A(0 + bc_y^A)$, with $\bar{k}^A = \text{const.}$, from Eq. (4.5.21) we find

$$\frac{\mathrm{d}k_y^A}{\mathrm{d}t} = k_x^A \partial_y \beta^x \tag{4.5.33}$$

$$\implies bc_y^A = B\frac{2\pi}{L}\int_{t_*}^{t} dt' \frac{1}{a^3}\cos\frac{2\pi y_A(t')}{L} + \mathcal{O}(b^2) \approx B\frac{2\pi}{L}\int_{t_*}^{t} dt' \frac{1}{a^3} \tag{4.5.34}$$

$$\implies c_y^A(\tau) = -\frac{2\pi B}{3bL}\left(\frac{2}{H_0}\right)^4 \tau^{-2} + \kappa_c^A \tag{4.5.35}$$

where we have used that $\cos b \approx 1$ for $b \ll 1$, $B = 3ba_*^2/4\pi$ is the amplitude of β^x, and κ_c^A is an integration constant. Using this result we can work out y_A from Eq. (4.5.23) as

$$\frac{\mathrm{d}y_A}{\mathrm{d}t} = \sqrt{\gamma^{xx}}\frac{k_y^A}{|k_x^A|} \tag{4.5.36}$$

$$\implies y_A(\tau) = b\left[\frac{\pi B}{3bL}\left(\frac{2}{H_0}\right)^4 \tau^{-2} + \kappa_c^A \tau\right] + \kappa_y^A\,, \tag{4.5.37}$$

where in the last line we have used Eq. (4.5.35), and κ_y^A is an integration constant. We can now use the conditions $y_A(t_*) = y_A(t_O) = 0$ to determine the integration constants κ_c^A and κ_y^A, although only the former is necessary for the evaluation of the linear observable. From this we have

$$\kappa_c^A = \frac{\pi B}{3bL}\left(\frac{2}{H_0}\right)^4 \frac{\tau_O + \tau_*}{\tau_*^2 \tau_O^2}\,. \tag{4.5.38}$$

Using this result into Eq. (4.5.35) and evaluating at τ_O, after some algebra we find that

$$c_y^A|_O = \frac{6 + \mathcal{H}_* L}{(2 + \mathcal{H}_* L)^3}\,, \tag{4.5.39}$$

where we have used that $\tau_* = 2/\mathcal{H}_*$ and $H_0 = \mathcal{H}_* a_*^{1/2}$.

Ray B

Similarly, for ray B it is straightforward to show that

$$y_B(t) = -L + (\tau - \tau_*)\,, \tag{4.5.40}$$

so that the trajectory along the y-direction is unperturbed and the time of arrival compatible with Eq. (4.5.28) is again $\tau_O = L + \tau_*$. This shows that at the linear level both rays A and B arrive simultaneously at O.

For the x-direction, from Eq. (4.5.22) we have

$$\frac{\mathrm{d}x_B}{\mathrm{d}t} = b a^{-1} c_x^B - \beta^x(y_B)\,, \tag{4.5.41}$$

and then we see that ray B gets deflected along the x direction by the frame-dragging perturbation, as expected. Since c_x^B (unlike c_y^A) remains constant because $dk_x/dt = 0$, integrating both sides we find

$$x_B(t) = x_B(t_*) + \left[b\int_{t_*}^{t} dt' a^{-1} c_x^B - \int_{t_*}^{t} dt' \beta^x(y_B(t'))\right] \tag{4.5.42}$$

$$= b\left[c_x^B(\tau - \tau_*) - \frac{3a_*^2}{4\pi}\int_{\tau_*}^{\tau} d\tau' a^{-2} \sin\frac{2\pi(\tau' - \tau_*)}{L}\right]\,, \tag{4.5.43}$$

where in the last step we have used the solution $y_B(t')$ already calculated in Eq. (4.5.40).

Next, in order to determine c_x^B we use the conditions for the final positions of the rays arriving at the observer. We then evaluate Eq. (4.5.43) at the time of arrival $\tau_O = \tau_* + L$. From this, we find

$$c_x^B|_O = \frac{32\pi^2}{\mathcal{H}_* L}\int_0^{2\pi} d\xi \frac{\cos\xi}{(4\pi + \mathcal{H}_* L \xi)^3}\,, \tag{4.5.44}$$

where $\xi = 2\pi(\tau' - \tau_*)/L$.

Finally, using this last result alongside Eq. (4.5.39) we find that the linear observable given by Eq. (4.5.29). Thus, we find

$$\cos\vartheta_{\rm lin} = b\left[\frac{6+\mathcal{H}_*L}{(\mathcal{H}_*L+2)^3} + \frac{32\pi^2}{\mathcal{H}_*L}\int_0^{2\pi}\frac{\cos\xi}{(4\pi+\mathcal{H}_*L\xi)^3}d\xi\right]. \tag{4.5.45}$$

The observable Eq. (4.5.45) allows us to validate the simulation predictions in the linear regime. We notice that the distance L enters in this result under the combination $\mathcal{H}_*L$, which is a dimensionless quantity (recall that $c = 1$). Then, we can also get some insight about this result by considering two different limits for $\mathcal{H}_*L$; in the case $\mathcal{H}_*L \ll 1$ we have $\cos\vartheta_{\rm lin} \approx 3b/4$, while in the limit $\mathcal{H}_*L \gg 1$ it behaves as $\cos\vartheta_{\rm lin} \approx 2b\mathcal{H}_*^{-2}L^{-2}$. The fact that in the former case the limiting value is independent of $\mathcal{H}_*L$ reflects the fact that the time it takes for the light to reach the observer is much shorter than the dynamical time scale over which the perturbation decays. In the second limit, the light rays are able to travel for long enough time to become sensitive to the damping of the shift vector.

4.6 Results

Let us now discuss the simulation results of the shearing-dust universe. In the following, we will focus on discussing how the results from GRAMSES compare to linear theory predictions as well as to other GR codes, and we refer the reader to Adamek et al. (2020) for more details about the results from the latter. To facilitate the comparison, all GR codes use the same ray-tracing algorithm (adapted to their respective gauge) to evaluate the final observable Eq. (4.1.1).

For the parameter space of this problem, we choose ten values for the simulation box L relative to the initial background Hubble factor, given by $H_*L = 2^n$ for $n = [-7, ..., 2]$. For each value of H_*L we choose three values of the amplitude parameter as $b = [0.5, 0.05, 0.005] \times (H_*L)^2$. This allows us to explore situations that lie within the linear and nonlinear regimes, as well as cases where matter evolves for a sufficiently long time to develop shell crossing. Hence, a total of 30 simulation are run.

Before discussing the results, let us recall that GRAMSES obtains the metric and extrinsic curvature components by solving elliptic-type equations on a mesh, which means the mesh resolution places a limit on the accuracy of its solutions through the discretisation error. In the results shown below we have used a mesh with 256^3 cells, while we have found that using 128^3

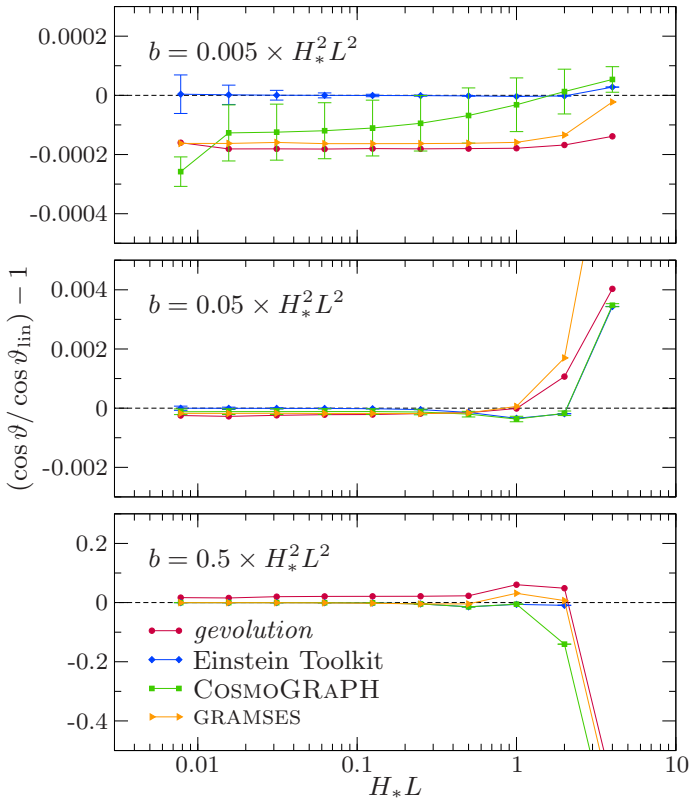

Figure 4.3: Numerical results for the observable Eq.(4.1.1) obtained from GRAMSES (orange triangles), as well as from *gevolution* (red circles), the Einstein Toolkit (blue diamonds) and COSMOGRAPH (green squares). For the latter two, error bars obtained from three different spatial resolutions are shown. The different cases for the amplitude parameter b are shown in the different panels, being top (bottom) the closest (farthest) from linear perturbation theory regime. Plot taken from Adamek et al. (2020).

and 64^3 cells leads to larger inaccuracies even in the linear regime, where higher-order terms neglected by the conformal flatness approximation are subdominant. The same discretisation error occurs for all equations being solved, and so it can affect particle movements and thereby accumulate over time. It is therefore important to choose a sufficiently fine grid to suppress this error. Note that for finite differencing at a fixed order, the discretisation error is determined by the number of cells per side instead of the physical size of a cell. We do not use AMR for the simulations to facilitate the comparison with GR codes that do not have such an option.

Figure 4.3 shows the results of the observable Eq. (4.1.1) obtained from GRAMSES simulations (orange triangles), as well as from other GR codes (as indicated by the legend), for the different values of the amplitude parameter b (the different panels). The top panel of Fig. 4.3 shows the results for the smallest amplitude of the frame-dragging, i.e., $b = 0.005 \times H_*^2 L^2$. We find agreement between GRAMSES and the linear solution to within 0.02% for all values

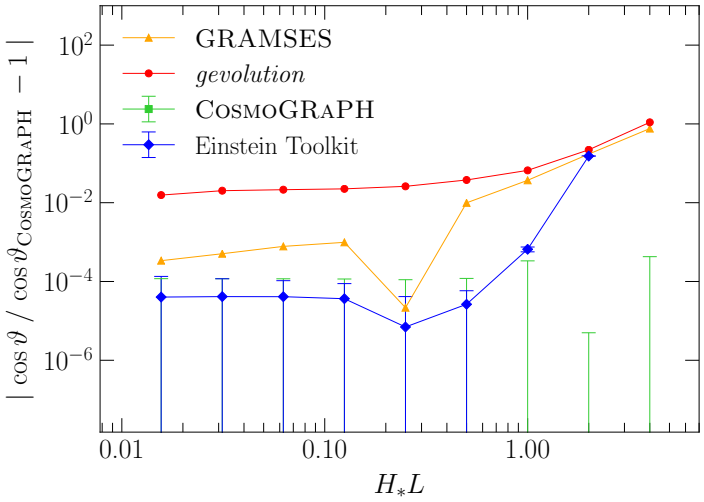

Figure 4.4: Same as the bottom panel of Fig. 4.3, but plotted relative to the result obtained from CosmoGRaPH rather than to linear theory. Plot taken from Adamek et al. (2020)

of H_*L, as well as good agreement with the other GR codes. The deviation from the linear solution remains mostly flat in the results from GRAMSES, as this is dominated by the constant mesh discretisation error from the fixed grid size used.

The middle panel of Figure 4.3 shows the cases with the amplitude parameter fixed as $b = 0.05 \times H_*^2 L^2$. In this case, we find that measurable deviations from the linear solution start to appear at $H_*L \gtrsim 1$. These deviations follow an overall similar trend in all codes, and are below $\sim 1\%$ for all the box size values used in this study. Nonetheless, the results from GRAMSES and *gevolution* (red dots) show a qualitatively similar deviation from the linear prediction, while the two full (hyperbolic) numerical relativity codes, FLRW solver (blue diamonds) and CosmoGRaPH (green squares), agree within their error bars. The latter are obtained from runs using three different spatial resolutions. In the case of GRAMSES, errors might arise in this regime due to the conformal flatness approximation, which neglects tensor modes that might be excited during the nonlinear evolution of the system at $\mathcal{O}(b^2)$ and beyond. Notice that, in contrast, *gevolution* calculates the tensor modes with the weak-field expansion and therefore can evaluate their impact on the light propagation with the ray-tracing code within such an approximation.

The bottom panel of Figure 4.3 shows the most extreme case with $b = 0.5 \times H_*^2 L^2$, which is close to the limit set by the weak energy condition. As expected, in this case we see the strongest deviations from the linear prediction, although we find that the latter still holds to a good approximation down to $H_*L \simeq 1$, as confirmed by all four codes. We have clipped the data-points for the most extreme case, $H_*L = 4$, in the bottom panel of Figure 4.3 to facilitate

the visualisation of the deviations at smaller H_*L. In this case, we find deviation from the linear solution for GRAMSES of -0.68, for *gevolution* of -0.619, and for CosmoGRaPH of -0.8183 ± 0.0004. The data point at $H_*L = 4$ could not be obtained in the case of the FLRW solver, since no null geodesics connecting either A or B to O were found, likely due to the breakdown of the fluid approximation in this regime. Figure 4.4 shows more clearly the results from the bottom panel of Fig. 4.3, as the result from each code is not plotted relative to linear theory but respect to that calculated from CosmoGRaPH. We can observe that GRAMSES agrees with the latter code to within $\lesssim 0.1\%$ for small values of H_*L. This difference grows to $\simeq 100\%$ for the most extreme case $H_*L = 4$, where tensor modes omitted by GRAMSES during the evolution can introduce errors with respect to a full numerical relativity code.

In order to support the validity of the previous comparison, we next check the numerical convergence of the observable presented in Figure 4.3 as a function of resolution. We expect different rates of convergence for each code, due to different dominant error sources that depend on the numerical scheme implemented. The convergence rate can be calculated by evaluating the observable at three different simulation resolutions, Δx_1, Δx_2, and Δx_3. For a method of order p, the error will be $\mathcal{O}(\Delta x^p)$, and the convergence rate of the observable angle ϑ is given by

$$\mathcal{C} = \frac{\vartheta_{\Delta x_1} - \vartheta_{\Delta x_2}}{\vartheta_{\Delta x_2} - \vartheta_{\Delta x_3}}, \tag{4.6.1}$$

while the theoretical (expected) convergence rate is

$$\mathcal{C}_{\text{expected}} = \frac{\Delta x_1^p - \Delta x_2^p}{\Delta x_2^p - \Delta x_3^p}\,. \tag{4.6.2}$$

Figure 4.5 shows the convergence rate Eq. (4.6.1), relative to the theoretical convergence rate for each code Eq. (4.6.2). The order of the integration scheme implemented in each code, p, is shown in the legend. For the comparison, we use the scenario that corresponds to the top panel of Figure 4.3, given that this is the closest case to the linear regime and hence under theoretical control. In the case of GRAMSES, the convergence rate is calculated based on simulations with resolutions of 64^3, 128^3 and 256^3 cells. We find that GRAMSES shows a very consistent convergence rate, which for $H_*L \lesssim 1$ agrees to within 0.3% with the expected value, and within 4% (0.5%) for $H_*L = 2$ (4). This behaviour is likely because, unlike other codes, in GRAMSES the solutions are obtained from elliptic-type equations, hence time integration for the metric — which can introduce additional errors — is not used.

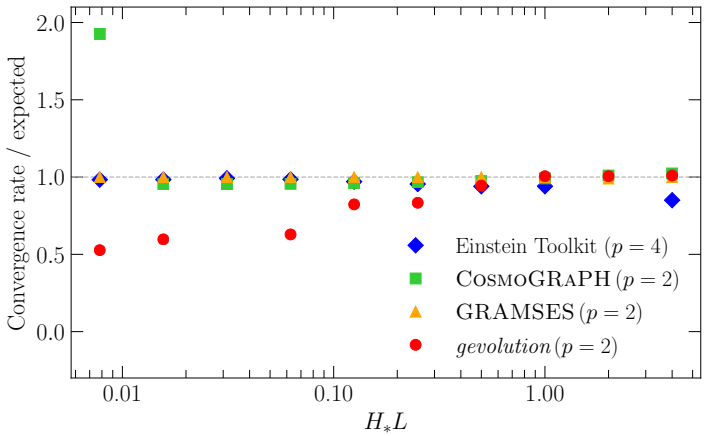

Figure 4.5: Convergence rate test, relative to the expected value given by Eq. (4.6.2). The results from GRAMSES are calculated based on three different resolutions: 64^3, 128^3 and 256^3 cells, and are shown in orange triangles, which corresponds to a finite-difference method of order $p = 2$. Plot taken from Adamek et al. (2020)

4.7 Summary

In this Chapter, we have implemented and run simulations of a very specific model, dubbed 'shearing-dust' universe, where the matter dynamics is allowed to mainly excite the vector modes of the metric, which is associated with the frame-dragging effect. Being the leading order post-Friedmann (post-Newtonian) correction to Newtonian gravity, any relativistic code should aim to calculate this accurately. At the same time, this test has the unique property that it is applicable only to codes that calculate relativistic effects.

We have used this problem to perform a code validation of GRAMSES, for which we compared results against perturbation theory, and also with state-of-the-art GR codes. Given that each code implements a different numerical method and/or a particular approximation of GR, this study provides a valuable test to assess their consistency and limitations. While the full results are discussed in Adamek et al. (2020), in this Chapter we have focused on the details relevant for GRAMSES. In this code, the main limitation comes from the use of the conformal flatness approximation, in which tensor modes of the metric and curvature are neglected, and therefore is not possible to study gravitational waves at the moment.[10]

The comparison shows that, for perturbations with amplitude $b = 0.005 \times H_*^2 L^2$, GRAMSES is able to match linear theory within 0.02% for all box sizes studied here, and the agreement amongst the different codes is good overall. For larger perturbations, with amplitudes $b \in$

[10] Extended versions of this scheme that include tensor modes have been proposed in Cordero-Carrion et al. (2012). These, however, have not been implemented in GRAMSES so far.

$\{0.05, 0.5\} \times H_*^2 L^2$, the results agree with with linear theory within 0.1% and 1%, respectively, in the regime where $H_* L \lesssim 1$. In the case of GRAMSES, deviations from the linear solution in cases well into the linear regime are dominated by the mesh discretisation error, which cause a constant offset from linear theory. For larger perturbations, the main source of deviations from the results from other codes is expected to be the conformal flatness approximation, which neglects tensor modes that could appear during nonlinear evolution, and are within the expected $\mathcal{O}(b^2)$ truncation error.

Besides the comparison discussed in this Chapter, it might be useful to investigate other relativistic effects to further assess the capabilities of the different GR codes on different scenarios. These include the development of spatial curvature (e.g., Tian et al., 2021), the magnetic part of the Weyl tensor, and back-reaction of structure formation onto the expansion rate (e.g., Macpherson et al., 2018b), among others. As in the present case, the aforementioned effects do not have a Newtonian counterpart and hence might probe useful for this purpose.

Chapter 5

The gravitomagnetic effect and vorticity in ΛCDM

5.1 Introduction

While the dynamics of the LSS of the universe is mainly governed by scalar perturbations, vector and tensor degrees of freedom are promising alternatives for exploring the nature of dark matter and gravity. The effects of the vector modes of the spacetime metric on matter such as frame dragging and geodetic precession have been measured in the Solar system during the last decade (Everitt et al., 2011), but there is still no cosmological signal detected. The recent observation of radio galaxies showing coherent angular velocities on scales of ~ 20 Mpc at $z = 1$ reported by Taylor & Jagannathan (2016) motivates seeking a physical interpretation in terms of vector modes, but it has not been possible to establish a clear connection so far (Cusin et al., 2017; Bonvin et al., 2018). More recently, and motivated by the accurate data provided by *Gaia* DR2, a simple model to explain the flat rotation curve of the Milky Way in terms of frame dragging has been proposed in Crosta et al. (2020).

In ΛCDM cosmology, vector modes are typically neglected. In a perfect fluid, vorticity – the covariant curl of the 4-velocity field – satisfies a homogenous nonlinear equation, hence it vanishes exactly, i.e. at all orders in perturbation theory (Lu et al., 2009), unless it is either introduced by initial conditions[1] or generated by physics beyond the fluid model. Moreover, vorticity is not generated by standard inflationary scenarios, and even if it was, this type of

[1] Even if non zero initially, during expansion a first-order vorticity in a standard perfect fluid is red-shifted away.

perturbation quickly decays during the matter-dominated era. Nonetheless, vorticity is found to be generated dynamically via shell (orbit) crossing of matter, a phenomenon extremely common at late times whose modelling is beyond the grasp of the single-streaming fluid regime. Therefore, N-body simulations represent a valuable tool for the study of vorticity generation (Pueblas & Scoccimarro, 2009; Hahn et al., 2015; Jelic-Cizmek et al., 2018).

In the Poisson gauge, generalising the longitudinal gauge to include tensor and vector perturbations (Bertschinger, 1993), the latter are encoded by the non-diagonal spacetime metric components, the shift vector $B_i \equiv g_{0i}$, and represent in this gauge the gauge-invariant gravitomagnetic vector potential (Bardeen, 1980). In ΛCDM, safely assuming purely scalar perturbations at first-order, the shift vector vanishes at the linear level, while at second order it satisfies a constraint equation sourced by the product of first-order density and velocity perturbations. However, it is expected that, just like vorticity, the gravito-magnetic field also receives corrections from phenomena beyond the perfect fluid description.

The impact of vector modes on LSS observables is expected to be small relative to the scalar perturbations, both from perturbative (Lu et al., 2009) and non-perturbative analyses (Bruni et al., 2014; Adamek et al., 2016a), although it can represent a new systematic which needs to be taken into account (Bonvin et al., 2018). For instance, their effect on gravitational lensing seems not to be strong enough to be detectable by current observations (Thomas et al., 2015b; Saga et al., 2015; Gressel et al., 2019), and the imprints of the vector potential in the angular power spectrum and bispectrum of galaxies are also weak (Durrer & Tansella, 2016; Jolicoeur et al., 2019), although a vector perturbation can be isolated from the full signal if it violates statistical isotropy and defines a preferred frame (see, e.g., Tansella et al., 2018). On the other hand, the vector potential power spectrum is known to peak around the equality scale (Lu et al., 2009), and its behaviour as well as impact on observables at highly nonlinear scales remains largely unexplored, although deviations from perturbation theory can be significant (Bruni et al., 2014). Furthermore, in popular $f(R)$ gravity models, vector modes can have considerable deviations from GR on small scales (Thomas et al., 2015a), so these could also play a role in discriminating cosmological models.

The work of Pueblas & Scoccimarro (2009) provided the first insights into the generation of vorticity via shell crossing using N-body simulations, which allowed them to quantify its impact on the density and velocity power spectra estimates from linear perturbation theory. In particular, vorticity was found to peak in the outskirts of virialised structures as particle velocities in inner regions are strongly aligned with density gradients, as also found later

in Hahn et al. (2015) from a different set of simulations. Although – contrary to vorticity – the investigation of the gravitomagnetic vector field in principle requires a completely general-relativistic numerical framework as Newtonian simulations only model a single scalar gravitational potential, Φ, in Bruni et al. (2014) and Thomas et al. (2015c) a novel method to extract its power spectrum by post-processing the momentum density field from a Newtonian simulation was introduced. This is motivated by the fact that the leading contribution to the shift vector in post-Friedmann expansion (Milillo et al., 2015) is sourced by the transverse part of the momentum density field. Although this method neglects the feedback of the shift vector into the simulation dynamics, this approximation is well justified as perturbation theory estimates that the magnitude of the vector potential is at most one percent of the scalar gravitational potential (Lu et al., 2009).

Cosmological codes which are capable of simulating vector modes of the metric have been only recently developed (e.g., Adamek et al., 2016b,a; Mertens et al., 2016; Giblin et al., 2017; Macpherson et al., 2017; Barrera-Hinojosa & Li, 2020), and have proven robust enough to study different relativistic distortions in the LSS; (see Adamek et al., 2020, for an actual comparison of frame-dragging observables in a toy universe simulated using these codes). In particular, the cross correlation between the shift vector and vorticity has been studied in Jelic-Cizmek et al. (2018) using the relativistic N-body code *gevolution* (Adamek et al., 2016b,a), showing that the vector potential is only weakly sourced by vorticity alone, which is subdominant compared with the density-dependent terms coming from the transverse projection of the *full* momentum field, in qualitative agreement with post-Friedmann expansion results from Bruni et al. (2014); Thomas et al. (2015c).

The objective of this Chapter is to study the vector modes of both the gravitational and matter velocity fields from large sub-horizon scales down to deeply nonlinear scales using the GRAMSES code (Barrera-Hinojosa & Li, 2020; Barrera-Hinojosa & Li, 2020), which has been introduced in Chapter 2. We expand on previous studies in the following ways: (i) similarly to Jelic-Cizmek et al. (2018), we provide a direct calculation of the gravitomagnetic field, represented by the shift vector, from the simulation, also relaxing the weak-field approximation in our approach; (ii) we present results for scales in the deeply nonlinear regime which have not been previously explored in this context, and which are accessible thanks to the adaptive-mesh refinement (AMR) capabilities of GRAMSES. For the first time, we explore the gravitomagnetic vector potential in dark matter haloes in a broad range of halo masses; (iii) furthermore, we quantify the gravitomagnetic acceleration inside the dark matter haloes and compare this against the standard gravitational one.

We note that, with the exception of Jelic-Cizmek et al. (2018), previous studies of vorticity use simulations that incorporate a softening length scale, a numerical parameter used to prevent divergences in the calculation of inter-particle forces which also determines the spatial resolution. In GRAMSES – similarly to *gevolution* – the metric components and their spatial derivatives are calculated on a Cartesian mesh. AMR codes, such as GRAMSES, are generally slower than fixed-mesh-resolution codes such as *gevolution* which can benefit from efficient standard libraries such as FFTW, but their adaptively-produced mesh structure in high-density regions allows them to be more focused on the fine details in such regions, without increasing the overall cost of the simulation substantially. Therefore, they provide complementary ways to study the vector modes from cosmological simulations.

The rest of this Chapter is organised as follows. In Section 5.2 we fix our notations and briefly describe the general-relativistic formalism and methods implemented in the GRAMSES code that are relevant for the vector modes. In Section 5.3.1 we show the results for the different power spectra of the velocity field components as well as of the gravitomagnetic potential. Then, in Section 5.3.2, we focus on dark matter haloes, providing comparisons of the gravitomagnetic potential and corresponding acceleration with the scalar counterparts.

Throughout this Chapter, Greek indices are used to label spacetime vectors and run over $(0, 1, 2, 3)$, while Latin indices run over $(1, 2, 3)$. Unless otherwise stated, we follow the unit convention that the speed of light $c = 1$.

5.2 Method and definitions

For the sake of clarity and completeness, let us briefly summarise the terminology and conventions adopted in this Chapter, which in some part stem from GRAMSES' implementation itself.

In order to solve the gravitational sector equations and geodesic equations, GRAMSES adopts the $3 + 1$ formalism in which the spacetime metric takes the form

$$\mathrm{d}s^2 = g_{\mu\nu}\mathrm{d}x^\mu \mathrm{d}x^\nu = -\alpha^2 \mathrm{d}t^2 + \gamma_{ij}\left(\beta^i \mathrm{d}t + \mathrm{d}x^i\right)\left(\beta^j \mathrm{d}t + \mathrm{d}x^j\right), \tag{5.2.1}$$

where α is the lapse function, β^i the shift vector and γ_{ij} the induced metric on the spatial hypersurfaces, which in the constrained formulation adopted by GRAMSES is approximated by a conformally-flat metric, $\gamma_{ij} = \psi^4 \delta_{ij}$, with ψ being the conformal factor and δ_{ij} the Kronecker delta.

In the $3+1$ formalism $n_\mu = (-\alpha, 0)$ is the unit timelike vector normal to the time slices, the 3-dimensional spatial hypersurfaces with metric γ_{ij}, and Eulerian observers are those with 4-velocity n^μ. The energy density ρ and momentum density S_i measured by these normal observers are given by the following projections of the energy-momentum tensor $T^{\mu\nu}$,

$$\rho \equiv n_\mu n_\nu T^{\mu\nu} \,, \tag{5.2.2}$$

$$S_i \equiv -\gamma_{i\mu} n_\nu T^{\mu\nu} \,, \tag{5.2.3}$$

where the action of n_μ projects onto the timelike direction, while $\gamma_{\mu\nu} = g_{\mu\nu} + n_\mu n_\nu$ projects onto the spatial hypersurface. Eq. (5.2.2) and (5.2.3) are the source terms for the Hamiltonian constraint and momentum constraint, respectively. Additionally, the spatial stress and its trace are defined as

$$S_{ij} \equiv \gamma_{i\mu}\gamma_{j\nu} T^{\mu\nu} \,, \qquad S = \gamma^{ij} S_{ij} \,, \tag{5.2.4}$$

which, in addition to ρ and S_i, appear in the evolution equations for the extrinsic curvature tensor. In GRAMSES, the (dark) matter sector is represented by an ensemble of non-interacting simulation particles of rest mass m and four-velocity $u^\mu = dx^\mu/d\tau$, where τ is an affine parameter. The equations for the gravitational sector are numerically solved based on conformal matter sources, which are scaled using $\gamma = \det(\gamma_{ij})$ as

$$s_0(\mathbf{x}) \equiv \sqrt{\gamma}\rho \quad \propto m\alpha u^0 \,, \tag{5.2.5}$$

$$s_i(\mathbf{x}) \equiv \sqrt{\gamma} S_i \;\; \propto m u_i \,, \tag{5.2.6}$$

$$s_{ij}(\mathbf{x}) \equiv \sqrt{\gamma} S_{ij} \propto m \frac{u_i u_j}{\alpha u^0} \,. \tag{5.2.7}$$

In these, $\mathbf{x}$ is a (discrete) position vector on the cartesian simulation grid and the proportionality symbol in each equation stands for the standard cloud-in-cell (CIC) weights used for the particle-mesh projection (Hockney & Eastwood, Inc., Bristol, PA, USA, 1988). From Eqs. (5.2.5)-(5.2.7) we have the following useful relations:

$$s_0 = \rho\Gamma \,, \tag{5.2.8}$$

$$s_i = \frac{\rho}{\Gamma} u_i \,, \tag{5.2.9}$$

$$s_{ij} = \frac{\rho}{\Gamma^2} u_i u_j \,, \qquad \Longrightarrow \; s = \rho(1 - \Gamma^{-2}) \,, \tag{5.2.10}$$

$$u_i = \Gamma^2 \frac{s_i}{s_0} \,, \tag{5.2.11}$$

where $\Gamma \equiv \alpha u^0 = \sqrt{1 + \gamma^{ij} u_i u_j}$ is the Lorentz factor. For a perfect fluid, $s \equiv \sqrt{\gamma} S$ is

proportional to pressure in linear theory, and then it vanishes for CDM (dust) in this regime. Naturally, s also vanishes in the non-relativistic limit.

The equations of motion for collisionless particles correspond to the geodesic equation $u^\mu \nabla_\mu u_\nu = 0$, which in the $3+1$ form reads

$$\frac{\mathrm{d}u_i}{\mathrm{d}t} = -\Gamma \partial_i \alpha + u_j \partial_i \beta^j - \alpha \frac{u_j u_k}{2\Gamma} \partial_i \gamma^{jk} \,, \tag{5.2.12}$$

$$\frac{\mathrm{d}x^i}{\mathrm{d}t} = \alpha \frac{\gamma^{ij} u_j}{\Gamma} - \beta^i . \tag{5.2.13}$$

In Eq. (5.2.12), the term $u_j \partial_i \beta^j$ corresponds to a force that is absent in both the Newtonian limit and the linear perturbation regime. In the case where β^j is purely a vector-type perturbation (e.g., the Poisson gauge), this force term is known as *gravitomagnetic force*, in formal analogy with the magnetic Lorentz force.

5.2.1 Vector decomposition

Given that in this Chapter we are particularly interested in vector modes (transverse modes), we start by splitting a vector field V^i ($\mathbf{V}$) as

$$\mathbf{V} = \mathbf{V}_\parallel + \mathbf{V}_\perp \,, \tag{5.2.14}$$

where $\mathbf{V}_\parallel$ and $\mathbf{V}_\perp$ are respectively the scalar (irrotational) and vector (rotational) components, i.e., these satisfy

$$\boldsymbol{\nabla} \times \mathbf{V}_\parallel = \mathbf{0}, \quad \boldsymbol{\nabla} \cdot \mathbf{V}_\perp = 0 \,. \tag{5.2.15}$$

In the case of the velocity field[2] u_i ($\mathbf{u}$), we define the velocity divergence and vorticity as

$$\theta \equiv \boldsymbol{\nabla} \cdot \mathbf{u} \,, \tag{5.2.16}$$

$$\boldsymbol{\omega} \equiv \boldsymbol{\nabla} \times \mathbf{u} \,. \tag{5.2.17}$$

As usual, the power spectra of these quantities are respectively defined as

$$\left\langle \theta(\mathbf{k}) \theta^*(\mathbf{k}') \right\rangle = \delta(\mathbf{k} - \mathbf{k}')(2\pi)^3 P_\theta(k) \,, \tag{5.2.18}$$

$$\left\langle \boldsymbol{\omega}^i(\mathbf{k}) \boldsymbol{\omega}^{*j}(\mathbf{k}') \right\rangle = \delta(\mathbf{k} - \mathbf{k}')(2\pi)^3 \frac{1}{2} \left(\delta^{ij} - \frac{k^i k^j}{k^2} \right) P_{\boldsymbol{\omega}}(k) \,, \tag{5.2.19}$$

[2] We use $\mathbf{u}$ to represent the velocity u_i rather than u^i, as it is the former that is used in the $3+1$ form of the geodesic equations (5.2.12) and (5.2.13) which are implemented in GRAMSES. u_i is what we call 'CMC-MD-gauge velocity', and is different from u^i. See Chapter 2 for more details.

and the velocity power spectrum satisfies the relation

$$P_{|\mathbf{u}|} = k^2(P_\theta + P_\omega)\,. \tag{5.2.20}$$

The power spectrum of the vector modes of the shift vector is defined in analogous way to Eq. (5.2.19).

5.2.2 Gauge choice and the constraint for the vector potential

For solving the gravitational and geodesic equations, GRAMSES implements a constrained formulation of GR (Bonazzola et al., 2004; Cordero-Carrión et al., 2009), in which both the tensor modes of the spatial metric and the transverse-traceless (TT) part of the extrinsic curvature are neglected during the evolution. In contrast, the scalar and vector modes of the gravitational field are treated fully nonlinearly. In order to do this in a robust way, the formalism adopts the constant-mean-curvature slicing (Smarr & York, 1978a; Shibata, 1999; Shibata & Sasaki, 1999) and a minimal-distortion gauge condition under the conformal flatness approximation (Smarr & York, 1978b). Contrary to the Poisson gauge, in this gauge the shift vector contains both scalar and vector $(1+2)$ degrees of freedom. At linear order, the latter modes match the gauge-invariant shift vector from the Poisson gauge (Matarrese et al., 1998a; Lu et al., 2009), while the mismatch in the scalar piece reflects the fact that the time foliations are different in these two gauges. Then, in this formalism the components of the shift vector are solved from a combination of the $3+1$ evolution equation for the extrinsic curvature, the momentum constraint and the gauge conditions (Barrera-Hinojosa & Li, 2020)

$$(\Delta_L\beta)^i = 16\pi\alpha\psi^{-6}s^i + \partial_j(\alpha\psi^{-6})\bar{A}^{ij}_L\,, \tag{5.2.21}$$

where $s^i = \delta^{ij}s_i$, $(\Delta_L\beta)^i := \partial^2\beta^i + \partial^i(\partial_j\beta^j)/3$ denotes the flat-space vector Laplacian operator, and

$$\bar{A}^{ij}_L = \partial^i W^j + \partial^j W^i - \frac{2}{3}\delta^{ij}\partial_k W^k\,, \tag{5.2.22}$$

is the longitudinal part of the traceless extrinsic curvature tensor. The auxiliary potential W_i introduced in Eq. (5.2.22) is directly solved from the momentum constraint equation,

$$(\Delta_L W)_i = 16\pi s_i\,. \tag{5.2.23}$$

Then, from Eq. (5.2.21) we note that, at leading order, the shift vector is sourced by the momentum field and thus $\beta^i \propto W^i$ by Eq. (5.2.23), while differences appear at higher order due to the extrinsic curvature tensor sourcing β^i. Given that throughout this Chapter we will

be interested in the vector modes of the shift vector, this is decomposed in the same fashion of Eq. (5.2.14), i.e.

$$\beta^i = B^i + \beta^i_{\parallel}\,, \tag{5.2.24}$$

where $B^i \equiv \beta^i_{\perp}$ ($\mathbf{B}$) is referred to as the vector potential or gravitomagnetic potential, and $\beta^i_{\parallel}$ is the scalar mode of the shift. Let us note that, using Eq. (5.2.9), the curl of the conformal momentum density field s_i ($\mathbf{s}$) can be written non-perturbatively as

$$\boldsymbol{\nabla} \times \mathbf{s} = \Gamma^{-1}[(1+\delta)\boldsymbol{\omega} + \boldsymbol{\nabla}\delta \times \mathbf{u} - \boldsymbol{\nabla}\Gamma \times \mathbf{s}]\,, \tag{5.2.25}$$

where $\delta = \rho/\bar{\rho} - 1$ is the density contrast and $\bar{\rho}$ is the mean density. Previous studies have shown that the terms $\delta\boldsymbol{\omega}$ and $\boldsymbol{\nabla}\delta \times \mathbf{u}$ in the r.h.s. of Eq. (5.2.25) are the main sources for the vector potential (Bruni et al., 2014; Thomas et al., 2015c; Jelic-Cizmek et al., 2018), while the contribution from vorticity itself is subdominant at all scales. In the r.h.s. of Eq. (5.2.25), the last term and the overall modulation by the Lorentz Factor Γ arise due to the definition of $\mathbf{s}$ in Eq. (5.2.9), and both contributions vanish in the linear regime and the non-relativistic limit.

5.3 Results

For the investigation in this chapter, we have run a high-resolution simulation using GRAMSES, with a comoving box size $L_{\rm box} = 256\ h^{-1}$Mpc and $N_{\rm part} = 1024^3$ dark-matter particles, corresponding to a particle mass resolution of $1.33 \times 10^9\ h^{-1}\mathrm{M}_\odot$. Because GRAMSES makes use of AMR in high-density regions, the spatial resolution is not uniform throughout the simulation volume: while the coarsest (domain) grid has $N_{\rm part}$ cells, corresponding to a comoving spatial resolution of 0.25 h^{-1}Mpc, the most refined (high density) regions reach a resolution of $128^3 \times N_{\rm part}$ grid elements, with corresponding spatial resolution of 2 h^{-1}kpc.

Initial conditions suitable for the relativistic simulation, and based on the Zel'dovich approximation, were generated at $z = 49$ with a modified version of 2LPTic code (Crocce et al., 2006) fed with the matter power spectrum obtained from a modified version of CAMB (Lewis et al., 2000) that works for the particular gauge needed for GRAMSES. More details on this can be found in Chapter 3. The cosmological parameters adopted for the simulation are $\{\Omega_\Lambda,\ \Omega_m,\ \Omega_K,\ h\} = \{0.693, 0.307, 0, 0.68\}$ and a primordial spectrum with amplitude $A_s = 2.1 \times 10^{-9}$, spectral index $n_s = 0.96$ and a pivot scale $k_{\rm pivot} = 0.05\ \mathrm{Mpc}^{-1}$.

In order to measure the velocity fields from simulation snapshots, we use the publicly-available

DTFE code (Cautun & van de Weygaert, 2011) which is based on the Delaunay tessellation method, although other methods have been explored in the literature during the last few years. Notably, the phase-interpolation method introduced in Abel et al. (2012) shows better performance than DTFE in shell-crossing regions (Hahn et al., 2015), where the finite-difference estimation of velocity divergence and vorticity across caustics can be problematic due to the multiply-valued nature of the velocity field. Nonetheless, the power spectra of these two fields are not strongly affected by this since the volume-weighted contribution from caustics is negligible, and both methods converge when nonlinear scales are well resolved. In addition, while the vorticity power spectrum is affected by resolution effects, this is weakly affected by finite-volume effects (Pueblas & Scoccimarro, 2009; Jelic-Cizmek et al., 2018). We note that, while the initial velocity field is vorticity-free by construction, spurious vorticity will be present at some degree due to the numerical errors introduced by particle-mesh projections. In addition, shell-crossing events – which source vorticity – are rare at high redshift, and its insufficient sampling restricts the possibility of estimating the velocity field robustly. Therefore, in this Chapter we shall focus mainly on low redshifts, $z < 1.5$, at which vorticity results are expected to be robust. Contrary to the velocity field, the gravitomagnetic potential is already solved by the code on a Cartesian mesh so there is no need for post-processing particle-mesh projections.

It is worthwhile to mention that, although the GR simulations do not necessitate the specification of a cosmological background (Barrera-Hinojosa & Li, 2020), in our approach the notion of redshift is still used and should be understood as the standard, background one. This is achieved through the constant-mean-curvature slicing condition, which allows us to fix the trace of the extrinsic curvature of the spatial hypersurfaces as $K = -3H(t)$, where the Hubble parameter H can be conveniently fixed via 'fiducial' Friedmann equations (Giblin et al., 2018; Barrera-Hinojosa & Li, 2020). In addition, even though in the gauge adopted by GRAMSES the scalar gravitational potentials as well as the matter fields are not gauge-invariant quantities, gauge effects are only prominent on large scales and become strongly suppressed for modes inside the horizon. Since in this work we are mainly interested in the latter, as well as in redshifts below $z = 1.5$ (in which the horizon is already larger than the box size), we do not explore potential gauge issues further.

Figure 5.1 provides a visual representation of the density field (top left), velocity divergence (top right), the magnitude[3] of the vorticity vector field, $\omega \equiv |\boldsymbol{\omega}| = (\omega_x^2 + \omega_y^2 + \omega_z^2)^{1/2}$ (bottom

[3]For this we use the flat metric δ_{ij}.

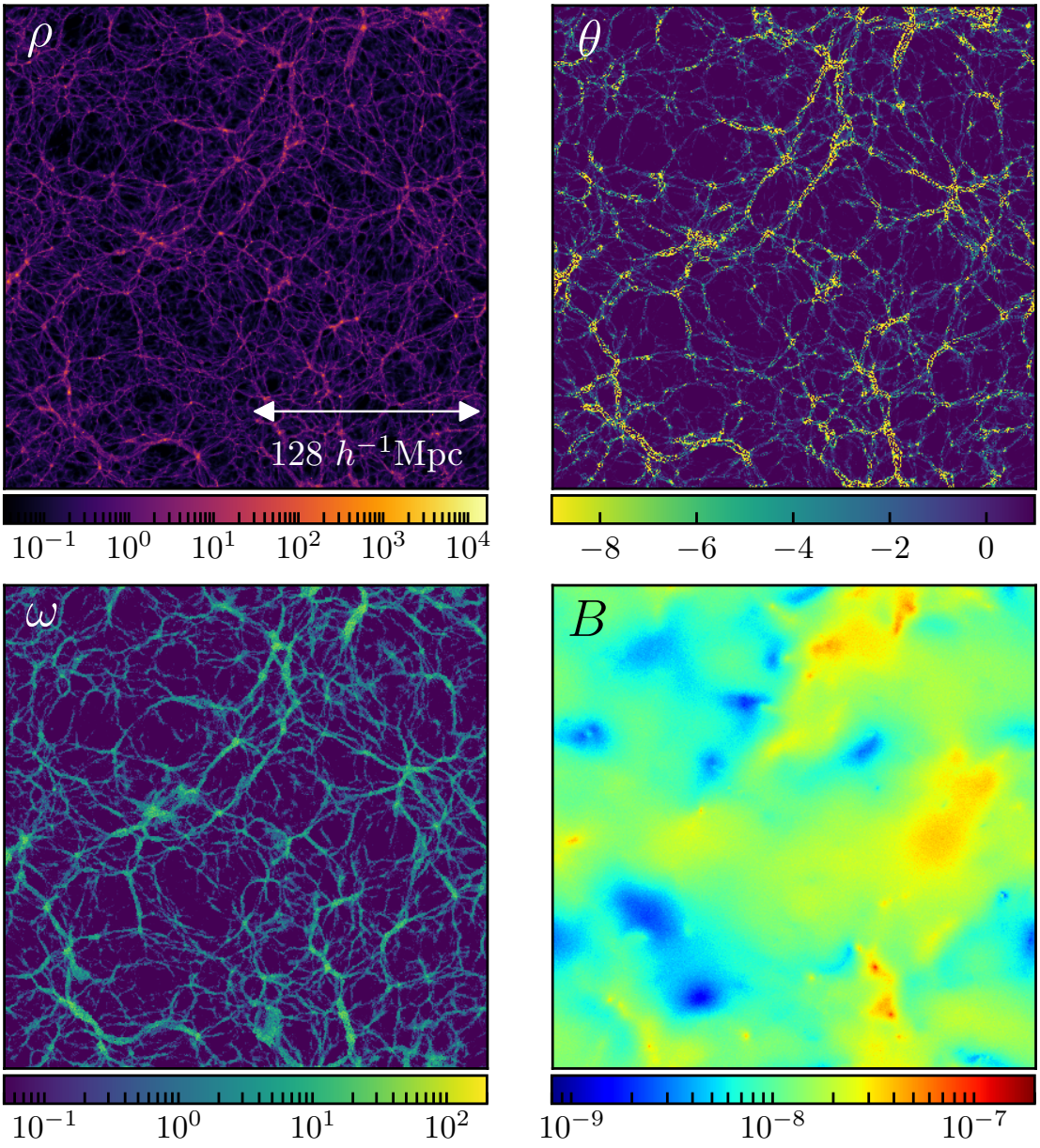

Figure 5.1: A slice of the simulation box at $z = 0$ showing the density (top left), velocity divergence (top right), vorticity (bottom left) and vector potential magnitude (bottom right) fields. The velocity values shown are normalised by $\mathcal{H}f$, where $\mathcal{H} \equiv aH$ is the conformal Hubble parameter and f is the linear growth rate in ΛCDM. The density field is normalised by its mean value in the simulation box.

left), and the vector potential magnitude, $B \equiv |\mathbf{B}| = (B_x^2 + B_y^2 + B_z^2)^{1/2}$ (bottom right), across a slice of the simulation box at $z = 0$. From this figure, it is clear that the density field has a similar large-scale distribution to the velocity divergence, consistently with linear perturbation theory. Since velocity divergence can take negative values, we use a linear scale on its map, with a cutoff of extreme values to help visualisation. As expected, the velocity divergence is negative in collapsing regions due to matter in-fall, and positive in voids and

low-density regions. The vorticity field also shows a clear correlation with both density and velocity divergence. However, we should bear in mind that, as we have discussed before, the velocity divergence and vorticity estimated by DTFE are not completely reliable near caustics (Hahn et al., 2015), and therefore such maps only provide qualitative information and an accurate picture on large scales.

From the bottom right panel in Fig. 5.1, we observe that the magnitude of the vector potential has some degree of correlation with the structures observed in density, velocity divergence and vorticity, particularly in very high-density and low-density regions. As shown by Eqs. (5.2.21)-(5.2.25), the vector potential is not sourced by any of these components alone but is correlated with the rotational part of the full momentum density field. This panel also shows that the distribution of the vector potential magnitude is a great deal smoother than the cases of matter and velocity fields. This is expected since the vector potential components satisfy the elliptic-type equation (5.2.21), and then long-wavelength modes become dominant due to the Laplacian operator ∂^2. Although not included here, the same happens in the case of the conformal factor ψ which satisfies the Hamiltonian constraint (or the Poisson equation in the Newtonian limit). From the quantitative side, we note that the vector potential magnitude seems to typically remain between $\mathcal{O}(10^{-8})$ and $\mathcal{O}(10^{-7})$, with some peaks of a few times $\mathcal{O}(10^{-7})$ only in very specific regions.

We will explore the behaviour of the vector modes in more detail in the next sections.

5.3.1 Power spectra

In this section we analyse the power spectra of the velocity field and gravitomagnetic vector potential. The auto and cross spectra of matter quantities such as density, velocity divergence and vorticity (which are measured with DTFE from particle data) are calculated using NBODYKIT (Hand et al., 2018). In contrast, the vector (as well as scalar) potential values are calculated and stored by GRAMSES in cells of hierarchical AMR meshes, and the spectrum is measured by a different code that is able to handle such mesh data directly and to write it on a regular grid by interpolation (the 'AMR-FFT method', He et al., 2015). While the vector potential spectrum can also be measured in the same way as the matter quantities by writing its values at the particles' positions rather than in AMR cells, which means DTFE and NBODYKIT can be used, the above method yields better results on small scales; as shown in Appendix C, the 'DTFE+NBODIKIT' method is affected by shot noise at larger scales than the 'AMR-FFT' method. In all figures, we normalise the velocity power spectra by the fac-

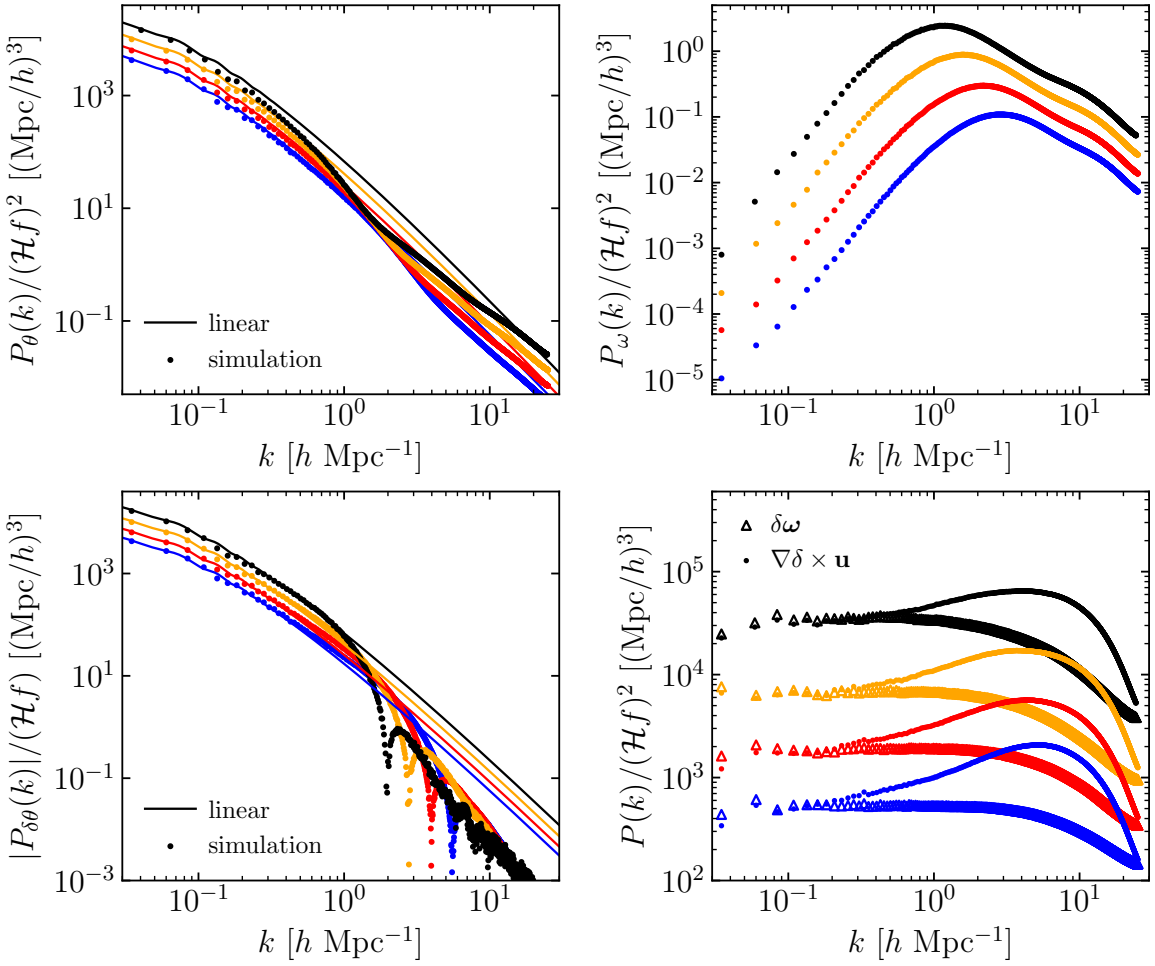

Figure 5.2: Various auto and cross power spectra involving the velocity field for $z = 0$ (black), $z = 0.5$ (orange), $z = 1$ (red) and $z = 1.5$ (blue). The top left and top right panels show the velocity divergence power spectrum and vorticity power spectrum, respectively, both of which are normalised by $(\mathcal{H}f)^2$. Bottom left: the cross spectrum between density and velocity divergence. Since in linear theory $P_{\delta\theta} < 0$, we plot its absolute magnitude normalised by $\mathcal{H}f$. The discontinuity corresponds to the flip in sign on nonlinear scales, after which density and velocity divergence become correlated. Bottom right: the power spectrum of $\delta\boldsymbol{\omega}$ and $\boldsymbol{\nabla}\delta \times \mathbf{u}$, which are the main source terms for the metric vector potential, c.f. Eq. (5.2.25). These are normalised by $(\mathcal{H}f)^2$. In the two left panels, the solid lines denote the corresponding linear-theory predictions.

tor $(\mathcal{H}f)^2$, where $\mathcal{H} = aH$ is the conformal Hubble parameter of the reference Friedmann universe, and f the linear growth rate in ΛCDM parameterised as (Linder, 2005)

$$f(a) = \Omega_m(a)^{6/11}, \tag{5.3.1}$$

where $\Omega_m(a) = \Omega_m a^{-3}/(H/H_0)^2$. In this way, the amplitude of P_θ matches that of the matter power spectrum in the linear regime, where the continuity equation $\delta = -\theta/(\mathcal{H}f)$ is expected to hold.

Figure 5.2 shows the velocity divergence power spectrum (top left panel), the vorticity power spectrum (top right panel), the cross spectrum between density and velocity divergence (bottom left) and the power spectrum of two different contributions to the momentum field (bottom right) at different redshifts in the range $0 \leq z \leq 1.5$. In the case of velocity divergence, we find a very good agreement with linear theory at scales $k \leq 0.1\ h\mathrm{Mpc}^{-1}$ for all redshifts. Above that scale, deviations become stronger towards lower redshifts, and a localised power loss ('dip') eventually develops around $k \approx 1.2\ h\mathrm{Mpc}^{-1}$. In the case of the vorticity power spectrum, we note that towards large scales this is several orders of magnitude smaller than velocity divergence, while at around $k \sim 1\ h\mathrm{Mpc}^{-1}$ the spectrum starts to peak and they become comparable. Note that, unlike the velocity divergence, there is no standard perturbation theory prediction for the vorticity as this exactly vanishes in the perfect fluid description. Interestingly, the 'dip' in the velocity divergence power spectrum is at the similar position to the peak in the vorticity power spectrum, which has been interpreted as the consequence of shell crossing occurring around those scales, where the angular momentum can be large enough to dampen the growth of structures as it forces particles to rotate around them (Jelic-Cizmek et al., 2018).

Note that, due to the high cost[4] of GR simulations using GRAMSES, we have not performed runs with even higher resolutions to check the convergence of the velocity and vorticity power spectra. A useful convergence test for *gevolution* simulations was done in Jelic-Cizmek et al. (2018) (see Fig. 6 there), which shows that the amplitude of P_ω decreases as the force resolution increases. The simulations there have the same box size of $L_{\mathrm{box}} = 256\ h^{-1}\mathrm{Mpc}$, and the run labelled 'high resolution 1' has the same mesh resolution as our domain grid (1024^3 cells); while this resolution is eight times poorer than that of the run labelled 'high resolution 2', which has 2048^3 cells, the AMR nature of GRAMSES means that higher resolution can be achieved in high-density regions – with the highest resolution attained in our run being equivalent to a regular mesh with $128^3 \times 1024^3$ cells. Hence, since 'high resolution' 1 and 2 are already converged in Jelic-Cizmek et al. (2018), we conclude that our simulation has also converged to at least a similar level.

The cross spectra $P_{\delta\theta}$ is useful for detecting deviations from linear theory and provides information about shell crossing. Considering the continuity equation, the linear-theory

[4] A GR simulation using GRAMSES takes about an order of magnitude longer than an equivalent Newtonian simulation using default RAMSES, partly due to the 10 (compared to one) GR metric potentials to be solved, and partly due to the cost of preparing the source terms for the nonlinear equations that govern the metric potentials, as well as the additional MPI communications.

expectation is that $P_{\theta\delta}/(\mathcal{H}f) = -P_\delta$, but towards shell-crossing scales the initial (linear) anti-correlation of δ and θ is lost and correlations appear (Hahn et al., 2015). From the bottom left panel of Fig. 5.2 we find that the anti-correlation drops dramatically and flips sign at $k \approx 2\ h\mathrm{Mpc}^{-1}$ at $z = 0$, which is slightly higher than the scale at which the vorticity spectrum peaks as also found in previous studies (Jelic-Cizmek et al., 2018).

The bottom right panel of Fig. 5.2 shows the power spectra of $\delta\boldsymbol{\omega}$ and $\boldsymbol{\nabla}\delta \times \mathbf{u}$, which are the main source terms for the metric vector potential in Eq. (5.2.25). In particular, the contribution of $\boldsymbol{\omega}$ to Eq. (5.2.25) is already small compared to $\delta\boldsymbol{\omega}$ on nonlinear scales because $\delta \gg 1$. We find good agreement with the $z = 0$ results shown in Bruni et al. (2014) based on a post-Friedmann expansion. We find that towards higher redshifts the contribution due to $\boldsymbol{\nabla}\delta \times \mathbf{u}$ starts to become larger than that of $\delta\boldsymbol{\omega}$ at slightly larger scales.

Although vorticity vanishes in standard perturbation theory, the effective field theory of LSS (EFTofLSS) predicts that its power spectrum today can be characterised by a power law over a range of scales (Carrasco et al., 2014). On large scales, we can find the slope of the vorticity power spectrum by fitting a power law,

$$P_{\boldsymbol{\omega}}(k) = A_\omega k^{n_\omega}\,, \tag{5.3.2}$$

where n_ω is the large-scale spectral index, and A_ω the amplitude that is not fixed by theory. The EFTofLSS predicts $n_\omega = 3.6$ for $0.1\ h\mathrm{Mpc}^{-1} \lesssim k \lesssim 0.2\ h\mathrm{Mpc}^{-1}$ and $n_\omega = 2.8$ for $0.2\ h\mathrm{Mpc}^{-1} \lesssim k \lesssim 0.6\ h\mathrm{Mpc}^{-1}$ (Carrasco et al., 2014). Previous N-body simulations have found $n_\omega \approx 2.5$ for $k \lesssim 0.1\ h\mathrm{Mpc}^{-1}$ (Hahn et al., 2015); a similar value was found at $k \lesssim 0.4\ h\mathrm{Mpc}^{-1}$ in Jelic-Cizmek et al. (2018). Moreover, on scales $k \gtrsim 1\ h\mathrm{Mpc}^{-1}$, there is partial evidence suggesting that the spectral index approaches the asymptotic value $n_\omega^{\mathrm{NL}} \to -1.5$ (Hahn et al., 2015).

Figure 5.3 shows the best fits of the power law (5.3.2) to the simulation data at $z = 0$ on large scales (small scales) with their corresponding spectral index n_ω (n_ω^{NL}), and the shaded region represents the interval of validity for the fit. On large sub-horizon scales, we find $n_\omega \approx 2.7$, which is slightly higher than previous simulations results in the literature, and slightly lower than the EFTofLSS prediction. Notice, however, that there is not complete overlap between the region used for the fit and the EFTofLSS prediction used for comparison as the latter extends up to $k \sim 0.6\ h\mathrm{Mpc}^{-1}$ but it is clear that the slope of the power spectrum already decreases at $k \sim 0.32\ h\mathrm{Mpc}^{-1}$. In addition, the slope does not seem to become steeper at larger scales as predicted by the EFTofLSS, a feature also found by the previous study (Jelic-

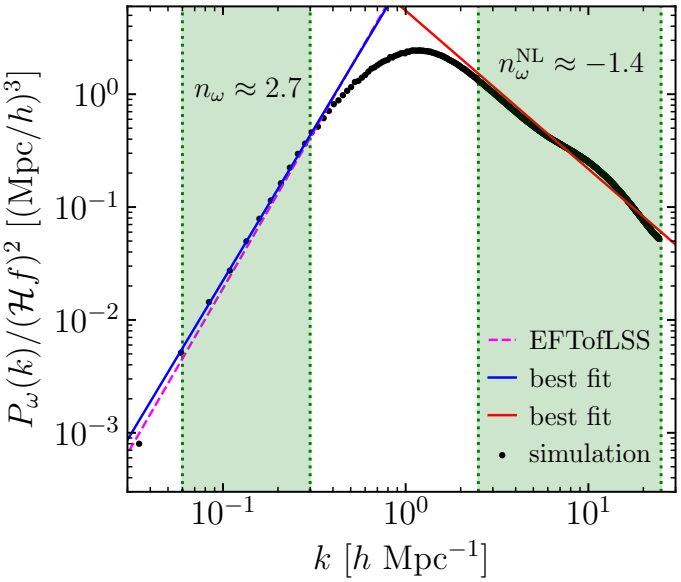

Figure 5.3: Power-law fitting of the vorticity power spectrum at $z = 0$. The solid blue and solid red lines show the best fits of the simulation data (black dots) on large and small scales, respectively, while the shaded regions represent the validity interval for each fit. As a reference, the dashed magenta line shows the EFTofLSS prediction from Carrasco et al. (2014) for the region $0.2\ h\text{Mpc}^{-1} \lesssim k \lesssim 0.6\ h\text{Mpc}^{-1}$, which only has a small overlap with the fitting region used on large sub-horizon scales.

Cizmek et al., 2018), which is likely related to the large-scale cutoff imposed by the finite box of the simulation. Toward smaller scales, we find the spectral index $n_\omega^{\rm NL} \approx -1.4$, which is slightly less steep than that suggested in Hahn et al. (2015). However, there is a slight but clear increase in power at around $k \sim 7\ h\text{Mpc}^{-1}$ which introduces an oscillatory feature not captured by a perfect power law.

As originally proposed in Pueblas & Scoccimarro (2009), it is also interesting to characterise the evolution of the large-scale vorticity power spectrum as

$$P_{\boldsymbol{\omega}}(k;z) = \left(\frac{D_+(z)}{D_+(0)}\right)^{\gamma_\omega} P_{\boldsymbol{\omega}}(k;z=0)\,, \tag{5.3.3}$$

where $D_+(z)$ is the linear growth rate at z and γ_ω a new parameter. In Pueblas & Scoccimarro (2009), the best-fit value found is $\gamma_\omega = 7 \pm 0.3$ using the snapshots $z = 0, 1, 3$, which is overall consistent with Thomas et al. (2015c); Jelic-Cizmek et al. (2018), although the latter references suggest values $\gamma_\omega \geq 7$. Moreover, these have only considered snapshots with $z \leq 1$ since the scaling breaks down at higher redshifts, which is likely related to resolution effects in the sampling of vorticity due to a lower fraction of particles undergoing shell crossing at higher redshifts.

The top panels of Fig. 5.4 show the results for the best fist of the $D_+^{\gamma_\omega}$ scaling of Eq. (5.3.3)

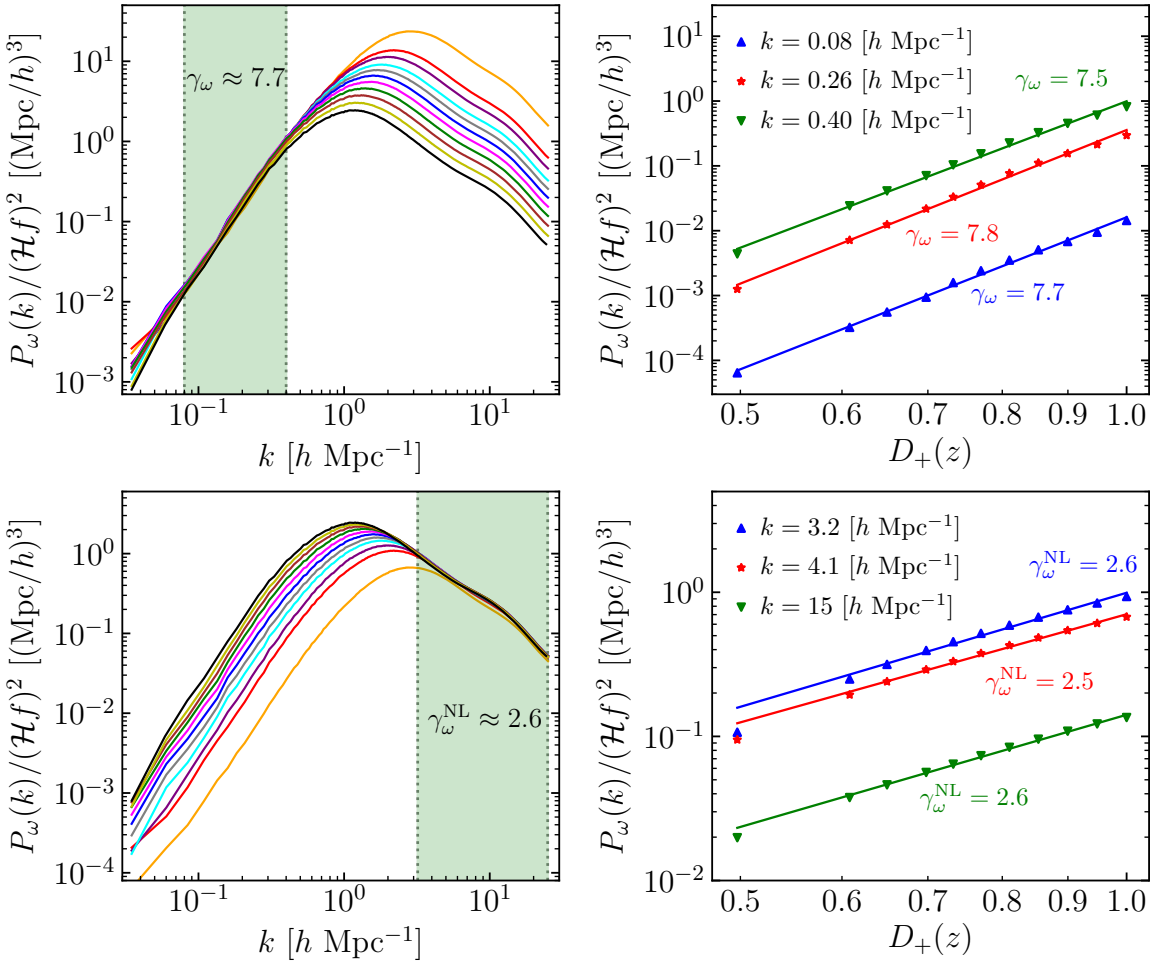

Figure 5.4: Power-law modelling of the time evolution of the vorticity power spectrum based on Eq. (5.3.3). Top panels show results for the large scales regime and the bottom panels analogous results for nonlinear scales. Top left: vorticity power spectra at different redshifts scaled using $\gamma_\omega = 7.7$. Shaded regions represent the interval of validity considered for the fit, and the colours {orange, red, purple, cyan, gray, blue, magenta, green, brown, yellow, brown, black} correspond to $z = \{1.5, 1, 0.85, 0.7, 0.6, 0.5, 0.4, 0.3, 0.2, 0.1, 0\}$, respectively. Bottom left: similar to top left panel but for nonlinear scales. Right panels: Time evolution of the vorticity power spectrum for a set of fixed k-modes as a function of $D_+(z)$ (normalised by today's value of D_+). The solid lines correspond the best fit curves with the respective power-law indices γ_ω and $\gamma_\omega^{\rm NL}$ shown. On the bottom right panel, the data point for $z = 1.5$ has not been included for the fit, as the bottom left panel shows a clear discrepancy with lower redshifts.

using several snapshots below $z = 1.5$. The top left panel of Fig. 5.4 shows the power spectrum at these various redshifts scaled using $(D_+(z)/D_+(0))^{7.7}$, while in the top right panel we select three different modes from the shaded green region of the top left panel and find the corresponding value of γ_ω from a best fit to the corresponding vorticity spectra. We find that there is some scale dependence in γ_ω and the amplitude of the vorticity power spectrum evolves approximately with $\gamma \approx 7.7$ over the scales $0.08 \lesssim k \lesssim 0.4\, h\text{Mpc}^{-1}$, which is

higher than other simulation results in the literature (Pueblas & Scoccimarro, 2009; Thomas et al., 2015c; Jelic-Cizmek et al., 2018). However, compared to the latter two references, in the case here we are able to fit the amplitude up to $z = 1.5$ before the scaling breaks down. Besides the results from Jelic-Cizmek et al. (2018) based on the *gevolution* code, which works in a fixed-resolution grid, previous studies of vorticity use N-body simulation codes in which a softening length scale in the force calculation determines the spatial resolution. In the case of GRAMSES, the AMR capabilities allow one to achieve high spatial resolution ($\sim 2\ h^{-1}$kpc) in high-density regions.

We can extend the previous analysis to model the time evolution of the vorticity power spectrum at nonlinear scales, in terms of a new scale-independent parameter $\gamma_\omega^{\rm NL}$ in Eq. (5.3.3). From Fig. 5.2, it is clear that the power spectrum evolves more slowly in this regime compared with large scales, and so we expect $\gamma_\omega^{\rm NL}$ to be smaller than γ_ω. In the bottom left panel of Fig. 5.4, we show the scaling of the vorticity spectra by $(D_+(z)/D_+(0))^{2.6}$, where we find that such evolution works as a good approximation on scales $k \gtrsim 3.2\ h{\rm Mpc}^{-1}$. In the bottom right panel we show the best-fit value of $\gamma_\omega^{\rm NL}$ for three different k-modes. In this case, unlike in the previous fit for large sub-horizon scales, we have not considered the $z = 1.5$ spectrum for the fit as from the bottom left panel it is already clear that the scaling for such spectrum (orange solid line) would deviate from the lower redshift results. This result suggests that the amplitude of the vorticity power spectrum can be actually estimated using a scale-independent parameter in the power law of Eq. (5.3.3) on deeply nonlinear scales. However, there is an obvious scale dependence in the transition between the large- and small-scale regimes which is not captured by these parameterisations and requires further investigation.

Let us now discuss the results for the vector potential. In ΛCDM cosmology, this appears as a second-order perturbation at its lowest order, which in the case of a perfect fluid is sourced by the product of the first-order density contrast and velocity divergence (Matarrese et al., 1998b; Lu et al., 2009). However, the single-stream fluid description of CDM breaks down at late times when shell crossing occurs, and then we expect corrections to the vector potential particularly at quasi-linear and nonlinear scales.

The second-order perturbation theory prediction for the dimensionless power spectrum of $\mathbf{B}$,

$$\Delta_{\mathbf{B}}(k) \equiv \frac{k^3}{2\pi^2} P_{\mathbf{B}}(k), \tag{5.3.4}$$

is given by (Lu et al., 2009)

$$\Delta_{\mathbf{B}}(k) = \frac{9\Omega_m^2 H_0^4}{2a^2k^2} \int_0^\infty {\rm d}w \int_{|1-w|}^{1+w} {\rm d}u \Pi \left[\Delta_\delta(ku)\Delta_v(kw) - \frac{w}{u}\Delta_{\delta v}(ku)\Delta_{\delta v}(kw) \right], \tag{5.3.5}$$

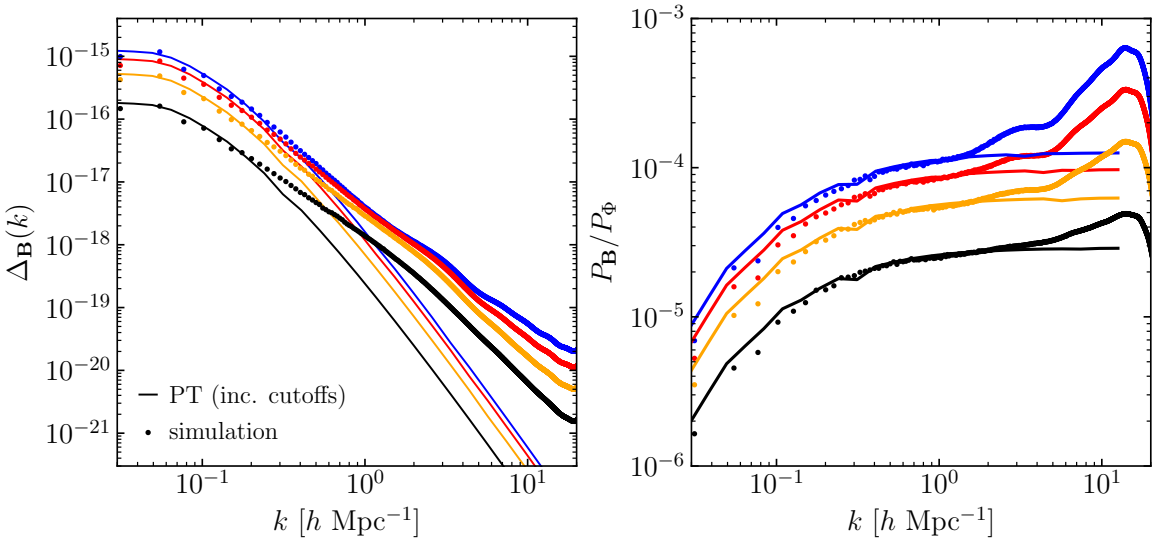

Figure 5.5: Left: The dimensionless power spectrum of the vector potential, $\Delta_{\mathbf{B}}(k) = k^3 P_{\mathbf{B}}(k)/(2\pi^2)$. The solid lines represent the corresponding second-order perturbation theory predictions (Lu et al., 2009), in which cutoffs have been introduced in the convolution calculation to accommodate the lack of power in the simulation results on large scales due to box size. Right: The ratio between the power spectrum of the vector potential and that of the scalar gravitational potential defined as the fully nonlinear perturbation to the lapse function, i.e., $\Phi \equiv \alpha - 1$. In both panels, each colour corresponds to $z = 0$ (black), $z = 0.5$ (orange), $z = 1$ (red) and $z = 1.5$ (blue).

where Δ_δ and Δ_v are the dimensionless power spectra of the density perturbation and velocity potential v, $\Delta_{\delta v}$ their cross spectrum, and $\Pi(u, w) = u^{-2}w^{-4}\left[4w^2 - (1 + w^2 - u^2)^2\right]$ is an integration kernel that depends on $w = k'/k$ and $u = \sqrt{1 + w^2 - 2w\cos\vartheta}$, with $\cos\vartheta$ defined by $\cos\vartheta = \mathbf{k}' \cdot \mathbf{k}/(kk')$. At any given scale, the convolution in Eq. (5.3.5) couples different k-modes of δ and v. Since the simulation can only access modes within a finite k-range, this is equivalent to having a large-scale ($k_{\rm min}$) and small-scale ($k_{\rm max}$) cutoffs in Eq. (5.3.5), therefore leading to a lower amplitude of $P_{\mathbf{B}}$ than the true result. For instance, Adamek et al. (2016a) found that in order to get good agreement between simulation results and perturbation-theory calculations using Eq. (5.3.5), the box should be large enough to contain the matter-radiation equality scale. In practice, to account for this effect due to missing k-modes, to compare with Eq. (5.3.5), we use the large-scale cutoff $k_{\rm min} \sim 0.8 \times 2\pi/L$, i.e. 80 percent of the fundamental mode of the box, as well as a small-scale cutoff $k_{\rm max} = \pi N_{\rm part}^{1/3}/L$, which corresponds to the Nyquist wavenumber of the coarsest grid used by the simulation. The left panel of Fig. 5.5 shows the simulation measurements of the dimensionless power spectrum of the vector potential at four different redshifts, and their corresponding perturbation-theory predictions. At $z \geq 1$ we see good agreement between the simulation and perturbation-theory results up to $k \sim 0.3$ hMpc^{-1}, while at $z = 0$ discrepancies start already at $k \sim 0.2$ hMpc^{-1}, which is

qualitatively consistent with Adamek et al. (2014); Bruni et al. (2014); see also Andrianomena et al. (2014) for a prescription of the nonlinear corrections to the perturbation-theory result using HALOFIT. At highly nonlinear scales the amplitude of the spectrum measured from the simulation can be more than two orders of magnitude higher than the perturbation-theory prediction. Note that at all four redshifts the simulation spectra flatten at the largest k-mode sampled by the simulation box, which can be interpreted as a finite-box effect.

The right panel of Fig. 5.5 shows the ratio between the power spectra of vector potential $\mathbf{B}$ and that of the scalar potential Φ measured from the simulation, the latter defined as the fully nonlinear perturbation to the lapse function in the metric (5.2.1), i.e. $\Phi \equiv \alpha - 1$. At $z = 0$, we find the ratio to be within 2×10^{-5} and 4×10^{-5} for $0.2\ h\mathrm{Mpc}^{-1} \lesssim k \lesssim 10\ h\mathrm{Mpc}^{-1}$, which is in good agreement with Bruni et al. (2014). The ratio reaches a peak of 5×10^{-5} at $k \sim 15\ h\mathrm{Mpc}^{-1}$, after which it starts to decrease. At higher redshift the evolution of $\mathbf{B}$ makes the ratio larger. Our results confirm that the ratio between both potentials reach the percent-level on nonlinear scales at $z = 0$. As pointed out by Bruni et al. (2014), though this ratio is close to the value found in Lu et al. (2009) for the ratio between scalar and vector modes in perturbation theory, here the fully nonlinear $\mathbf{B}, \Phi$ fields are used. In fact, the vector potential power spectrum from the left panel of Fig. 5.5 can be over two orders of magnitude larger than that found in the latter reference.

5.3.2 The vector potential and frame-dragging acceleration in dark matter haloes

Let us further analyse the vector potential on nonlinear scales by investigating its magnitude inside the dark matter haloes from the above general-relativistic simulation. For this we have generated halo catalogues using the phase-space Friends-of-Friends halo finder ROCKSTAR (Behroozi et al., 2013). From this catalogue we then get their centre positions, radii R_{200c} and masses M_{200c}. The latter two are defined respectively as the distance from the halo centre which encloses a mean density of 200 times the critical density of the universe as a given redshift, and the mass enclosed within such a sphere.

Unfortunately, the small-scales inaccuracies in the estimation of the velocity divergence and vorticity fields with DTFE due to caustics prevents us from studying their behaviour in haloes alongside the vector potential. We have tested that indeed, the velocity estimations are strongly affected by resolution and do not converge either using a resolution for the tessellation grid similar to the mean inter-particle distance of dark matter particles in the haloes or

otherwise. The phase-interpolation method was used in Hahn et al. (2015) to successfully estimate the vorticity in haloes in the case of warm dark matter, but still it is not possible to robustly measure this from CDM simulations either: this is related to the difficulty of resolving the perturbations up to highly nonlinear scales in the CDM case, which in models such as warm dark matter is not required as the spectrum truncates at some finite free-streaming scale. On the other hand, the scalar and vector potentials are not affected by the aforementioned issues, as they are directly calculated and stored by GRAMSES in the hierarchical AMR meshes.

Figure 5.6 shows density (left column), vector potential magnitude (middle column) and scalar gravitational potential (right column) in the vicinity of three selected dark matter haloes at $z = 0$, with masses $M_h \approx 6.5 \times 10^{15}\ h^{-1}\mathrm{M}_\odot$ (top row), $M_h \approx 3.0 \times 10^{13}\ h^{-1}\mathrm{M}_\odot$ (middle row) and $M_h \approx 3.1 \times 10^{12}\ h^{-1}\mathrm{M}_\odot$ (bottom row). In all cases, the map centre is aligned with the halo centre and the width of the shown region corresponds to four times the halo radius R_{200c}. As also shown in Fig 5.1, overall we observe some degree of correlation between the vector potential and the matter density, but clearly not at the level of the scalar potential. In particular, in the case of the most massive halo (top row) we can see that while both potentials peak towards the halo centre, unlike for the scalar potential, the global maximum of the vector potential within the shown region is actually found in the lower left part of the map, where there appears to be another, smaller, halo infalling towards the central one. Again, this qualitative difference is not surprising since the vector potential is sourced by the transverse part of the momentum density, Eq. (5.2.25), while the matter source term for the scalar potential is the density contrast itself (up to higher-order terms). As before, we can also see that both potentials are smoother than the density field owing to the elliptic-type nature of their equations (Barrera-Hinojosa & Li, 2020), in which short-wavelength modes are suppressed. In addition, in the most massive halo we can observe that the scalar potential tends to be more spherically symmetric around the centre than B, which displays large values in most part of the left and upper part of the map. Indeed, although the low-density (dark) regions in the bottom right and top left parts of the density map are of similar characteristics, and these are clearly correlated with the Φ map, these are not correlated with features in the B map at all.

For the halo shown in the middle row of Fig. 5.6, the density and potential contours have more similar shapes to each other than in the most massive halo. Nonetheless, the scalar potential again seems to decay more rapidly outside R_{200c} than the vector potential magnitude. This also seems to be the case in the halo shown in the bottom panels, although in this case the

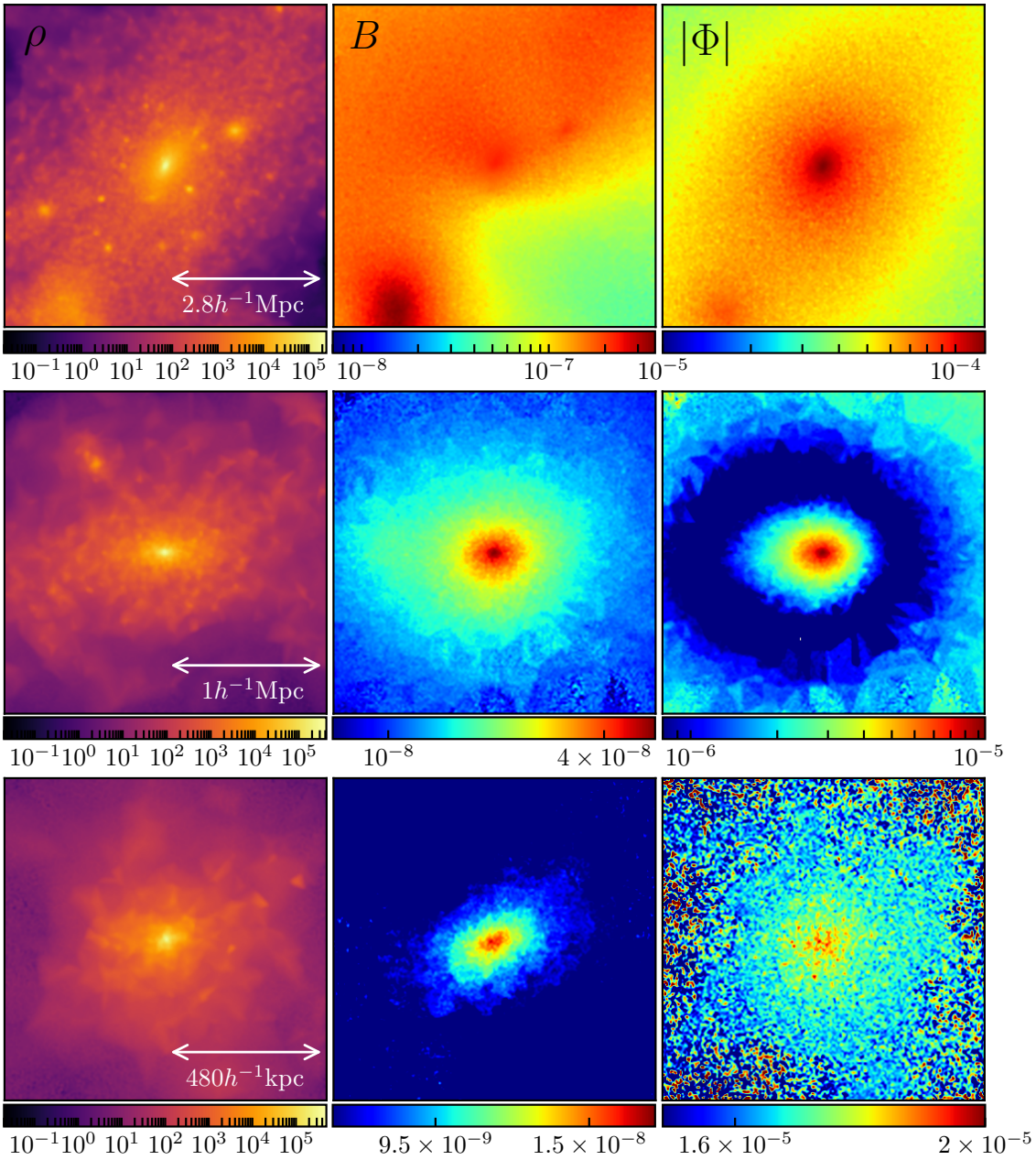

Figure 5.6: Visualisation of three selected dark matter haloes at $z = 0$, with masses $M_h = 6.5{\times}10^{14}\ h^{-1}\mathrm{M}_\odot$ (top row), $M_h = 3.0{\times}10^{13}\ h^{-1}\mathrm{M}_\odot$ (middle row) and $M_h = 3.1{\times}10^{12}\ h^{-1}\mathrm{M}_\odot$ (bottom row). In each row, each panel shows, from left to right: matter density, magnitude of the vector potential and absolute magnitude the scalar gravitational potential (since typically $\Phi \leq 0$ in the inner parts of a halo). Interpolation has been used to display smoother maps. All maps are in logarithmic scale.

potentials are smaller and shallower. Note that, for the halo in the middle panels, $|\Phi|$ is largest in the central region (red/orange/green), decays when one moves further away from the halo centre (blue), but grows again far from the halo (green); this is because this halo resides in a low-density environment, with a positive environmental contribution to the total

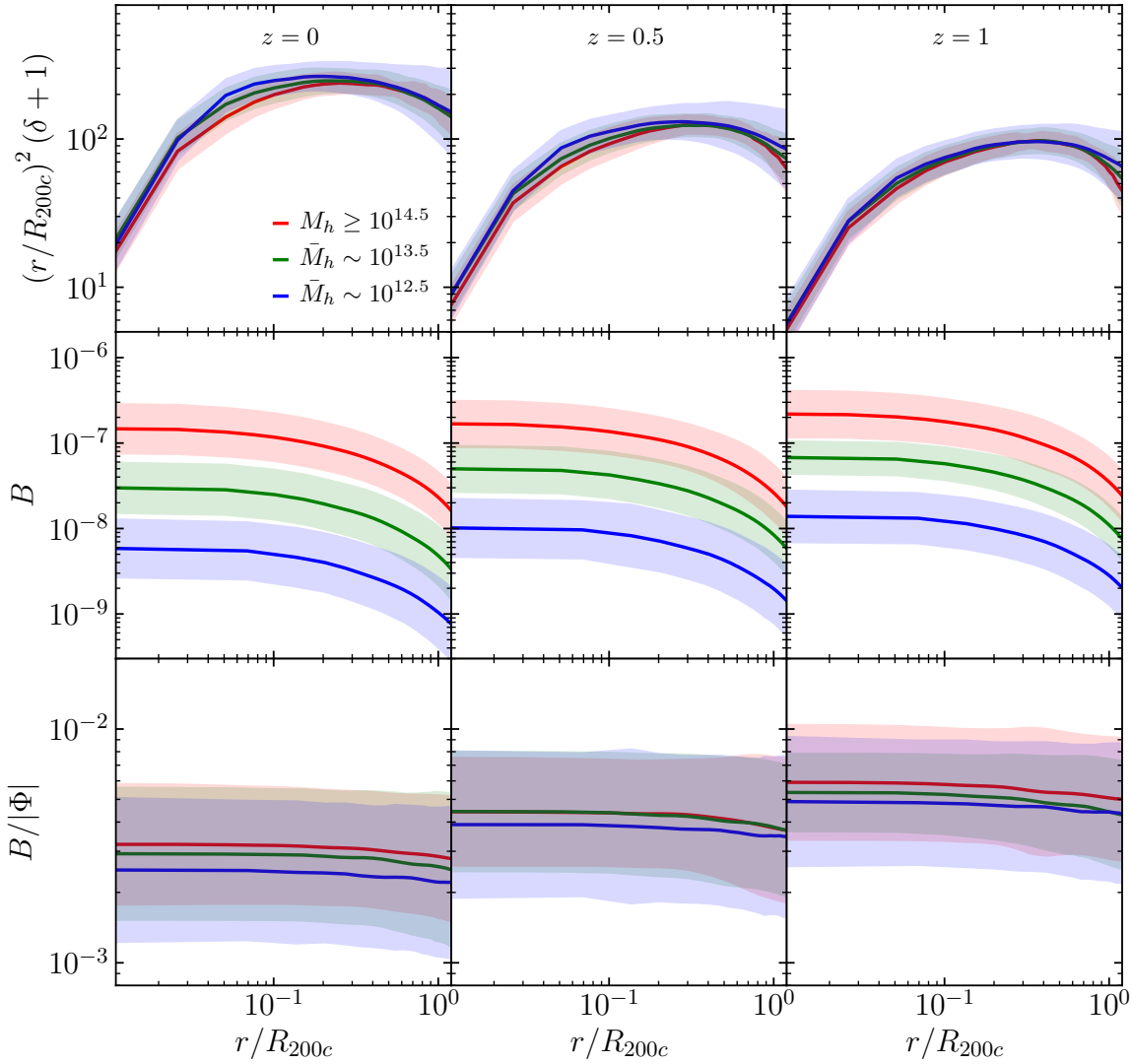

Figure 5.7: Halo profiles (spherical averages) at $z = 0$ (left column), $z = 0.5$ (middle column) and $z = 1$ (right column). Each row shows, from top to bottom, density, vector potential magnitude and its ratio against the scalar gravitational potential. In the case of the potentials, their spherical-average at R_{200c} has been subtracted from each individual halo profile as a way to remove their environmental contributions. The upper, middle and lower halo mass ranges are represented by red, green and blue, respectively, for which the solid line shows the mean calculated over all haloes in a given mass range, and the shaded regions are the 1σ regions. The values of M_h shown in the inset are in units of $h^{-1}\mathrm{M}_\odot$.

potential so that the latter crosses zero.

It is important to bear in mind that, although the halo centres are approximately located at a local maximum of $|\Phi|$, the potentials themselves are not an observable quantity: it is the gradient of the potentials that contributes as force terms in the geodesic equation (5.2.12), while the values of the potential themselves can be largely influenced by their environments. In this subsection, we are mainly interested in haloes which are isolated and therefore less

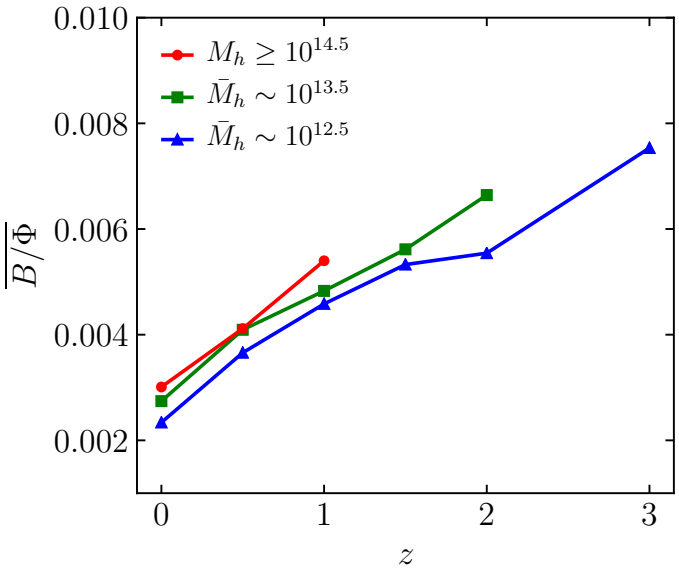

Figure 5.8: Evolution of the ratio between the vector potential and the scalar gravitational potential for the different halo mass ranges. At each redshift, the value shown corresponds to the average of the ratio for $r \leq R_{200c}$. We have only included cases where the number of haloes in a given mass range is greater than ten at a given redshift. The values of M_h shown in the inset are in units of $h^{-1}\mathrm{M}_\odot$.

affected by environments. To select such haloes, we try to split the potential at each point into two contributions: one from the halo itself and one from its environment, i.e., well beyond a distance R_{200c} from its centre. Since the potentials are not necessarily spherically symmetric, as it is evident from the top row of Fig. 5.6, as a crude way, we shall take the spherical average in a radial bin at $2R_{200c}$ and subtract this from the values at smaller radii, which allows one to get "shifted" radial halo profiles for both Φ and B that vanish at $2R_{200c}$. For Φ (B) we expect this profile to monotonically increase (decrease) to zero as r increases to $2R_{200c}$, for well-isolated relaxed haloes.

Figure 5.7 shows, from the top to the bottom row, the radial profiles of density, the vector potential magnitude and its ratio against the scalar gravitational potential. All profiles have been measured from the centres of a sample of haloes in different mass ranges, for three redshifts: $z = 0$ (left column), $z = 0.5$ (middle column) and $z = 1$ (right column). For this we have selected three subsamples of haloes with $\mathcal{O}(100)$ haloes each based on mass cuts: we define a higher mass range $M_h \geq 10^{14.5}\ h^{-1}\mathrm{M}_\odot$, an intermediate mass range with mean mass $\bar{M}_h = 10^{13.5}\ h^{-1}\mathrm{M}_\odot$, and a lower mass range with mean mass $\bar{M}_h = 10^{12.5}\ h^{-1}\mathrm{M}_\odot$. For each halo from a given mass range, we then calculate the spherical average of the density, vector potential and scalar potential up to $2R_{200c}$, and average over the full population. As mentioned in the previous paragraph, in the case of the potentials we have subtracted their

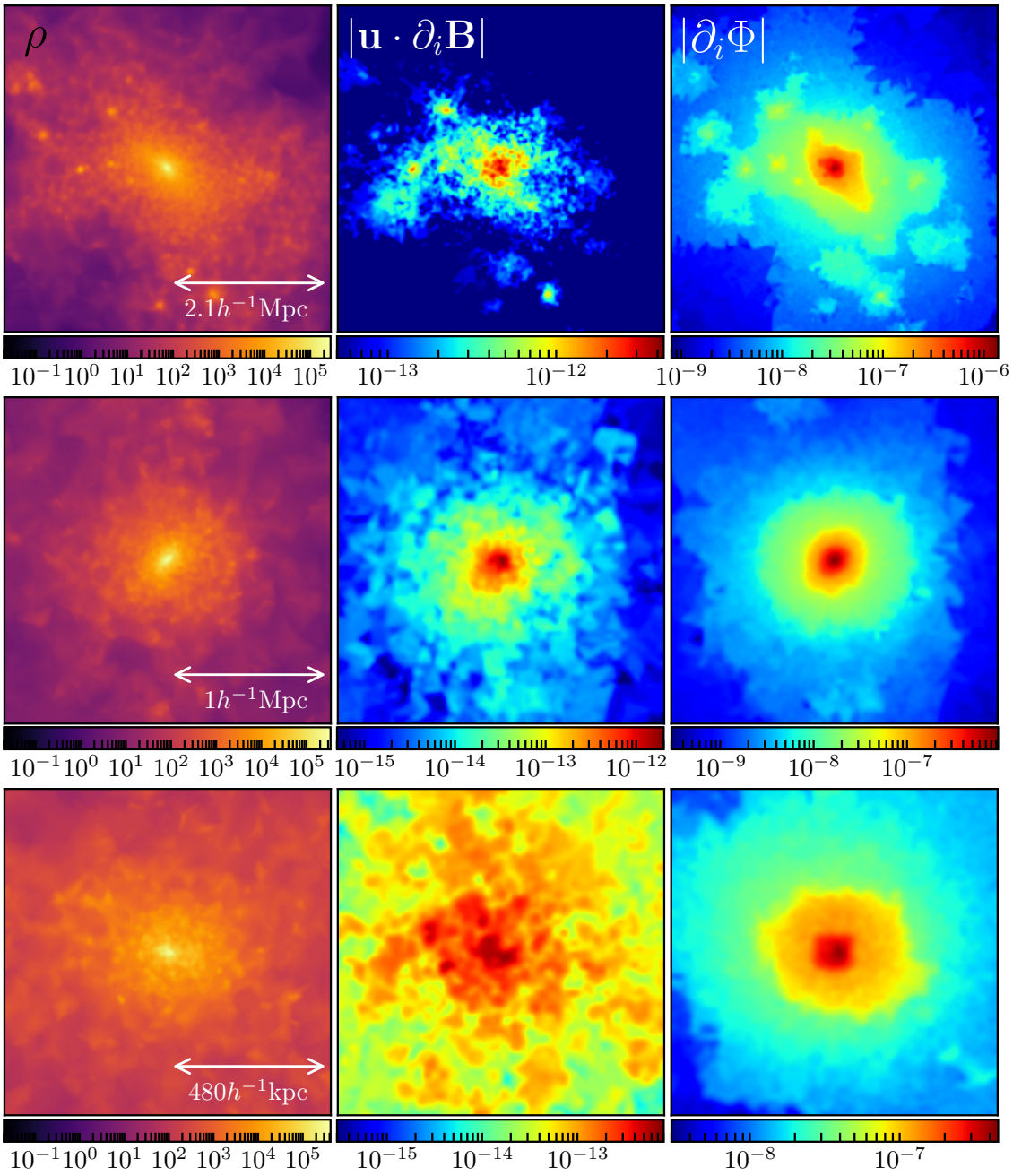

Figure 5.9: Visualisation of three selected dark matter haloes at $z = 0$, with masses $M_h = 2.7{\times}10^{14}\ h^{-1}\mathrm{M}_\odot$ (top row), $M_h = 3.3{\times}10^{13}\ h^{-1}\mathrm{M}_\odot$ (middle row) and $M_h = 3.2{\times}10^{12}\ h^{-1}\mathrm{M}_\odot$ (bottom row). In each row, each column shows, from left to right: matter density, the magnitude of the gravitomagnetic acceleration and the magnitude of the standard gravitational acceleration, the latter two in units of h cm/s^2. Interpolation has been used to display smoother maps. All maps are in logarithmic scale.

average values at $2R_{200c}$ in the profile of each individual halo. In this process, we have discarded the haloes in which the resulting spherical average of B becomes negative for some $r < R_{200c}$ after the subtraction, which typically happens in lower mass haloes due to their

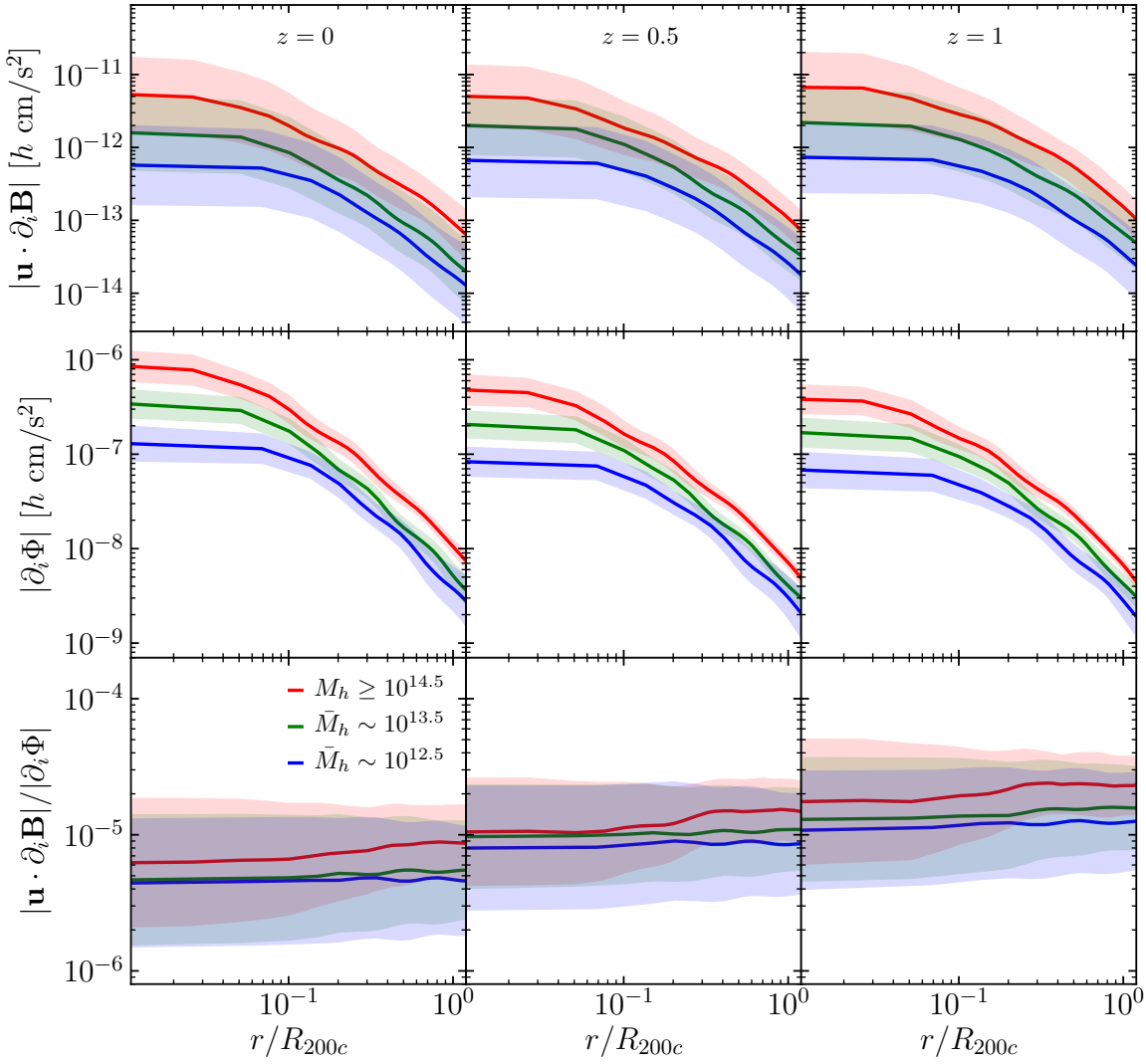

Figure 5.10: Halo profiles (spherical averages) at $z = 0$ (left column), $z = 0.5$ (middle column) and $z = 1$ (right column). In a given column, each row shows, from top to bottom, the gravitomagnetic (frame-dragging) acceleration, standard gravitational acceleration and their ratio. The upper, middle and lower halo mass ranges are represented by red, green and blue, respectively, for which the solid line shows the mean calculated over all haloes in a given mass range, and the shaded regions are the 1σ regions. The values of M_h shown in the inset are in units of $h^{-1}\mathrm{M}_\odot$.

shallow potentials. However, these haloes are the most abundant type and hence we retain a sample of size $\mathcal{O}(100)$ even at $z = 1$, while the number of haloes in the middle and higher mass bins is around ~ 50 at that same redshift.

From Fig. 5.7 we find that at the 1σ level there is a clear correlation between halo mass and the magnitude of the gravitomagnetic potential, which can differ by up to two orders of magnitude between halos with masses close to $10^{12.5}$ $h^{-1}\mathrm{M}_\odot$ and those with masses larger than $10^{14.5}$ $h^{-1}\mathrm{M}_\odot$. In all cases, the vector potential flattens toward the halo centres and it

decreases towards the outskirts. However, from the bottom row of Fig. 5.7 we find that the ratio between vector and scalar potentials is roughly constant inside haloes across all masses and redshifts considered, and the dependence of this ratio upon halo mass is quite weak as all means lie within 1σ of each other. At $z = 0$, we find that the ratio is a few times 10^{-3}, which is roughly consistent with the value inferred from the ratio of $\mathcal{O}(10^{-5})$ between the power spectra of the vector and scalar potentials at $k \gtrsim \mathcal{O}(0.1)\ h\mathrm{Mpc}^{-1}$, as shown in Fig. 5.5 (note that the subtraction of the environmental contributions in these potentials essentially removes the long-wavelength contributions to $\overline{B/\Phi}$, thereby marking this comparison with Fig. 5.5 reasonable; but as we only look at a small fraction of the total volume, inside a sub-group of haloes, we of course should not expect an exact equality). At $z = 0.5$ and $z = 1$, the picture is qualitatively the same apart from the increase in the amplitude of the vector potential.

In CDM simulations, it is well known that the density profile of haloes can be described by the universal Navarro-Frenk-White (NFW; Navarro et al., 1996) fitting formula, which has a corresponding analytical prediction for the Newtonian potential profiles of haloes. The constancy of $B/|\Phi|$ inside haloes which is found here implies that it might be straightforward to derive an analytical fitting function for the B profiles in haloes, which is closely related to the NFW function, though this will not be pursued here.

Given that Fig. 5.7 shows that the ratio between the vector and scalar potentials is roughly constant inside the halos – and we have checked that such constant ratio holds even above $z = 1$ – we can characterise this ratio by a single number at each halo mass and redshift. As an extension of the bottom row of Fig. 5.7, Fig. 5.8 shows the mean value of such ratio calculated within $r < R_{200c}$ at different redshifts. Since the number of haloes in a given mass bin decreases towards higher redshifts, here we only consider cases in which the number of haloes in a given mass range is greater than ten at a given redshift. We find that for all mass bins $\overline{B/\Phi}$ increases almost linearly with redshift. At redshift $z = 2$ the rate of change of this ratio with respect to redshift slows down slightly for the lowest mass range (blue line), after which it picks up again: this could be due to a lack of simulation resolution at high z. Observationally, the ratio between vector and scalar potentials is particularly relevant for weak lensing, as post-Newtonian calculations show that the relative correction to the Newtonian convergence field κ is proportional to B/Φ (Sereno, 2002, 2003; Bruni et al., 2014). Therefore, Fig. 5.8 suggests that, in the case of dark matter haloes, the lensing convergence correction due to the gravitomagnetic potential is between the $\mathcal{O}(10^{-3})$ and $\mathcal{O}(10^{-2})$ level, in agreement with previous studies (Sereno, 2007; Cuesta-Lazaro et al., 2018;

Tang et al., 2021). Moreover, this only depends weakly on the halo mass and could be more easily detected on high-mass haloes at high redshifts. However, we note that at higher orders in the post-Newtonian expansion, new contributions from the time derivative of B appear (Bruni et al., 2014; Thomas et al., 2015b) as well, which requires further inspection.

Besides investigating the potentials, we can also look at the force that each of these exert on the particles according to Eq. (5.2.12), which shows that the total force is mainly composed by two contributions; the standard gravitational force arising from the gradient of the scalar potential (first term on the r.h.s.), and the gravitomagnetic force (contained in the second term on the r.h.s.) which is responsible for the frame-dragging effect. The latter is naturally not taken into account in Newtonian gravity. The third term in the r.h.s of Eq. (5.2.12) is subdominant and so we shall not explore it here.

Figure 5.9 is a visualisation of the magnitude of the gravitomagnetic acceleration (middle column) and that of the standard gravitational acceleration (right column) in units of h cm/s^2, in the vicinity of three different dark matter haloes. These haloes have similar masses to those shown in Fig. 5.6. We find that the forces are correlated with the density field up to some degree, particularly in the haloes in the middle and bottom rows, although the gravitomagnetic force seems to be less smooth than the Newtonian one. For the halo in the top row, there is a clearer difference between the forces compared to the other two cases. The peaks of the gravitomagnetic acceleration seem to occur at the density peaks but the opposite is not true, and there is no clear correspondence between their amplitudes. Interestingly, in this halo the values of gravitomagnetic force around a few times 10^{-13} h cm/s^2 (green region) extend around the centre and towards the left part of the map, where the density field has already decreased by various orders of magnitude. This kind of asymmetry between both kinds of maps might be due to the actual dynamical state of the particles in a given region. Even if the density is low, if the particles' velocity happens to be aligned with the gradient of the vector potential components they will contribute significantly to $|\mathbf{u} \cdot \partial_i \mathbf{B}|$.

As before, we can calculate the spherical averages of the forces, which allows us to get radial profiles (although no subtraction from radial bins beyond $2R_{200c}$ is required this time). Figure 5.10 shows a comparison of the gravitomagnetic (frame-dragging) acceleration and the standard gravitational one in dark matter haloes in an analogous way to the scalar and vector potential profiles shown in Fig. 5.7. We find that the magnitude of the gravitomagnetic force is larger towards the inner parts of the halo, and the dependence on the halo mass is weaker than in the case of the scalar gravitational potential. As we discussed before, this can also

be explained by the fact that the gravitomagnetic force not only depends on density but on the actual dynamical state of particles. Similarly to the behaviour of $B/|\Phi|$, from Fig. 5.10 we find that the ratio of the two corresponding forces also remains fairly constant inside the haloes, although in the most massive haloes it tends to increase toward the outskirts. A weak dependence on halo mass is found at all redshifts. In Adamek et al. (2016a) the maximum gravitomagnetic acceleration measured from the simulation box at $z = 0$ is found to be roughly $7 \times 10^{-12}\ h$ cm/s^2 for the highest resolution used (125 h^{-1}kpc), while the value measured from lower resolution runs decreases monotonically. From Fig. 5.10 we find that this is comparable with our results for haloes in the upper mass range at the 1σ level. However, we note that for the most massive halo in our simulation, we find the maximum value of the gravitomagnetic acceleration to be $7 \times 10^{-11}\ h$ cm/s^2, i.e. roughly one order of magnitude higher. This difference could be explained by the AMR feature of our simulation, in which the most refined regions are resolved with a resolution of 2 h^{-1}kpc. In addition, GRAMSES treats the vector potential non-perturbatively, although the difference due to higher-order corrections is likely to be subdominant with respect to the aforementioned resolution dependence.

5.4 Summary

We have investigated the vector modes of the matter fields as well as those of the ΛCDM space-time metric, from large sub-horizon scales to deeply nonlinear scales using a high-resolution run of the general-relativistic N-body GRAMSES code introduced in Chapter 2. On the one hand, vorticity vanishes at the non-perturbative level in a perfect fluid description and yet it is generated dynamically due to the collisionless nature of dark matter. On the other hand, the metric vector potential – responsible for frame-dragging – appears beyond linear order in perturbation theory and is not solved for in Newtonian simulations. Therefore, the physics behind the vector modes is highly non-trivial and numerical simulations play an important role in their study. Although the relativistic nature of the code is not particularly exploited from the point of view of vorticity, the vector potential is a prime quantity as this is not part of Newtonian gravity and therefore not implemented in Newtonian simulations.

To this end, we have run a high-resolution N-body simulation using GRAMSES, that employs $N_{\rm part} = 1024^3$ particles in a box of comoving size $L_{\rm box} = 256\ h^{-1}$Mpc. In GRAMSES, the GR metric potentials – in the fully constrained formalism and conformally flat approximation – are solved on meshes in configuration space. The AMR capabilities of GRAMSES allows it

to start off with a regular grid with 1024^3 cells, and hierarchically refine it in high-density regions to reach a spatial resolution of 2 h^{-1}kpc in the most refined places, namely dark matter haloes. This enables a quantitative analysis of the behaviour of vector modes in such regions.

The key findings presented in this Chapter are summarised as follows:

1. On scales $0.06 \lesssim k \lesssim 0.3$ hMpc^{-1}, the vorticity power spectrum can be characterised by the power law in Eq. (5.3.2) with an index $n_\omega \approx 2.7$, a value that is overall consistent with recent simulation results of Hahn et al. (2015); Jelic-Cizmek et al. (2018). On nonlinear scales ($2.3 \lesssim k \lesssim 20$ hMpc^{-1}), the power spectrum can again be described by a power-law function, but the index changes to $n_\omega^{\rm NL} \approx -1.4$, close to the asymptotic value of -1.5 suggested by Hahn et al. (2015); cf. Fig. 5.3.

2. On scales $0.1 \lesssim k \lesssim 0.4$ hMpc^{-1} the amplitude of the vorticity power spectrum seems to evolve as $\sim [D_+(z)/D_+(0)]^{7.7}$ at $z \leq 1.5$, which is higher than previous values found in the literature (Thomas et al., 2015c; Jelic-Cizmek et al., 2018). Nonetheless, these references also found larger values than the scaling with the seventh power originally proposed in Pueblas & Scoccimarro (2009). On scales $k \gtrsim 3.5$ hMpc^{-1}, the evolution of the amplitude of the power spectrum can be similarly neatly described as $\sim [D_+(z)/D_+(0)]^{2.6}$ up to $z = 1$; cf. Fig. 5.4.

3. The vector potential power spectrum remains below 4×10^{-5} relative to the scalar gravitational potential down to $k = 20$ hMpc^{-1}; cf. Fig. 5.5.

4. Inside dark matter haloes, the magnitude of the vector potential peaks towards the centres at $\sim 10^{-7}$ for haloes more massive than $10^{14.5}$ h^{-1}M$_\odot$, which can reduce by two orders of magnitude in haloes of masses around $10^{12.5}$ h^{-1}M$_\odot$. Its ratio against the scalar gravitational potential remains typically a few times 10^{-3} inside the haloes, regardless of their mass (cf. Fig. 5.7). The ratio $B/|\Phi|$ remains nearly flat within the halo radius R_{200c}, for the halo redshift ($z < 3$) and mass ($10^{12.5} \sim 10^{15}$ h^{-1}M$_\odot$) ranges checked, and this constant increases roughly linearly with z; cf. Fig. 5.8.

5. The magnitude of the gravitomagnetic acceleration also peaks at the halo centres where it can reach a few times 10^{-11} h cm/s^2 in haloes above $\sim 10^{14.5}$ h^{-1}M$_\odot$. Its ratio against the standard gravitational acceleration remains around $\sim 10^{-5}$ on average, regardless of the halo mass and distance from the halo centre; cf. Fig. 5.10. This suggests that the effect of the gravitomagnetic force on cosmic structure formation is, even for the most

massive structures, negligible – however, note that we have not studied the behaviour in low-density regions, i.e., voids.

While we have presented a first study of the gravitomagnetic potential in dark matter haloes with general-relativistic simulations, there are several possible extensions in this direction. The analysis of the gravitomagnetic potential and forces done here could be extended to galaxies, e.g., by constructing a catalogue using certain semi-analytic models. It is then possible to calculate the gravitomagnetic accelerations of galaxies based on their coordinates and velocities. However, as we have seen above, this acceleration is much weaker than the standard gravitational acceleration, and the impact of baryons on small scales still remains to be assessed. The implementation of (magneto)hydrodynamics in the default RAMSES code could be used in conjunction with the general-relativistic implementation of GRAMSES as a first approximation to address this question, although we generally expect that uncertainties in baryonic physics should surpass GR effects.

A perhaps more interesting possibility is to self-consistently implement massive neutrinos and radiation in this relativistic code. In Chapter 3 we have introduced a method to generate initial conditions for GRAMSES simulations that does not require back-scaling. It is therefore natural to evolve these matter components which are neglected in traditional simulations (e.g., Adamek et al., 2017b). On the same vein, a Newtonian (quasi-static) implementation of modified gravity models on GRAMSES would allow one to study the gravitomagnetic potential in such types of theory. In particular, the modified gravity code ECOSMOG (Li et al., 2012; Li et al., 2013) is based on RAMSES and can be easily made compatible with GRAMSES for this purpose.

In this Chapter, we have primarily focused on the general-relativistic physical quantities that could impact cosmic structure formation, and this can ultimately only be observed by detecting photons (McDonald, 2009; Croft, 2013; Bonvin et al., 2014; Alam et al., 2017b). Therefore, besides the gravitomagnetic force acting on massive particles, it is also important to study how vector modes, as well as other GR effects, could influence the photon trajectories on nonlinear scales, and what is the consequent impact on observables, e.g. lensing (Thomas et al., 2015b; Saga et al., 2015; Gressel et al., 2019). This requires the implementation of general-relativistic ray tracing algorithms (e.g. Barreira et al., 2016; Breton et al., 2019; Lepori et al., 2020; Reverdy, 2014) and is left as a future project.

Chapter 6

Detecting the cosmological gravitomagnetic effect via weak lensing-kSZ cross-correlations

6.1 Introduction

In General Relativity (GR), the propagation of light can be distorted not only by the Newtonian (scalar) potential, but also by the vector (spin-1) and tensor (spin-2) degrees of freedom of the gravitational field. With the advent of various upcoming large-scale structure surveys such as EUCLID (Laureijs et al., 2011), LSST (Weinberg et al., 2013) and SKA (Dewdney et al., 2013), a renewed interest to understand in detail the impact of the vector potential on observables has emerged in recent years (e.g., Schäfer & Bartelmann, 2006; Andrianomena et al., 2014; Saga et al., 2015; Thomas et al., 2015a; Cuesta-Lazaro et al., 2018; Tang et al., 2021). There has also been growing interest in the gravitomagnetic effects on smaller astronomical systems. For instance, it has been argued that the observed flat rotation curves of galaxies potentially admits an alternative explanation — in the absence of dark matter – by a GR velocity profile sourced by frame-dragging (Crosta et al., 2020), although a realistic model for this is still required. Furthermore, a mission specially designed to measure the gravitomagnetic field of the Milky Way, and of its dark matter halo, has been recently proposed in Tartaglia et al. (2021).

Although vector modes are not introduced by the standard inflationary model (e.g., Bassett et al., 2006), the late-time gravitomagnetic potential of the Λ-cold-dark-matter (ΛCDM) cosmology is generated dynamically: before shell crossing, this is sourced by the coupling of

scalar perturbations of the matter fluid — the overdensity and velocity divergence fields — and hence this is typically referred to as the scalar-induced cosmological vector mode (Matarrese et al., 1994; Lu et al., 2008, 2009). More generally, the gravitomagnetic field is sourced and sustained over time by the rotational (divergence-free) component of the momentum flux of matter, and the latter also receives contributions from the vorticity field generated due to, e.g., shell crossing of CDM. As shown in Lu et al. (2008, 2009), second-order perturbation theory predicts that, on scales above the matter-radiation equality scale (i.e., the horizon scale at the time of matter-radiation equality), the power spectrum of the gravitomagnetic field is strongly suppressed with respect to the Newtonian potential, but on sub-equality scales the relative amplitude can reach about 1%, which is also supported by N-body simulations (Thomas et al., 2015b; Adamek et al., 2016a; Barrera-Hinojosa et al., 2021).

Even though the effect of the gravitomagnetic force in cosmological structure formation is small due to the low velocities of non-relativistic matter (Adamek et al., 2016a; Barrera-Hinojosa et al., 2021) — see also Chapter 5, which is at most of order $\mathcal{O}(1\%)$ of the speed of light, it is not *a priori* obvious that the impact on observations is negligible, since this requires to quantify the effect on the propagation of photons. However, so far all investigations have found that the gravitomagnetic effects in light propagation are subdominant with respect to their Newtonian (scalar) counterparts. For instance, it has been shown that the corrections to the observed galaxy number counts induced by the vector modes are too small to be detected by the upcoming surveys (Durrer & Tansella, 2016). Similarly, the second-order gravitomagnetic corrections to the lensing convergence field have also been found to have an overall negligible impact in most cases (Schäfer & Bartelmann, 2006; Thomas et al., 2015b; Cuesta-Lazaro et al., 2018), although these can still dominate over other relativistic effects in surveys with SKA-like source distributions (Andrianomena et al., 2014).

In the context of lensing, B-modes represent a characteristic signal imprinted by vector perturbations that, in principle, might be used to disentangle these from the effects of scalar perturbations (although B-modes are also induced by tensor perturbations, i.e., gravitational waves, their contribution is subdominant). However, as shown by Saga et al. (2015), a detection of the B-modes is not within the reach of upcoming galaxy surveys, although it has been argued that the large volume covered by future 21cm observations could improve the signal-to-noise ratio. In the same spirit, Tang et al. (2021) has recently proposed an estimator to measure the dipole feature in the lensing convergence field that is induced by the stacked rotation of clusters, although they predict that this signal is unlikely to be detected by LSST.

As originally suggested by Schäfer & Bartelmann (2006), a potentially promising and yet unexplored way to extract the gravitomagnetic effects from lensing observations is via the cross correlation with a second observable, in particular with the kinetic Sunyaev-Zel'dovich (kSZ) effect (Sunyaev & Zeldovich, 1980; Ostriker & Vishniac, 1986). The kSZ effect is a secondary CMB anisotropy induced by the scattering of CMB photons off fast-moving free electrons in the intergalactic medium. This particular signal is chosen because, just like the gravitomagnetic field, it is sourced by the momentum field of matter. More precisely, on small angular scales — where the kSZ effect dominates over the primary CMB — only rotational modes of the momentum field of matter will survive during the line-of-sight integration and contribute to this effect (e.g., Zhang et al., 2004). Hence, the cross correlation between the kSZ effect and the gravitomagnetic convergence field is roughly proportional to the auto-correlation of either of the two effects. Furthermore, the kSZ effect is uncorrelated with the Newtonian (scalar) weak-lensing signal at the two-point level due to the statistical isotropy of the velocity field (Dore et al., 2004), making it an ideal probe to extract the gravitomagnetic (vector) contribution of the convergence field.

In this Chapter we will explore, for the first time, the detectability of the cosmological gravitomagnetic field via cross correlation of the weak-lensing convergence field — that contains both Newtonian and gravitomagnetic contributions — and the kSZ effect. Because in practice it is not always easy to separate the kSZ effect from the primary CMB, we shall consider the cross correlation between the total lensing convergence and a total CMB temperature map, the latter including the kSZ effect integrated over lines of sight. We will also discuss the impact of other secondary CMB anisotropies on this cross correlation.

The outline of the remainder of this Chapter is as follows. In Section 6.2 we discuss the key theoretical aspects of the gravitomagnetic contribution to the weak-lensing convergence field, its angular power spectrum and the convergence-kSZ cross angular power spectrum. In Section 6.3 we present the details and specifications of the N-body simulations used to model the observables. In Section 6.4.1 we describe the methodology that we use to generate the sky maps for the above observables, while we devote Section 6.4.2 to study in detail the unphysical (i.e., beyond the effect of cosmic variance) non-zero cross-correlation of kSZ and the scalar part of the convergence field found from the maps. Then, in Section 6.5 we present the main results of this study, in which we quantify the signal-to-noise ratio of the gravitomagnetic signal based on a high-resolution simulation. In Section 6.5.2 we discuss the detectability of this signal with current and upcoming weak lensing surveys, such as EUCLID (Laureijs et al., 2011) and Vera C. Rubin Observatory (LSST; Weinberg et al., 2013), and

CMB experiments including the Simons Observatory (Ade et al., 2019) and CMB Stage IV (CMB-S4; Abazajian et al., 2016). Finally, in Section 6.6 we summarise the main results from this investigation.

6.2 Theory

In this Chapter, we consider a perturbed Friedmann-Lemaître-Robertson-Walker (FLRW) metric in the weak-field regime. In the Poisson (or longitudinal) gauge including scalar and vector modes, this is given by (Ma & Bertschinger, 1995; Matarrese et al., 1998b)

$$\mathrm{d}s^2 = -\left(1+2\frac{\Phi}{c^2}\right)c^2\mathrm{d}t^2 + a^2\left(1-2\frac{\Psi}{c^2}\right)\mathrm{d}\mathbf{x}^2 + 2a^2\frac{\mathbf{B}}{c^3}\cdot\mathrm{d}\mathbf{x}c\mathrm{d}t\,. \tag{6.2.1}$$

Here, t is cosmic time, $\mathbf{x}$ are comoving spatial Cartesian coordinates, a is the scale factor, c is the speed of light, Φ and Ψ are the scalar degrees of freedom corresponding to the Bardeen potentials, and $\mathbf{B} \equiv (B^x, B^y, B^z)$ is the gauge-invariant vector gravitomagnetic (frame-dragging) potential (Bardeen, 1980), which satisfies the divergence-free (transverse) condition $\nabla\cdot\mathbf{B} = 0$, where ∇ denotes the derivative with respect to the comoving coordinates. Throughout this work we will neglect the gravitational slip and set $\Phi = \Psi$, which is identified as the Newtonian gravitational potential. On the other hand, in the weak-field approximation the matter fields such as density, velocity and momentum are treated as non-perturbative fields.

The metric Eq. (6.2.1) can also be obtained in a post-Newtonian (or more precisely, a Post-Friedmann) expansion up to leading order in $1/c^3$ (Schneider et al., 1992; Sereno, 2002), which is valid at all scales (Bruni et al., 2014; Milillo et al., 2015). In this approach, the dynamics of CDM is not modified by the presence of $\mathbf{B}$ at this order in the expansion, but observables are still affected through its effect on the photon geodesics, which is one of the main approximations assumed throughout this investigation.

The Newtonian potential satisfies the Poisson equation

$$\nabla^2\Phi = \frac{3H_0^2\Omega_m}{2a}\delta\,, \tag{6.2.2}$$

where δ is the gauge-invariant density contrast, H_0 the Hubble constant, and Ω_m the present-day matter density parameter. The gravitomagnetic potential satisfies an analogue elliptic-type equation, in which the source term is the rotational component of the momentum density

field. This is given by (Bruni et al., 2014)

$$\frac{1}{4}\nabla\times\nabla^2\mathbf{B}=\frac{3H_0^2\Omega_m}{2a}\nabla\times\left[(1+\delta)\frac{\mathbf{v}}{c}\right], \tag{6.2.3}$$

where $\mathbf{q}=(1+\delta)\mathbf{v}$ is the momentum field of matter, $\mathbf{v}=\mathrm{d}\mathbf{x}/\mathrm{d}t$ being the peculiar velocity. In Eq. (6.2.3), the curl operator has been applied on both sides to remove the scalar component of the momentum field, which does not contribute to $\mathbf{B}$. Eq. (6.2.3) is derived from the $0i$-component of the Einstein equations, keeping the leading-order terms in the post-Friedmann expansion, which are proportional to $1/c^3$. At higher orders in this expansion, corrections to this equation appear at $\mathcal{O}(1/c^5)$ (Milillo et al., 2015). In contrast, the GR counterpart used by the GRAMSES code discussed in the previous chapters, e.g. Eq. (5.2.21)[1], is formally valid at all orders in $1/c$, and thus it includes as sources not only the relativistic momentum field of matter — which includes the Lorentz factor and volume deformations — but also a term proportional to the extrinsic curvature which is not present in Eq. (6.2.3) (at least up to this order in the expansion).

Note that Eq. (6.2.3) here has different a-factors compared to Eq. (3) of Bruni et al. (2014) due to the different conventions on the definition of $\mathbf{B}$, which can have either an upper or lower index, and of the peculiar velocity. The advantage of Eq. (6.2.3) is that, up to a factor of $1/4$, it has the identical form as Eq. (6.2.2) apart from the matter source term, thus putting the two potentials on equal footing. Furthermore, this also offers a clear and compact way to write down the total lensing convergence field in the presence of gravitomagnetic effects, as discussed in the next subsection.

6.2.1 The gravitomagnetic contributions to lensing convergence

In the post-Newtonian regime, the total deflection angle of photons caused by a slowly moving perfect fluid can be obtained by replacing the standard lensing potential by an effective lensing potential given as (e.g., Schneider et al., 1992; Sereno, 2003; Schäfer & Bartelmann, 2006)

$$\Phi\to\Phi+\frac{1}{2c}\mathbf{B}\cdot\hat{\mathbf{n}}\,, \tag{6.2.4}$$

[1]Notice, however, that in Eq. (5.2.21), the shift vector has also a scalar mode due to the constant-mean-curvature slicing used in GRAMSES, which is not the case of the Poisson gauge or post-Friedmann expansion, where $\mathbf{B}$ only contains vector modes.

where $\hat{\mathbf{n}}$ is the unit vector of the line-of-sight (LOS) direction. Therefore, the total lensing convergence field can be written as

$$\kappa_{\rm GR}(\hat{\mathbf{n}}) = \kappa_\Phi + \kappa_{\mathbf{B}}\,, \tag{6.2.5}$$

where the standard (Newtonian) and gravitomagnetic contributions to the convergence field are respectively given by

$$\kappa_\Phi(\hat{\mathbf{n}}) = \int \mathrm{d}\chi K_{\kappa_\Phi}(\chi)\delta(\chi\hat{\mathbf{n}}, z)\,, \tag{6.2.6}$$

$$\kappa_{\mathbf{B}}(\hat{\mathbf{n}}) = \int \mathrm{d}\chi K_{\kappa_{\mathbf{B}}}(\chi)[\mathbf{q}_\perp \cdot \hat{\mathbf{n}}](\chi\hat{\mathbf{n}}, z)\,. \tag{6.2.7}$$

Here, χ is the comoving distance, $\mathbf{q}_\perp$ is the rotational (divergence-free) component of the momentum field, and K_{κ_Φ} is the standard weak-lensing kernel

$$K_{\kappa_\Phi}(\chi) = \frac{3}{2}\frac{H_0^2\Omega_m}{ac^2}\int_0^\chi \mathrm{d}\chi' \frac{\chi(\chi'-\chi)}{\chi'}\frac{\mathrm{d}\chi'}{\mathrm{d}z}p\left(z(\chi')\right)\,, \tag{6.2.8}$$

while the gravitomagnetic lensing kernel satisfies (Schäfer & Bartelmann, 2006)

$$K_{\kappa_{\mathbf{B}}} = \frac{2}{c}K_{\kappa_\Phi}\,. \tag{6.2.9}$$

In these, $p_z(z)$ is the normalised source redshift distribution, $\int \mathrm{d}z p_z(z) = 1$, and the LOS integration is carried out up to the farthest source. For definiteness, in this work we use a single source galaxy redshift z_s (corresponding to a comoving distance χ_s) with the source distribution given by

$$p_z(\chi(z)) = \delta^{\rm D}(\chi - \chi_s)\,, \tag{6.2.10}$$

in which $\delta^{\rm D}$ is the Dirac δ function. In reality, $p_z(\chi)$ is a continuous distribution that depends on the specific galaxy survey used. Notice that in this post-Friedmann approximation, the gravitomagnetic convergence field, Eq. (6.2.7), is written in terms of the rotational modes of the momentum field using (6.2.3), just as it is customary to express κ_Φ in terms of the density field via (6.2.2).

Under the Limber approximation, the angular power spectrum of the standard weak-lensing convergence, Eq. (6.2.6), is given by

$$C_\ell^{\kappa_\Phi} = \frac{9}{4}\frac{H_0^4\Omega_m^2}{c^4}\int_0^{\chi_s}\mathrm{d}\chi\frac{(\chi_s-\chi)^2}{\chi_s^2 a(\chi)^2}P_\delta\left(k=\frac{\ell}{\chi}, z(\chi)\right)\,, \tag{6.2.11}$$

where P_δ is the 3D matter power spectrum. On the other hand, the angular power spectrum of the gravitomagnetic contribution, Eq. (6.2.7), has a very similar mathematical structure to

the kSZ effect — since both effects are sourced by the rotational component of the momentum field along the LOS — and hence we discuss these two in the next subsection.

6.2.2 The convergence-kSZ cross angular power spectrum

The gravitomagnetic contribution to the lensing convergence power spectrum is about five orders of magnitude smaller than the standard Newtonian contribution (Andrianomena et al., 2014), and even with future Stage-IV galaxy surveys such as EUCLID the former is still expected to be dominated over by cosmic variance (e.g., Cuesta-Lazaro et al., 2018). As a result, to detect the gravitomagnetic lensing effect in real observations, the lensing probe has to be cross correlated with some other observable.

As suggested by Schäfer & Bartelmann (2006) previously, the secondary CMB anisotropy caused by the kSZ effect (see Appendix D for a brief summary) is a suitable observable to cross correlate with the gravitomagnetic lensing effect, since the former is also sourced by the integrated momentum field of matter along the LOS. Moreover, the kSZ effect has negligible correlation with the standard Newtonian contribution to the total lensing convergence field at the two-point level, due to the statistical isotropy of the velocity field (Scannapieco, 2000; Castro, 2003; Dore et al., 2004), which in combination with the previous point allows kSZ to single out the gravitomagnetic contribution in the lensing signal. In other words, denoting as $b(\hat{\mathbf{n}}) = -\Delta T(\hat{\mathbf{n}})/\bar{T}$ the temperature change of CMB photons along the LOS direction $\hat{\mathbf{n}}$ due to the kSZ effect, we have that the angular cross correlation between kSZ and the total convergence field (which is what observations give) reduces to

$$\langle b\kappa_{\rm GR}\rangle = \langle b\kappa_{\mathbf{B}}\rangle\,, \tag{6.2.12}$$

where the angular brackets denote ensemble average.

The vanishing of the cross spectrum between κ_Φ and the kSZ effect can also be understood as follows: while the overdensity field can be correlated with a cluster that moves toward us, in an infinite universe there are equal chances for this to be correlated with one moving away from us, and thus the average over all possible lines of sight vanishes. At a more general level, the isotropy of the velocity field implies that, along the LOS, odd statistics of this field are subdominant with respect to even statistics (Andrei S. Monin, & A. M. Yaglom, 1971; Jaffe & Kamionkowski, 1998; Scannapieco, 2000; Castro, 2003). This feature makes kSZ an interesting candidate to potentially extract the gravitomagnetic effect in weak-lensing, and Eq. (6.2.12) is the signal to measure the gravitomagnetic field that we will study in this

Chapter. In particular, in this study we will restrict our attention to the post-reionisation contribution to the kSZ signal, hence we assume that the electron density field closely follows the density field of baryons. Moreover, for simplicity we assume a fully ionised medium, i.e., we set $\chi_{\rm e} = 1$ in Eq. (D.0.3).

The angular power spectra of the two sky observables appearing in the right hand side of Eq. (6.2.12), as well as their cross spectrum, can be derived as follows. Neglecting the contribution from the longitudinal (curl-free) component of the momentum field to the kSZ effect, from Eq. (6.2.7) and Eq. (D.0.5) we can write the two effects as a weighted LOS integral for a general sky observable X which is sourced by the rotational component of the momentum field of matter along the LOS, i.e.,

$$X(\hat{\mathbf{n}}) = \int \mathrm{d}\chi K_X(\chi)[\mathbf{q}_\perp \cdot \hat{\mathbf{n}}]\,(\chi\hat{\mathbf{n}}, z)\ , \tag{6.2.13}$$

where the kernels for the gravitomagnetic convergence field and the kSZ effect are respectively given by Eq. (6.2.9), and

$$K_b(\chi) = \frac{\sigma_{\rm T}\bar{n}_{\rm e,0}}{c} a(\chi)^{-2} e^{-\tau}\ . \tag{6.2.14}$$

As usual, the cross angular power spectrum between two observables, X and Y, where $X, Y = b, \kappa_{\mathbf{B}}$ (X can be the same as Y) is defined as

$$C_\ell^{XY}\delta_{\ell\ell'}\delta_{mm'} = \left\langle a_{\ell m}^X a_{\ell' m'}^{Y*} \right\rangle\ . \tag{6.2.15}$$

After some standard derivations in the context of Limber integrals (see Appendix D), it can be shown that the cross angular spectrum of these two momentum-sourced observables is given by

$$C_\ell^{XY} = \frac{1}{2}\int \mathrm{d}\chi \chi^{-2} K_X(\chi) K_Y(\chi) P_{q_\perp}\left(k = \frac{\ell}{\chi}, z(\chi)\right)\ , \tag{6.2.16}$$

where $P_{q_\perp}$ is the 3D power spectrum of the rotational component of the momentum field of matter. In this case, for the power spectrum of a rotational vector field $\mathbf{V}$, such as $\mathbf{B}$ or $\mathbf{q}_\perp$, we use the definition

$$\left\langle \mathbf{V}^i(\mathbf{k})\mathbf{V}^{*j}(\mathbf{k}')\right\rangle = \delta^{\rm D}(\mathbf{k}-\mathbf{k}')(2\pi)^3\frac{1}{2}\left(\delta^{ij} - \frac{k^i k^j}{k^2}\right) P_{\mathbf{V}}(k)\,, \tag{6.2.17}$$

where δ^{ij} is the Kronecker delta. Eq. (6.2.16) is the expression for both the angular auto power spectrum of $\kappa_{\mathbf{B}}$ and kSZ, and the cross angular spectrum between them. We remark that in the above result, the contribution from the longitudinal component of the momentum field along the LOS to the kSZ effect has been neglected. As shown by Park et al. (2016), the

contribution from the longitudinal component peaks on very large angular scales, where this can dominate over the contribution from the rotational component, but it rapidly decays and becomes subdominant above $\ell \sim 100$. Since we are interested in the latter regime, we expect Eq. (6.2.16) to hold up to a good approximation. We also notice that, although the cross-correlation of either of these two observables with κ_Φ is expected to identically vanish due to the statistical isotropy of the velocity field (Dore et al., 2004), an exact cancellation might not actually take place in observations due to, e.g., cosmic variance, which can represent a noise for the physical signal Eq. (6.2.12).

6.3 Simulations

In order to model the convergence field Eq. (6.2.5) and the kSZ effect Eq. (D.0.1) we ultimately require to characterise the density and momentum field of matter, the latter being intrinsically nonlinear. While these can be respectively calculated from first- and second-order perturbation theory, at low redshift the results are expected to breakdown above $\ell \sim 100$. Given that in this Chapter we are interested in studying the lensing-kSZ cross-correlation on smaller angular scales, and at the same time quantify the effect of cosmic variance on this signal, we therefore resort to use a suite of 30 statistically independent N-body simulations with $N = 1024^3$ dark matter particles in a comoving box size $L_{\rm box} = 1\ h^{-1}$Gpc, which are run with the RAMSES code (Teyssier, 2002), i.e., using Newtonian gravity. The latter is sufficient take into account the gravitomagnetic effects at leading order in the Post-Friedmann expansion, since the dynamics of CDM is not affected by $\mathbf{B}$ at this order, but there is an effect in the propagation of light (Bruni et al., 2014). Hence, to evaluate the gravitomagnetic convergence field in Eq. (6.2.7) we can simply use the momentum field from these Newtonian simulation. The initial conditions were generated at $z = 49$ with the 2LPTic code (Crocce et al., 2006), using as input a matter power spectrum from CAMB (Lewis et al., 2000), and the simulations are evolved from $z = 49$ to $z = 0$. The cosmological parameters adopted for the simulation are $[\Omega_\Lambda,\ \Omega_m,\ \Omega_K,\ h] = [0.693, 0.307, 0, 0.68]$ and a primordial spectrum with amplitude $A_s = 2.1 \times 10^{-9}$, spectral index $n_s = 0.96$ and a pivot scale $k_{\rm pivot} = 0.05\ {\rm Mpc}^{-1}$. Here Ω_Λ and Ω_K are, respectively, the density parameters for the cosmological constant Λ and curvature K, and h is the dimensionless Hubble constant, $h \equiv H_0/(100\ {\rm km/s/Mpc})$.

In addition to the 30 Newtonian simulations described above, we also use a single realisation of a high-resolution, general-relativistic N-body simulation run with GRAMSES (Barrera-Hinojosa & Li, 2020; Barrera-Hinojosa & Li, 2020), which adopts the same cosmological pa-

rameters given above, and it starts from the same seed as one of the 30 Newtonian simulations. This simulation tracks $N = 1024^3$ particles in a simulation box of $L_{\rm box} = 256\ h^{-1}$Mpc, and thanks to adaptive-mesh-refinement (AMR) settings it has resolved scales down to 2 h^{-1}kpc. Given that this simulation is fully relativistic, the gravitomagnetic field is solved and outputted by the code during the evolution, and the gravitomagnetic force acting on CDM particles is included. This simulation has been recently used to study the vector potential of ΛCDM in Chapter 5, where more details can be found, and it complements the suite of Newtonian simulations in two particular aspects: firstly, it serves as a fully-relativistic counterpart to the post-Friedmann approach used throughout this investigation, and secondly it provides a substantial increase in resolution which can be used to test numerical resolution effects which, as we will show, can play an important role in the noise estimation for the gravitomagnetic signal from mock maps.

6.4 Methodology

6.4.1 Modelling the observables

To model the lensing convergence field and the kSZ effect, we take two different approaches, both of which use the particle data (positions and velocities) from the snapshots of the simulations detailed in Section 6.3. In the first approach, we use this data to interpolate the density and momentum fields onto a grid, and perform LOS projections to generate mock sky maps using HEALPIX (Górski et al., 2005). In the second approach, we measure the 3D power spectra of the density and momentum fields from the simulation data, and use them to evaluate the theoretical Limber integrals Eqs. (6.2.11, 6.2.16). The 3D spectra of the density and momentum fields, which are obtained using the DTFE code (Schaap & van de Weygaert, 2000; Cautun & van de Weygaert, 2011) from particle data, are measured using NBODYKIT (Hand et al., 2018). To single out the rotational component of the momentum field to evaluate Eq. (6.2.16), we take the curl of this field using a 3-point finite-difference approximation, and use the identity $P_{\mathbf{q}_\perp}(k) = P_{\nabla\times\mathbf{q}}(k)/k^2$. We carry out this procedure with the 30 Newtonian N-body simulations.

In the case of the single GRAMSES simulation counterpart, the situation is slightly different as the vector (as well as scalar) potential values are calculated and stored by the code in the cells of the hierarchical AMR meshes, and the 3D power spectrum of the gravitomagnetic field itself is therefore measured using a code that is able to handle such mesh data directly

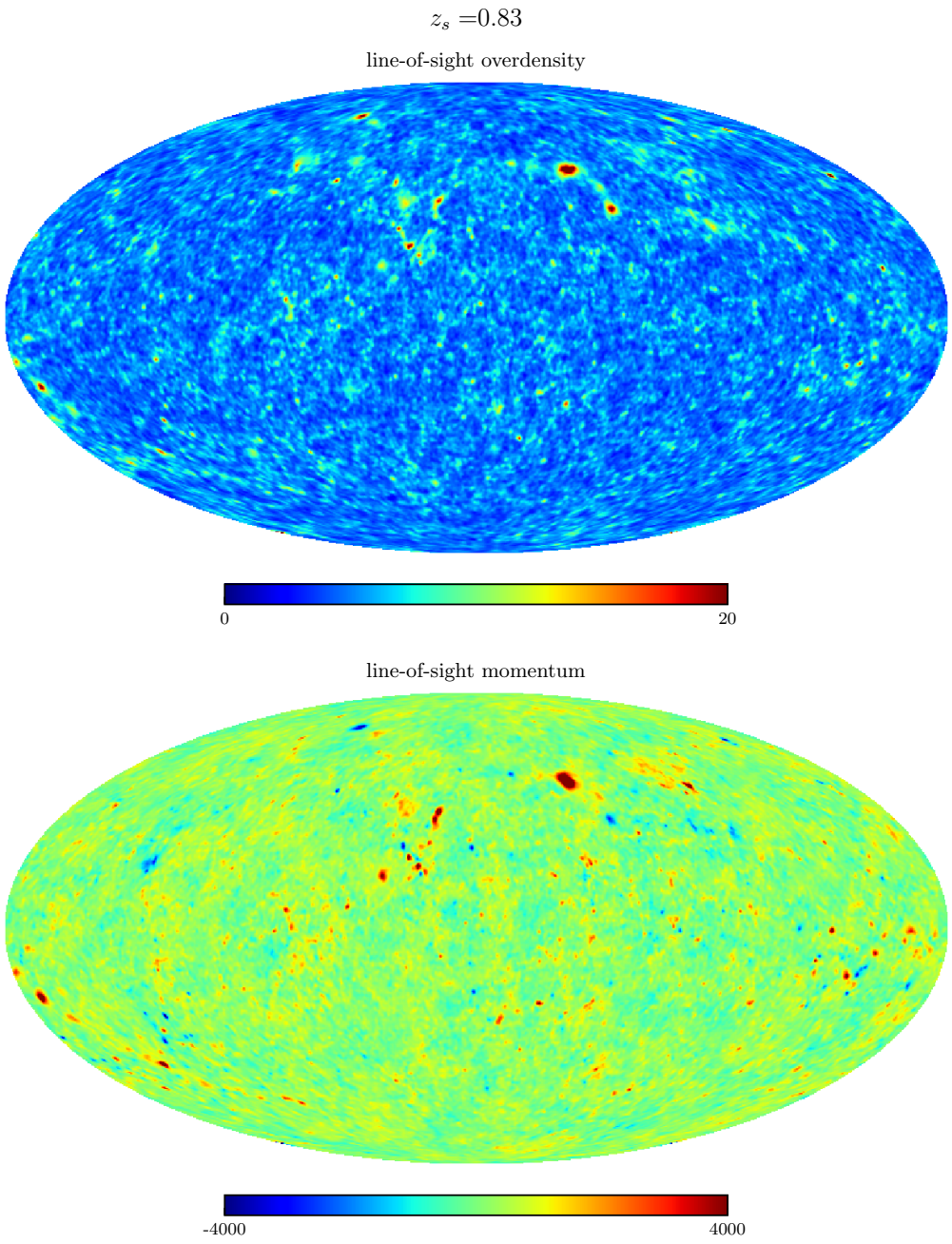

Figure 6.1: Examples of full-sky maps for a redshift-zero observer generated by line-of-sight projections using the particle data from a $L = 1\ h^{-1}$Gpc-box simulation, up to the comoving distance $\chi_s = 2\ h^{-1}$Gpc (corresponding to $z_s = 0.83$). *Top*: Projected density field. *Bottom*: Projected momentum field in units of km/s. To help visualisation, the maps have been smoothed using a Gaussian beam with a full-width-half-maximum of 1 degree and only display a limited range of values (as indicated by the colour bars). No kernel weights have been used in these line-of-sight projections. The cross-correlation between these example maps will allow us to pick up the gravitomagnetic effect.

and to write it on a regular grid by interpolation (He et al., 2015). In this way, the 3D power spectrum measured from this high-resolution simulation is accurate down to $k = 15\ h\mathrm{Mpc}^{-1}$ (see Appendix C), which allow us to extend our analysis up to smaller angular scales than with the 1 h^{-1}Gpc simulations. Comparing the two sets of simulations not only allows us to assess the impact of simulation resolution, but can also serve as a cross check of the gravitomagnetic field power spectra calculated in different ways.

The sky maps in the first approach are generated using an onion-shell technique, in which an observer is placed in a random position of the simulation box and the fields are projected along different lines of sight in radial shells of fixed comoving distance, in our case with thickness of 100 h^{-1}Mpc. Then, to generate the convergence field and kSZ maps for the given observer, the HEALPIX maps of the shells (pixels) are weighted by the appropriate integration kernels corresponding to each observable, i.e., Eqs. (6.2.8, 6.2.9, 6.2.14). In this process, the simulation box is tiled multiple times to cover the volume enclosed by a sphere up to the comoving distance of the source, χ_s, if needed. Finally, the angular power spectra of a resulting sky map, or the cross correlation between two different maps, is measured with ANAFAST subroutines included in HEALPIX.

Figure 6.1 is an example of the full-sky maps of projected density and momentum along the LOS up to $z_s = 0.83$ for an observer located at $z = 0$, without applying any kernel weights, using the data from one of the 1 h^{-1}Gpc-box simulations. A visual inspection of Fig. 6.1 shows a clear correlation between the density (top) and momentum (bottom) field maps. Along the overdense lines of sight, the projected momentum field can be in either of the two directions; in an infinite universe one would expect this to be an exact symmetry, which makes the cross correlation between the projected density and momentum fields vanish. However, due to the finite box size, this does not happen exactly, as is evident from the fact that in this particular case there are more lines of sight with positive values of the projected momentum field (i.e. pointing away from the observer) than negative values. This means that the kSZ-κ_Φ cross correlation measured from sky maps made from these simulations would not exactly vanish on large scales, although it is expected to eventually vanish on small scales, where the effect of cosmic variance is suppressed. It is therefore important to accurately quantify the degree of cross-correlation between these two effects, which can become a source of noise for the physical signal in Eq. (6.2.12). A standard way to measure the degree of correlation

between two random fields is by the cross-correlation coefficient, defined as

$$\mathrm{Corr}_{XY}(\ell) = \frac{C_\ell^{XY}}{\sqrt{C_\ell^{XX} C_\ell^{YY}}} \,. \tag{6.4.1}$$

We will proceed to measure the auto- and cross-angular power spectra from the maps and compare with the theoretical predictions in Section 6.4.2. In particular, we will present the cross-correlation coefficient between κ_Φ and the kSZ effect measured from the sky maps, and show that the measurement depends sensitively on simulation resolution. However, provided that the simulation resolution is high enough, our result suggests that the covariance of the kSZ-κ_Φ cross angular power spectrum found in the map measurements agrees well with the corresponding theoretical prediction of sample variance, Eq. (6.4.2) below. Readers who are not interested in the noise validation can skip directly to Section 6.5 and 6.5.2, where the scientific results are presented and discussed.

6.4.2 Comparison of auto- and cross-power spectra from mock maps and the Limber approximation

Given that the cross correlation between κ_Φ and the kSZ effect vanishes theoretically, the resulting data when measuring this quantity from the sky maps can be very noisy, with strong fluctuations around 0 from one ℓ-mode to the next. Thus, for the subsequent analysis we will bin the spectrum data in ℓ-space, which will cancel out most of the oscillations and reduce the noise, hence leading to smoother measurements. In the remainder of this Section, we bin the data into 11 ℓ-bins spaced logarithmically between $\ell_{\rm min} = 40$ and $\ell_{\rm max} = 2000$.

The top panels in the two rows of Fig. 6.2 show the angular power spectra of the two contributions to the lensing convergence field, i.e., κ_Φ (top curves) and $\kappa_{\mathbf{B}}$ (bottom curves) in Eq. (6.2.5), and of the kSZ effect (b; middle curves), at different comoving distances of the lensing source, χ_s (different panels). These spectra are measured from the HEALPIX maps (circles) or calculated with the Limber-approximation integrals (black solid line), and for the former we show the mean and 1σ regions from the 30 realisations with a box size of 1 h^{-1}Gpc. We find an overall very good agreement between the two methods, especially for $\kappa_{\mathbf{B}}$ and kSZ, up to $\ell \sim 1000$, where the pixel resolution effect in the HEALPIX maps starts to appear. Notice that the ratio between the angular power spectrum of $\kappa_{\mathbf{B}}$ and κ_Φ is about $\mathcal{O}(10^{-5})$, which is of the same order as the ratio between the 3D power spectra of the corresponding potentials (see, e.g., Fig. 5 of Barrera-Hinojosa et al., 2021).

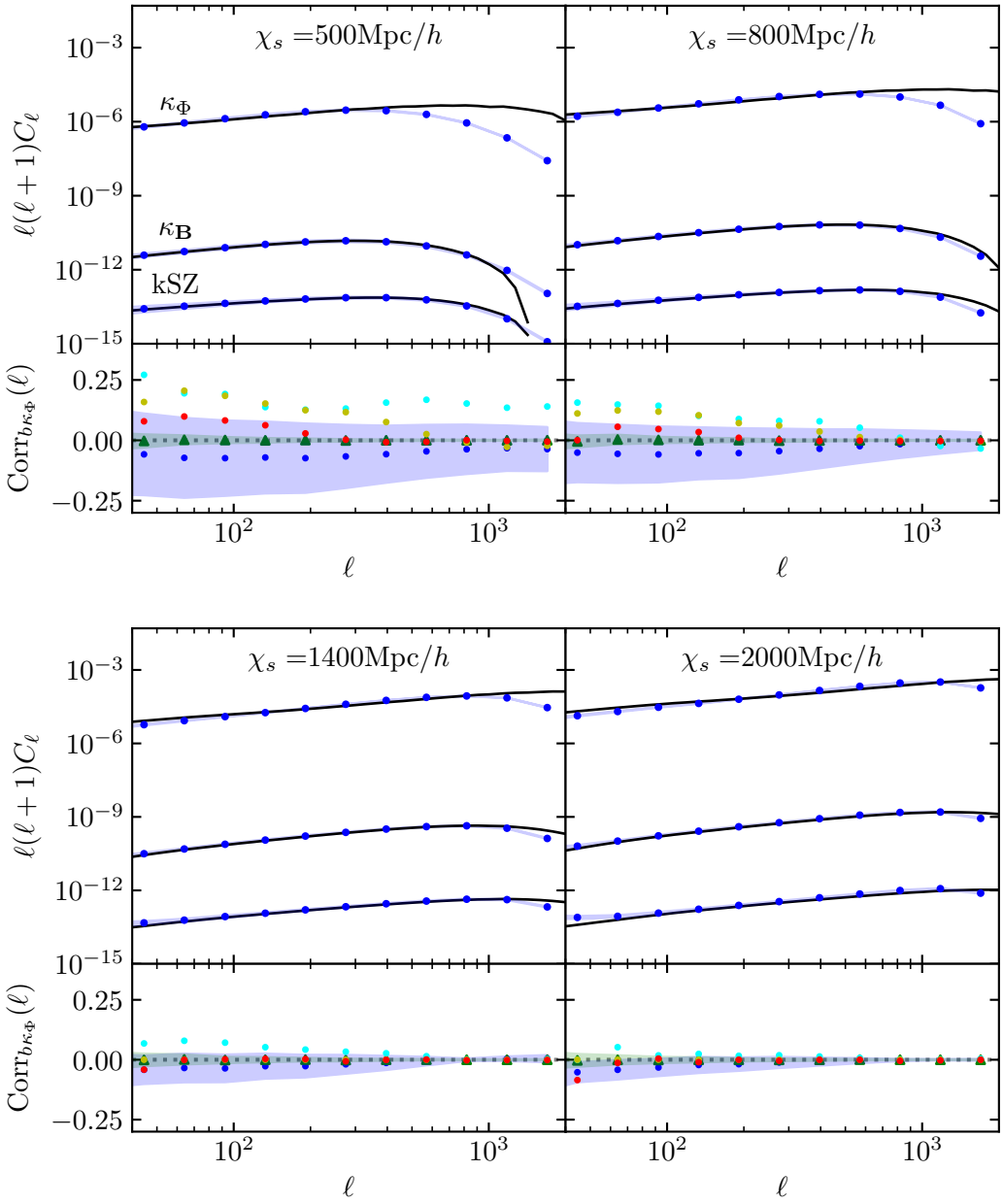

Figure 6.2: *Top panels*: Angular power spectra of the Newtonian (κ_Φ) and gravitomagnetic ($\kappa_\mathbf{B}$) contributions to the convergence field and the kSZ effect (b) for different comoving distances up to $\chi_s = 2000\ h^{-1}$Mpc (which corresponds to $z_s = 0.83$) from a redshift-zero observer. The black solid lines show the Limber-approximated integrals evaluated with the 3D power spectra measured from the 1 h^{-1}Gpc-box simulations, while blue circles show the mean of the 30 HEALPIX maps from the same simulations, and shaded blue region the corresponding 1σ standard deviation. *Bottom panels*: Cross-correlation coefficient of kSZ-κ_Φ (expected to be zero in theory). The blue circles and blue shaded area respectively correspond to the mean and 1σ scatter of the 'same-seed' case, while green circles represent the analogue result for the 'cross-seed' case (see main text for details). The cyan, yellow and red circles correspond to the cross-correlation coefficient obtained from a single, same realisation (seed), with box size $L = 1\ h^{-1}$Gpc, $L = 500\ h^{-1}$Mpc, and $L = 256\ h^{-1}$Mpc, respectively. The results use 11 ℓ-bins spaced logarithmically between $\ell_{\rm min} = 40$ and $\ell_{\rm max} = 2000$. The kSZ-κ_Φ cross-correlation is only fully consistent with zero for the simulation with the highest resolution ($L = 256\ h^{-1}$Mpc), indicating that it is necessary to use this high resolution simulation to make reliable predictions for the signal and noise of the gravitomagnetic effect.

The bottom panels in the two rows of Fig. 6.2 show the cross-correlation coefficient, Eq. (6.4.1), for kSZ-κ_Φ measured from the mock maps. To study this cross correlation in detail, we measure it in two ways: first by picking both sky maps from the same realisation[2] (dubbed 'same seed' below), and then picking each map from a different realisation (dubbed 'cross seed'). In the first case, we then average over all 30 realisations as before, while in the second case we average over all possible combinations. We find that these approaches give very different results. First, we note that in the 'cross seed' case, the mean (green triangles) is consistent with zero, the standard deviation (green shaded region) is symmetric around the horizontal dashed line (0), and its magnitude consistently decreases toward small angular scales. In contrast, in the same-seed case we find that on large and intermediate scales the mean (blue circles) is not very consistent with zero, and the standard deviation (blue shaded region) is much larger than in the previous case and does not consistently decrease with ℓ.

In order to pinpoint the origin of the above discrepancy, we have conducted a test of the numerical resolution. In addition to the 'same seed' and 'cross seed' results, in the bottom panels of the two rows in Fig. 6.2 we show the cross-correlation coefficients measured from sky maps made from simulations that use a single, fixed, initial condition random seed, with three different box sizes: $1h^{-1}$Gpc (cyan symbols), 500 h^{-1}Mpc (yellow) and $256h^{-1}$Mpc (red). We find that: (i) the cross-correlation coefficient consistently decreases with increasing resolution, with the $256h^{-1}$Mpc box giving cross-correlation coefficient values that are very close to 0; (ii) the deviation of $\mathrm{Corr}_{b\kappa_\Phi}(\ell)$ from 0 is strongest for lower lensing source reshift (smaller χ_s), which is likely because these maps enclose a much smaller volume. Then, since the LOS projection (in terms of the Limber approximation) probes modes $k = \ell/\chi$, these sky maps critically depend on contributions from small scales which may not be well resolved by some of the simulations. Nevertheless, even for $\chi_s = 500h^{-1}$Mpc, the $256h^{-1}$Mpc box gives a $\mathrm{Corr}_{b\kappa_\Phi}$ that is very close to 0. Hence, we conclude that this is a numerical resolution effect due to unresolved scales close to the observer's location as a consequence of lack of resolution in the simulations. In the 'cross-seeds' case, this issue is not present as each field is taken from a different realisation and hence are statistically independent, regardless of resolution effects.

We now compare the covariance of the kSZ-κ_Φ cross correlation measured from the sky maps with the theoretical expectation for the effect of cosmic variance. In the latter case, the

[2] We always use a single simulation box, if necessary tiling it multiple times as described above, to obtain a given sky map. In this sense, each realisation of map corresponds to a single realisation of simulation.

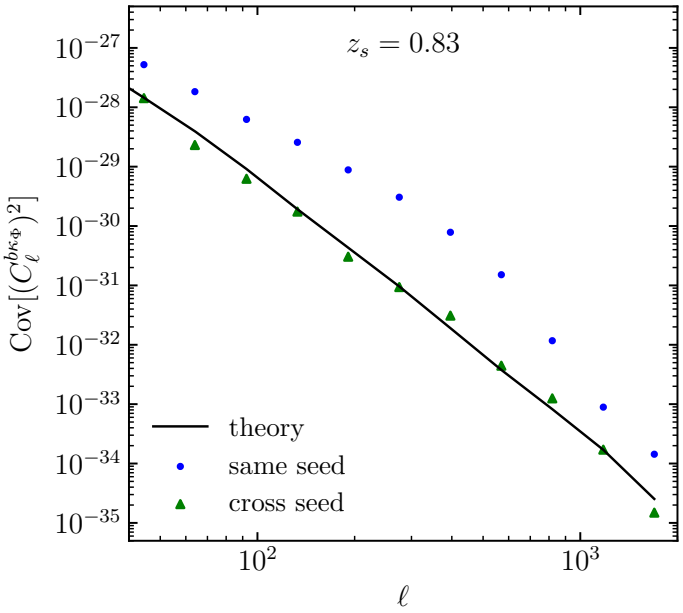

Figure 6.3: Comparison of the covariance of the kSZ (b)-κ_Φ cross-angular power spectrum from HEALPIX maps and the theoretical prediction, Eq. (6.4.2), at $z_s = 0.83$. The results use 11 ℓ-bins spaced logarithmically between $\ell_{\rm min} = 40$ and $\ell_{\rm max} = 2000$. The 'cross seed' case agrees with the theoretical prediction very well, indicating the robustness for the estimate of cosmic variance.

covariance of the cross angular power spectrum between two Gaussian fields, A and B, is given by (e.g., Cabré et al., 2007)

$$\mathrm{Cov}\left[\left(C_\ell^{AB}\right)^2\right] = \frac{1}{\Delta\ell f_{\rm sky}(2\ell+1)}\left[\left(C_\ell^{AB}\right)^2 + C_\ell^A C_\ell^B\right], \tag{6.4.2}$$

where $f_{\rm sky}$ is the observed fraction of the sky, and $\Delta\ell$ is the width of the multipole bins, which is assumed to be independent of ℓ, i.e., no off-diagonal terms in the covariance matrix. For the particular case of κ_Φ and kSZ, the theoretical cross angular power spectrum in the right hand side of Eq. (6.4.2) vanishes and only the second term in the square bracket contributes.

Figure 6.3 shows the covariance of the cross angular spectrum between κ_Φ and the kSZ effect at $z_s = 0.83$ measured from the same-seed maps (blue circles) and cross-seed maps (green triangles) from the 1 h^{-1}Gpc-box simulations, and the theoretical prediction Eq. (6.4.2) (solid black line). We find that the latter is in very good agreement with the results from the cross-seeds case maps across all scales, while the covariance in the same-seed case maps, which is affected by the resolution effects discussed above, can become over one order of magnitude larger at around $\ell \simeq 500$ and thus strongly degrade the signal-to-noise estimation of the gravitomagnetic signal Eq. (6.2.12). As in the above discrepancy, this is not unexpected since the sky observables take the form of LOS integrals, hence the numerical resolution

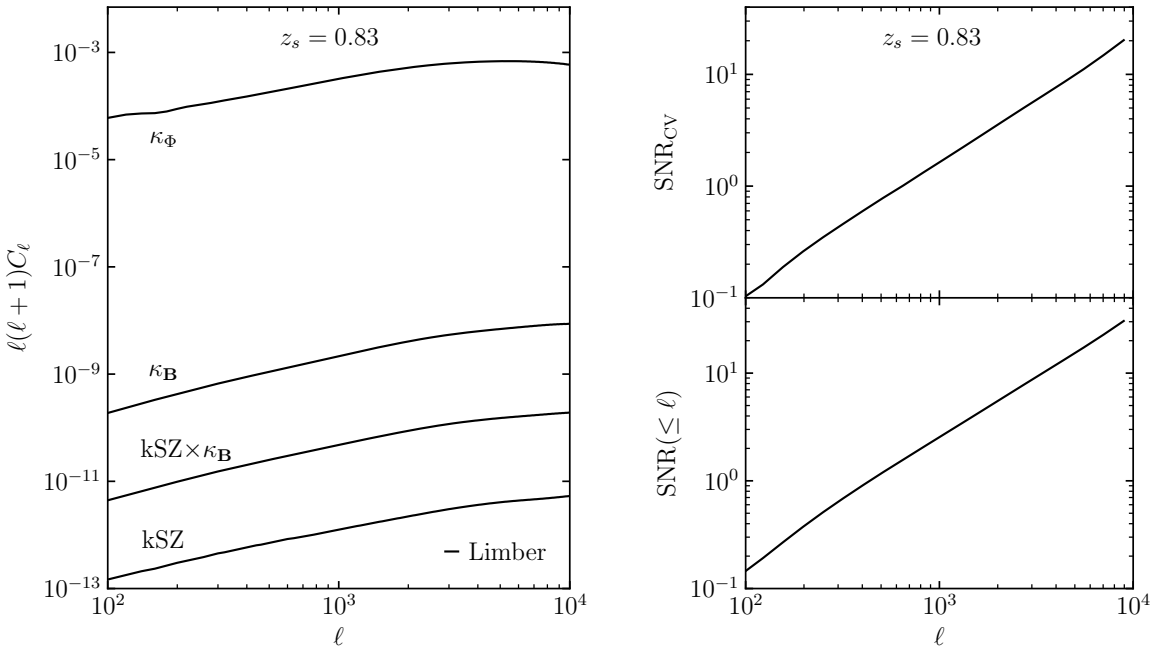

Figure 6.4: *Left panel*: Angular power spectrum of the two contributions to the lensing convergence field and the kSZ effect (b), and the cross angular power spectrum of kSZ-$\kappa_{\mathbf{B}}$. These are obtained from Limber-approximated integrals evaluated with the 3D power spectra measured from the simulation with box size $L = 256\ h^{-1}$Mpc. *Top right panel*: Theoretical signal-to-noise ratio (SNR) for the kSZ-$\kappa_{\mathbf{B}}$ cross-correlation, corresponding to the idealised case where the noise is dominated by the cosmic variance of the kSZ-$\kappa_{\rm GR}$ signal itself. *Bottom right panel*: Cumulative SNR corresponding to the top plot. The results use 23 ℓ-bins spaced logarithmically between $\ell_{\rm min} = 40$ and $\ell_{\rm max} = 10^4$.

errors due to unresolved scales close to the observer's location can propagate up to higher redshifts (comoving distances) and contaminate the final result. It is worthwhile to remark that, even though the lensing kernel down-weights the radial shells that are closer to the observer, and hence suppresses the relative contribution of these numerical resolution effects when projecting up to a high redshift (e.g., $z_s = 0.83$ as in our case), the result shows that the cross correlation is still considerably large compared to the effect of sample variance only.

6.5 Results

In this section, we will more quantitatively assess the gravitomagnetic lensing effect signal and its detectability. This will be done in the context of cross correlating two observables — a total lensing convergence field containing the gravitomagnetic effect, and a total CMB temperature map that contains the (integrated) kSZ effect. We quantify this using the usual

signal-to-noise ratio (SNR),

$$\left(\frac{S}{N}\right)^2_\ell = \frac{\left(C_\ell^{AB}\right)^2}{\mathrm{Cov}\left[\left(C_\ell^{AB}\right)^2\right]}\,, \tag{6.5.1}$$

where C_ℓ^{AB} is the cross angular spectrum between two generic observables A and B, and Cov denotes the covariance matrix. In the ideal scenario, the covariance matrix in Eq. (6.5.1) is dominated by the effect of cosmic variance and Eq. (6.4.2) directly applies. However, for a realistic estimation of the SNR, the covariance also needs to include the following two contributions: (*i*) instrumental noises in the sky maps of A and B; (*ii*) spurious signals caused by other physical effects, such as the primary and other secondary CMB anisotropies in the case of a CMB temperature map.

Our main objective is to forecast the detectability of the gravitomagnetic effect for various future galaxy surveys and CMB experiments (Section 6.5.2). However, before that, we will first calculate a 'theoretical SNR' (Section 6.5.1), by applying Eq. (6.5.1) while neglecting all instrumental noises and considering a pure kSZ map with no other CMB primary or secondary effects. The latter is useful for assessing, in an idealised situation, the potential of isolating the gravitomagnetic contribution to the total lensing signal by cross-correlating with kSZ — this can serve as an upper bound of the SNR in real observations.

6.5.1 Theoretical signal-to-noise ratio

Let us first investigate the SNR for the kSZ-$\kappa_{\mathbf{B}}$ cross correlation in the most idealised case, i.e., accounting for only the variance contributed by $\kappa_{\rm GR}$ and kSZ (b) themselves. We will include other source of noise such as the primordial CMB and instrumental noise in Section 6.5.2.

Because of the good agreement in the noise predictions from theory and maps shown in Fig. 6.3, to calculate the SNR we resort to using the Limber prediction Eq. (6.2.16) to model the signal, taking as input the 3D power spectrum measured from the high-resolution simulation, and use Eq. (6.4.2) to quantify the noise, with the two fields A, B being respectively the kSZ contribution to the CMB temperature fluctuation, b, and the total lensing convergence, $\kappa_{\rm GR} = \kappa_\Phi + \kappa_{\mathbf{B}}$. The angular power spectra are binned into 23 ℓ-bins logarithmically spaced between $\ell_{\rm min} = 40$ and $\ell_{\rm max} = 10^4$. Then, using the fact that, at the theory level, the kSZ-κ_Φ cross correlation vanishes and hence does not contribute to the first noise term in the square

bracket of Eq. (6.4.2), the SNR becomes

$$\left(\frac{S}{N}\right)_{\ell,\mathrm{CV}} = \sqrt{\Delta\ell f_{\mathrm{sky}}(2\ell+1)}\frac{C_\ell^{b\kappa_{\mathbf{B}}}}{\sqrt{\left(C_\ell^{b\kappa_{\mathbf{B}}}\right)^2 + C_\ell^b C_\ell^{\kappa_{\mathrm{GR}}}}}$$
$$\approx \sqrt{\Delta\ell f_{\mathrm{sky}}(2\ell+1)}\frac{C_\ell^{b\kappa_{\mathbf{B}}}}{\sqrt{C_\ell^b C_\ell^{\kappa_\Phi}}}\,, \tag{6.5.2}$$

where in the second line we have approximated $C_\ell^{\kappa_{\mathrm{GR}}} \approx C_\ell^{\kappa_\Phi}$ since, as shown in Fig. 6.2 and Fig. 6.4, $C_\ell^{\kappa_{\mathbf{B}}}$ is suppressed by about five orders of magnitude with respect to the Newtonian contribution, and we have also used that $\left(C_\ell^{b\kappa_{\mathbf{B}}}\right)^2 \ll C_\ell^b C_\ell^{\kappa_\Phi}$ (as shown by the left panel of Fig. 6.4) to neglect the first term in the denominator. Notice that we have used the subscript CV to highlight that, to obtain this theoretical SNR, only the cosmic variances in κ_{GR} and kSZ (b) are included in the noise.

Given that the high-resolution simulation is fully relativistic, instead of evaluating Eq. (6.2.16) using the 3D power spectrum of the momentum field measured from the simulation, in this case we directly use the 3D power spectrum of the gravitomagnetic field that is calculated and outputted by GRAMSES during the simulation, $P_{\mathbf{B}}(k)$, and the integration kernel for the convergence field Eq. (6.2.7) is modified according to Eq. (6.2.3)[3]. Conversely to the logic behind the Post-Friedmann (or Post-Newtonian) approach — in which the gravitomagnetic effect is ultimately written in terms of the rotational modes of the 3D momentum field — in this case we use Eq. (6.2.3) to convert $P_{\mathbf{B}}(k)$ into $P_{\mathbf{q}_\perp}(k)$ to evaluate the kSZ effect using the same spectrum data. At this point, it is worthwhile to remark that the gravitomagnetic potential power spectrum measured from the high-resolution simulation (and correspondingly the 3D momentum power spectrum) suffers from a power suppression due to the small box size (Zhang et al., 2004; Iliev et al., 2007). Indeed, it has been found that this effect appears prominently if the matter-radiation equality scale is not sampled (Adamek et al., 2016a; Barrera-Hinojosa et al., 2021). As discussed in the Appendix B of Park et al. (2013), in the context of the momentum power spectrum and the kSZ effect (which formally involves the same calculation), the large-scale power loss can be corrected for by using perturbation theory. For this, we calculate the ratio between the second-order perturbation theory predictions of $P_{\mathbf{B}}(k)$, Eq. (D.0.19), evaluated in two ways: one which matches the simulation results on

[3] Although, rigorously speaking, GRAMSES uses a different gauge than the N-body gauge used by the Newtonian simulations (Fidler et al., 2016), both share the same definition of spatial coordinates, and the gravitomagnetic potential indeed corresponds to the gauge-invariant one defined in the Poisson gauge.

large scales (i.e., which is also suppressed by a large-scale cut-off scale[4]), and another which does not include any cut-off and hence does not miss any power on large scales. Then, to get the corrected power spectrum we multiply this ratio to the $P_{\mathbf{B}}(k)$ measured from the simulation, and use this to evaluate Eq. (6.2.16). Although we repeat this procedure for each available snapshot, we have checked that this correction factor is redshift-independent.

Another important aspect to take into account when evaluating the Limber integrals is the time evolution of the 3D spectra. Given that we can only measure these from a finite number of snapshots, to parameterise the time evolution of $P_{\mathbf{B}}(k,z)$ and $P_{\Phi}(k,z)$ we measure these from the available simulation snapshots ($z=0,0.5,1,1.5$) and interpolate among them. For the κ_{Φ} case we use the linear growth rate D_+, given by (Linder, 2005)

$$D_+(a) = \exp\int_1^a \mathrm{d}\ln a' \Omega_m(a')^{6/11}\,, \tag{6.5.3}$$

with $\Omega_m(a) = \Omega_m a^{-3}/(H/H_0)^2$, as the 'time' variable for the interpolation; more explicitly, the interpolation is linear in D_+^2. Since $P_{\mathbf{B}}(k,z)$ is sourced by the rotational component of the momentum field $\mathbf{q} = (1+\delta)\mathbf{v}$, to interpolate this for the calculation of kSZ and $\kappa_{\mathbf{B}}$ we also use the linear continuity equation,

$$\mathbf{v}(\mathbf{k},a) = -i\frac{Hf}{k^2}\mathbf{k}\delta(\mathbf{k},a)\,, \tag{6.5.4}$$

where $f = \mathrm{d}\ln D_+/\mathrm{d}\ln a$ is the linear growth rate; here $(HfD_+)^2$ is used as the 'time' variable for the interpolation to ensure that it gives the correct time-evolution behaviour at large linear scales. Evidently, these interpolations involve a certain degree of approximation at the small nonlinear scales, but we have checked that our result does not change significantly if we use fixed simulation snapshots or different time interpolation schemes.

Figure 6.4 represents one of the main results of this investigation. The left panel shows the angular power spectra of the different effects based on the high-resolution simulation, which allows us to resolve scales down to $\ell = 10^4$. The top right panel of Fig. 6.4 shows the theoretical SNR, in which the error is calculated using Eq. (6.5.2), i.e., by only including the effects of sample variances in the kSZ-κ_{GR} signal, with the angular power spectra therein corresponding to those shown in the left panel. We find that, with $z_s = 0.83$, a SNR of $\simeq 10$ is achieved at $\ell \simeq 5000$, while this can reach $\simeq 20$ at $\ell \simeq 10^4$. The bottom right panel of Fig. 6.4 shows the cumulative SNR corresponding to the top panel of the same figure, which

[4]This is achieved by restricting the k range (in particularly the lower end) for the matter and velocity divergence power spectra used in the evaluation of the perturbation-theory result, Eq. (D.0.19), to the same as probed by the high-resolution simulation.

Table 6.1: Experimental specifications for the weak lensing surveys and CMB experiments considered in this work.

Survey	n_g (galaxies per arcmin^2)	σ_ϵ	$f_{\rm sky}$
EUCLID	30	0.22	0.36
LSST	40	0.22	0.5
Experiment	$\theta_{\rm FWHM}$ [arcmin]	Δ_T [μK-arcmin]	$f_{\rm sky}$
PLANCK	5	3.1	0.82
CMB-S4	1.4	1	0.4
Simons Obs.	1.4	6	0.4

can reach almost 15 (30) at $\ell \simeq 5000$ (10^4). These estimates will, of course, be downgraded once we have included realistic instrument noises and other spurious effects, as discussed in the next subsection. The same is expected to occur when baryonic effects are taken into account, although the latter is beyond the scope of this study.

6.5.2 Detectability with current and future observations

Let us now investigate the detectability of the gravitomagnetic signal with current and future observations. In real observations, the kSZ effect is imprinted in the measured CMB temperature map along with a number of primary and secondary anisotropies. Because the latter is what will be used to cross correlate with weak lensing, to assess the detection of the kSZ-$\kappa_{\mathbf{B}}$ cross-correlation, we need to consider all the relevant contributions contained in a full CMB map. In particular, it is essential to include the cosmic variance effect from the primordial CMB, as this signal dominates over kSZ on scales down to $\ell \sim 3000$. We will discuss these effects and how they are expected to affect the sought-after physical signal below.

The signal-to-noise per individual mode of the lensing-kSZ cross correlation, Eq. (6.2.12), is given by Eq. (6.5.1), which can now be written more explicitly as

$$\left(\frac{S}{N}\right)^2_\ell = \frac{\left(C_\ell^{b\kappa_{\mathbf{B}}}\right)^2}{\mathrm{Cov}\left[\left(C_\ell^{\mathrm{T}\kappa_{\rm GR}}\right)^2\right]}\,, \tag{6.5.5}$$

where $C_\ell^{b\kappa_{\mathbf{B}}} = C_\ell^{b\kappa_{\rm GR}}$ is again the physical signal we are after, while $C^{\mathrm{T}\kappa_{\rm GR}}$ is the cross angular power spectrum between the total CMB temperature map (T) and the total lensing convergence field, $\kappa_{\rm GR}$. Neglecting the correlations induced by the incomplete sky coverage, the covariance matrix can be approximated as

$$\frac{\mathrm{Cov}\left[\left(C_\ell^{\mathrm{T}\kappa_{\rm GR}}\right)^2\right]}{[\Delta\ell f_{\rm sky}(2\ell+1)]^{-1}} \approx \left(C_\ell^{b\kappa_{\mathbf{B}}}\right)^2 + \left(C_\ell^{\rm T} + N_\ell^{\rm T}\right)\left(C_\ell^{\kappa_{\rm GR}} + N_\ell^{\kappa_{\rm GR}}\right), \tag{6.5.6}$$

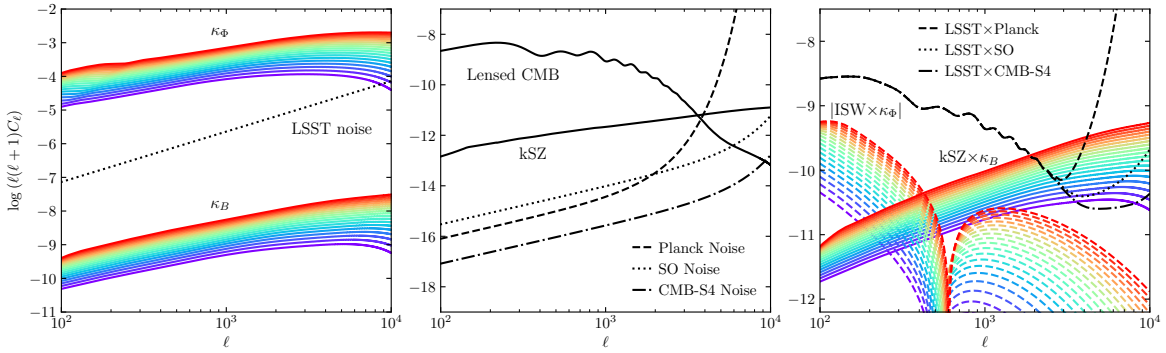

Figure 6.5: Comparison of the various angular power spectra and noise levels of weak-lensing surveys and CMB experiments. *Left panel*: Newtonian (upper solid lines) and gravitomagnetic (lower solid lines) contributions to the lensing convergence field, which indicate that the latter is around 5 orders of magnitude smaller, and is well below the expected noise level of future weak lensing surveys such as LSST. *Middle panel*: kSZ effect and the lensed CMB signals (as indicated by legends), and the noise levels for three CMB experiments: PLANCK (dashed), SO (dotted) and CMB-S4 (dot-dashed). The kSZ effect dominates over the lensed CMB signal at $\ell \gtrsim 3500$. *Right panel*: the cross spectrum of kSZ-$\kappa_{\mathbf{B}}$ (solid lines), which is the signal we are after, and the absolute value of the cross spectrum between the ISW effect and κ_Φ (dashed lines), which represents a potential source of contamination for the kSZ-$\kappa_{\mathbf{B}}$ signal. The dashed, dotted and dot-dashed black lines are, respectively, the expected noise level for the cross correlation of weak lensing data from an LSST-like survey and CMB data from PLANCK, SO and CMB-S4. The kSZ-$\kappa_{\mathbf{B}}$ signal is well above the noise levels of future experiments on scales $\ell \gtrsim 3000$. In all panels, the different colours correspond to lensing source redshifts between $z_s = 0.4$ (purple, lowest amplitude) and $z_s = 1.4$ (red, highest amplitude), with a separation Δz_s equivalent to a comoving distance of $\chi = 100\ h^{-1}$Mpc.

where C_ℓ^{T} is the total angular power spectrum of the CMB temperature, which includes the kSZ effect, the integrated Sachs-Wolfe (ISW) effect, and the weak lensing of the CMB. Frequency-dependent secondary effects on the CMB, such as the cosmic infrared background (CIB) and thermal SZ (tSZ) effect, are assumed to have already been cleaned and hence are not included in the T map here. For the lensed CMB angular-power spectrum we use the output from CAMB, to which we add the kSZ contribution calculated using the Limber approximation, Eq. (6.2.16). Since the available simulation data only covers up to $z = 1.5$, kSZ is only integrated up to this redshift (rather than up to $z \sim 6$, which corresponds to the end of reionisation). When cross correlating a CMB map including other secondary effects and a galaxy weak lensing map, we need to consider if these secondary CMB signals can lead to spurious correlations which contaminate the sought-after signal, $C^{b\kappa_{\mathbf{B}}}$, particularly through cross correlations with κ_Φ, because $|\kappa_\Phi| \gg |\kappa_{\mathbf{B}}|$, so that any such spurious signal can potentially be as strong as, if not stronger than, $C^{b\kappa_{\mathbf{B}}}$ itself. At small angular scales, the CMB power spectrum is dominated by lensing, with the lensed temperature at sky position $\vec{\theta}$

approximately given by

$$T^{\rm lensed}(\vec{\theta}) = T^{\rm unlensed}(\vec{\theta}) + \vec{\nabla}T \cdot \vec{\nabla}\phi\,, \tag{6.5.7}$$

where ϕ is the CMB lensing potential. Because $\vec{\nabla}T$ has no correlation with the late-time large-scale structures in theory, we expect the correction term in Eq. (6.5.7) to have zero theoretical cross correlation with weak lensing κ_Φ: note this is different from the cases of cross correlating the CMB lensing deflection angle or convergence field (in both cases $\vec{\nabla}T$ has been removed through de-lensing reconstruction (Planck Collaboration et al., 2020)), or the squared CMB field (e.g., Dore et al., 2004), with weak lensing. On the other hand, the ISW effect, along with its nonlinear counterpart, the Rees-Sciama (RS) effect, can have a nonzero cross correlation with weak lensing (Hu, 2002); we have explicitly calculated this spurious signal using the method described in Appendix E, and found it to be subdominant compared to the kSZ-$\kappa_{\mathbf{B}}$ cross power spectrum $C_\ell^{b\kappa_{\mathbf{B}}}$ at the small angular scales of interest to us, as will be discussed below. Therefore, in Eq. (6.5.6) we have neglected the contribution from $C_\ell^{\rm ISW\kappa_\Phi}$, thus approximating $\left(C_\ell^{\rm T\kappa_{GR}}\right)^2$ by $\left(C_\ell^{b\kappa_{\mathbf{B}}}\right)^2$.

In Eq. (6.5.6), N_ℓ^X represents the contribution from the instrumental noise to the measured angular power spectrum of each effect. For the lensing signal (cosmic shear), we assume that the dominant error comes from the intrinsic ellipticity of galaxies, i.e.,

$$N_\ell^{\kappa_{\rm GR}} = \frac{\sigma_\epsilon^2}{n_{\rm gal}}\,, \tag{6.5.8}$$

where σ_ϵ^2 is the variance of the intrinsic ellipticity of galaxies, and $n_{\rm gal}$ the number of source galaxies per arcmin^2. For the CMB signal, we consider the error due to instrumental noise and beam smearing, given as (Knox, 1995)

$$N_\ell^{\rm T} = \left(\frac{\Delta_T}{\bar{T}}\right)^2 \exp\left[\ell^2\theta_{\rm FWHM}/(8\ln 2)\right], \tag{6.5.9}$$

where Δ_T is the noise level, $\bar{T}$ is the mean temperature of the CMB, and $\theta_{\rm FWHM}$ is the full width at half-maximum of the beam. Table 6.1 summarises the main specifications of the lensing surveys and CMB experiments considered in this section.

Figure 6.5 shows various angular power spectra assuming different lensing source redshifts (colour-coded; see the figure caption) and the noise levels for different weak-lensing surveys and CMB experiments. The left panel shows the two contributions to the total convergence field and the expected shape noise level of LSST, which shows that it will not be possible to detect the gravitomagnetic convergence via lensing alone (Andrianomena et al., 2014; Cuesta-

Lazaro et al., 2018). The middle panel shows the kSZ signal along with the lensed CMB signal, which dominates over the former down to $\ell \sim 3500$, as well as the noise levels of PLANCK (dashed), and of two next-generation CMB experiments; the Simons Observatory (SO, dotted) and CMB-S4 (dot-dashed). We note that the kSZ effect is above the expected noise levels of the latter two CMB experiments. Finally, the right panel shows the kSZ-$\kappa_{\mathbf{B}}$ cross spectrum and the total noise. We find that, while for PLANCK the signal is almost completely dominated by the instrumental resolution on small angular scales, the situation improves considerably with the Simons Observatory and CMB-S4, in which the signal is well above the noise on scales $\ell \gtrsim 3000$, which suggests that a potential future detection can be achieved on very small angular scales. In the right panel of Fig. 6.5 we have also included the signal due to the spurious cross correlation between the ISW effect and weak lensing (colour-coded, dashed) mentioned above. This is calculated from Eq. (E.0.14) using the nonlinear matter power spectra at different redshifts predicted by CAMB with HALOFIT. We find that, at $\ell \gtrsim 3000$, this spurious signal is over one order of magnitude smaller than the gravitomagnetic signal at all redshifts, and two orders of magnitude lower at $\ell \gtrsim 5000$. Furthermore, the signal is below the noise level expected for all experiments herein considered. Hence, in the following SNR forecast we use Eq. (6.5.6) to estimate the covariance, in which the ISW-κ_{Φ} cross-correlation is neglected.

Figure 6.6 shows the predicted SNR for different source redshifts (colour-coded; see the figure caption). In the case of cross correlating LSST with PLANCK (left panel), we find that the instrumental resolution of PLANCK is the main limiting factor, which does not allow one to yield a significant detection. However, with the improved resolution of the upcoming CMB experiments such as CMB-S4 and the Simons Observatory (middle and right panels), a significant detection might be achieved on small angular scales. With a lensing source redshift of $z_s = 1.4$ in LSST (right panel), in combination with the Simons Observatory, we find that the cumulative SNR can reach around 3 (4) at $\ell \approx 5000$ (10^4), while in the case of CMB-S4 this can reach almost 5 (9) at $\ell \approx 5000$ (10^4). The results are similar in the case of EUCLID in combination with the two aforementioned CMB experiments (middle panel), although the SNR is slightly lower than for LSST due to the smaller sky coverage and mean number of galaxies expected for this survey. The results show that the majority of the cumulative SNR comes from $\ell \gtrsim 2000$, and that the SNR is mainly determined by the beam size of the CMB experiment, followed by its noise level, Δ_T.

From Fig. 6.6 we can also observe that the detection SNR increases with source redshift in general (for a given CMB experiment). This is expected: as the redshift range for the

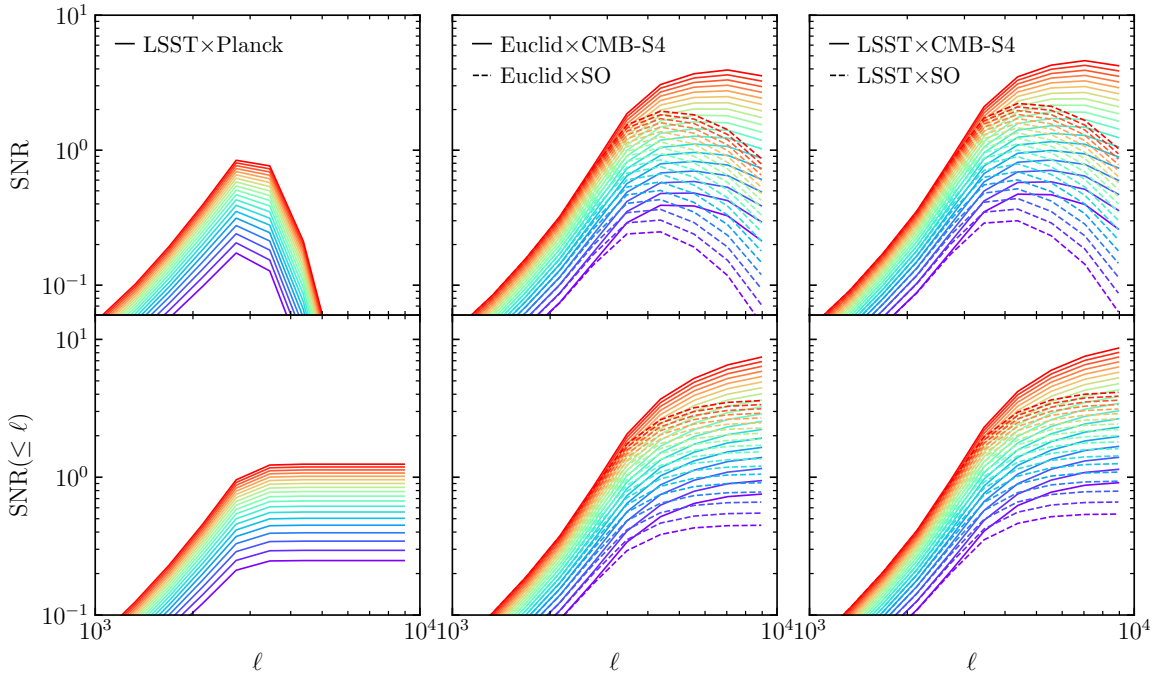

Figure 6.6: Signal-to-noise (SNR; top panels) and cumulative SNR (bottom panels) predictions for the kSZ-$\kappa_{\mathbf{B}}$ signal via cross-correlation of different weak-lensing surveys and CMB experiments for lensing source redshifts between $z_s = 0.4$ (purple, lowest amplitude) and $z_s = 1.4$ (red, highest amplitude), with a separation Δz_s equivalent to a comoving distance of $\chi = 100\ h^{-1}$Mpc. *Left panels*: forecast for LSST and PLANCK, which shows that a detection is not possible due to the angular resolution of the latter experiment. *Middle panels*: forecast for EUCLID in combination with CMB-S4 (solid) and the Simons Observatory (SO, dashed). *Right panels*: forecast for LSST in combination with CMB-S4 (solid) and the Simons Observatory (dashed). The angular resolution of next-generation CMB experiments may allow a significant detection of the gravitomagnetic effect. The results use 23 ℓ-bins spaced logarithmically between $\ell_{\rm min} = 40$ and $\ell_{\rm max} = 10^4$.

LOS projection increases, the cross correlation between the gravitomagnetic lensing ($\kappa_{\mathbf{B}}$) and the kSZ effect (b) also enhances; the covariance matrix also increases, but not by as much given that $C_\ell^{\rm T}$ is not affected. This implies that it is possible to improve the prospect of observationally detecting the gravitomagnetic effect by using deeper lensing surveys. Because our high-resolution simulation does not have snapshots at even higher z, in this work we only have considered a limited source redshift range, and we plan to revisit this topic in the future using larger simulations. Likewise, using a CMB lensing signal – whose kernel peaks at $z \sim 2$ – instead of cosmic shear, may also enhance the overall lensing-CMB cross-correlation signal, and it is likely to boost the SNR. This may also have the benefit of using the lensing convergence map and the temperature map from a single CMB experiment, without a weak lensing survey. Existing data from ACT (Darwish et al., 2021) may provide such a possibility.

6.6 Summary

In this Chapter, we have explored the possibility of detecting the cosmological gravitomagnetic (frame-dragging) effect via cross correlation of weak-lensing convergence maps, which include the gravitomagnetic contributions, with the kSZ effect that is imprinted as a secondary anisotropy in the CMB temperature maps. The latter is chosen because – apart from very large angular scales – it is sourced by the rotational modes of the momentum field of matter along the LOS, just like the former effect, and at the same time is not correlated with the standard (Newtonian) component of the convergence field at the two-point level (Dore et al., 2004). Thus, the cross-correlation is able to extract the gravitomagnetic contribution from a lensing convergence map. To model the cross-correlation signal and its covariance we have used the data from 30 Newtonian N-body simulations, as well as a single high-resolution, general relativistic simulation. Performing LOS projections and generating HEALPIX maps, we have found that small, unresolved scales close to the observer's location due to an insufficient simulation resolution can induce significant spurious variance in the cross correlation between the Newtonian component of the convergence and the kSZ effect. On the other hand, by cross correlating HEALPIX maps of fields taken from different realisations, such an artificial noise is not present and the covariance agrees well with the theoretical prediction of cosmic variance effects, Eq. (6.4.2). Then, to quantify the SNR we resort to model the signal based on the single high-resolution simulation and the Limber-approximated integral Eq. (6.2.16), and we estimate the noise by either Eq. (6.4.2), which includes only the effect of cosmic variance – and allows us to calculate a theoretical upper bound of the SNR – or Eq. (6.5.6), which also include all the major relevant effects for observations. In the former case, we find that at $z_s = 0.83$, the cumulative SNR can reach ~ 15 already at $\ell \simeq 5000$, and about 30 at $\ell \simeq 10^4$.

We then forecast the SNR for current CMB data from PLANCK, in combination with future-weak lensing surveys such as EUCLID and LSST, finding that the gravitomagnetic effect cannot be robustly probed using this method as the angular resolution of PLANCK is not sufficient to explore the small angular scales where the theoretical SNR rises most rapidly (Fig. 6.4). However, based on future CMB experiments such as the Simons Observatory and CMB-S4, our forecast shows that this effect can be detected decisively, especially with lensing sources further afield.

The result above is based on the assumption that several important late-time secondary effects on the CMB, such as the thermal SZ effect and CIB, could be reliably disentangled

from the primary CMB signal, and the SNR can be degraded if such 'cleaning' is not fully complete. We also expect that at the small scales ($\ell \gtrsim 3000$) where the SNR of the effect is relatively significant, the impact of baryons on both weak lensing and CMB observables can also be significant and hence downgrade the SNR. Modelling the impact of baryonic effects on the SNR above this regime is beyond the scope of this investigation and is left as future work. On the other hand, given that for the kSZ effect the longitudinal modes of the momentum field are subdominant with respect to the rotational-modes contribution above $\ell \sim 100$ (Park et al., 2016), we do not expect them to affect our predictions.

The realistic possibility of detecting the cosmological gravitomagnetic effect with future weak-lensing surveys and CMB experiments suggests that it is worthwhile to explore the lensing-kSZ cross-correlation in the context of dark energy and modified gravity theories, in which the amplitude of both the kSZ effect (e.g., Bianchini & Silvestri, 2016; Mitchell et al., 2021) and the gravitomagnetic field (Thomas et al., 2015a; Reverberi & Daverio, 2019) can be significantly enhanced. Thus, we expect to find a larger signal in these models, which could potentially be used as a new way to constrain deviations from ΛCDM. On the other hand, it also worthwhile to study the gravitomagnetic effects in CMB lensing and its cross correlation with CMB temperature maps. Given that the kernel of the former effect peaks at $z \sim 2$, this would allow one to include more signal from higher redshifts than a weak-lensing survey, and it is likely to boost the SNR. We leave these investigations as future work.

Chapter 7

Conclusion

7.1 Summary of the thesis

In Chapter 2 we have introduced GRAMSES, a new pipeline for nonlinear cosmological N-body simulations in GR. This code adopts the ADM $(3+1)$ formalism of GR, with constant mean curvature and minimum distortion gauge fixings, which provides a fully nonlinear and background independent framework for relativistic cosmology. Employing a fully constrained formulation (Cordero-Carrión et al., 2009), the Einstein equations are reduced to a set of ten elliptic-type equations which are solved using multigrid relaxation with AMR, and three hyperbolic equations for the evolution of tensor degrees of freedom. The current version of GRAMSES neglects the latter by using the conformal flatness approximation, which allows it to compute the two scalar and two vector degrees of freedom of the metric. We described the methodology, implementation, code tests and first results for simulations in a ΛCDM universe. Inheriting the efficient AMR and massive parallelisation infrastructure from the publicly-available N-body and hydrodynamic simulation code RAMSES, GRAMSES is ideal for studying the detailed behaviour of spacetime inside virialised cosmic structures and hence accurately quantifying the impact of backreaction effects on the cosmic expansion, as well as for investigating GR effects on cosmological observables using cosmic-volume simulations.

In Chapter 3 we have addressed the generation of ICs for GRAMSES. In the gauge adopted by this code the linear growth rate is scale-dependent, and the standard method for realising initial particle data is not straightforwardly applicable. We have introduced a new method, in which the initial positions of particles are generated from the displacement field realised for a matter power spectrum as usual, but the velocity is calculated by finite-differencing the displacement fields around the initial redshift. In this way, all the information required for

setting up the initial conditions is drawn from three consecutive input matter power spectra, and additional assumptions such as scale-independence of the linear growth factor and growth rate are not needed. We implemented this method in a modified version of the 2LPTic code, and demonstrated that in a Newtonian setting it can reproduce the velocity field given by the default 2LPTic code with subpercent accuracy. We also showed that the matter and velocity power spectra of the initial particle data generated for GRAMSES simulations using this method agree very well with the linear-theory predictions in the particular gauge used by GRAMSES. Finally, we discussed corrections to the finite difference calculation of the velocity when radiation is present, as well as additional corrections implemented in GRAMSES to ensure consistency. The method presented is not restricted to GRAMSES but it can be applied in ICs generation for GR simulations in generic gauges, and simulations of cosmological models with scale-dependent linear growth rate.

In Chapter 4, we presented the results of a code comparison of GRAMSES against state-of-the-art GR codes. In this, we simulated solutions to Einstein's field equations dominated by the effect of frame-dragging — the leading order post-Newtonian effect — and we applied a ray-tracing algorithm to study its effect on the photon propagation. We found that the code is able to match linear theory with subpercent accuracy where the latter is applicable, and at the same time it has an overall good agreement with the results from other codes at the nonlinear regime. Furthermore, in a resolution test the code showed a very consistent convergence rate, which is likely due to the constrained formulation of GR that is implemented, in which the gravitomagnetic potential (as well as the scalar potentials) is solved from an elliptic-type equation and hence avoids errors due to time integration. This demonstrates that GRAMSES is able to produce robust results for this very important effect.

In Chapter 5 we investigated the vorticity field of CDM and the gravitomagnetic potential, which correspond to the rotational (vector) components of the gravitational and velocity fields, respectively. Based on a high-resolution simulation run with GRAMSES, we studied the generation of vorticity at low redshift, providing fits to the shape and evolution of its power spectrum over a range of scales. By analysing the gravitomagnetic potential, which is absent in Newtonian simulations, in dark matter haloes with masses ranging from $\sim 10^{12.5}\ h^{-1}\mathrm{M}_\odot$ to $\sim 10^{15}\ h^{-1}\mathrm{M}_\odot$, we find that its magnitude correlates with the halo mass, peaking in the inner regions. Nevertheless, on average, its ratio against the scalar gravitational potential remains fairly constant, below percent level, decreasing roughly linearly with redshift and showing a weak dependence on halo mass. Furthermore, we showed that the gravitomagnetic acceleration in haloes peaks towards the core and reaches almost $10^{-10}\ h\ \mathrm{cm/s}^2$ in the most

massive halo of the simulation. This is found to be about one order of magnitude larger than results from previous lower-resolution GR simulations in the literature. However, regardless of the halo mass, the ratio between the gravitomagnetic force and the standard gravitational force is typically at around the 10^{-5} level inside the haloes, again without significant radius dependence. The result confirms that gravitomagnetic effects have negligible impact on structure formation, even for the most massive structures, although its behaviour in low density regions remains to be explored. Likewise, the impact on photons and hence observations is yet to be quantified.

In Chapter 6, we explored the possibility of detecting the lensing effect that is induced by the gravitomagnetic field by cross-correlating the weak lensing convergence field with a second observable. For the latter, we use a CMB temperature map imprinted with the kSZ signal since this effect shares a common origin with frame-dragging: both are sourced by the momentum field of matter. This approach allows us to extract the gravitomagnetic effect from a total convergence map because the cross correlation between the standard Newtonian contribution to the weak-lensing convergence field, κ_Φ, and the kSZ effect is expected to vanish. We studied the cross correlations with a suite of large-volume Newtonian N-body simulations and a small-volume, high-resolution, general-relativistic N-body simulation counterpart. We showed that insufficient simulation resolution can introduce significant spurious correlations between κ_Φ and kSZ.

Based on the high-resolution simulation, we found that the cumulative signal-to-noise ratio (SNR) of the kSZ-gravitomagnetic convergence field can reach almost 15 (30) at $\ell \simeq 5000$ (10^4) if only cosmic variance is considered. Then, we made forecast for next-generation lensing surveys such as EUCLID and LSST, and CMB experiments such as Simons Observatory and CMB-S4, and find that the cumulative SNR can exceed 5 (9) at $\ell \simeq 5000$ (10^4). This result indicates that the cosmological gravitomagnetic effect can be detected, provided that several foreground contaminations can be reliably removed.

7.2 Future work

In order to make realistic mock observations for the next generation of LSS surveys, we require simulations with large box size and high spatial (force) resolution. This is a major challenge for relativistic codes, which are intrinsically more computationally expensive than a Newtonian counterpart. In this regard, GRAMSES offers a balance between solving

a background-free GR formulation that can keep scalar and vector modes fully nonlinear, and the ability to run large-volume simulations while resolving small scales very accurately, thanks to AMR.

In the context of relativistic effects, there are strong motivations to be able to probe the small-scale, highly-nonlinear regime, e.g., deep inside dark matter haloes. For example, to study the characteristic dipole feature that appears in the redshift-space cross-correlation between different population of galaxies (Bonvin et al., 2014) we need to accurately predict the gravitational redshifts of galaxies inside haloes (Zhu et al., 2017). On the other hand, in Barrera-Hinojosa et al. (2021) we have shown that a high-resolution GR simulation predicts amplitudes of the gravitomagnetic force an order of magnitude larger than a particle-mesh GR simulation with a lower spatial resolution. Above all, a high resolution GR simulation will help us resolve the substructures of haloes, allowing us to use techniques such as abundance matching to populate them by mock galaxies with more realistic spatial distributions to measure relativistic effects accurately.

The generation of relativistic mock LSS observables comprise two steps: (i) generating mock galaxies from the simulations and (ii) modelling the light propagation across the inhomogeneous universe. For (i), a high-resolution simulation will make it is possible to use both halo occupation distribution and abundance matching techniques. The most physically realistic way to implement (ii) is to use ray-tracing facilities, which for GRAMSES can be adapted from the MAGRATHEA code (Reverdy et al., 2017). Such a infrastructure could solve the photon geodesics connecting sources to observers using the high-resolution (AMR) data of the spacetime metric from the simulations. Alternatively to ray-tracing, approximate methods such as LIGER (Borzyszkowski et al., 2017) can serve to generate mock relativistic effects via post-processing.

Based on the aforementioned points, which serve as motivation for the use of large-volume, high-resolution GR simulations, we outline some potential directions for future work below.

Disentangling gravitomagnetic effects in the lensing convergence field

As a natural extension to the investigation presented in Chapter 6, the distortion imprinted by the gravitomagnetic potential in the lensing convergence field can be investigated using convergence maps constructed via ray tracing, which naturally include the gravitomagnetic effects in the photon propagation. This will allow us to evaluate the convergence-kSZ cross correlation more realistically in comparison with Chapter 6, for instance by accounting for

the evolution of structures in the simulations. An interesting branch for this project is to investigate the kSZ-lensing cross correlation in dark energy and modified gravity models, where both signals are expected to be enhanced, which could potentially lead to developing a new probe to constrain deviations from ΛCDM with future experiments.

Measuring the imprints of relativistic effects in the observed LSS

A characteristic signal of some relativistic effects, such as the Doppler effect and gravitational redshift, is the asymmetry in the cross correlation between different type of matter tracers such as faint and bright galaxies, and the 21 cm signal — also manifested as an imaginary part in the cross-power spectrum (McDonald, 2009) — which is one of the aims of future LSS surveys. We can measure such a feature with specially designed estimators (e.g., the 'shell' estimator introduced in Croft (2013)) or, more commonly, by the odd multipoles in a multipole expansion (Bonvin, 2014). The dipole term in the cross correlation has been explored using high-resolution (AMR) Newtonian simulations with ray tracing in Breton et al. (2019), and more recently in Guandalin et al. (2021) using GR-particle-mesh simulations with fixed spatial resolution across the simulation volume. On the other hand, the 'shell' estimator has been applied to Newtonian simulations with relativistic effects introduced by hand in Croft (2013) and Zhu et al. (2017), which lack a GR counterpart. Importantly, it has been shown that uncertainties in how the potential wells of the sub-haloes are mapped to the potential of galaxies can strongly impact the predictions of the gravitational redshift (Zhu et al., 2017), making it crucial to evaluate the relativistic signal using realistic mock galaxy catalogues. Hence, a high-resolution GRAMSES simulation can be very useful to study the relativistic dipole feature.

7.3 Concluding remarks

The realistic modelling of observables for future sky surveys and CMB experiments requires N-body simulations that incorporate — at least at some degree — relativistic effects in the pipeline. In the last few years, cosmological general-relativistic simulations have quickly evolved to supply this need, with various independent codes now fully functional. Nonetheless, some challenges still need to be overcome, such as the inclusion of baryonic effects — an aspect that remains exclusive to Newtonian simulations — which could affect the signal of the relativistic effects. At the same time, we have found that the cosmological signal of a

characteristic effect such as frame-dragging can be extracted via cross-correlation methods for its detection with future experiments.

Approximations such as the constrained formulation of GR implemented in GRAMSES — in which tensor modes are neglected — or the weak-field expansion of *gevolution*, are arguably necessary in order to make large-volume GR simulations of cosmic structure formation computationally feasible and competitive to modelling GR effects for next-generation galaxy surveys. In the same vein, given that in Chapter 5 we showed that, while AMR capabilities can be important to accurately quantifying some effects such as frame-dragging in haloes, its effects on CDM particles remain nonetheless very weak, further optimisations of the simulations might be possible. Indeed, we have done preliminary tests using GRAMSES as a post-processing tool to calculate the gravitomagnetic field based on an snapshot of a Newtonian simulation (which could be regarded effectively as a 'Post-Friedmann simulation'), finding similar results to a GRAMSES simulation. Hence, we believe that such a method could also prove useful for the efficient prediction of relativistic effects, although some effects such as cosmological back-reaction might still require a full GR simulation.

Appendix A

Leapfrog scheme for time evolution of particles

GRAMSES uses the usual leapfrog or Stormer-Verlet scheme for particle movements. In this scheme, the position and momentum (or velocity) of a given particle from step n to step $(n+1)$, with a time interval Δt, are updated using the following prescription,

$$p^{n+1/2} = p^n - \frac{\Delta t}{2} H_x \left(x^n, p^{n+1/2}\right), \tag{A.0.1}$$

$$x^{n+1} = x^n + \frac{\Delta t}{2}\left[H_p(x^n, p^{n+1/2}) + H_p(x^{n+1}, p^{n+1/2})\right], \tag{A.0.2}$$

$$p^{n+1} = p^{n+1/2} - \frac{\Delta t}{2} H_x \left(x^{n+1}, p^{n+1/2}\right), \tag{A.0.3}$$

where $n+1/2$ is the middle between the two neighbouring timesteps t^n and t^{n+1}, p is the conjugate momenta to the canonical variable x, $H(x,p)$ is the Hamiltonian of the system, and H_x, H_p are the partial derivatives of $H(x,p)$ with respect to x and p respectively. In the case of Newtonian gravity $H = p^2/2m + \Phi_N(x)$, where $p = mv$ and $\Phi_N(x)$ is the Newtonian gravitational potential, the Hamiltonian H is completely separable for x and v, and the above operations reduce to the standard Kick-Drift-Kick (KDK) scheme

$$v^{n+1/2} = v^n - \frac{\Delta t}{2}\partial_x \Phi_N(x^n) \tag{A.0.4}$$

$$x^{n+1} = x^n + \Delta t v^{n+1/2} \tag{A.0.5}$$

$$v^{n+1} = v^{n+1/2} - \frac{\Delta t}{2}\partial_x \Phi_N(x^{n+1}) \tag{A.0.6}$$

Apparently, this makes the system explicit, i.e., the right-hand sides of Eqs. (A.0.4)-(A.0.6) do not depend on the quantities (which are at step $(n+1)$) on the left-hand sides. Although from Eqs. (A.0.4) and (A.0.6) it would seem that we need to do two force calculations per

time step, this is not actually the case since $\partial_x \Phi_N(x^{n+1})$ in (A.0.6) is the same as the force in (A.0.4) in the next step, so the second Kick (A.0.6) operation can wait until the following (i.e., the $(n+1)$th) timestep when $\Phi_N(x^{n+1})$ has been solved. In other words, in practice the second Kick operation (A.0.6) for the $n$the timestep is done after the Newtonian potential is solved in the $(n+1)$th timestep; in RAMSES this is called synchronisation as it finally 'synchronises' all particle velocities to the correct time before these velocities can be used to move (Drift) the particles.

In the case of GR, the Hamiltonian of a free particle,in the 3+1 formalism is

$$H = \alpha\sqrt{m^2 + \gamma^{ij} p_i p_j} - \beta^i p_i \tag{A.0.7}$$

where $p_i = m u_i$ is the (spatial) momentum. Using Hamilton's equations

$$\frac{\mathrm{d}x^i}{\mathrm{d}t} = \frac{\partial H}{\partial p_i}\,, \tag{A.0.8}$$

$$\frac{\mathrm{d}p_i}{\mathrm{d}t} = -\frac{\partial H}{\partial x^i}\,, \tag{A.0.9}$$

we can derive the equation of motion for this system, i.e., the geodesic equations (2.4.46)-(2.4.48). We note that in this case the Hamiltonian (A.0.7) is not separable, because there is the multiplication of γ^{ij} (which depends on x) and $p_i p_j$ under the square root. Therefore, the leapfrog system (A.0.1)-(A.0.3) is implicit and not straightforward to implement as in the Newtonian case. The simplest approximation to make the system explicit is to evaluate the Hamiltonian derivatives at the wrong phases, i.e.,

$$u^{n+1/2} = u^n + \frac{\Delta t}{2} F(x^n, u^n), \tag{A.0.10}$$

$$x^{n+1} = x^n + \Delta t \mathcal{V}(x^n, u^{n+1/2}), \tag{A.0.11}$$

$$u^{n+1} = u^{n+1/2} + \frac{\Delta t}{2} F(x^{n+1}, u^{n+1/2}), \tag{A.0.12}$$

where

$$F_i = -\frac{W}{c}\partial_i \Phi + u_j \partial_i \beta^j - \frac{W^2 - c^2}{Wc} \frac{1 + \frac{\Phi}{a^2c^2}}{1 - \frac{\Psi}{2a^2c^2}} \partial_i \Psi\,, \tag{A.0.13}$$

$$\mathcal{V}^i = \left(1 + \frac{\Phi}{a^2c^2}\right)\left(1 - \frac{\Psi}{2a^2c^2}\right)^{-4} \frac{c}{W}\delta^{ij} u_j - \beta^i. \tag{A.0.14}$$

Notice that here, for evaluating $\mathcal{V}(x^n, u^{n+1/2})$ used in (A.0.11) according to (A.0.14), we use the current value of the gravitational fields (Φ, Ψ, α and β_i) and only the quantities depending on u_j (including W) are updated (to $t^{n+1/2}$). Likewise, in (A.0.12) the force term $F(x^{n+1}, u^{n+1/2})$ uses the updated velocities for the explicit dependence on $u^{n+1/2}$ as well as

for the source terms for the fields at the new timestep. Finally, for repeating the process, in (A.0.10) we use the updated velocities for the explicit dependences on u^n and geometric fields based on the updated particles positions (with sources at $u^{n+1/2}$).

Let us remark that even if in the Hamiltonian formalism the variables (x, p) are independent (conjugate) variables, and in the second Kick step (A.0.12) the various gravitational fields appearing in $F(x^{n+1}, u^{n+1/2})$ are solved at the final positions, e.g. $\Phi(x^{n+1})$, the source terms for their equations have used the velocities $u^{n+1/2}$ because we have not yet synchronised by the time we evaluate these sources at timestep $(n + 1)$, and thus the fields carry a delayed information about the velocities by half a timestep. Again, this issue is not present in the Newtonian case since the gravitational field Φ_N is only sourced by the mass density field which depends only on the particles position but not on their velocities. A possible way to get around this is to temporarily update the velocity before carrying (A.0.12) using Poisson equation for the Newtonian gravitational potential Φ_N, giving us an estimated updated velocity, namely

$$u_N^{n+1} = u^{n+1/2} - \frac{\Delta t}{2}\partial_x \Phi_N \,, \tag{A.0.15}$$

which can be used (as an approximation) in the source terms for the GR potentials. After solving the field equations for these the velocity is then reverted back to $u^{n+1/2}$, after which 'true' synchronisation (A.0.12) is performed.

In principle, the above scheme could be further improved by introducing an extra step to update the position in such a way that the symplecticity of the scheme is restored (although time-reversal invariance is still broken). However, since for simulations with AMR the adaptive timesteps render the KDK scheme non-symplectic even in the Newtonian case, we shall not explain these alternatives, which are more complicated, in detail here.

Appendix B

Mapping of linear equations from the CMC-MD gauge

In this Appendix we include further details on the mapping between the linearised version of GRAMSES equations and their standard synchronous gauge and Newtonian gauge counterparts. For simplicity, in this discussion we focus on scalar perturbations only, so that the gauge transformation can be written as $\xi_\mu = (\xi_0, \partial_i \xi)$, but the results can be extended to include vector modes straightforwardly.

B.1 Field equations

Let us show the correspondence between the field equations in the synchronous and CMC-MD gauges at linear level. We shall ignore the prime notation used for the gauge-transformed variables in Section 3.3 and instead use Φ, β_i, Ψ and h_{ij} to denote the metric perturbations in the CMC-MD gauge. For the synchronous gauge metric Eq. (3.4.16), we use the variables h, $h^{\parallel}_{ij}$, η and μ following exactly the convention of Ma & Bertschinger (1995). Using that, at linear order, the MD gauge condition Eq. (2.2.22) reduces to $\partial^i h_{ij} = 0$, from Eq. (3.3.9) we find the following condition for the spatial transformation ξ

$$2a^{-2}\xi = h + 6\eta\,. \tag{B.1.1}$$

Likewise, because the CMC gauge is defined by a condition over K, it is useful to derive the explicit gauge transformation for this quantity. The extrinsic curvature at the linear level is

given by

$$K_{ij} = -H(1-\Phi)\gamma_{ij} + \dot{\Psi}\gamma_{ij} - \frac{a^2}{2}\dot{h}_{ij} + \frac{1}{2}(\partial_i\beta_j + \partial_j\beta_i)\,, \tag{B.1.2}$$

and its trace given by $K = -3H(1-\Phi) + 3\dot{\Psi} + a^{-2}\delta^{ij}\partial_i\beta_j$. Then, using the gauge transformations Eqs. (3.3.5)-(3.3.8) on the right-hand side of the latter, we find that K transforms as

$$K = K' + 3\dot{H}\xi_0 + \gamma^{ij}\partial_i\partial_j\xi_0\,. \tag{B.1.3}$$

As expected, Eq. (B.1.3) is independent of ξ^i and can be used to connect the time coordinate defined by the CMC foliation with that in any other gauge regardless of the choice of spatial coordinates. For the case of synchronous gauge, using that $K_{\rm S} = -3H - \dot{h}/2$ and Eq. (2.2.17), we find

$$\dot{h} = -6\dot{H}\xi_0 - 2\gamma^{ij}\partial_i\partial_j\xi_0\,, \tag{B.1.4}$$

where $\gamma^{ij}\partial_i\partial_j = a^{-2}\delta^{ij}\partial_i\partial_j \equiv a^{-2}\partial^2$.

Let us now consider the Hamiltonian constraint and Eq. (3.2.3). These are given at the linear order by

$$\partial^2\Psi = 4\pi G a^2\delta\rho, \tag{B.1.5}$$

$$\partial^2\Phi + 3\dot{H}a^2\Phi = 4\pi G a^2\delta\rho + 12\pi G a^2\delta P, \tag{B.1.6}$$

where $\delta\rho = \bar{\rho}\delta^{\rm C}$ with $\delta^{\rm C}$ is the density contrast in the CMC-MD gauge. Using the gauge transformations Eq. (3.3.8) and Eq. (3.3.13), Eq. (B.1.5) can be rewritten in terms of the synchronous gauge and gauge transformation variables as

$$-\frac{1}{6}\partial^2 h - H\partial^2\xi_0 + \frac{1}{3}a^{-2}\partial^4\xi = 4\pi G a^2\bar{\rho}\delta^{\rm S} - 12\pi G a^2 H(\bar{\rho}+\bar{P})\xi_0\,. \tag{B.1.7}$$

Applying the gauge relations Eq. (B.1.1) and Eq. (B.1.4), the left-hand side of this equation becomes

$$-H\partial^2\xi_0 = \frac{1}{2}a^2 H\dot{h} + 3H\dot{H}a^2\xi_0 = \frac{1}{2}a^2 H\dot{h} - 12\pi G a^2(\bar{\rho}+\bar{P})H\xi_0\,, \tag{B.1.8}$$

where in the second equality we have used the background relation

$$\dot{H} = -4\pi G(\bar{\rho}+\bar{P})\,. \tag{B.1.9}$$

Therefore, Eq. (B.1.8) can be simplified as

$$\partial^2\eta + \frac{1}{2}a^2 H\dot{h} = 4\pi G a^2\bar{\rho}\delta^{\rm S}\,, \tag{B.1.10}$$

which is the (00) Einstein equation in synchronous gauge (Ma & Bertschinger, 1995).

Next, let us consider how Eq. (B.1.6) transforms. Using the gauge transformations Eq. (3.3.5) and Eq. (3.3.13), as well as the gauge transformation for the pressure perturbation $\delta P^{\rm C} = \delta P^{\rm S} + \dot{\bar{P}}\xi_0$, Eq. (B.1.6) can be rewritten as

$$\partial^2\dot{\xi}_0 + 3\dot{H}a^2\dot{\xi}_0 = 4\pi G a^2\delta\rho^{\rm S} - 12\pi G a^2 H(\bar{\rho}+\bar{P})\xi_0 + 12\pi G a^2\delta P^{\rm S} + 12\pi G a^2\dot{\bar{P}}\xi_0\,. \quad \text{(B.1.11)}$$

In order to eliminate ξ_0 and $\dot{\xi}_0$ from the left-hand side of this equation, we take the time derivative of the gauge relation Eq. (B.1.4), to get

$$-\frac{1}{2}\ddot{h} - H\dot{h} = 4\pi G\left(\delta\rho^{\rm S} + 3\delta P^{\rm S}\right) - 12\pi G H(\bar{\rho}+\bar{P})\xi_0 + 3\ddot{H}\xi_0 + 6H\dot{H}\xi_0 + 12\pi G\dot{\bar{P}}\xi_0\,, \quad \text{(B.1.12)}$$

and taking the time derivative of Eq. (B.1.9) allows us to get rid of $\ddot{H}$ and all terms proportional to ξ_0 in the right-hand side of Eq. (B.1.12), leaving

$$-\frac{1}{2}\ddot{h} - H\dot{h} = 4\pi G\left(\delta\rho^{\rm S} + 3\delta P^{\rm S}\right)\,, \quad \text{(B.1.13)}$$

which is equivalent to the linear combination of Einstein equations $2\times(00)+(ii)$ in synchronous gauge (Ma & Bertschinger, 1995) (where (ii) denotes the trace of the (ij) components of the Einstein equation).

Next, let us consider the momentum constraint, which gives the longitudinal part of the conformal curvature tensor $\bar{A}_{ij}$. This is given at linear order by (Barrera-Hinojosa & Li, 2020)

$$\left(\bar{\Delta}_L W\right)_i = \partial^2 W_i + \frac{1}{3}\partial_i\delta^{kl}\partial_k W_l = 8\pi G a^3\left(\bar{\rho}+\bar{P}\right)u_i^{\rm C}\,, \quad \text{(B.1.14)}$$

with

$$\bar{A}_{ij} = \left(\bar{L}W\right)_{ij} \equiv \partial_i W_j + \partial_j W_i - \frac{2}{3}\delta_{ij}\partial_k W^k\,. \quad \text{(B.1.15)}$$

We will use Eq. (B.1.15) to solve W_i first, and then substitute into Eq. (B.1.14) to get an equation that contains the peculiar velocity. The right-hand side of Eq. (B.1.15) can be written as

$$\left(\bar{L}W\right)_{ij} = 2\left(\partial_i\partial_j - \frac{1}{3}\delta_{ij}\partial^2\right)W\,, \quad \text{(B.1.16)}$$

where, given that we specialise to the scalar mode only, we have introduced the variable W such that $W_i = \partial_i W$. Using the fact that at the linear level $\bar{A}_{ij} = aA_{ij}$, from the traceless

part of (B.1.2) we find

$$\bar{A}_{ij} = -\frac{1}{2}a^3\dot{h}_{ij} + \frac{1}{2}a\left(\partial_i\beta_j + \partial_j\beta_i\right) - \frac{1}{3}a\delta^{kl}\partial_k\beta_l\delta_{ij}\,, \tag{B.1.17}$$

and, using Eq. (3.3.6) to get rid of β_i, as well as Eq. (3.3.9) to get rid of $\dot{h}_{ij}$, we find

$$\bar{A}_{ij} = -a\left(\partial_i\partial_j - \frac{1}{3}\delta_{ij}\partial^2\right)\xi_0 - \frac{1}{2}a^3\left(\partial_i\partial_j - \frac{1}{3}\delta_{ij}\partial^2\right)\dot{\mu}\,, \tag{B.1.18}$$

where μ is a synchronous gauge scalar perturbation variable whose relation with h, η is given below. Combining Eq. (B.1.16) and Eq. (B.1.18) gives the result

$$W = -\frac{1}{2}a\xi_0 - \frac{1}{4}a^3\dot{\mu}\,. \tag{B.1.19}$$

Using the gauge transformation for u_i, Eq. (3.3.14), in the right-hand side of Eq. (B.1.14), then applying ∂^i on both sides and substituting the result Eq. (B.1.19), we get

$$-\frac{2}{3}a\partial^2\partial^2\xi_0 - \frac{1}{3}a^3\partial^4\dot{\mu} = 8\pi G a^3\left(\bar{\rho}+\bar{P}\right)\left(\partial^i u_i^{\rm S} - \partial^2\xi_0\right)\,. \tag{B.1.20}$$

Now, using Eq. (B.1.4) to eliminate $\partial^2\partial^2\xi_0$ from the left-hand side of this equation, as well as the synchronous gauge relation $\partial^2\mu = h + 6\eta$, we have

$$\frac{1}{3}a^3\partial^2\dot{h} + 2\dot{H}a^3\partial^2\xi_0 - \frac{1}{3}a^3\partial^2\left(\dot{h}+6\dot{\eta}\right) = 8\pi G a^3\left(\bar{\rho}+\bar{P}\right)\left(\partial^i u_i^{\rm S} - \partial^2\xi_0\right)\,. \tag{B.1.21}$$

Finally, by using the first and second Friedmann equations, we can eliminate the terms proportional to $\partial^2\xi_0$ from the above equation, which reduces to

$$-2\partial^2\dot{\eta} = 8\pi G(\bar{\rho}+\bar{P})\theta^{\rm S}\,, \tag{B.1.22}$$

where $\theta^{\rm S} = \partial^i u_i^{\rm S}$. This corresponds to the $(0i)$ Einstein equation in synchronous gauge (Ma & Bertschinger, 1995).

B.2 Equations of motion

Let us provide a complementary derivation of the relation $u^i_{\rm C} = u^i_{\rm N}$ mentioned in Section 3.3. For this, we consider the geodesic equations for non-relativistic particles, which at the linear level are given by Eqs. (3.4.32) and (3.4.33). We next show that in the linear perturbation regime, the equation for $u^i_{\rm C}$ is identical to that of $u^i_{\rm N}$ in the Newtonian gauge.

Inverting the relation in Eq. (3.4.34) for u^i and taking one time derivative, we have

$$\dot{u}^i_{\rm C} = \frac{\rm d}{{\rm d}t}\left(\gamma^{ij}u^{\rm C}_j - \beta^i\right) = -2H\gamma^{ij}u^{\rm C}_j - \gamma^{ij}\partial_j\Phi - \dot{\beta}^i\,, \tag{B.2.1}$$

where in the second step we have used Eq. (3.4.32) to get rid of $\dot{u}^{\rm C}_j$. Now, using Eq. (3.4.34) and $\beta^i = a^{-2}\delta^{ij}\beta_j$, we obtain

$$\dot{u}^i_{\rm C} = -2Hu^i_{\rm C} - \gamma^{ij}\partial_j\Phi - \gamma^{ij}\dot{\beta}_j\,. \tag{B.2.2}$$

To make a connection with the Newtonian gauge we consider the metric Eq. (3.4.7). From the gauge transformations Eq. (3.3.5)-(3.3.9) we find the following relations between the CMC-MD and Newtonian gauge metric perturbations

$$\Phi = \psi + \dot{\xi}_0, \tag{B.2.3}$$

$$\beta_i = -\dot{\xi}_i - \partial_i\xi_0 + 2H\xi_i, \tag{B.2.4}$$

$$\Psi = \phi - H\xi_0 + \frac{1}{3}\gamma^{ij}\partial_j\xi_i, \tag{B.2.5}$$

$$h_{ij} = -a^{-2}\left(\partial_j\xi_i + \partial_i\xi_j\right) + \frac{2}{3}\gamma^{kl}\partial_l\xi_k\delta_{ij}\,. \tag{B.2.6}$$

By using the MD gauge condition $\partial^i h_{ij} = 0$ in Eq. (B.2.6), we find $\xi_i = 0$ in this case. Then, after applying the gauge transformations for Φ and β_i, Eqs. (B.2.3) and (B.2.4), the equation of motion Eq. (B.2.2) becomes

$$\dot{u}^i_{\rm C} + 2Hu^i_{\rm C} + \gamma^{ij}\partial_j\psi = 0\,, \tag{B.2.7}$$

which is identical to the Newtonian gauge counterpart, $\dot{u}^i_{\rm N} + 2Hu^i_{\rm N} + \gamma^{ij}\partial_j\psi = 0$. This equation-level equivalence is not surprising given that $u^i_{\rm C} = u^i_{\rm N}$, which is a consequence of $\xi_i = 0$.

To make connection with synchronous gauge, we combine the geodesic equations to eliminate u_i and get a second order differential equation for x^i,

$$\frac{{\rm d}^2x^i}{{\rm d}t^2} + 2H\frac{{\rm d}x^i}{{\rm d}t} + a^{-2}\delta^{ij}\partial_j\Phi + a^{-2}\delta^{ij}\dot{\beta}_j = 0\,, \tag{B.2.8}$$

which is for the CMC-MD gauge. We can rewrite this equation in terms of the gauge transformation and synchonous gauge variables, using Eqs. (3.3.5) and (3.3.6), to find

$$\partial_i\Phi + \dot{\beta}_i = -\partial_i\ddot{\xi} + 2\dot{H}\partial_i\xi + 2H\partial_i\dot{\xi}\,. \tag{B.2.9}$$

The particle coordinate in the synchronous gauge, denoted as $x^i_{\rm S}$, is related to the CMC-MD gauge coordinate x^i as $x^i = x^i_{\rm S} + a^{-2}\delta^{ij}\partial_j\xi$. Taking the time derivatives of the latter and substituting the resulting expressions into Eq. (B.2.8) gives

$$\frac{{\rm d}^2x^i_{\rm S}}{{\rm d}t^2} + 2H\frac{{\rm d}x^i_{\rm S}}{{\rm d}t} = 0\,, \tag{B.2.10}$$

as we expect to find in the synchronous gauge.

Appendix C

Comparison of power spectrum calculation methods for the potentials

In Section 5.3.1 of Chapter 5, the power spectrum of density, velocity and vorticity has been measured from particle-type data using DTFE and NBODYKIT, while the spectrum of the scalar and vector potentials has been measured using a different code that is able to read their values calculated and stored by GRAMSES in cells of hierarchical AMR meshes and interpolate them to a regular grid for the power spectrum measurement. We call this method the 'AMR-FFT' method, which was introduced in He et al. (2015), where more details can be found. An alternative to using this AMR-FFT method to calculate the power spectrum of the potentials is by writing their values with GRAMSES at the particles' positions rather than in AMR cells, so that DTFE can be used to read such 'particle-type' data and interpolate this to a regular grid, where NBODYKIT can be applied to measure the spectrum. We call this method 'DTFE+NBODYKIT'.

Figure C.1 shows the dimensionless power spectra at $z = 1$ of the scalar potential Φ (left panel) and the vector potential spectrum (right panel), measured by these two methods, where solid lines represent the perturbation-theory predictions. In both methods the FFT grid size is 2048^3, as is the tessellation grid size used for DTFE. We find that both methods have good agreement on large scales, specially at $k \gtrsim 0.1\ h\mathrm{Mpc}^{-1}$, where the effect of cosmic variance is not present. However, in the region $k \gtrsim 3\ h\mathrm{Mpc}^{-1}$ the AMR-FFT method has better performance than DTFE+NBODYKIT which blows up. This is because the AMR-FFT

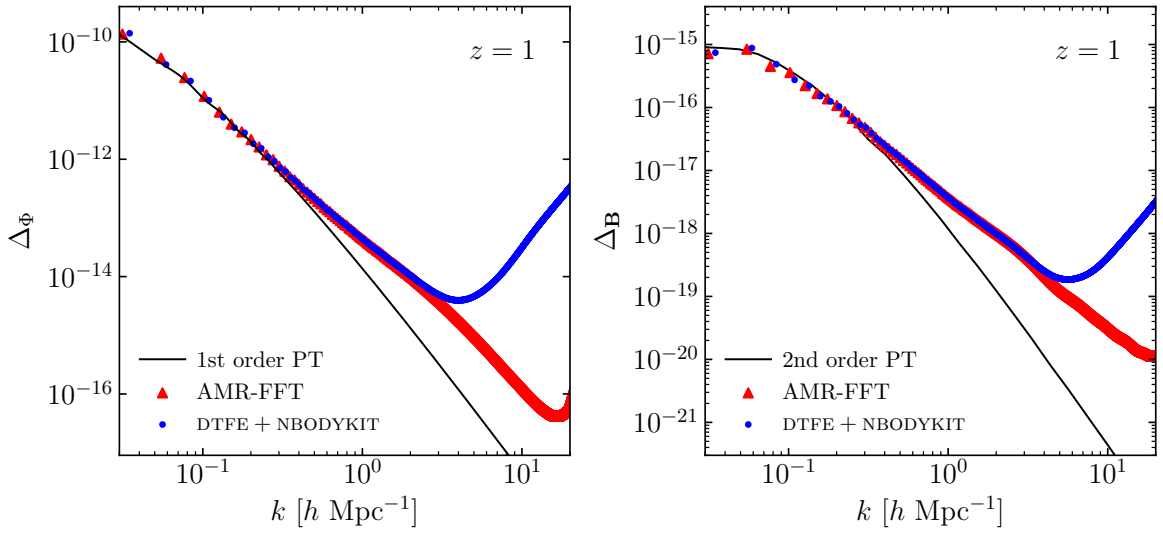

Figure C.1: Comparison of the power spectra of the scalar and vector potentials measured with the AMR-FFT method, and NBODYKIT combined with DTFE. In both methods the grid size used for the FFT is 2048^3, and is equal to the tessellation grid size used in DTFE. Both panels show the dimensionless power spectrum $\Delta(k) = k^3P(k)/(2\pi^2)$ of the respective field. *Left*: The dimensionless power spectrum of the of the scalar gravitational potential Φ defined as the fully nonlinear perturbation to the lapse function, i.e., $\Phi \equiv \alpha - 1$. The solid line represents the first-order perturbation theory prediction of the Bardeen potential from CAMB. *Right*: The dimensionless power spectrum of the vector potential $\mathbf{B}$. The solid line corresponds to the second-order perturbation theory result from Eq. (5.3.5). All results are at $z = 1$.

method can reach higher resolution by using the potential information in the AMR cells, and because DTFE does a volume weighted average of the field which smears out small-scale features. Therefore, the spectrum of the scalar and vector potentials from the simulation shown in Fig. 5.5 are measured by the AMR-FFT method, which yields robust results up to $k \sim 15\ h\text{Mpc}^{-1}$.

Appendix D

The kinetic Sunyaev-Zel'dovich (kSZ) effect

CMB photons can interact with fast-moving free electrons in the intergalactic medium (IGM) via inverse Compton scattering, which subsequently changes their energy and imprints a secondary CMB anisotropy known as the kinetic Sunyaev-Zel'dovich (kSZ) effect (Sunyaev & Zeldovich, 1980). The temperature fluctuation along the line-of-sight (LOS) vector $\hat{\mathbf{n}}$ due to this effect can be described by the following LOS integral,

$$b(\hat{\mathbf{n}}) \equiv -\frac{\Delta T(\hat{\mathbf{n}})}{\bar{T}} = \int \mathrm{d}\tau e^{-\tau} \frac{\hat{\mathbf{n}} \cdot \mathbf{v}}{c} = \sigma_{\mathrm{T}} \int \mathrm{d}l e^{-\tau} \frac{n_{\mathrm{e}} v_{\mathrm{r}}}{c} \,, \tag{D.0.1}$$

in which $\bar{T}$ is the mean temperature of the CMB, σ_{T} and τ are respectively the Thomson scattering cross section and optical depth, c is the speed of light, n_{e} is the number density of free electrons, and $v_r = \mathbf{v} \cdot \hat{\mathbf{n}}$ is the LOS component of the electron velocity field.

Since Eq. (D.0.1) is an effect integrated from $z = 0$ to the last scattering surface, $z \approx 1100$, the kSZ signal has two distinct contributions, one coming from the post-reinoisation epoch, in which the IGM is nearly fully ionised and the electron density field closely follows the density field of baryons; and the contribution from the epoch of reionisation, where n_{e} suffers strong temporal and spatial variations. As the goal of this paper is to study the cross correlation of the kSZ effect with a weak lensing survey such as LSST and EUCLID, throughout the present analysis we restrict our attention to the post-reionisation kSZ signal.

The specific ionised momentum field of the ionised medium can be defined as

$$\mathbf{q} \equiv \chi_{\mathrm{e}}(1 + \delta)\mathbf{v} \,, \tag{D.0.2}$$

where δ is the baryon density contrast, and

$$\chi_{\rm e} \equiv \frac{n_{\rm e}}{n_{\rm H} + 2n_{\rm He}}\,, \tag{D.0.3}$$

denotes the ionised fraction, with $n_{\rm H}$, $n_{\rm He}$ being the number densities for hydrogen and helium, respectively. Also, defining

$$\bar{n}_{\rm e,0} \equiv n_{\rm H,0} + n_{\rm He,0}\,, \tag{D.0.4}$$

Eq. (D.0.1) can be rewritten as

$$b = \frac{\sigma_{\rm T}\bar{n}_{\rm e,0}}{c}\int {\rm d}\chi \frac{1}{a^2} e^{-\tau}\mathbf{q}\cdot\hat{\mathbf{n}}\,, \tag{D.0.5}$$

where χ is the comoving distance along the LOS. Using the Fourier transform of Eq. (D.0.5), we get

$$b = \frac{\sigma_{\rm T}\bar{n}_{\rm e,0}}{c}\int {\rm d}\chi \frac{1}{a^2(\chi)} e^{-\tau}\int \frac{{\rm d}^3\mathbf{k}}{(2\pi)^3}\left[\hat{\mathbf{n}}\cdot\tilde{\mathbf{q}}(\mathbf{k},\chi)\right] e^{-i\chi\mathbf{k}\cdot\hat{\mathbf{n}}}\,, \tag{D.0.6}$$

where $\mathbf{k}$ is the wavevector, i is the imaginary number unit, and $\tilde{\mathbf{q}}$ is the momentum vector in Fourier space. One can decompose $\tilde{\mathbf{q}}$ into a longitudinal (scalar) and a rotational (vector) part:

$$\tilde{\mathbf{q}} = \tilde{\mathbf{q}}_{\parallel} + \tilde{\mathbf{q}}_{\perp}, \quad \text{with} \quad \tilde{\mathbf{q}}_{\parallel} = (\tilde{\mathbf{q}}\cdot\hat{\mathbf{k}})\hat{\mathbf{k}}\,, \tag{D.0.7}$$

where $\hat{\mathbf{k}}$ is the unit vector in the direction of the wavevector. Substituting this into Eq. (D.0.6) gives (Park et al., 2013)

$$b = \frac{\sigma_{\rm T}\bar{n}_{\rm e,0}}{c}\int {\rm d}\chi \frac{1}{a^2(\chi)} e^{-\tau}\int \frac{{\rm d}^3\mathbf{k}}{(2\pi)^3}\left[x\tilde{q}_{\parallel}(\mathbf{k},\chi) - \cos\left(\phi_{\hat{\mathbf{q}}} - \phi_{\hat{\mathbf{n}}}\right)\sqrt{1-x^2}\tilde{q}_{\perp}(\mathbf{k},\chi)\right] e^{-ik\chi x}\,, \tag{D.0.8}$$

where $\tilde{q}_{\parallel} = |\tilde{\mathbf{q}}_{\parallel}|$, $x \equiv \hat{\mathbf{k}}\cdot\hat{\mathbf{n}}$, $\phi_{\hat{\mathbf{q}}}$ and $\phi_{\hat{\mathbf{n}}}$ are respectively the angle between $\mathbf{q}, \hat{\mathbf{n}}$ and $\mathbf{k}$. The exponential function in the integral represents a fast oscillation along the LOS, which means that the integrand cancels out, leading to negligible integral result. There are two exceptions to this: (1) if $k \to 0$, or (2) if $x \to 0$. (1) represents a long-wave mode which has a small amplitude and therefore contributes little to the integral anyway. (2) represents a case where $\mathbf{k}$ is perpendicular to the LOS, $\hat{\mathbf{n}}$. In other words, only the $\mathbf{k}$ modes that are perpendicular to the LOS contribute to the kSZ effect non-negligibly. But in this case we can see from Eq. (D.0.8) that the first term in the brackets vanishes since $x \to 0$, and therefore only the rotational momentum field $\tilde{q}_{\perp}$ remains, giving (e.g., Park et al., 2013)

$$b \simeq -\frac{\sigma_{\rm T}\bar{n}_{\rm e,0}}{c}\int {\rm d}\chi \frac{1}{a^2(\chi)} e^{-\tau}\int \frac{{\rm d}^3\mathbf{k}}{(2\pi)^3}\cos\left(\phi_{\hat{\mathbf{q}}} - \phi_{\hat{\mathbf{i}}}\right)\sqrt{1-x^2}\tilde{q}_{\perp}(\mathbf{k},\chi)e^{-ik\chi x}\,. \tag{D.0.9}$$

With some lengthy derivation (see, e.g., Appendix A of Park et al., 2013), one gets the following expression for the kSZ (b) angular power spectrum

$$C_\ell^b = \frac{1}{2}\left[\frac{\sigma_{\rm T}\bar{n}_{\rm e,0}}{c}\right]^2 \int \mathrm{d}\chi \frac{1}{\chi^2 a^4(\chi)} e^{-2\tau} P_{q_\perp}\left(k=\frac{\ell}{\chi},\chi\right) , \tag{D.0.10}$$

where $P_{q_\perp}$ is the 3D power spectrum of $q_\perp$, the rotational momentum field. Assuming that the velocity field is completely longitudinal, as it is the case for a pressureless perfect fluid, $P_{q_\perp}$ appears only at second order through the following convolution:

$$P_{q_\perp}(k,z) = \int \frac{\mathrm{d}^3\mathbf{k}'}{(2\pi)^3}(1-\mu^2)\left[P_{\delta\delta}\left(|\mathbf{k}-\mathbf{k}'|\right)P_{vv}(k') - \frac{k'}{|\mathbf{k}-\mathbf{k}'|}P_{\delta v}\left(|\mathbf{k}-\mathbf{k}'|\right)P_{\delta v}(k')\right] , \tag{D.0.11}$$

where $\mu = \hat{\mathbf{k}}\cdot\hat{\mathbf{k}}'$. If we define

$$w \equiv k'/k, \quad u \equiv |\mathbf{k}-\mathbf{k}'|/k\,, \tag{D.0.12}$$

then

$$\mu = \frac{1+w^2-u^2}{2w}\,, \tag{D.0.13}$$

and Eq. (D.0.11) can be recast as

$$P_{q_\perp}(k,z) = \frac{k^3}{4\pi^2}\int_0^\infty \mathrm{d}w \int_{|1-w|}^{1+w} \mathrm{d}u\Pi'\left[P_{\delta\delta}\left(ku\right)P_{vv}(kw) - \frac{w}{u}P_{\delta v}\left(ku\right)P_{\delta v}(kw)\right] , \tag{D.0.14}$$

where

$$\Pi' \equiv uw\frac{4w^2-(1+w^2-u^2)}{4w^2}\,. \tag{D.0.15}$$

Given that the gravitomagnetic field is sourced by the rotational modes of the momentum field through Eq. (6.2.3), Eq. (D.0.14) has a similar form to the gravitomagnetic potential power spectrum, which in the case of a pressureless perfect fluid is given by, e.g., Lu et al. (2008)

$$\Delta_{\mathbf{B}}(k) = \frac{9\Omega_m^2 H_0^2}{2a^2c^2k^2}\int_0^\infty \mathrm{d}w \int_{|1-w|}^{1+w} \mathrm{d}u\Pi\left[\Delta_{\delta\delta}(ku)\Delta_{vv}(kw) - \frac{w}{u}\Delta_{\delta v}(ku)\Delta_{\delta v}(kw)\right] , \tag{D.0.16}$$

where the dimensionless power spectrum Δ_{ab} is defined as

$$\Delta_{ab} \equiv \frac{k^3}{2\pi^2}P_{ab}\,, \tag{D.0.17}$$

with a, b standing for two fields, and

$$\Pi \equiv \frac{1}{u^2w^2}\frac{4w^2-(1+w^2-u^2)}{4w^2}\,. \tag{D.0.18}$$

Indeed, substituting Eq. (D.0.17) into Eq. (D.0.16) gives

$$P_{\mathbf{B}}(k) = \frac{k}{2\pi^2}\frac{9\Omega_m^2 H_0^2}{2a^2c^2}\int_0^\infty \mathrm{d}w \int_{|1-w|}^{1+w} \mathrm{d}u\Pi' \left[P_{\delta\delta}(ku)P_{vv}(kw) - \frac{w}{u}P_{\delta v}(ku)P_{\delta v}(kw)\right] , \quad \text{(D.0.19)}$$

which differs from (D.0.14) only in the prefactor (and the fact that here the density and velocity power spectra are for all matter, rather than free electrons only; the two are closely related) including a k^2.

Following the Appendix A of Park et al. (2013), we can derive a Limber-integral expression (which has been used extensively in this paper) for the cross angular power spectrum between $\kappa_{\mathbf{B}}$ and the kSZ effect (b). Given the above mathematical similarity between the two effects, the detailed steps will not be repeated here to be concise as the calculation is similar to the derivation of the kSZ auto-power spectrum. For generality, consider two 2D fields $X(\hat{\mathbf{n}})$ and $Y(\hat{\mathbf{n}})$ which are both related to the projection of the LOS momentum field $\mathbf{q}\cdot\hat{\mathbf{n}}$:

$$X, Y(\hat{\mathbf{n}}) = \int \mathrm{d}z K_{X,Y}(\chi) \int \frac{\mathrm{d}^3\mathbf{k}}{(2\pi)^3}\left[\hat{\mathbf{n}}\cdot\tilde{\mathbf{q}}\left(\mathbf{k}, z(\chi)\right)\right] e^{-i\chi\mathbf{k}\cdot\hat{\mathbf{n}}} , \quad \text{(D.0.20)}$$

where $K_{X,Y}(s)$ are respectively the LOS projection kernels for observables X and Y, which are functions of the comoving distance χ. The cross angular power spectrum between X and Y, C_ℓ^{XY}, is defined as

$$C_\ell^{XY}\delta_{\ell\ell'}\delta_{mm'} = \left\langle a_{\ell m}^X a_{\ell' m'}^{Y*}\right\rangle , \quad \text{(D.0.21)}$$

where $\langle\cdots\rangle$ denotes ensemble average, $*$ denotes the complex conjugate, and $a_{\ell m}^{X,Y}$ are the spherical harmonic decomposition coefficients for X and Y,

$$a_{\ell m}^{X,Y} = \int \mathrm{d}^2\hat{\mathbf{n}} X, Y(\hat{\mathbf{n}}) Y_\ell^{m*}(\hat{\mathbf{n}}) , \quad \text{(D.0.22)}$$

with Y_ℓ^m being the spherical harmonic function of degree ℓ and order m. Hence, C_ℓ^{XY} can be expressed as a weighted LOS integration of the 3D power spectrum of the rotational component of the LOS momentum field $\mathbf{q}\cdot\hat{\mathbf{n}}$, $P_{q_\perp}$, as:

$$C_\ell^{XY} \simeq \frac{1}{2}\int \mathrm{d}\chi \chi^{-2} K_X(\chi) K_Y(\chi) P_{q_\perp}\left(k = \frac{\ell}{\chi}, z(\chi)\right) . \quad \text{(D.0.23)}$$

Appendix E

The ISW-weak lensing cross correlation

In this appendix we derive an expression for the cross angular power spectrum between the integrated Sachs-Wolfe effect and weak lensing convergence. For simplicity, we assume again a single lensing source redshift z_s. The derivation follows the appendix of Cai et al. (2009), see also (Seljak, 1996; Smith et al., 2009; Nishizawa, 2014). The CMB temperature fluctuation induced by the ISW effect along the LOS direction $\hat{\mathbf{n}}$ is given by

$$\Theta \equiv \frac{\Delta T\left(\hat{\mathbf{n}}\right)}{\bar{T}} = \frac{2}{c^2}\int_{t_{\rm LSS}}^{t_0} \dot{\Phi}\left(t, \chi(t)\hat{\mathbf{n}}\right) \mathrm{d}t\,, \tag{E.0.1}$$

where $\bar{T}$ is the mean CMB temperature, t is the cosmic time, χ is the comoving distance along the LOS, and $\dot{\Phi}$ the time derivative of the gravitational potential Φ; t_0 and $t_{\rm LSS}$ are respectively the values of t at the observer (today) and the last-scattering surface. The spherical harmonic coefficients of Θ, defined in the same way as in Eq. (D.0.22), can be expressed as

$$a^{\Theta}_{\ell m} = \frac{i^\ell}{\pi^2 c^2}\int_{t_{\rm LSS}}^{t_0} \mathrm{d}t \int \mathrm{d}^3\mathbf{k}\dot{\Phi}(\mathbf{k}, a(\chi)) j_\ell(k\chi) Y^{m*}_\ell\left(\hat{\mathbf{k}}\right)\,, \tag{E.0.2}$$

where i is the imaginary number unit, the scale factor a is written as a function of the comoving LOS distance χ, $\chi_s \equiv \chi\left(z_s\right)$ the comoving distance of the source, and $\Phi(\mathbf{k})$ the Fourier transform of $\Phi(\boldsymbol{\chi})$:

$$\Phi\left(\mathbf{k}\right) = \frac{1}{(2\pi)^3}\int \mathrm{d}^3\boldsymbol{\chi}\Phi(\boldsymbol{\chi})\exp(i\mathbf{k}\cdot\boldsymbol{\chi})\,. \tag{E.0.3}$$

In deriving Eq. (E.0.2), we have used the spherical harmonic expansion of a plane wave:

$$\exp\left(i\mathbf{k}\cdot\boldsymbol{\chi}\right) = 4\pi\sum_{\ell m} i^{\ell} j_{\ell}(k\chi) Y_{\ell}^{m*}(\hat{\mathbf{k}}) Y_{\ell}^{m}(\hat{\mathbf{n}})\,, \tag{E.0.4}$$

and the orthonormality of the spherical harmonics:

$$\int_{\Omega} \mathrm{d}^2\hat{\mathbf{n}} Y_{\ell}^{m*}(\hat{\mathbf{n}}) Y_{\ell'}^{m'}(\hat{\mathbf{n}}) = \delta_{\ell'\ell}\delta_{m'm}\,, \tag{E.0.5}$$

where Ω denotes the solid angle, and $\delta_{\ell'\ell}$ and $\delta_{m'm}$ are the Kronecker deltas. The spherical harmonic expansion coefficient of the weak lensing convergence field, κ,

$$\kappa\left(\hat{\mathbf{n}}\right) = \frac{3H_0^2\Omega_m}{2c^2}\int_0^{\chi_s}\mathrm{d}\chi\frac{(\chi_s-\chi)\chi}{\chi_s}\frac{\delta}{a}\,, \tag{E.0.6}$$

can be similarly obtained, as

$$a_{\ell m}^{\kappa} = \frac{3H_0^2\Omega_m}{4\pi^2c^2} i^{\ell}\int_0^{\chi_s}\mathrm{d}\chi\frac{(\chi_s-\chi)\chi}{\chi_s a(\chi)}\int\mathrm{d}^3\mathbf{k}\delta(\mathbf{k},a(\chi))j_{\ell}(k\chi)Y_{\ell}^{m*}\left(\hat{\mathbf{k}}\right)\,, \tag{E.0.7}$$

where $\delta(\mathbf{k},a)$ is the Fourier transform of the density contrast field at scale factor a. Using the definition of the cross angular power spectrum given in Eq. (D.0.21), we get, after some lengthy but straightforward derivation,

$$C_{\ell}^{\Theta\kappa} = \frac{3H_0^2\Omega_m}{c^5}\int_0^{\chi_s}\mathrm{d}\chi\frac{\chi_s-\chi}{\chi_s\chi}P_{\dot{\Phi}\delta}\left(k=\frac{\ell}{\chi},a(\chi)\right)\,, \tag{E.0.8}$$

where we have used $c\mathrm{d}t = -a(t)\mathrm{d}\chi$, and the 3D cross power spectrum between $\dot{\Phi}$ and δ, $P_{\dot{\Phi}\delta}$, is given by

$$(2\pi)^3\delta^{(3)}\left(\mathbf{k}-\mathbf{k}'\right)P_{\dot{\Phi}\delta}(k,a) = \left\langle\dot{\Phi}^*(\mathbf{k},a)\delta(\mathbf{k}',a)\right\rangle\,, \tag{E.0.9}$$

where $\delta^{(3)}(\mathbf{k}-\mathbf{k}')$ is the 3D Dirac δ function. To evaluate $P_{\dot{\Phi}\delta}$, we make use of the Fourier-space Poisson equation,

$$-k^2\Phi(\mathbf{k}) = \frac{3}{2}H_0^2\Omega_m\frac{\delta(\mathbf{k})}{a}\,, \tag{E.0.10}$$

to get the derivative of $\Phi(\mathbf{k})$, as

$$\dot{\Phi}(\mathbf{k}) = -\frac{3}{2}\left(\frac{H_0}{k}\right)^2\Omega_m\left[\frac{\dot{\delta}(\mathbf{k})}{a}-\frac{H}{a}\delta(\mathbf{k})\right]\,, \tag{E.0.11}$$

with $H=\dot{a}/a$ being the Hubble expansion rate at a. Therefore, we have

$$\left\langle\dot{\Phi}^*(\mathbf{k})\delta(\mathbf{k}')\right\rangle = -\frac{3}{2}\left(\frac{H_0}{k}\right)^2\Omega_m\left\langle\frac{\dot{\delta}(\mathbf{k})}{a}-\frac{H}{a}\delta(\mathbf{k}),\delta(\mathbf{k}')\right\rangle\,, \tag{E.0.12}$$

and

$$P_{\dot{\Phi}\delta} = -\frac{3a}{4}\left(\frac{H_0}{k}\right)^2\Omega_m\frac{\mathrm{d}}{\mathrm{d}t}\left(a^{-2}P_{\delta\delta}(k,a)\right)\,, \tag{E.0.13}$$

where $P_{\delta\delta}$ is the matter power spectrum. Using the above relation, Eq. (E.0.8) can be simplified as

$$C_\ell^{\Theta\kappa} = \frac{9H_0^4\Omega_m^2}{4c^4\ell^2}\int_0^{z_s} \mathrm{d}z \frac{(\chi_s-\chi)\,\chi}{\chi_s}\frac{\mathrm{d}}{\mathrm{d}z}\left[(1+z)^2 P_{\delta\delta}\left(k=\frac{\ell}{\chi}, z\right)\right] . \tag{E.0.14}$$

where we have changed the integration variable and time derivatives to z. The $C_\ell^{\Theta\kappa}$ cross angular power spectrum is shown in the right panel of Fig. 6.5, for which Eq. (E.0.14) is evaluated using the nonlinear matter power spectra at different redshifts predicted by CAMB with HALOFIT. We find qualitatively similar result to the cross spectrum between the ISW effect and galaxies (e.g., Fig. 5 of Cai et al., 2009).

Bibliography

Abazajian, K.N., et al. (CMB-S4). *CMB-S4 Science Book, First Edition*. ArXiv e-prints (2016). arXiv:1610.02743.

Abbott, B.P., et al. (LIGO Scientific Collaboration and Virgo Collaboration). *Observation of Gravitational Waves from a Binary Black Hole Merger*. Phys. Rev. Lett., **116** (2016), 061102. URL https://link.aps.org/doi/10.1103/PhysRevLett.116.061102.

Abbott, B.P., et al. (LIGO Scientific, Virgo, Fermi GBM, INTEGRAL, IceCube, AstroSat Cadmium Zinc Telluride Imager Team, IPN, Insight-Hxmt, ANTARES, Swift, AGILE Team, 1M2H Team, Dark Energy Camera GW-EM, DES, DLT40, GRAWITA, Fermi-LAT, ATCA, ASKAP, Las Cumbres Observatory Group, OzGrav, DWF (Deeper Wider Faster Program), AST3, CAASTRO, VINROUGE, MASTER, J-GEM, GROWTH, JAGWAR, CaltechNRAO, TTU-NRAO, NuSTAR, Pan-STARRS, MAXI Team, TZAC Consortium, KU, Nordic Optical Telescope, ePESSTO, GROND, Texas Tech University, SALT Group, TOROS, BOOTES, MWA, CALET, IKI-GW Follow-up, H.E.S.S., LOFAR, LWA, HAWC, Pierre Auger, ALMA, Euro VLBI Team, Pi of Sky, Chandra Team at McGill University, DFN, ATLAS Telescopes, High Time Resolution Universe Survey, RIMAS, RATIR, SKA South Africa/MeerKAT). *Multi-messenger Observations of a Binary Neutron Star Merger*. Astrophys. J., **848**(2) (2017), L12. arXiv:1710.05833.

Abel, T., Hahn, O., Kaehler, R. *Tracing the dark matter sheet in phase space*. Monthly Notices of the Royal Astronomical Society, **427**(1) (2012), 61–76. ISSN 1365-2966. URL http://dx.doi.org/10.1111/j.1365-2966.2012.21754.x.

Adamek, J., Barrera-Hinojosa, C., Bruni, M., et al. *Numerical solutions to Einstein's equations in a shearing-dust universe: a code comparison*. Classical and Quantum Gravity, **37**(15) (2020), 154001. arXiv:2003.08014.

Adamek, J., Brandbyge, J., Fidler, C., et al. *The Effect of Early Radiation in N-Body*

Simulations of Cosmic Structure Formation. Monthly Notices of the Royal Astronomical Society, **470**(1) (2017a), 303. ISSN 0035-8711, 1365-2966. arXiv:1703.08585.

Adamek, J., Clarkson, C., Durrer, R., et al. *Does small scale structure significantly affect cosmological dynamics?* Phys. Rev. Lett., **114**(5) (2015), 051302. arXiv:1408.2741.

Adamek, J., Daverio, D., Durrer, R., et al. *General Relativistic N-body simulations in the weak field limit*. Phys. Rev., **D88**(10) (2013), 103527. arXiv:1308.6524.

Adamek, J., Daverio, D., Durrer, R., et al. *General relativity and cosmic structure formation*. Nature Phys., **12** (2016a), 346. arXiv:1509.01699.

Adamek, J., Daverio, D., Durrer, R., et al. *gevolution: a cosmological N-body code based on General Relativity*. JCAP, **1607**(07) (2016b), 053. arXiv:1604.06065.

Adamek, J., Durrer, R., Kunz, M. *N-body methods for relativistic cosmology*. Class. Quant. Grav., **31**(23) (2014), 234006. arXiv:1408.3352.

Adamek, J., Durrer, R., Kunz, M. *Relativistic N-body simulations with massive neutrinos*. JCAP, **1711**(11) (2017b), 004. arXiv:1707.06938.

Ade, P., et al. (Simons Observatory). *The Simons Observatory: Science goals and forecasts*. JCAP, **02** (2019), 056. arXiv:1808.07445.

Aghamousa, A., et al. (DESI). *The DESI Experiment Part I: Science,Targeting, and Survey Design* (2016). arXiv:1611.00036.

Aghanim, N., et al. (Planck). *Planck 2018 results. VI. Cosmological parameters* (2018). arXiv:1807.06209.

Alam, S., Croft, R.A.C., Ho, S., et al. *Relativistic Effects on Galaxy Redshift Samples due to Target Selection*. Mon. Not. Roy. Astron. Soc., **471**(2) (2017a), 2077. arXiv:1709.07856.

Alam, S., Zhu, H., Croft, R.A.C., et al. *Relativistic distortions in the large-scale clustering of SDSS-III BOSS CMASS galaxies*. Mon. Not. Roy. Astron. Soc., **470**(3) (2017b), 2822. arXiv:1709.07855.

Alcubierre, M. *Introduction to 3+1 numerical relativity*. International series of monographs on physics. Oxford Univ. Press, Oxford (2008). URL https://cds.cern.ch/record/1138167.

Alic, D., Bona-Casas, C., Bona, C., et al. *Conformal and covariant formulation of the Z4 system with constraint-violation damping.* Phys. Rev., **D85** (2012), 064040. arXiv:1106.2254.

Andrei S. Monin,, A. M. Yaglom. *Statistical Fluid Mechanics*, volume 2. MIT Press, Cambridge, Mass. (1971).

Andrianomena, S., Clarkson, C., Patel, P., et al. *Non-Linear Relativistic Contributions to the Cosmological Weak-Lensing Convergence.* Journal of Cosmology and Astroparticle Physics, **2014**(06) (2014), 023. ISSN 1475-7516.

Arnowitt, R., Deser, S., Misner, C.W. *Dynamical Structure and Definition of Energy in General Relativity.* Phys. Rev., **116** (1959), 1322. URL https://link.aps.org/doi/10.1103/PhysRev.116.1322.

Bardeen, J.M. *Gauge Invariant Cosmological Perturbations.* Phys. Rev. D, **22** (1980), 1882.

Barreira, A., Llinares, C., Bose, S., et al. *RAY-RAMSES: a code for ray tracing on the fly in N-body simulations.* JCAP, **1605**(05) (2016), 001. arXiv:1601.02012.

Barrera-Hinojosa, C., Li, B. *GRAMSES: a new route to general relativistic N-body simulations in cosmology. Part I. Methodology and code description.* JCAP, **2020**(1) (2020), 007. arXiv:1905.08890.

Barrera-Hinojosa, C., Li, B. *GRAMSES: a new route to general relativistic N-body simulations in cosmology. Part II. Initial Conditions.* Journal of Cosmology and Astroparticle Physics, **2020**(04) (2020), 056. ISSN 1475-7516. arXiv:2001.07968.

Barrera-Hinojosa, C., Li, B., Bruni, M., et al. *Vector modes in ΛCDM: the gravitomagnetic potential in dark matter haloes from relativistic N-body simulations.* Mon. Not. Roy. Astron. Soc., **501**(4) (2021), 5697. arXiv:2010.08257.

Bassett, B.A., Tsujikawa, S., Wands, D. *Inflation dynamics and reheating.* Rev. Mod. Phys., **78** (2006), 537. arXiv:astro-ph/0507632.

Baugh, C.M., Gaztanaga, E., Efstathiou, G. *A comparison of the evolution of density fields in perturbation theory and numerical simulations - II. Counts-in-cells analysis.* MNRAS, **274** (1995), 1049. arXiv:astro-ph/9408057.

Baumgarte, T.W., Shapiro, S.L. *On the numerical integration of Einstein's field equations.* Phys. Rev., **D59** (1999), 024007. arXiv:gr-qc/9810065.

Baumgarte, T.W., Shapiro, S.L. *Numerical relativity: solving Einstein's equations on the computer*. Cambridge University Press (2010).

Behroozi, P.S., Wechsler, R.H., Wu, H.Y. *The ROCKSTAR Phase-space Temporal Halo Finder and the Velocity Offsets of Cluster Cores*. ApJ, **762**(2) (2013), 109. arXiv:1110.4372.

Bentivegna, E., Bruni, M. *Effects of nonlinear inhomogeneity on the cosmic expansion with numerical relativity*. Phys. Rev. Lett., **116**(25) (2016), 251302. arXiv:1511.05124.

Bertschinger, E. *Cosmological dynamics: Course 1*. In *Les Houches Summer School on Cosmology and Large Scale Structure (Session 60)* (1993), pages 273–348. arXiv:astro-ph/9503125.

Bertschinger, E. *Multiscale Gaussian random fields for cosmological simulations*. Astrophys. J. Suppl., **137** (2001), 1. arXiv:astro-ph/0103301.

Bianchini, F., Silvestri, A. *Kinetic Sunyaev-Zel'dovich effect in modified gravity*. Phys. Rev. D, **93**(6) (2016), 064026. arXiv:1510.08844.

Blas, D., Lesgourgues, J., Tram, T. *The Cosmic Linear Anisotropy Solving System (CLASS). Part II: Approximation schemes*. JCAP, **2011**(7) (2011), 034. arXiv:1104.2933.

Bona, C., Ledvinka, T., Palenzuela, C., et al. *General covariant evolution formalism for numerical relativity*. Phys. Rev., **D67** (2003), 104005. arXiv:gr-qc/0302083.

Bonazzola, S., Gourgoulhon, E., Grandclement, P., et al. *A Constrained Scheme for Einstein Equations Based on Dirac Gauge and Spherical Coordinates*. Physical Review D, **70**(10) (2004), 104007. ISSN 1550-7998, 1550-2368. arXiv:gr-qc/0307082.

Bonvin, C. *Isolating Relativistic Effects in Large-Scale Structure*. Classical and Quantum Gravity, **31**(23) (2014), 234002. ISSN 0264-9381, 1361-6382.

Bonvin, C., Andrianomena, S., Bacon, D., et al. *Dipolar modulation in the size of galaxies: The effect of Doppler magnification*. Mon. Not. Roy. Astron. Soc., **472**(4) (2017), 3936. arXiv:1610.05946.

Bonvin, C., Durrer, R. *What Galaxy Surveys Really Measure*. Physical Review D, **84**(6) (2011), 063505. ISSN 1550-7998, 1550-2368. arXiv:1105.5280.

Bonvin, C., Durrer, R., Gasparini, M.A. *Fluctuations of the Luminosity Distance*. Physical Review D, **73**(2) (2006), 023523. ISSN 1550-7998, 1550-2368. arXiv:astro-ph/0511183.

Bonvin, C., Durrer, R., Khosravi, N., et al. *Redshift-Space Distortions from Vector Perturbations.* Journal of Cosmology and Astroparticle Physics, **2018**(02) (2018), 028. ISSN 1475-7516.

Bonvin, C., Hui, L., Gaztañaga, E. *Asymmetric Galaxy Correlation Functions.* Physical Review D, **89**(8) (2014), 083535. ISSN 1550-7998, 1550-2368.

Bonvin, C., Hui, L., Gaztanaga, E. *Optimising the measurement of relativistic distortions in large-scale structure.* JCAP, **1608**(08) (2016), 021. arXiv:1512.03566.

Borzyszkowski, M., Bertacca, D., Porciani, C. *LIGER: mock relativistic light-cones from Newtonian simulations.* Mon. Not. Roy. Astron. Soc., **471**(4) (2017), 3899. arXiv:1703.03407.

Breton, M.A., Rasera, Y., Taruya, A., et al. *Imprints of relativistic effects on the asymmetry of the halo cross-correlation function: from linear to non-linear scales.* Mon. Not. Roy. Astron. Soc., **483**(2) (2019), 2671. arXiv:1803.04294.

Bruni, M., Thomas, D.B., Wands, D. *Computing General Relativistic effects from Newtonian N-body simulations: Frame dragging in the post-Friedmann approach.* Phys. Rev., **D89**(4) (2014), 044010. arXiv:1306.1562.

Buchert, T. *On Backreaction in Newtonian cosmology.* Mon. Not. Roy. Astron. Soc., **473**(1) (2018), L46. arXiv:1704.00703.

Buchert, T., Ehlers, J. *Averaging inhomogeneous Newtonian cosmologies.* Astron. Astrophys., **320** (1997), 1. arXiv:astro-ph/9510056.

Buchert, T., Räsänen, S. *Backreaction in late-time cosmology.* Ann. Rev. Nucl. Part. Sci., **62** (2012), 57. arXiv:1112.5335.

Buchert, T., et al. *Is there proof that backreaction of inhomogeneities is irrelevant in cosmology?* Class. Quant. Grav., **32** (2015), 215021. arXiv:1505.07800.

Cabré, A., Fosalba, P., Gaztañaga, E., et al. *Error Analysis in Cross-Correlation of Sky Maps: Application to the Integrated Sachs–Wolfe Detection.* Monthly Notices of the Royal Astronomical Society, **381**(4) (2007), 1347. ISSN 1365-2966.

Cai, Y.C., Cole, S., Jenkins, A., et al. *Towards accurate modelling of the integrated Sachs–Wolfe effect: the non-linear contribution.* Mon. Not. Roy. Astron. Soc., **396** (2009), 772. arXiv:0809.4488.

Carrasco, J.J.M., Foreman, S., Green, D., et al. *The Effective Field Theory of Large Scale Structures at Two Loops*. JCAP, **07** (2014), 057. arXiv:1310.0464.

Castro, P.G. *Bispectrum and the Trispectrum of the Ostriker-Vishniac Effect*. Physical Review D, **67**(12) (2003), 123001. ISSN 0556-2821, 1089-4918.

Cautun, M.C., van de Weygaert, R. *The DTFE public software: The Delaunay Tessellation Field Estimator code*. ArXiv e-prints (2011), arXiv:1105.0370. arXiv:1105.0370.

Challinor, A., Lewis, A. *The linear power spectrum of observed source number counts*. Phys. Rev., **D84** (2011), 043516. arXiv:1105.5292.

chan Hwang, J., Noh, H., Gong, J.O. *Second-order Solutions of Cosmological Perturbation in the Matter-dominated Era*. The Astrophysical Journal, **752**(1) (2012), 50. URL https://doi.org/10.1088%2F0004-637x%2F752%2F1%2F50.

Chisari, N.E., Zaldarriaga, M. *Connection between Newtonian simulations and general relativity*. Phys. Rev., **D83** (2011), 123505. [Erratum: Phys. Rev.D84,089901(2011)], arXiv:1101.3555.

Colombi, S., Jaffe, A.H., Novikov, D., et al. *Accurate estimators of power spectra in N-body simulations*. Mon. Not. Roy. Astron. Soc., **393** (2009), 511. arXiv:0811.0313.

Cordero-Carrión, I., Cerdá-Durán, P., Dimmelmeier, H., et al. *Improved constrained scheme for the Einstein equations: An approach to the uniqueness issue*. Phys. Rev. D, **79** (2009), 024017. URL https://link.aps.org/doi/10.1103/PhysRevD.79.024017.

Cordero-Carrion, I., Cerda-Duran, P., Ibanez, J.M. *Gravitational waves in dynamical spacetimes with matter content in the Fully Constrained Formulation*. Phys. Rev., **D85** (2012), 044023. arXiv:1108.0571.

Cordero-Carrión, I., Ibáñez, J.M., Gourgoulhon, E., et al. *Mathematical Issues in a Fully-Constrained Formulation of Einstein Equations*. Physical Review D, **77**(8) (2008), 084007. ISSN 1550-7998, 1550-2368. arXiv:0802.3018.

Cordero-Carrion, I., Ibanez, J.M., Gourgoulhon, E., et al. *Mathematical Issues in a Fully-Constrained Formulation of Einstein Equations*. Phys. Rev., **D77** (2008), 084007. arXiv:0802.3018.

Cordero-Carrión, I., Vasset, N., Novak, J., et al. *Excision scheme for black holes in constrained evolution formulations: Spherically symmetric case.* Phys. Rev., **D90**(4) (2014), 044062. arXiv:1306.5976.

Crocce, M., Pueblas, S., Scoccimarro, R. *Transients from Initial Conditions in Cosmological Simulations.* Monthly Notices of the Royal Astronomical Society, **373**(1) (2006), 369. ISSN 0035-8711, 1365-2966. arXiv:astro-ph/0606505.

Croft, R.A.C. *Gravitational Redshifts from Large-Scale Structure.* Monthly Notices of the Royal Astronomical Society, **434**(4) (2013), 3008. ISSN 0035-8711, 1365-2966.

Crosta, M., Giammaria, M., Lattanzi, M.G., et al. *On Testing CDM and Geometry-Driven Milky Way Rotation Curve Models with Gaia DR2.* Monthly Notices of the Royal Astronomical Society, **496**(2) (2020), 2107. ISSN 0035-8711, 1365-2966.

Cuesta-Lazaro, C., Quera-Bofarull, A., Reischke, R., et al. *Gravitational Corrections to Light Propagation in a Perturbed FLRW-Universe and Corresponding Weak Lensing Spectra.* Monthly Notices of the Royal Astronomical Society, **477**(1) (2018), 741. ISSN 0035-8711, 1365-2966. arXiv:1801.03325.

Cusin, G., Tansella, V., Durrer, R. *Vorticity Generation in the Universe: A Perturbative Approach.* Physical Review D, **95**(6) (2017), 063527. ISSN 2470-0010, 2470-0029.

Darwish, O., Madhavacheril, M.S., Sherwin, B.D., et al. *The Atacama Cosmology Telescope: a CMB lensing mass map over 2100 square degrees of sky and its cross-correlation with BOSS-CMASS galaxies.* MNRAS, **500**(2) (2021), 2250. arXiv:2004.01139.

Daverio, D., Dirian, Y., Mitsou, E. *General Relativistic Cosmological N-body Simulations I: time integration* (2019). arXiv:1904.07841.

Dewdney, P.E., et al. . `http://skatelescope.org` (2013).

Dore, O., Hennawi, J.F., Spergel, D.N. *Beyond the Damping Tail: Cross-Correlating the Kinetic Sunyaev-Zel'dovich Effect with Cosmic Shear.* The Astrophysical Journal, **606**(1) (2004), 46. ISSN 0004-637X, 1538-4357.

Durrer, R., Tansella, V. *Vector Perturbations of Galaxy Number Counts.* Journal of Cosmology and Astroparticle Physics, **2016**(07) (2016), 037. ISSN 1475-7516. arXiv:1605.05974.

Dvali, G.R., Gabadadze, G., Porrati, M. *4-D gravity on a brane in 5-D Minkowski space.* Phys. Lett. B, **485** (2000), 208. arXiv:hep-th/0005016.

Dyson, F.W., Eddington, A.S., Davidson, C. *IX. A determination of the deflection of light by the sun's gravitational field, from observations made at the total eclipse of May 29, 1919.* Philosophical Transactions of the Royal Society of London. Series A, Containing Papers of a Mathematical or Physical Character, **220**(571-581) (1920), 291. arXiv:https://royalsocietypublishing.org/doi/pdf/10.1098/rsta.1920.0009, URL https://royalsocietypublishing.org/doi/abs/10.1098/rsta.1920.0009.

East, W.E., Wojtak, R., Abel, T. *Comparing Fully General Relativistic and Newtonian Calculations of Structure Formation.* Phys. Rev., **D97**(4) (2018), 043509. arXiv:1711.06681.

East, W.E., Wojtak, R., Pretorius, F. *Einstein-Vlasov Calculations of Structure Formation* (2019). arXiv:1908.05683.

Einstein, A. *Approximative Integration of the Field Equations of Gravitation.* Sitzungsber. Preuss. Akad. Wiss. Berlin (Math. Phys.), **1916** (1916a), 688.

Einstein, A. *Die Grundlage der allgemeinen Relativitätstheorie.* Annalen der Physik, **354**(7) (1916b), 769. arXiv:https://onlinelibrary.wiley.com/doi/pdf/10.1002/andp.19163540702, URL https://onlinelibrary.wiley.com/doi/abs/10.1002/andp.19163540702.

Elbers, W., Frenk, C.S., Jenkins, A., et al. *An optimal nonlinear method for simulating relic neutrinos* (2020). arXiv:2010.07321.

Everitt, C.W.F., DeBra, D.B., Parkinson, B.W., et al. *Gravity Probe B: Final Results of a Space Experiment to Test General Relativity.* Physical Review Letters, **106**(22) (2011), 221101. ISSN 0031-9007, 1079-7114.

Fidler, C., Rampf, C., Tram, T., et al. *General relativistic corrections to N-body simulations and the Zel'dovich approximation.* Phys. Rev., **D92**(12) (2015), 123517. arXiv:1505.04756.

Fidler, C., Tram, T., Rampf, C., et al. *Relativistic Interpretation of Newtonian Simulations for Cosmic Structure Formation.* JCAP, **1609**(09) (2016), 031. arXiv:1606.05588.

Fidler, C., Tram, T., Rampf, C., et al. *General relativistic weak-field limit and Newtonian N-body simulations.* JCAP, **1712**(12) (2017a), 022. arXiv:1708.07769.

Fidler, C., Tram, T., Rampf, C., et al. *Relativistic initial conditions for N-body simulations.* JCAP, **1706**(06) (2017b), 043. arXiv:1702.03221.

Flender, S.F., Schwarz, D.J. *Newtonian versus relativistic cosmology.* Phys. Rev., **D86** (2012), 063527. arXiv:1207.2035.

Friedmann, A. *Über die Krümmung des Raumes.* Zeitschrift fur Physik, **10** (1922), 377.

Friedmann, A. *Über die Möglichkeit einer Welt mit konstanter negativer Krümmung des Raumes.* Zeitschrift fur Physik, **21**(1) (1924), 326.

Garoffolo, A., Raveri, M., Silvestri, A., et al. *Detecting Dark Energy Fluctuations with Gravitational Waves.* arXiv:2007.13722 [astro-ph, physics:gr-qc] (2020). arXiv:2007.13722.

Gaztanaga, E., Bonvin, C., Hui, L. *Measurement of the dipole in the cross-correlation function of galaxies.* JCAP, **1701**(01) (2017), 032. arXiv:1512.03918.

Giblin, J.T., Mertens, J.B., Starkman, G.D. *Departures from the Friedmann-Lemaitre-Robertston-Walker Cosmological Model in an Inhomogeneous Universe: A Numerical Examination.* Phys. Rev. Lett., **116**(25) (2016), 251301. arXiv:1511.01105.

Giblin, J.T., Mertens, J.B., Starkman, G.D. *A cosmologically motivated reference formulation of numerical relativity.* Class. Quant. Grav., **34**(21) (2017), 214001. arXiv:1704.04307.

Giblin, J.T., Mertens, J.B., Starkman, G.D., et al. *The Limited Accuracy of Linearized Gravity* (2018). arXiv:1810.05203.

Giusarma, E., Alam, S., Zhu, H., et al. *Relativistic asymmetries in the galaxy cross-correlation function* (2017). arXiv:1709.07854.

Goldwirth, D.S., Piran, T. *Spherical inhomogeneous cosmologies and inflation: Numerical methods.* Phys. Rev., **D40** (1989), 3263.

Górski, K.M., Hivon, E., Banday, A.J., et al. *HEALPix: A Framework for High-Resolution Discretization and Fast Analysis of Data Distributed on the Sphere.* ApJ, **622**(2) (2005), 759. arXiv:astro-ph/0409513.

Gressel, H.A., Bonvin, C., Bruni, M., et al. *Full-sky weak lensing: a nonlinear post-Friedmann treatment.* JCAP, **05** (2019), 045. arXiv:1902.00059.

Guandalin, C., Adamek, J., Bull, P., et al. *Observing Relativistic Features in Large-Scale Structure Surveys – I. Multipoles of the Power Spectrum.* Monthly Notices of the Royal Astronomical Society, **501**(2) (2021), 2547. ISSN 0035-8711, 1365-2966.

Gundlach, C., Martin-Garcia, J.M., Calabrese, G., et al. *Constraint damping in the Z4 formulation and harmonic gauge.* Class. Quant. Grav., **22** (2005), 3767. arXiv:gr-qc/0504114.

Hahn, O., Angulo, R.E., Abel, T. *The Properties of Cosmic Velocity Fields.* Monthly Notices of the Royal Astronomical Society, **454**(4) (2015), 3920. ISSN 0035-8711, 1365-2966.

Hall, A., Bonvin, C., Challinor, A. *Testing general relativity with 21-cm intensity mapping.* Phys. Rev. D, **87**(6) (2013), 064026. arXiv:1212.0728.

Hand, N., Feng, Y., Beutler, F., et al. *nbodykit: an open-source, massively parallel toolkit for large-scale structure.* Astron. J., **156**(4) (2018), 160. arXiv:1712.05834.

He, J.h., Li, B., Hawken, A.J. *Effective dark matter power spectra in $f(R)$ gravity.* Phys. Rev. D, **92**(10) (2015), 103508. arXiv:1505.03656.

Heinesen, A., Buchert, T. *Solving the curvature and Hubble parameter inconsistencies through structure formation-induced curvature.* Class. Quant. Grav., **37**(16) (2020), 164001. [Erratum: Class.Quant.Grav. 37, 229601 (2020)], arXiv:2002.10831.

Hockney, R.W., Eastwood, J.W. *Computer Simulation using particles.* Taylor & Francis (Inc., Bristol, PA, USA, 1988).

Hopkins, P.F. *A new class of accurate, mesh-free hydrodynamic simulation methods.* Mon. Not. Roy. Astron. Soc., **450**(1) (2015), 53. arXiv:1409.7395.

Hu, W. *Dark synergy: Gravitational lensing and the CMB.* Phys. Rev. D, **65** (2002), 023003. arXiv:astro-ph/0108090.

Hu, W., Sawicki, I. *Models of f(R) Cosmic Acceleration that Evade Solar-System Tests.* Phys. Rev. D, **76** (2007), 064004. arXiv:0705.1158.

Hubble, E. *A relation between distance and radial velocity among extra-galactic nebulae.* Proceedings of the National Academy of Sciences, **15**(3) (1929), 168. ISSN 0027-8424. arXiv:https://www.pnas.org/content/15/3/168.full.pdf, URL `https://www.pnas.org/content/15/3/168`.

Iliev, I.T., Pen, U.L., Bond, J.R., et al. *The Kinetic Sunyaev-Zel'dovich Effect from Radiative Transfer Simulations of Patchy Reionization.* Astrophys. J., **660** (2007), 933. arXiv:astro-ph/0609592.

Isenberg, J.A. *Waveless approximation theories of gravity.* Int. J. Mod. Phys., **D17** (2008), 265. arXiv:gr-qc/0702113.

Jaffe, A.H., Kamionkowski, M. *Calculation of the Ostriker-Vishniac Effect in Cold Dark Matter Models.* Physical Review D, **58**(4) (1998), 043001. ISSN 0556-2821, 1089-4918.

Jelic-Cizmek, G., Lepori, F., Adamek, J., et al. *The generation of vorticity in cosmological N-body simulations.* JCAP, **1809**(09) (2018), 006. arXiv:1806.05146.

Jolicoeur, S., Allahyari, A., Clarkson, C., et al. *Imprints of local lightcone projection effects on the galaxy bispectrum IV: Second-order vector and tensor contributions.* JCAP, **03** (2019), 004. arXiv:1811.05458.

Kaiser, N. *Why there is no Newtonian backreaction.* Mon. Not. Roy. Astron. Soc., **469**(1) (2017), 744. arXiv:1703.08809.

Kidder, L.E., Scheel, M.A., Teukolsky, S.A. *Extending the lifetime of 3-D black hole computations with a new hyperbolic system of evolution equations.* Phys. Rev., **D64** (2001), 064017. arXiv:gr-qc/0105031.

Knox, L. *Determination of inflationary observables by cosmic microwave background anisotropy experiments.* Phys. Rev. D, **52** (1995), 4307. arXiv:astro-ph/9504054.

Lahav, O., Lilje, P.B., Primack, J.R., et al. *Dynamical effects of the cosmological constant.* Monthly Notices of the Royal Astronomical Society, **251**(1) (1991), 128. ISSN 0035-8711. arXiv:https://academic.oup.com/mnras/article-pdf/251/1/128/18523334/mnras251-0128.pdf, URL https://doi.org/10.1093/mnras/251.1.128.

Laureijs, R., Amiaux, J., Arduini, S., et al. *Euclid Definition Study Report.* ArXiv e-prints (2011). arXiv:1110.3193.

Lemaître, G. *Expansion of the universe, A homogeneous universe of constant mass and increasing radius accounting for the radial velocity of extra-galactic nebulae.* MNRAS, **91** (1931), 483.

Lepori, F., Adamek, J., Durrer, R., et al. *Weak-lensing observables in relativistic N-body simulations.* MNRAS, **497**(2) (2020), 2078. arXiv:2002.04024.

Lesgourgues, J. *The Cosmic Linear Anisotropy Solving System (CLASS) I: Overview.* arXiv e-prints (2011), arXiv:1104.2932. arXiv:1104.2932.

Lewis, A., Challinor, A., Lasenby, A. *Efficient computation of CMB anisotropies in closed FRW models.* Astrophys. J., **538** (2000), 473. arXiv:astro-ph/9911177.

Li, B., Zhao, G.B., Koyama, K. *Exploring Vainshtein mechanism on adaptively refined meshes.* JCAP, **2013**(5) (2013), 023. arXiv:1303.0008.

Li, B., Zhao, G.B., Teyssier, R., et al. *ECOSMOG: An Efficient Code for Simulating Modified Gravity.* JCAP, **1201** (2012), 051. arXiv:1110.1379.

Lichnérowicz, A. *Sur les équations relativistes de la gravitation.* Bulletin de la Société Mathématique de France, **80** (1952), 237. URL http://http://www.numdam.org/item/BSMF_1952__80__237_0.

Linder, E.V. *Cosmic growth history and expansion history.* Phys. Rev. D, **72** (2005), 043529. URL https://link.aps.org/doi/10.1103/PhysRevD.72.043529.

Linder, E.V., Cahn, R.N. *Parameterized Beyond-Einstein Growth.* Astropart. Phys., **28** (2007), 481. arXiv:astro-ph/0701317.

Lu, T.H.C., Ananda, K., Clarkson, C. *Vector Modes Generated by Primordial Density Fluctuations.* Physical Review D, **77**(4) (2008), 043523. ISSN 1550-7998, 1550-2368.

Lu, T.H.C., Ananda, K., Clarkson, C., et al. *The cosmological background of vector modes.* JCAP, **0902** (2009), 023. arXiv:0812.1349.

Löffler, F., Faber, J., Bentivegna, E., et al. *The Einstein Toolkit: a community computational infrastructure for relativistic astrophysics.* Classical and Quantum Gravity, **29**(11) (2012), 115001. URL http://stacks.iop.org/0264-9381/29/i=11/a=115001.

Ma, C.P., Bertschinger, E. *Cosmological Perturbation Theory in the Synchronous and Conformal Newtonian Gauges.* The Astrophysical Journal, **455** (1995), 7. ISSN 0004-637X, 1538-4357. arXiv:astro-ph/9506072.

Macpherson, H., Price, D.J., Lasky, P.D. *Einstein's Universe: Cosmological structure formation in numerical relativity* (2018a). arXiv:1807.01711.

Macpherson, H.J., Lasky, P.D., Price, D.J. *Inhomogeneous Cosmology with Numerical Relativity.* Phys. Rev., **D95**(6) (2017), 064028. arXiv:1611.05447.

Macpherson, H.J., Lasky, P.D., Price, D.J. *The trouble with Hubble: Local versus global expansion rates in inhomogeneous cosmological simulations with numerical relativity.* Astrophys. J., **865**(1) (2018b), L4. arXiv:1807.01714.

Martel, H., Shapiro, P.R. *A convenient set of comoving cosmological variables and their application.* Mon. Not. Roy. Astron. Soc., **297** (1998), 467. arXiv:astro-ph/9710119.

Masaru, S. *Numerical Relativity.* 100 Years Of General Relativity. World Scientific Publishing Company (2015). ISBN 9789814699747. URL https://books.google.co.uk/books?id=7WbFCwAAQBAJ.

Matarrese, S., Mollerach, S., Bruni, M. *Relativistic second-order perturbations of the Einstein–de Sitter universe.* Physical Review D, **58**(4) (1998a), 043504. ISSN 0556-2821, 1089-4918. URL https://link.aps.org/doi/10.1103/PhysRevD.58.043504.

Matarrese, S., Mollerach, S., Bruni, M. *Second order perturbations of the Einstein-de Sitter universe.* Phys. Rev., **D58** (1998b), 043504. arXiv:astro-ph/9707278.

Matarrese, S., Pantano, O., Saez, D. *A Relativistic approach to gravitational instability in the expanding Universe: Second order Lagrangian solutions.* Mon. Not. Roy. Astron. Soc., **271** (1994), 513. arXiv:astro-ph/9403032.

McDonald, P. *Gravitational Redshift and Other Redshift-Space Distortions of the Imaginary Part of the Power Spectrum.* Journal of Cosmology and Astroparticle Physics, **2009**(11) (2009), 026. ISSN 1475-7516.

Mertens, J.B., Giblin, J.T., Starkman, G.D. *Integration of inhomogeneous cosmological spacetimes in the BSSN formalism.* Phys. Rev., **D93**(12) (2016), 124059. arXiv:1511.01106.

Milillo, I., Bertacca, D., Bruni, M., et al. *Missing link: A nonlinear post-Friedmann framework for small and large scales.* Phys. Rev. D, **92**(2) (2015), 023519. arXiv:1502.02985.

Mitchell, M.A., Arnold, C., Hernández-Aguayo, C., et al. *The Impact of Modified Gravity on the Sunyaev-Zel'dovich Effect.* Monthly Notices of the Royal Astronomical Society, **501**(3) (2021), 4565. ISSN 0035-8711, 1365-2966. arXiv:2011.00013.

Nakamura, T., Oohara, K., Kojima, Y. *General Relativistic Collapse to Black Holes and Gravitational Waves from Black Holes.* Progress of Theoretical Physics Supplement, **90** (1987), 1. URL http://dx.doi.org/10.1143/PTPS.90.1.

Narikawa, T., Yamamoto, K. *Characterising linear growth rate of cosmological density perturbations in f(R) model.* Phys. Rev., **D81** (2010), 043528. [Erratum: Phys. Rev.D81,129903(2010)], arXiv:0912.1445.

Navarro, J.F., Frenk, C.S., White, S.D. *The Structure of cold dark matter halos.* Astrophys. J., **462** (1996), 563. arXiv:astro-ph/9508025.

Nishizawa, A.J. *The integrated Sachs-Wolfe effect and the Rees-Sciama effect.* Progress of Theoretical and Experimental Physics, **2014**(6) (2014), 06B110. arXiv:1404.5102.

Ostriker, J.P., Vishniac, E.T. *Generation of Microwave Background Fluctuations from Nonlinear Perturbations at the ERA of Galaxy Formation.* ApJ, **306** (1986), L51.

Park, H., Komatsu, E., Shapiro, P.R., et al. *THE IMPACT OF NONLINEAR STRUCTURE FORMATION ON THE POWER SPECTRUM OF TRANSVERSE MOMENTUM FLUCTUATIONS AND THE KINETIC SUNYAEV–ZEL'DOVICH EFFECT.* The Astrophysical Journal, **818**(1) (2016), 37. ISSN 1538-4357.

Park, H., Shapiro, P.R., Komatsu, E., et al. *THE KINETIC SUNYAEV-ZEL'DOVICH EFFECT AS A PROBE OF THE PHYSICS OF COSMIC REIONIZATION: THE EFFECT OF SELF-REGULATED REIONIZATION.* The Astrophysical Journal, **769**(2) (2013), 93. ISSN 0004-637X, 1538-4357.

Perlmutter, S., Aldering, G., Goldhaber, G., et al. *Measurements of* Ω *and* Λ *from 42 High-Redshift Supernovae.* The Astrophysical Journal, **517**(2) (1999), 565. URL https://doi.org/10.1086/307221.

Pettinari, G.W., Fidler, C., Crittenden, R., et al. *The intrinsic bispectrum of the Cosmic Microwave Background.* JCAP, **1304** (2013), 003. arXiv:1302.0832.

Planck Collaboration, Aghanim, N., Akrami, Y., et al. *Planck 2018 results. VIII. Gravitational lensing.* A&A, **641** (2020), A8. arXiv:1807.06210.

Press, W.H., Teukolsky, S.A., Vetterling, W.T., et al. *Numerical Recipes: The Art of Scientific Computing.* Cambridge University Press, 3 edition (2007).

Pretorius, F. *Numerical relativity using a generalized harmonic decomposition.* Class. Quant. Grav., **22** (2005), 425. arXiv:gr-qc/0407110.

Pretorius, F., East, W.E. *Black Hole Formation from the Collision of Plane-Fronted Gravitational Waves.* Phys. Rev., **D98**(8) (2018), 084053. arXiv:1807.11562.

Prunet, S., Pichon, C., Aubert, D., et al. *Initial Conditions for Large Cosmological Simulations.* Astrophys. J. Suppl., **178** (2008), 179. arXiv:0804.3536.

Pueblas, S., Scoccimarro, R. *Generation of Vorticity and Velocity Dispersion by Orbit Crossing*. Physical Review D, **80**(4) (2009), 043504. ISSN 1550-7998, 1550-2368.

Reverberi, L., Daverio, D. *`fRevolution` – Relativistic Cosmological Simulations in $f(R)$ Gravity I: Methodology* (2019). arXiv:1905.07345.

Reverdy, V. *PhD Thesis*. Laboratoire Univers et Th́eories (2014).

Reverdy, V., Alimi, J.M., Rasera, Y. *Light Propagation through Cosmic Structures Using Cosmological Simulations*. In *The Fourteenth Marcel Grossmann Meeting*. WORLD SCIENTIFIC, University of Rome "La Sapienza", Italy (2017). ISBN 978-981-322-659-3 978-981-322-660-9, pages 2302–2307.

Riess, A.G., Filippenko, A.V., Challis, P., et al. *Observational Evidence from Supernovae for an Accelerating Universe and a Cosmological Constant*. The Astronomical Journal, **116**(3) (1998), 1009. URL https://doi.org/10.1086/300499.

Riess, A.G., et al. *A 2.4% Determination of the Local Value of the Hubble Constant*. Astrophys. J., **826**(1) (2016), 56. arXiv:1604.01424.

Robertson, H.P. *Relativistic Cosmology*. Rev. Mod. Phys., **5** (1933), 62. URL https://link.aps.org/doi/10.1103/RevModPhys.5.62.

Roukema, B.F. *Replacing dark energy by silent virialisation*. Astron. Astrophys., **610** (2018), A51. arXiv:1706.06179.

Roukema, B.F., Ostrowski, J.J., Mourier, P., et al. *Does spatial flatness forbid the turnaround epoch of collapsing structures?* (2019). arXiv:1902.09064.

Rubin, V.C., Ford, W. Kent, J. *Rotation of the Andromeda Nebula from a Spectroscopic Survey of Emission Regions*. ApJ, **159** (1970), 379.

Saga, S., Yamauchi, D., Ichiki, K. *Weak lensing induced by second-order vector mode*. Phys. Rev. D, **92**(6) (2015), 063533. arXiv:1505.02774.

Sawicki, I., Bellini, E. *Limits of quasistatic approximation in modified-gravity cosmologies*. Phys. Rev. D, **92**(8) (2015), 084061. arXiv:1503.06831.

Scannapieco, E. *Is There a Detectable Vishniac Effect?* The Astrophysical Journal, **540**(1) (2000), 20. ISSN 0004-637X, 1538-4357.

Schaap, W.E., van de Weygaert, R. *Continuous fields and discrete samples: reconstruction through Delaunay tessellations.* A&A, **363** (2000), L29. arXiv:astro-ph/0011007.

Schäfer, B.M., Bartelmann, M. *Weak Lensing in the Second Post-Newtonian Approximation: Gravitomagnetic Potentials and the Integrated Sachs–Wolfe Effect.* Monthly Notices of the Royal Astronomical Society, **369**(1) (2006), 425. ISSN 0035-8711, 1365-2966.

Schaye, J., et al. *The EAGLE project: Simulating the evolution and assembly of galaxies and their environments.* Mon. Not. Roy. Astron. Soc., **446** (2015), 521. arXiv:1407.7040.

Schneider, P., Ehlers, J., Falco, E.E. *Gravitational Lenses.* Astronomy and Astrophysics Library. Springer Berlin Heidelberg, Berlin, Heidelberg (1992). ISBN 978-3-540-66506-9 978-3-662-03758-4.

Scoccimarro, R. *Transients from initial conditions: a perturbative analysis.* Mon. Not. Roy. Astron. Soc., **299** (1998), 1097. arXiv:astro-ph/9711187.

Scrimgeour, M., et al. *The WiggleZ Dark Energy Survey: the transition to large-scale cosmic homogeneity.* Mon. Not. Roy. Astron. Soc., **425** (2012), 116. arXiv:1205.6812.

Seljak, U. *Rees-Sciama Effect in a Cold Dark Matter Universe.* ApJ, **460** (1996), 549. arXiv:astro-ph/9506048.

Sereno, M. *Gravitational Lensing by Spinning and Radially Moving Lenses.* Physics Letters A, **305**(1-2) (2002), 7. ISSN 03759601.

Sereno, M. *Gravitational Lensing in Metric Theories of Gravity.* Physical Review D, **67**(6) (2003), 064007. ISSN 0556-2821, 1089-4918.

Sereno, M. *Kinematic Effect in Gravitational Lensing by Clusters of Galaxies: Kinematic Effect in GL by Galaxy Clusters.* Monthly Notices of the Royal Astronomical Society, **380**(3) (2007), 1023. ISSN 00358711.

Shibata, M. *3-D numerical simulation of black hole formation using collisionless particles: Triplane symmetric case.* Prog. Theor. Phys., **101** (1999), 251.

Shibata, M., Nakamura, T. *Evolution of three-dimensional gravitational waves: Harmonic slicing case.* Phys. Rev. D, **52** (1995), 5428. URL https://link.aps.org/doi/10.1103/PhysRevD.52.5428.

Shibata, M., Sasaki, M. *Black hole formation in the Friedmann universe: Formulation and computation in numerical relativity.* Phys. Rev., **D60** (1999), 084002. arXiv:gr-qc/9905064.

Smarr, L., York, J.W. *Kinematical Conditions in the Construction of Spacetime.* Physical Review D, **17**(10) (1978a), 2529. ISSN 0556-2821.

Smarr, L., York, J.W. *Radiation Gauge in General Relativity.* Physical Review D, **17**(8) (1978b), 1945. ISSN 0556-2821.

Smith, R.E., Hernández-Monteagudo, C., Seljak, U. *Impact of scale dependent bias and nonlinear structure growth on the integrated Sachs-Wolfe effect: Angular power spectra.* Phys. Rev. D, **80**(6) (2009), 063528. arXiv:0905.2408.

Springel, V. *The Cosmological simulation code GADGET-2.* Mon. Not. Roy. Astron. Soc., **364** (2005), 1105. arXiv:astro-ph/0505010.

Springel, V., et al. *Simulating the joint evolution of quasars, galaxies and their large-scale distribution.* Nature, **435** (2005), 629. arXiv:astro-ph/0504097.

Sunyaev, R.A., Zeldovich, Y.B. *The velocity of clusters of galaxies relative to the microwave background - The possibility of its measurement.* MNRAS, **190** (1980), 413.

Tang, C., Zhang, P., Luo, W., et al. *Measuring the gravitomagnetic distortion from rotating halos I: methods.* Astrophys. J., **911**(1) (2021), 44. arXiv:2009.12011.

Tansella, V., Bonvin, C., Cusin, G., et al. *Redshift-space distortions from vector perturbations. II. Anisotropic signal.* Physical Review D, **98**(10) (2018), 103515. ISSN 2470-0010, 2470-0029. URL https://link.aps.org/doi/10.1103/PhysRevD.98.103515.

Tartaglia, A., Bassan, M., Casalino, L., et al. *Detecting the Gravito-Magnetic Field of the Dark Halo of the Milky Way - the LaDaHaD Mission Concept: LaDaHaD.* Experimental Astronomy (2021). ISSN 0922-6435, 1572-9508.

Taylor, A.R., Jagannathan, P. *Alignments of radio galaxies in deep radio imaging of ELAIS N1.* Monthly Notices of the Royal Astronomical Society: Letters, **459**(1) (2016), L36–L40. ISSN 1745-3933. URL http://dx.doi.org/10.1093/mnrasl/slw038.

Teyssier, R. *Cosmological hydrodynamics with adaptive mesh refinement: a new high resolution code called ramses.* Astron. Astrophys., **385** (2002), 337. arXiv:astro-ph/0111367.

Thomas, D.B., Bruni, M., Koyama, K., et al. *f(R) gravity on non-linear scales: The post-Friedmann expansion and the vector potential.* JCAP, **1507**(07) (2015a), 051. arXiv:1503.07204.

Thomas, D.B., Bruni, M., Wands, D. *Relativistic weak lensing from a fully non-linear cosmological density field.* JCAP, **09** (2015b), 021. arXiv:1403.4947.

Thomas, D.B., Bruni, M., Wands, D. *The fully non-linear post-Friedmann frame-dragging vector potential: Magnitude and time evolution from N-body simulations.* Mon. Not. Roy. Astron. Soc., **452**(2) (2015c), 1727. arXiv:1501.00799.

Tian, C., Anselmi, S., Carney, M.F., et al. *Question of measuring spatial curvature in an inhomogeneous universe.* Phys. Rev. D, **103**(8) (2021), 083513. arXiv:2010.07274.

Valkenburg, W., Hu, B. *Initial conditions for cosmological N-body simulations of the scalar sector of theories of Newtonian, Relativistic and Modified Gravity.* JCAP, **1509**(09) (2015), 054. arXiv:1505.05865.

Vigneron, Q., Buchert, T. *Dark Matter from Backreaction? Collapse models on galaxy cluster scales* (2019). arXiv:1902.08441.

Vogelsberger, M., Genel, S., Springel, V., et al. *Properties of galaxies reproduced by a hydrodynamic simulation.* Nature, **509** (2014), 177. arXiv:1405.1418.

Walker, A.G. *On Milne's Theory of World-Structure.* Proceedings of the London Mathematical Society, **42** (1937), 90.

Weinberg, D.H., Mortonson, M.J., Eisenstein, D.J., et al. *Observational Probes of Cosmic Acceleration.* Phys. Rept., **530** (2013), 87. arXiv:1201.2434.

Weinberger, R., Springel, V., Pakmor, R. *The Arepo public code release.* Astrophys. J. Suppl., **248**(2) (2020), 32. arXiv:1909.04667.

Wilson, J.R., Mathews, G.J. *Relativistic hydrodynamics.* (1989), pages 306–314.

Yoo, J., Fitzpatrick, A.L., Zaldarriaga, M. *New perspective on galaxy clustering as a cosmological probe: General relativistic effects.* Phys. Rev., **D80** (2009), 083514. arXiv:0907.0707.

York, Jr., J.W. *Kinematics and dynamics of general relativity.* In L.L. Smarr, editor, *Sources of Gravitational Radiation* (1979), pages 83–126.

Zeldovich, Ya.B. *Gravitational instability: An Approximate theory for large density perturbations.* Astron. Astrophys., **5** (1970), 84.

Zhang, P.J., Pen, U.L., Trac, H. *Precision era of the kinetic Sunyaev-Zeldovich effect: Simulations, analytical models and observations and the power to constrain reionization.* Mon. Not. Roy. Astron. Soc., **347** (2004), 1224. arXiv:astro-ph/0304534.

Zhu, H., Alam, S., Croft, R.A.C., et al. *N-body simulations of gravitational redshifts and other relativistic distortions of galaxy clustering.* Mon. Not. Roy. Astron. Soc., **471**(2) (2017), 2345. arXiv:1709.07859.

Zwicky, F. *Die Rotverschiebung von extragalaktischen Nebeln.* Helvetica Physica Acta, **6** (1933), 110.